
UNIVERSITY OF
BIRMINGHAM

# Microstructure and Degradation Behaviour of Mg-Zn(-Ca) Alloys

**YU LU**

A thesis submitted to the University of Birmingham

for the degree of

**DOCTOR OF PHILOSOPHY**

2014

School of Metallurgy and Materials

University of Birmingham

Edgbaston

Birmingham

United Kingdom

B15 2T

# Preface

This research was carried out by Yu Lu in School of Metallurgy and Materials, University of Birmingham (from October 2010 to May 2014), under the supervision of Dr. Y. L. Chiu and Prof. I. P. Jones.

The present work is original and no part of the work has been submitted for another degree at any other university. Wherever other researchers' work has been drawn or cited, it is acknowledged in the text and the references are listed.

Parts of the work have been published as follows:

1. Y. Lu, A. R. Bradshaw, Y. L. Chiu, I. P. Jones, Investigation of the microstructure and bio-corrosion behaviour of Mg-Zn and Mg-Zn-Ca alloys, Materials Science Forum, Vol. 765 (2013), p. 788-792.
2. Y. Lu, A. R. Bradshaw, Y. L. Chiu, I. P. Jones, The role of $\beta_1'$precipitates in the bio-corrosion performance of Mg-3Zn in simulated body fluid, Journal of Alloys and Compounds, 614(2014), p.345-352

# Acknowledgements

I would like to sincerely thank Dr Yulung Chiu and Prof Ian Jones. There is an old Chinese saying that ‘Teaching a man how to fish is better than giving him a fish’ (from Lao Tzu). Now, I get the true meaning. Dr Yulung Chiu provides enlightening suggestions and innovative ideas which broadens my views and enhances my practical ability during my research. Prof Ian Jones not only supports my academic study with his wide scientific knowledge, but also improves my personal effectiveness with his encouragement and enthusiasm. It is enjoyable to work with two supervisors because of their kindness and sense of humour.

Many thanks are given to Dr Ming Chu and Dr Rengen Ding for their patience and practical guidance with the TEM operation skills. I would like to thank Mr Paul Stanley and Mrs Theresa Morris at Electron Microscope Centre for their guidance and help performing the SEM. I could never thank enough to Mr Andy Bradshaw not only for his truly incredible technical support during my experiments, but also for his precious kindness and encouragement.

I greatly acknowledge all the precious help and supports from Mr Alistair Watson at Nikon Metrology Limited and Mr Nick Corps at Bruker Limited.

Thanks to all my colleagues here: Kunle, Anqi, Ruiling, Xinxin, Thiago, Jing, Mingshi, Bo, Xinyu, Rayan, Zhaoyan, Gareth, Dan… It is a pleasant and wonderful experience to work with them. All of the support is of great appreciation.

My appreciation also goes to the financial support from the School of Metallurgy and Materials and China Scholarship Council (CSC). These have strongly supported me and helped me to devote all my time to do the research work.

Finally, I would like to thank my parents and boyfriend for their endless support, patience and love, which encourages me to be optimistic and enthusiastic of my study.

# Abstracts

Magnesium alloys are promising candidates for biomedical applications because of their advantageous properties as compared with other medical materials. However, a too high degradation rate can be a problem. There is a correct level of biodegradability for every application. It is not desirable for the material to degrade completely before tissue healing has taken place. In order to develop an alloy with an appropriate degradation rate, the microstructure - bio-corrosion rate relationship needs to be known.

In this study, the microstructural characterisation of Mg-3Zn(-0.3Ca) was analysed using optical microscopy (OM), scanning electron microscopy (SEM) and transmission electron microscopy (TEM). The second phases in the as-cast Mg-3Zn (MZ3) and Mg-3Zn-0.3Ca (MZX30) were identified: spherical ($\alpha$-Mg + MgZn) products in MZ3 and MgZn has a rhombohedral structure; ($\alpha$-Mg + $Ca_2Mg_6Zn_3$) products (globular and strip shaped) in MZX30 and $Ca_2Mg_6Zn_3$ has a trigonal structure. Quantitative TEM analysis is used to characterize the precipitation in the MZ3 with different ageing times at 160 ℃. The volume fraction of second phases and the grain size of MZX30 after different solution treatments were characterized quantitatively.

The corrosion morphologies of as-cast MZ3 and MZX30 after immersion test in a simulated body fluid at 37 ℃ were observed. It has been shown that corrosion initiates in the anodically active magnesium matrix in both as-cast MZ3 and MZX30. In the aged MZ3, it was found that nano-scale precipitates of MZ3 formed during ageing decrease the corrosion resistance. The increase in bio-corrosion rate with ageing time appears to be monotonic. A specific corrosion morphology in aged MZ3 was observed: parallel filament-like trenches which mirror the growth direction of the precipitates. The degradation rate of MZX30 changes with the solution treatment

parameters. The grain size and volume fraction of second phases are both key factors for controlling the bio-corrosion rate of MZX30. The minimum corrosion rate was observed in the MZX30 solution-treated at 420 $^{o}$C for 24 hours which has a balanced second phase volume fraction and grain size.

3D tomography obtained via FIB/SEM and Micro X-Ray CT was illustrated. 3D FIB tomography was used to show the internal lamellar structure of the ($\alpha$-Mg + MgZn) phases in the as-cast MZ3. MicroCT tomography of the as-cast MZX30 illustrated that the dendritic $\alpha$-Mg encloses a relatively large amount of ($\alpha$-Mg + $Ca_2Mg_6Zn_3$) phase mixture beneath the surface. 3D reconstructions of corroded as-cast MZ3 and MZX30 were shown. The corrosion of the magnesium matrix occurs on the sites adjacent to the second phases and penetrates into the interior of the sample.

An HA ($Ca_5(PO_4)_3 \cdot (OH)$) coating was formed on magnesium alloys consisting of dandelion-like aggregates of flake crystals with uniform morphology. It was found that the pitting corrosion on the HA-coated alloys occurs after long time immersion. The loose structure of the HA coating prevents its protection of the Mg substrate. The coated magnesium alloys suffers intensive corrosion due to galvanic corrosion after breaking down of the HA coating during immersion.

# Contents

# Chapter 1 Introduction

Biomaterial science is a compound subject covering biology, medical engineering and materials science [1]. Annually several million people suffer bone fracture or cardiovascular lesion caused by accidents or diseases. The internal bone implant, artificial joint and stent are in great demand [2]. Consequently, research into biomaterials has a profound impact.

Magnesium and its alloys have been widely used as structural materials in aerospace and automotive industries owing to good mechanical properties. Magnesium alloys, as a new kind of biomedical material, have attracted increasing attention due to their unique advantages, extremely low Young's modulus and weight, appropriate ductility and strength, excellent biocompatibility and attractive biodegradability [3-6]. Biodegradable magnesium alloys are breaking the current mould in biomaterial science of developing only corrosion resistant metals. In biomedical applications, magnesium alloys are ideal implants due to their outstanding comprehensive performance compared with other materials, such as stainless steel, polymers and ceramics.

Alloying magnesium is a necessary step to improve both mechanical and bio-corrosion properties. The choice of alloying elements is important. Alloying elements determine the microstructure and therefore influence the properties of alloys. In this study, calcium and zinc are selected to design bio-magnesium alloys. Alloying with Zn and Ca not only improves the hardness of magnesium alloys, thus to offer adequate support to the injured tissue/bone [7], but also they are non-toxic. Zinc is one of the most abundant nutritionally essential elements and is a co-factor for specific enzymes in bone [8, 9], and calcium is a major component in human bone

and beneficial to bone growth/healing [10]. It means Zn and Ca have good biocompatibilities.

Microstructure such as the distribution and volume fraction of second phase and grain size and chemical composition plays an important role in mechanical and bio-corrosion properties [11-13]. The effects of microstructure on the corrosion properties have been discussed, especially the influence of $Mg_{17}Al_{12}$ (β) in AZ91 [14-16]. However, there has been insufficient research on the effects of second phases in Mg-Zn(-Ca) alloys on their bio-corrosion performance, especially the influence of nano-scale second phase. Heat treatments offer an elegant way to modify the microstructure. The precipitation of Mg-3Zn alloys after ageing has been investigated and the volume fraction of nano-scale precipitates has been characterised quantitatively. The role of nano-scale precipitates on the hardness and bio-corrosion performance has been studied. After different solution treatments, the grain size and volume fraction of second phase change and hence the hardness and bio-corrosion behaviour are also modified. The relationship between the grain size and volume fraction of the ($\alpha$-Mg + $Ca_2Mg_6Zn_3$) phases and its bio-corrosion behaviour in solution-treated Mg-3Zn-0.3Ca alloys has been investigated.

Micro X-Ray computed tomography (Micro-CT) is a unique technique for the non-invasive, non-destructive 3-D characterization of materials in medicine, material science and biology. Micro-CT could characterize directly the 3D structure of alloys and also can handle large sample size with a simple sample preparation. This study offers the detailed analyses of the 3D characterisation of second phases in as-cast magnesium alloy and 3D distribution of bio-corrosion attack on magnesium alloys after immersion testing and thus reveals in a three-dimensional way the effect of microstructure on bio-corrosion. It is our interest to image the microstructures in 3D.

Surface modification is a simple way to alter the surface of an alloy specimen and control its bio-corrosion properties. A hydroxyapatite (HA) coating has been formed on Mg-3Zn(-0.3Ca) alloys to modify their bio-corrosion performance but still maintain good biocompatibility. The bio-degradation behaviour of coated Mg-3Zn(-0.3Ca) alloys has been studied via in vitro tests in simulated body fluid.

The outline of the thesis is as follows:

Chapter 2 presents an overview of the literature on biodegradable magnesium alloys, ways to improve the performance of bio-magnesium alloys, the corrosion behaviour of magnesium alloys and an introduction to the quantitative method of characterization of fine precipitates.

Chapter 3 summarizes the materials and methods used in the current study.

Chapter 4 characterizes the as-cast microstructure of Mg-3Zn and Mg-3Zn-0.3Ca alloys and presents the microstructural changes after different heat treatments. The 3D microstructural analyses of magnesium alloys are also investigated.

Chapter 5 investigates the relationship between the microstructure and biodegradation performance of Mg-3Zn(-0.3Ca) alloys and discusses the reasons for the variation of their bio-corrosion behaviour. The 3D structures of Mg-3Zn(-0.3Ca) alloys after immersing in simulated body fluid are reconstructed and discussed.

Chapter 6 is concerned with the HA coating of Mg-3Zn(-0.3Ca) alloys and its effect on biodegradation behaviour.

Chapter 7 draws some conclusions and gives some suggestions for future work.

The appendix describes a home-made vacuum melting and casting induction furnace for Mg alloys which has been used in this project.

# Chapter 2 Literature review

## 2.1 Introduction to magnesium

### 2.1.1 Atomic and crystal structure of magnesium

Magnesium is a chemical element with the symbol Mg. The crystal structure of pure magnesium is hexagonal close packed (HCP). The lattice parameters of pure magnesium are a= 0.32092 nm and c= 0.52105 nm, thus the c/a ratio is 1.6236. This actual value of c/a is very close to that of the ideal HCP crystal structure (1.633). The atomic positions, principal planes and directions are illustrated in Fig. 2.1 [17].

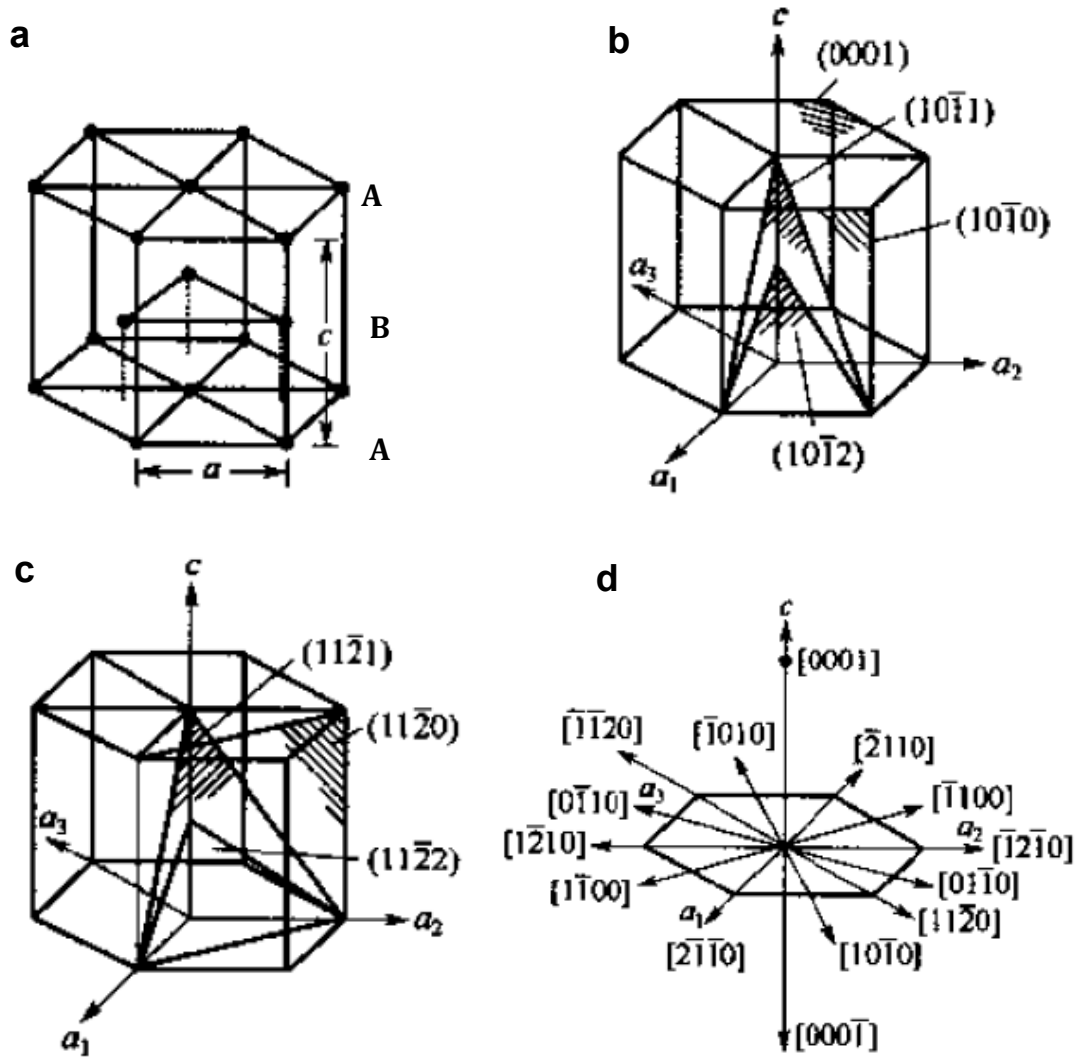


Fig. 2.1 The magnesium crystal: (a) atomic positions; (b) principal planes of the

$[1\bar{2}10]$ zone; (c) principal planes of the $[1\bar{1}00]$ zone; (d) principal directions (adapted from [17]).

### 2.1.2 Properties of magnesium

Magnesium is a ductile, brightly-coloured and chemically active metal. Magnesium is exceptionally lightweight with a low density of 1.739 g/cm$^3$ (at 293 K). This is the lightest practicable structural metal. The properties of pure magnesium are listed in Table 2.1 [18].

Table 2.1 Some basic properties of magnesium.

| **Properties** | **Temperature (K)** | **Value (units)** | **Properties** | **Temperature (K)** | **Value (units)** |
|---|---|---|---|---|---|
| Density | 293 | 1.739 (g/cm$^3$) | Standard Potential | 298 | -2.34 (V) |
| Young's Modulus | 298 | 45 (GPa) | Recrystallization Temperature | | 423 (K) |
| Melting Temperature | | 923 (K) | Vapour Pressure | 973 | 12.41 (mbar) |
| Boiling Temperature | | 1363 (K) | Brinell Hardness | 298 | 260 (MPa) |

### 2.1.3 Applications of magnesium

Magnesium was discovered in the late 1790's [19] and is the eighth most abundant element in the Earth's crust. Magnesium is also the third most commonly used structural metal, following iron and aluminium. It is popular because it can be easily machined, cast, forged and welded. Research into and applications of magnesium alloys have been in train for about two hundred years. During the Second World War, the development of magnesium alloys made remarkable progress in order to meet military needs, mostly in aircraft, in fuselages, engine parts and wheels. Nowadays, along with rapid developments in the auto, electronics and aerospace industries,

magnesium alloys are replacing the plastic enclosures which were used for mobiles, laptops and cameras due to its low weight, good stiffness, attractive metal lustre and favourable electromagnetic-shielding. It must be stressed that the development of magnesium-based alloys for biomedical applications has blossomed in recent years. In the past 10 years, there has been much literature concerning the bioabsorbable magnesium alloys. This work emphasized the possibility and performance of magnesium as a new class of degradable biomaterial for medical applications (e. g. Witte et al. [4, 5], Zheng et al. [20-22], Staiger et al. [23]).

## 2.2 Introduction to biomaterials

### 2.2.1 The concept of biomaterials

Biomaterial is a wide-ranging field, covering medical science, chemistry, biology and materials science (Fig. 2.2) [1]. A biomaterial is defined as a material intended to interface with biological systems to evaluate, treat, augment or replace any tissue, organ or function of the body [24]. Commonly, pacemakers, stents, sutures, bone plates and screws, needles, knee joints and catheters all constitute biomaterials. Biomaterials are used across a wide range of applications and have become a major industry in the 21st Century. According to the Health Industry Manufacturers Association (HIMA), the biomaterials and medical devices market maintains a robust growth. In the past 10 years, it has grown about 16% per year and reached 400 billion US dollars in 2010. Annually, several million patients have a significant requirement for biomaterials. Biomaterials are closer to people's lives than they might think.

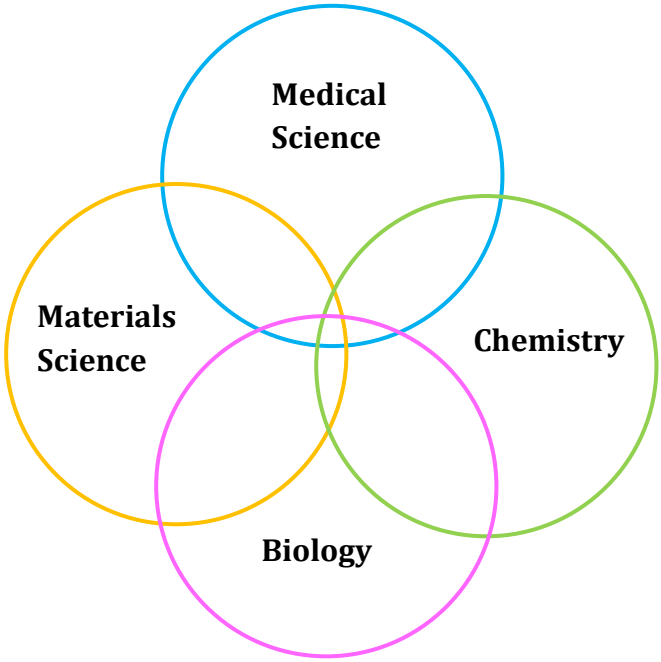


Fig. 2.2 Biomaterials encompasses various other disciplines.

### 2.2.2 Historical sketch of biomaterials

Metals have been used as biomaterials for more than 2000 years, for example, the Romans, Chinese and Aztecs used gold in dentistry 2000 years ago [25]. In the 1860s, Dr. J. Lister developed an aseptic surgical technique; thenceforth, the use of various metal devices such as wires and pins made of iron, gold, silver, platinum, etc. became largely practical and successful [26]. After the Second World War, biomaterials were developed rapidly and used extensively as internal fixation devices and implants [27]. Biomaterials can be categorized into two types: bioinert materials (first type) and bioactive and biodegradable materials (second type). The first type of biomaterials was as inert as possible in order to minimize the immune response and reduce the corrosion of the material itself. Typically these biomaterials are stainless steels and cobalt-chrome-based alloys. The second type is non-toxic or with little toxicity during use after implantation; in addition they can degrade while new tissue regenerates and heals. HA ($Ca_{10}(PO_4)_6(OH)_2$), HA as a coating on metals, polyglycolide (PGA), polylactide (PLA) and biodegradable Mg alloys all belong to this type.

### 2.2.3 Classification of biomaterials

During the past decades, remarkable progress has been made in the development of biomaterials. Generally, synthetic biomedical materials can be classified into: 1) Polymers; 2) Metals; 3) Ceramics and 4) Composite biomaterials. Table 2.2 summarizes these classes and gives some examples [28]. These materials are used in different applications as shown in Fig. 2.3 [29].

Table 2.2 Classification of biomaterials (adapted from [28]).

| **Synthetic Biomedical Materials** | **Examples** |
|---|---|
| Polymers | Ultra High Molecular Weight Polyethylene (UHMWPE), Polymethylmenthscsrylate (PMMA), Polyethyletherketone (PEEK), Silicone, Polyurethane (PU), Polytetrafluoroethylene (PTFE) |
| Metals | Stainless steel, Cobalt-based Alloys (Co-Cr-Mo), Titanium Alloy (Ti-Al-V), Gold, Platinum |
| Ceramics | Alumina ($Al_2O_3$), Zirconia ($ZrO_2$), Carbon, Hydroxyapatite [$Ca_{10}(PO_4)_6(OH)_2$], Tricalcium Phosphate [$Ca_3(PO_4)_2$], Bioglass [$Na_2O(CaO)(P_2O_3)(SiO_2)$], Calcium Aluminate [$Ca(Al_2O_4)$] |
| Composite biomaterials | Carbon Fibre (CF)/PEEK, CF/UHMWPE, CF/PMMA, Zirconia/Silica/NIS-GMA |

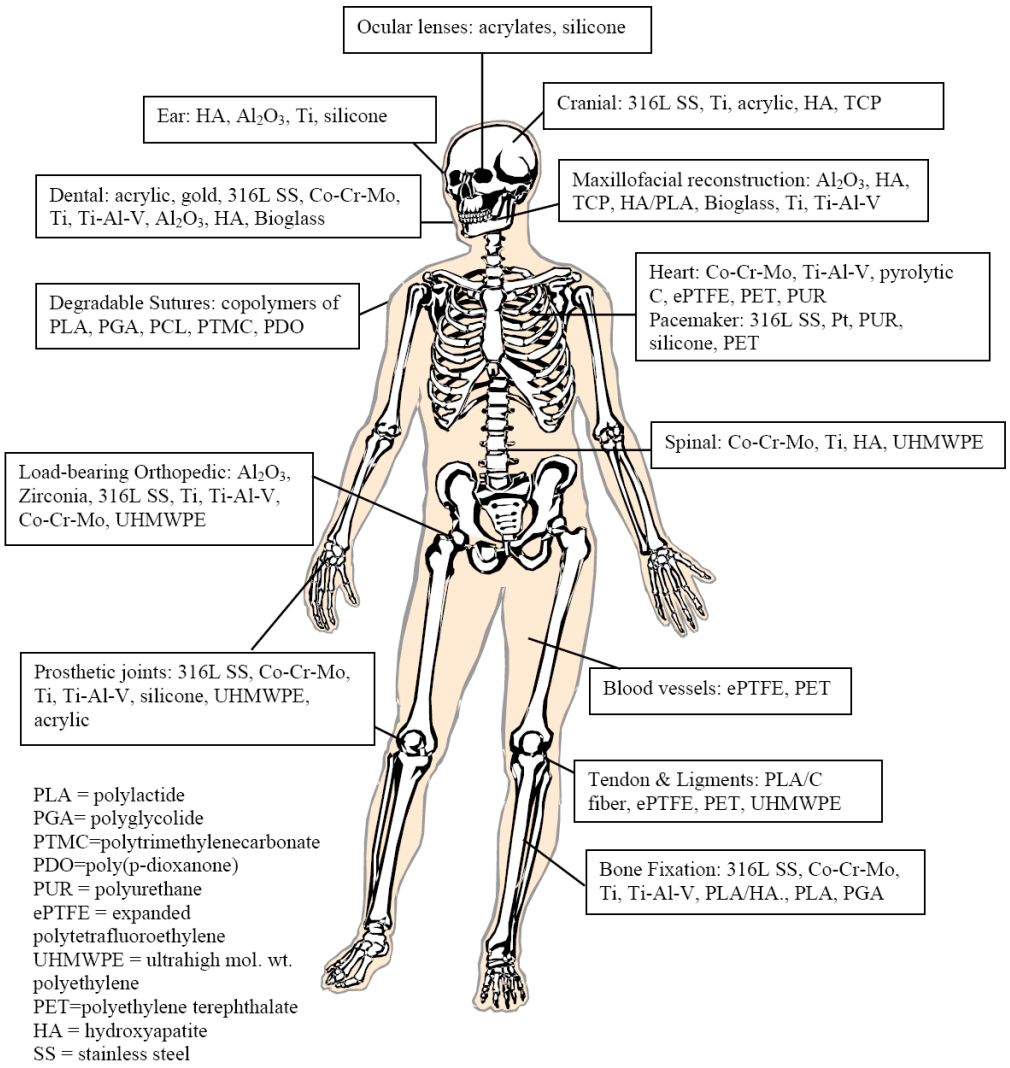


Fig. 2.3 Biomaterials in the human body (adapted from [29]).

Today, biomaterials occupy a large portion of the healthcare industry. Most medical devices also need biomaterial components, such as hip and knee replacements, replacement heart valves, heart-lung machines and synthetic vascular grafts. For instance, in the cardiovascular area, about 100,000 replacement heart valves and 300,000 vascular grafts are implanted annually in the USA [30]. Biomedical materials are in great demand. Thus, research into and development of biomaterials have a profound social impact and tremendous economic benefits.

## 2.3 Magnesium alloys as biomaterials

### 2.3.1 Preface

Magnesium possesses many of characteristics required of a biomaterial, such as outstanding biocompability, nontoxicity and noncarcinogenicity, low weight and density, relatively low price, good reproducibility and ease of fabrication and processing for large-scale production. Biodegradable magnesium alloys are breaking the mould in biomaterials science, which was developing corrosion resistant metals only. Biodegradable magnesium alloys have been studied as biomaterials for several decades. In 1945 they were used to treat gunshot wounds [31]. It must be emphasized that magnesium alloys can be biodegraded in the human body by natural corrosion as new tissue is formed. Therefore, bioabsorbable magnesium alloys with overall a splendid performance are becoming potential biomaterials. Nowadays, a lot of researchers are working in this pioneering field to develop new magnesium alloys for medical applications and to investigate their mechanical properties and corrosion performance [5, 22, 32-35].

### 2.3.2 Potential applications of biomedical magnesium alloys

Biodegradable magnesium alloys possess some outstanding advantages over other biomaterials, such as ceramics, polymers, etc. First of all, the density, elastic modulus and tensile strength of magnesium are closer to those for bone than for other implants (as shown in Table 2.3 [23, 36]). In particular, the stress shielding effect caused by the mismatch of elastic modulus between human bones and implants can be significantly mitigated. Bone is a living tissue and there is constant remodelling under imposed stress. If the load supporting the implant is too large, the bone beneath will bear a decreased load and become less dense and weaker because the stimulation and the continued remodelling which maintains bone mass is absent or reduced.

In Table 2.3, it can be seen that magnesium alloys have more appropriate mechanical properties than other biomaterials. Magnesium is an exceptionally lightweight metal with a density of 1.74-2.0 g/cm$^3$, which is close to that of bone (1.8-2.1 g/cm$^3$). Magnesium alloys are about 1/3 as dense as titanium alloys (4.4 g/cm$^3$) and around 1/5 as dense as stainless steel (7.9-8.1 g/cm$^3$). Magnesium alloys have an elastic modulus of 41-45 GPa, which is much lower than that of other traditional biomaterials, such as titanium alloys with 110-117 GPa and stainless steel with 205-210 GPa.

Table 2.3 Summary of the physical and mechanical properties of various implant materials in comparison with human bone [23, 36].

| | Density (g/cm$^3$) | Elastic modulus (GPa) | Tensile strength (MPa) | Fracture toughness (MPa$^{1/2}$) | Total Elongation (%) |
|---|---|---|---|---|---|
| Cortical bone$^{\ominus}$ | 1.8-2.1 | 3-20 | 35-283 | 3-6 | 1.07-2.10 |
| Cancellous bone$^{\ominus}$ | 1.0-1.4 | - | 1.5-38 | - | - |
| Magnesium alloys | 1.74-2.0 | 41-45 | 150-400 | 15-40 | 2-20 |
| Titanium alloy (TiAl6V4) | 4.4-4.5 | 110-117 | 830-1025 | 55-115 | 10-15 |
| Stainless steel (316L) | 7.9-8.1 | 205-210 | 480-620 | 50-200 | 30-40 |
| Co-Cr alloys | 8.3-9.2 | 230 | 450-1000 | - | - |
| Synthetic hydroxyapatites | 3.1 | 70-120 | 40-200 | 0.7 | - |

$^{\ominus}$ Different values are due to different races, age, testing conditions etc.

Secondly, an extremely important issue for biomedical materials is biocompatibility. Biocompatibility is the acceptance of an artificial implant by the surrounding tissues and by the body as a whole [37]. The element Mg is the fourth most abundant cation in the human body and $Mg^{2+}$ is an essential element for the human body (the daily

intake of $Mg^{2+}$ for a normal adult is about 300-400 mg). A high content of Mg is naturally found in the skeleton [38, 39]. Excess magnesium ions are harmless and can be excreted in the urine, while toxic element releases lead to metal allergy and skin disease, such as Ni in 316L. Magnesium is essential to the human metabolism and biological mechanisms [40]. It can stimulate the activity of enzymes and stabilize DNA and RNA [23, 39]. A number of in vivo and in vitro experiments have shown that magnesium alloys have good biocompatibility [41-43]. Witte et al. observed that the corrosion layer of magnesium alloys with an accumulation of biological calcium phosphates was in direct contact with the surrounding bone (Fig. 2.4 b)), while the polymer control shows lower bone area formed around it compared with a magnesium implant (Fig. 2.4 a)) [5]. It reveals that magnesium possesses a good biocompatibility. It has been reported that magnesium ions released from materials during gradual degradation benefit the growth and healing of tissues [5, 23].

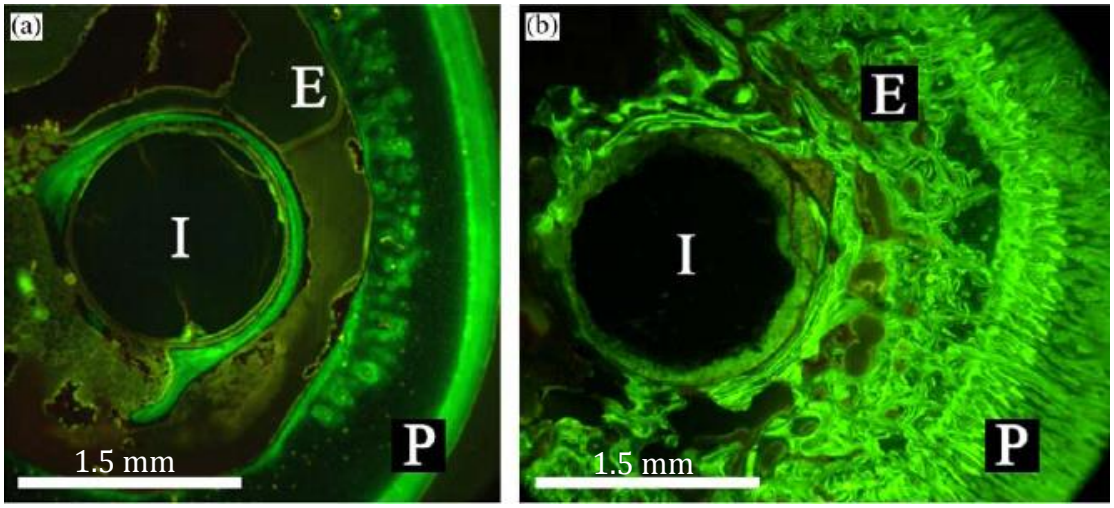


Fig. 2.4 Fluoroscopic images of cross-sections through a degradable polymer (a) and magnesium rod (b) implanted in the femurs of guinea pigs (adapted from [5]). In vivo staining of newly formed bone was resolved using calcein green. I: implant residual, P: periosteal formation, E: endosteal bone formation.

Thirdly, the high point of magnesium alloys as biomedical materials is

biodegradability. Magnesium alloys can be biodegraded in the human body by corrosion, which can eliminate second surgery for implant removal. Some in vivo studies showed that the degradation of magnesium alloy is harmless [5, 43, 44]. Additionally, it has been reported that magnesium stents can be successfully degraded and have a minimal effect on the surrounding tissue [45, 46].

Last, but not least, magnesium is not a precious or rare metal. The manufacture costs of biomedical devices can be significantly reduced on account of this advantage. This can lighten the financial burden on the patient.

### 2.3.3 Challenges for magnesium alloys as biomaterials

Although magnesium alloys possess many advantages, their main limitation as biomedical materials is their high corrosion rate. Magnesium has a high negative standard electrode potential of -2.34 V vs. the hydrogen electrode potential (NHE) at 25 ℃ [47]. In water, magnesium exhibits a potential of -1.75 V (NHE) because of the presence of a protective film [48]. It corrodes more quickly than other metallic materials, especially in a $Cl^-$ containing aqueous environment [49], including human body fluid or blood plasma. Biomaterials are contact with body fluid for a long term after implantation. A number of aggressive ions exists in the physiological environment, such as $Cl^-$, $HPO_4^{2-}$, $HCO^{3-}$ and $SO_4^{2-}$. The dissolution of magnesium is much faster in such an environment. It is desirable for a magnesium implant to remain present in the human body for more than 12 weeks to allow bone healing to take place, and then it should degrade gradually [5, 50]. But a too high degradation rate of magnesium alloys is an obstacle to its biomedical application.

Additionally, its mechanical properties are of concern. Initially, biodegradable magnesium alloys must support the injury and carry the load to provide a sufficient

time for tissue healing. The implant should gradually and slowly degrade and transfer the load to the human body over time [51]. Before the injury heals, the implant has constantly to sustain the injury and provide sufficient mechanical support. For orthopaedic biomaterial, a period of 3-4 months is requested for new bone formation and recovery of most of the bone's original strength [52]. It is expected that a biodegradable coronary stent should maintain its mechanical integrity for 6-12 months to allow for vessel remodelling and should completely degrade in 12-24 months [53].

### 2.3.4 Ways to improve the performance of magnesium alloys

Although fast corrosion kinetics can be generally beneficial in biodegradable alloys, there is a balance to be struck and magnesium alloys can have a significant problem if the corrosion rate is too high. Current magnesium alloys degrade too quickly in the human body and lose function before the tissue heals. Suitable strategies need to be developed to tailor the corrosion rate of biomedical magnesium alloys. For load bearing applications, good mechanical properties are required. Biomedical magnesium alloys are used as screws, pins and bone implants. To bend fixtures to fit properly requires an appropriate ductility. Magnesium alloys must also possess appropriate mechanical properties when applied as stents, for example, sufficient ductility for ease of fabrication and safe stent placement (ballooning requires ideally $\varepsilon_L \geq 15\%$); reasonable strength for supporting the blood vessel (implies ultimate tensile strength $\geq$ 250 MPa) [7]. However, pure magnesium does not suit the mechanical property requirements for medical application. Hence, Mg alloys are required.

#### 2.3.4.1 The effect of alloying elements

Alloying Mg is a necessary step to improve both corrosion performance and

mechanical properties. Alloying elements not only determine the composition and phase constitution of alloys, but also influence the distribution of the second phase. Various chemical elements such Al, Ca, Zn, Mn and the rare earths are used in magnesium biomaterials [54-60].

**1) Aluminium**

The maximum solubility of aluminium in magnesium is 12.7 wt%. As an alloying element, aluminium contributes to solid solution strengthening and precipitation strengthening and thus improves mechanical strength. Alloying Al with Mg can enhance the corrosion resistance [61]. The corrosion rate decreases significantly with the addition of aluminium up to 4 %, but there is little further improvement as the Al content increases to 9 % [14, 62]. However, it is also reported that Al causes the corrosion resistance to deteriorate. Al decreases the tolerance limit (impurity level) of iron from 170 wt.-ppm to 20 wt.-ppm [63]. This correlates with the formation of a passive Fe-Mn-Al intermetallic phase on solidification. Additionally, a high Al concentration increases the $Mg_{17}Al_{12}$ content, which accelerates the corrosion rate by forming galvanic couples [64].

The concentration of Al in normal blood serum is 2.1-4.8 μg/ L. It has been reported that Al is harmful to osteoblasts and to neuron function [65]. Its accumulation can cause muscle fibre damage and decreases osteoblast viability [66, 67]. Additionally, it is well documented that Al has a toxic influence in the serum or urine of patients who have had a total hip replacement [68].

**2) Calcium**

Calcium is a major component in human bone and is an important element in cell

signalling; released ions are beneficial for bone healing [69]. Ca can strengthen magnesium by both solution strengthening and precipitation strengthening. It can refine grain size to some extent and contributes to grain boundary strengthening, although as-cast Mg-Ca alloys are brittle at room temperature when the addition of Ca exceeds 5 wt%. Furthermore, Ca has a low density (1.55 g/cm$^3$), which endues the Mg-Ca alloy system with the advantage of having a similar density to bone [10, 69]. It is reported that the corrosion resistance can be improved by adding Ca moderately. The corrosion resistance improves significantly with small additions of Ca (<0.4 %) to Mg-0.6 wt% Si [13]. In as-cast Mg-Zn-Mn-Ca alloy, when Ca increases from 0.5 wt% to 1 wt%, the corrosion resistance is enhanced [58].

**3) Zinc**

Zinc is recognized as one of the most abundant and nutritionally essential elements in the human body and therefore is safe for biomedical applications. Zinc can improve both the corrosion resistance and the mechanical properties of magnesium. It has been reported that zinc is beneficial in increasing the tolerance limits of impurities and helps overcome the harmful corrosive effect of iron and nickel impurities [70, 71]. The addition of 1 wt% Zn to Mg can improve the tolerance limit (impurity level) of Ni [62]. It is reported that 3 wt% Zn increases the tolerance limit of Fe to 30 wt.-ppm and apparently decreases the corrosion rate for Fe concentrations up to 180 wt.-ppm in Mg-Al-Mn alloys [62]. The maximum solubility of zinc in magnesium is 6.2 wt%. Zn has a function in solid solution strengthening of magnesium, because Zn increases the critical resolved shear stress (CRSS) for basal slip [72]. Zn has a better strengthening effect than aluminium since regions of short-range order at the atomic scale form [73]. It can enhance castability but a higher concentration of Zn (>2 wt%) leads to embrittlement in combination with Al [70]. The limitation in adopting a higher content of Zn is the possibility of hot-cracking and the tendency to

microporosity during solidification.

**4) Manganese**

Manganese can refine the grain size and enhance the tensile strength of magnesium [74]. It has also been reported that the addition of Mn improves the ductility [36]. The important function of Mn lies in improving corrosion resistance, by converting iron and other metal elements (Al) into relatively harmless intermetallic compounds, such as $Al_6Mn(Fe)$ and $Al_3Mn(Fe)$. Manganese is an essential trace element (<0.8 μg/L in blood serum) and plays an important role in the metabolic cycle and the activation of multiple enzyme systems [75-77]. However, a high concentration of Mn may induce neurotoxicity [78].

**5) Rare earths**

Rare earth elements (RE) improve the mechanical characteristics, corrosion properties and creep resistance of magnesium alloys. Most RE can provide solid solution strengthening. Moreover, all RE can form complex intermetallic phases with Al or Mg. These intermetallic phases act as obstacles to dislocation movement at elevated temperatures and cause precipitation strengthening.

While most RE elements retard the corrosion of magnesium [36], the use of RE elements in magnesium alloys for biomedical purposes should be studied from the perspective of their potential cytotoxicity. Rare earth elements are not biologically essential for humans and are not found in the human body. Some rare earth elements such as Pr, Ce and Lu are toxic to the human body [5]. For example, an intraperitoneal $LD_{50}$ dose of $GdCl_3$ of 550 mg/kg is cytotoxic in mice. $GdNO_3$ induces acute toxicity at a concentration of 300 mg/kg in mice and of 230 mg/kg in rats [79, 80]. A high

concentration of Y can change the expression of some rat genes and have adverse effects on DNA transcription factors [81].

#### 2.3.4.2 Heat treatments

Heat treatments offer a simple method of changing the microstructure and modifying the mechanical and corrosion properties of alloys. As-cast magnesium alloys can attain higher strength via precipitation hardening after heat treatment. For as-cast magnesium alloys, the most popular precipitation hardening treatments are solution treating and natural aging (T4), natural aging only after casting (T5), and solution treating and artificially aging (T6). Solution treatment helps to reduce or eliminate brittle inter−dendritic networks in the as-cast structure. Thus, solution-treated alloys have better ductility than as-cast alloys, with some increase in strength. In general, the T6 heat treatment is employed in magnesium alloys to enhance the mechanical properties. This process involves two separate steps: solutionizing and ageing. The precipitates dissolve into the matrix during the solutionizing and then a supersaturated solid solution forms after quenching (SSSS); ageing leads to transformation from SSSS to matrix + fine precipitates.

The influence of heat treatment on the corrosion behavior of magnesium alloys has been investigated. For die-cast AZ63 alloy, better corrosion resistance is achieved in an aged sample than an as-cast sample [82]. Song proposed that the corrosion resistance of a solution-treated sample is better than that of aged sample in Mg-5Zn alloys: the large volume fraction of $Mg_xZn_y$ phases accelerated the micro-cathodic effect and resulted in a worse corrosion resistance [11]. The formation of fine precipitates in aged Mg-Dy alloys induced galvanic corrosion and decreased corrosion resistance in a 0.9 wt% NaCl solution [83]. Liang [84] found that the presence of base-centered orthorhombic $\beta'$ precipitates after ageing results in the decreased

corrosion resistance of Mg-7Gd-3Y-0.4Zr. Ageing decreases the corrosion resistance with increasing ageing time to 193 h, due to the formation of precipitates ($\beta''$ ($DO_{19}$), $\beta'$ (cbco) and $\beta_1$ (fcc)) in Mg-10Gd-3Y-0.4Zr alloy [85]. After different heat treatments, the microstructure is changed (second phase dissolves in the matrix after solution treatment and the fine precipitates form after ageing) and a change in grain size could be observed. As a result, the corrosion behaviour is modified.

#### 2.3.4.3 Surface modification

Hydroxyapatite (HA) - chemical formula $Ca_{10}(PO_4)_6(OH)_2$, is a form of calcium apatite. HA is commonly used in biomedical science due to its natural occurrence in the human body. Interestingly, 50% of bone weight is a modified form of HA and is known commonly as 'bone mineral' [86]. Hydroxyapatite is very attractive because of its excellent biocompatibility and bioactivity [87]. However, it does not possess the mechanical properties required for bearing load as expected of a hip joint or a bone pin for example. The important application of HA is bioactive coating on metallic substrates. So far, HA coated stainless steel and titanium alloy used as implants have been studied widely [88-90]. HA coated metallic materials combine attractive properties, good mechanical properties and excellent biocompatibility. There are many methods to prepare the HA coating, such as the sol-gel method [91, 92], electrophoretic deposition [93, 94] and sputtering [95, 96]. However, Mg has a high reactiveness which is not suitable to directly apply sol-gel coating on it, because it would react with the coating solution resulting in poor adhesion of the layer [97]. Electrophoretic deposition and sputtering work on Ti alloy or stainless steel [98], but Mg cannot endure such processing due to its low melting point (650 ℃) and poor heat resistance.

Electrochemical deposition method is attractive because they are cheap, easy to

operate and has the ability to cover complex shape surfaces [99]. Electrochemical deposition is easy to set up and can be done at room temperature. The morphology of the coating layer can be monitored and controlled by simply adjusting the electrochemical potential and electrolyte fluid concentration [90]. The coating of HA on implants and other medical devices via this technique has recently become popular, because calcium phosphate coating provides the necessary porosity required for bone ingrowths into the material surface and the metal lying beneath the coating shoulders the load placed upon the structure [100]. The previous study of hydroxyapatite coatings by Manso et al. [101] also suggested that this method is particularly attractive for coating metal implants that may have complicated shapes, like a screw.

Kannan and He et al. [102] indicated that the use of potentiostatic coating of calcium phosphate on magnesium alloys improves the resistance to corrosion. The coating voltage is controlled and adjusted to the correct level, meaning that the hydrogen evolution rate can be controlled. The optimal potentiostatic deposition of hydroxyapatite was carried out at a cathodic voltage of -2 V w.r.t SCE because low cathodic potential coating produces a uniform coating and low hydrogen evolution [103]. The sample coated at the cathodic voltage of -2 V w.r.t SCE has a more uniform coating than that of sample at -3 V w.r.t SCE.

## 2.4 Development of magnesium alloys for biomedical materials

### 2.4.1 Investigation of biodegradable magnesium alloys

Various types of magnesium alloys have been studied as biomedical materials. The mechanical properties and corrosion resistance have been investigated in vivo and in vitro. Fig. 2.5 illustrates the tensile strength and elongation combinations for magnesium alloys potentially suitable for medical applications [10, 13, 36, 42, 58, 104-109]. Extruded Mg-Zn-Mn shows excellent combined tensile strength and

elongation [110]. Mg-Zn and Mg-Zn-Ca systems exhibit relatively good tensile strength and elongation, 280 MPa and 18.8% in extruded Mg-Zn [104], 250 MPa and 17% in extruded Mg-Zn-Ca [111], respectively.

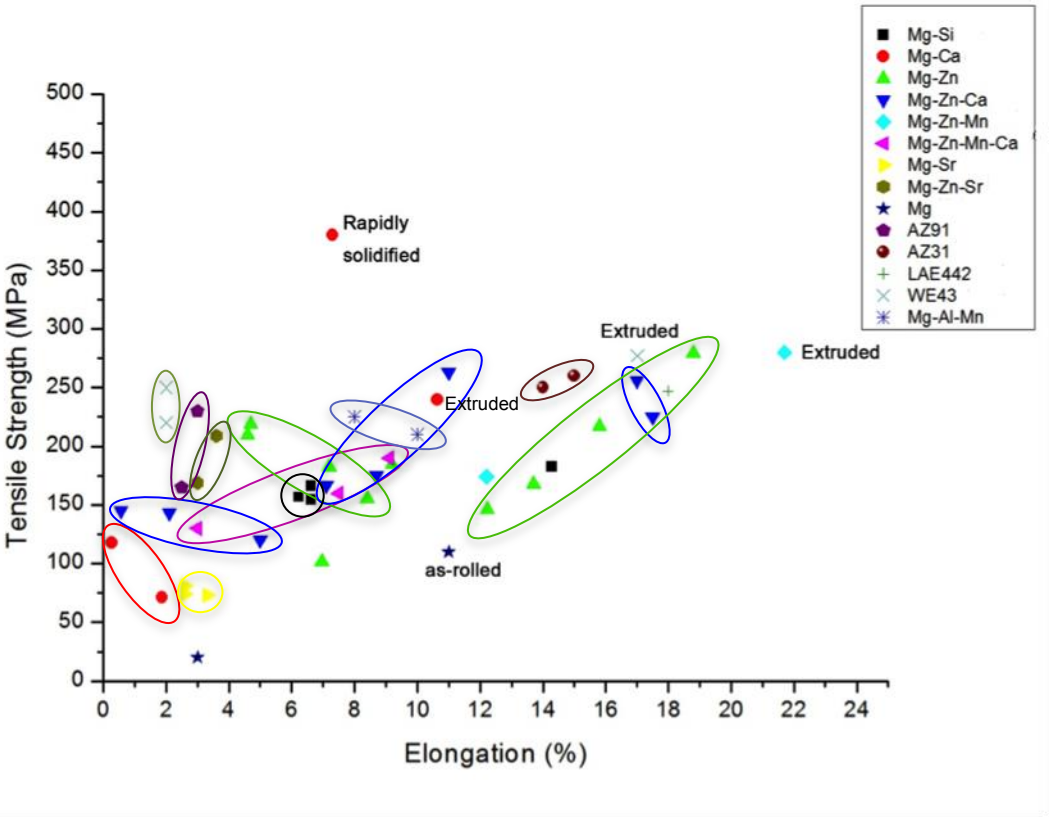


Fig. 2.5 Published tensile strength and elongation data for various magnesium alloys [10, 13, 36, 42, 58, 104-109].

The mass loss rate and corrosion rate of currently investigated bio-magnesium alloys are shown in Fig. 2.6 [54]. The test medium is a form of Eagle's essential medium which is often used for tissue culture. From Fig. 2.6, the degradation rates of magnesium alloys vary from 0.06 mg/cm$^2$/day to 18 mg/cm$^2$/day. AZ91 shows the best corrosion resistance while Mg-5Ca presents the worst corrosion resistance. Different binary magnesium alloys have been systematically investigated [42]. As illustrated in Fig. 2.7, Mg-1Y and Mg-1Si alloys possess the worst corrosion rate after 10 days' immersion, about 5.4 mg/cm$^2$/day. Mg-1Zn and Mg-1Al alloys show the best corrosion resistance: the degradation rate is around 1.1 mg/cm$^2$/day [42].

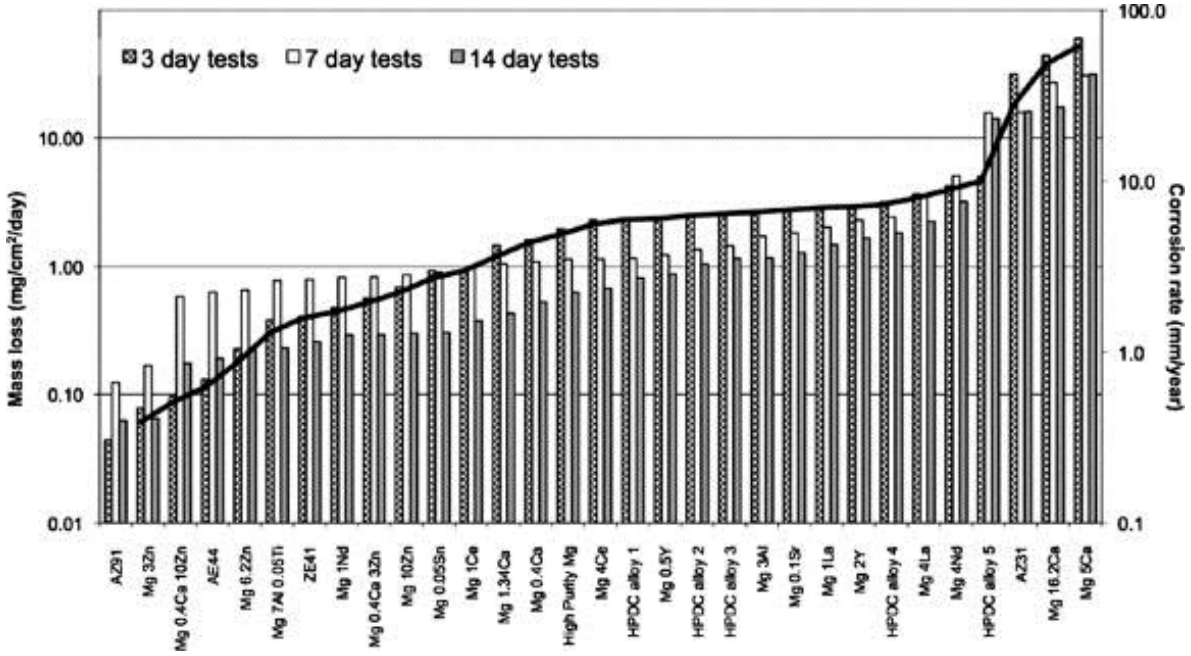


Fig. 2.6 Degradation rates determined for various magnesium alloys in Minimum Essential Medium (MEM) solution: HPDC Alloy 1 contains 1.8 wt% La, 0.97 wt% Ce, 0.7 wt% Nd and 0.4 wt% Zn. HPDC alloy 2 contains 2.98 wt% La, 0.26 wt% Nd and 0.4 wt% Zn. HPDC alloy 3 contains 2.3 wt% Ce and 0.32 Nd. HPDC alloy 4 contains 1.25 wt% La, 1.56 wt% Nd, 0.51 wt% Ce and 0.42 wt% Zn. HPDC alloy 5 contains 2.56 wt% La and 0.35 wt% Nd (adapted from [54]).

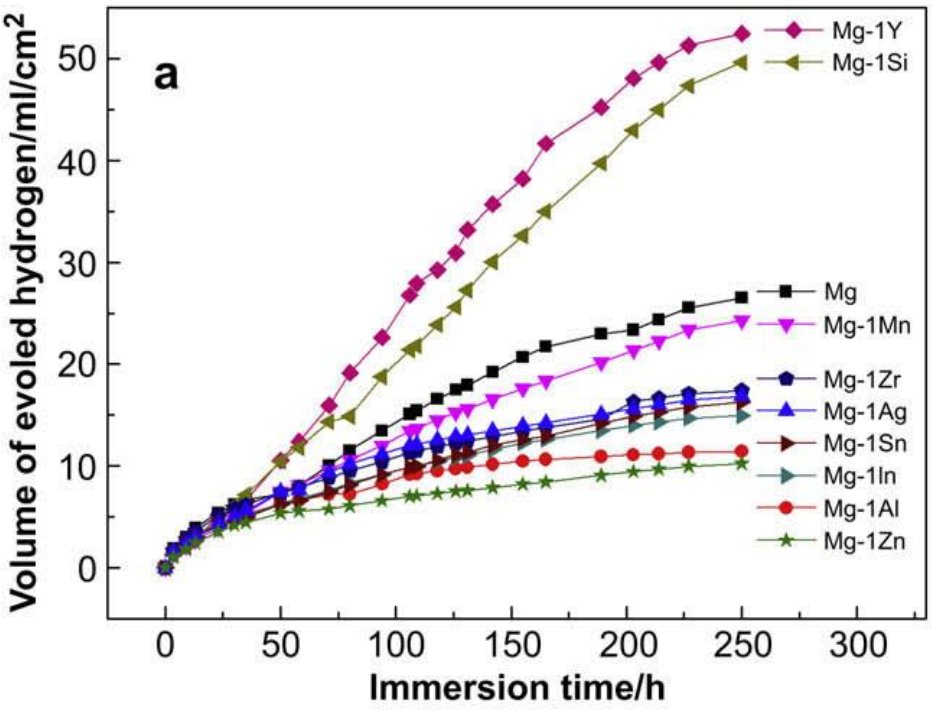


Fig. 2.7 Degradation rates of as-cast pure Mg and binary Mg alloys immersed in SBF solution for 10 days (adapted from [42]).

The magnesium biomaterials can be divided into three major groups: aluminium containing magnesium alloys, aluminium-free magnesium alloys and rare earth element containing alloys. Typical aluminium containing magnesium alloys are AZ31, AZ91, AE21, Ca modified AZ alloys and LAE442. The alloys AZ31, AZ91, WE43 and LAE442 have been investigated specifically with a view to bone implant applications [5, 43].

The popular aluminium-free magnesium alloys include Mg-Ca, Mg-Zn and Mg-Mn-Zn alloys. Although the addition of Ca can improve corrosion resistance and mechanical properties, the tensile strength and elongation of binary Mg-Ca alloys are not sufficient for load-bearing applications. The ultimate tensile strength and elongation of as-cast Mg-1Ca are 71.38 $\pm$ 3.01 MPa and 1.87 $\pm$ 0.14 %, respectively. The corrosion resistance also needs to be improved [112, 113]. Radiographic

examination suggested that Mg-Ca pins gradually degraded in vivo within 90 days and that newly formed bone was clearly seen after 3 months [10].

Some Mg-Zn alloys possess fine microstructures and show high ductility (uniform elongation of 20 %) with considerable strength (ultimate tensile strength ≈250 MPa) [113, 114], which suits stents. As regards in vivo experiments, Mg-Zn rods were implanted into the femoral shafts of rabbits and gradually absorbed at about 2.32 mm/yr degradation rate with newly formed bone surrounding the implant [104]. Histological examination proved that the in vivo degradation of Mg-Zn did not harm the important organs. This suggested that binary Mg-Zn alloy has good biocompatibility in vivo.

The corrosion resistance and tensile strength of Mg-Mn alloys are significantly improved by adding Zn [110, 115]. Mg-Mn-Zn alloy with 1.0 wt% Zn and 1.2 wt% Mn displayed a low corrosion rate (about 54 % degradation percentage after 18 weeks implantation in vivo) and good mechanical properties (tensile strength was 280 MPa and elongation was about 20 %). Mg-Mn-Zn alloys could bio-degrade in a biological environment without leaving residues at the implantation site and in the surrounding bone tissue [41].

Mg-Zn-Ca ternary alloys present appropriate mechanical properties (Mg-3 wt% Zn-1 wt% Ca: 160 MPa tensile strength and 8 % elongation) [116] but their corrosion resistance decreases with increasing addition of Zn [116, 117]. The extruded Mg-4 wt% Zn-0.2 wt% Ca still shows good mechanical properties, sufficient for bone fixing after 30 days immersion in SBF: the yield strength, ultimate tensile strength, elongation and elastic modulus of the alloy are degraded to 160 MPa, 220 MPa, 8.5 % and 40 GPa [111]. The degradation rate is around 1 mg/cm$^2$/day.

Binary Mg-RE alloys such as Mg-Y, Mg-Gd and Mg-Nd were designed for biomaterial applications. The Mg-Y-Zn alloys (such as ZW21 and WZ21) exhibit promising degradation properties and adequate mechanical properties [34]. Mg-Y-Zn alloys have high ductility (uniform elongation of 17-20 %) and adequate strength (ultimate tensile strength of 250-270 MPa) [118]. AE21 (aluminium (2 %) + rare earth metals (1 %)) [45] and WE43 [119] are both reported in the literature as being used for stents.

## 2.5 Introduction of Mg alloys in this work

### 2.5.1 Mg-Zn alloy

Zinc has great strengthening properties in both cast and wrought Mg alloys. According to the Mg-Zn phase diagram shown in Fig. 2.8 [120], zinc is soluble up to 6.2 wt % in magnesium at 325 ℃, and approximately 1.6 wt % at room temperature in the equilibrium state. There are five intermetallic phases: $Mg_7Zn_3$ , MgZn, $Mg_2Zn_3$ (also know as $Mg_4Zn_7$ [121]), $MgZn_2$ and $Mg_2Zn_{11}$. The $Mg_7Zn_3$ phase exists above 325 ℃. The crystal structure of this phase is orthorhombic, space group Immm, a=1.4083 nm, b=1.4486 nm, and c=1.4025 nm [122]. The structure of MgZn was not completely clarified by previous researchers. Khan [123] proposed that the crystal structure of this phase is rhombohedral and expressed the lattice parameters in a hexagonal version: a= 2.569 nm and c=1.8104 nm. However, this phase was reported by Gao [124] as base-centred monoclinic (space group C1c1 or C1 2/c1, with a=1.610 nm, b=2.579 nm, c= 0.880 nm, β=112.4 °). The $Mg_2Zn_3$ phases was first reported by Gallot and Graf, having a triclinic structure (a= 1.724 nm, b=1.445 nm, c=0.520 nm, α=96 °, β=89 °, γ=138 °) [125]. The $MgZn_2$ Laves phase has a hexagonal structure (space group $P6_3/mmc$, with a=0.5221 nm and c=0.8567 nm) [126]. The crystal structure of the $Mg_2Zn_{11}$ phase is cubic (space group $Pm\bar{3}$, a=0.8552 nm) [127].

An intermetallic phase will precipitate from the α-Mg matrix when the addition of Zn is over the ultimate concentration. For example, in Fig. 2.8, there is a red line representing 3 wt % Zn. Primary α-Mg forms when the temperature fall below the liquidus temperature (temperature B). The eutectic phases form because of the eutectic reaction with the decreasing temperature (below temperature A). Finally, the microstructure consists of α-Mg and eutectic (α-Mg + MgZn) product.

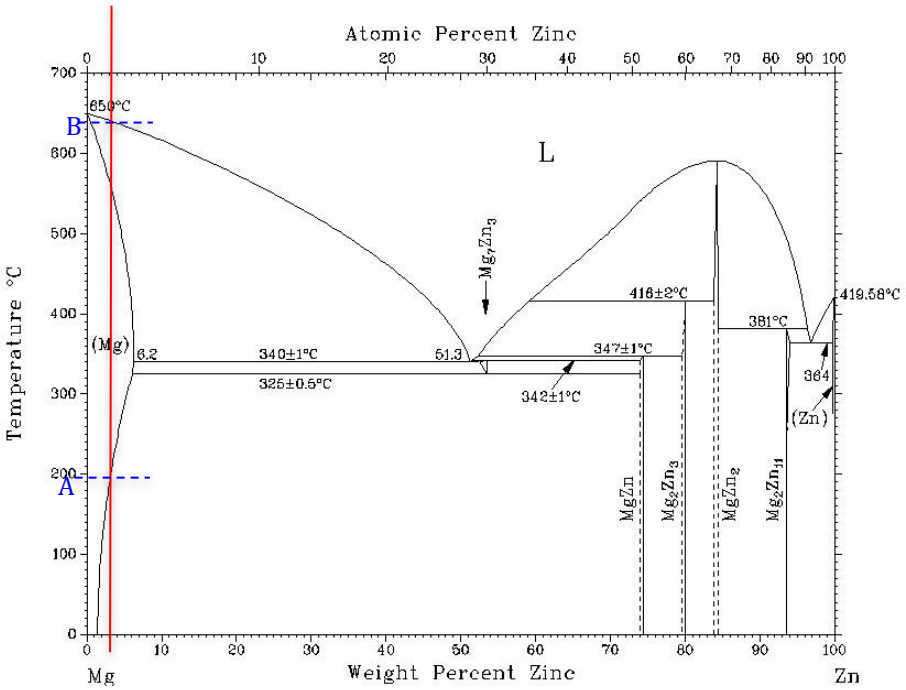


Fig. 2.8 The Mg-Zn binary phase diagram (adapted from [120]).

During ageing, the decomposition of the supersaturated magnesium solid solution (SSSS) is generally considered to occur according to the following sequence [128-133]:

$$\text{SSSS} \rightarrow \text{Guinier Preston (GP)zones} \rightarrow \beta_1' \rightarrow \beta_2' \rightarrow \beta \text{ equilibrium phase (MgZn)}$$

$\beta_1'$ ($Mg_4Zn_7$) typically has a rod (sometimes a blocky) morphology with its longitudinal direction along [0001] of the matrix. $\beta_1'$ has a base-centred monoclinic structure (a=2.596 nm, b=1.428 nm, c=0.514 nm, γ=102.5°) [134]. $\beta_2'$ ($MgZn_2$)

appears as coarse plates parallel to the basal plane of the matrix or occasionally as laths perpendicular to the basal plane. $\beta_2'$ has a hexagonal structure (a=0.523 nm, c=0.858 nm) [126, 134]. The structure of MgZn (β) phase is rhombohedral with a=2.569 nm and c=1.8104 nm [123].

### 2.5.2 Mg-Zn-Ca alloy

The solid solubility of Ca in Mg is very low (0.1 wt% at 350 ℃, 0.5 wt% at 450 ℃ and 0.9 wt% at 516 ℃) according to the Mg-Ca binary phase diagram [135]. In 1933, Paris plotted the first Mg-Zn-Ca ternary phase diagram. Then, Clark reported a 335℃ section of the Mg-Zn-Ca phase diagram which is shown in Fig. 2.9 [136]. Two ternary phases, $Ca_2Mg_5Zn_{13}$ (ω) and $Ca_2Mg_6Zn_3$ (β) are in equilibrium with magnesium solid solution. Four binary phases exist in this system, $Mg_7Zn_3$, MgZn, $Mg_2Zn_3$ and $Mg_2Ca$.

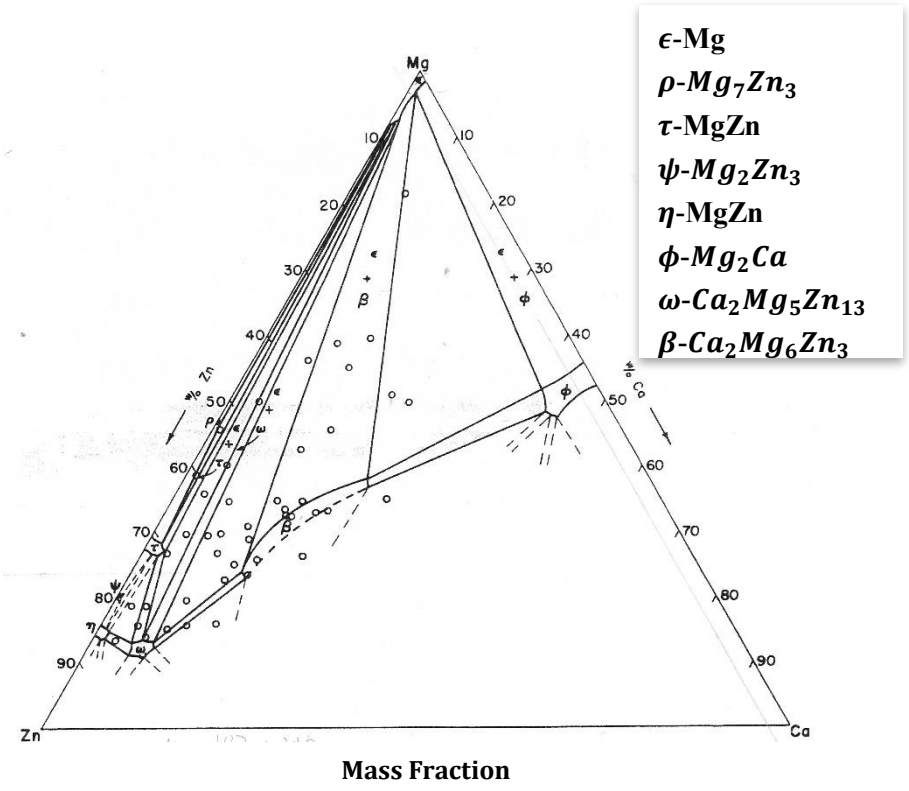


Fig. 2.9 The 335℃ section of the Mg-Ca-Zn phase diagram (adapted from [136]).

## 2.6 Quantitative characterisation of fine precipitates

Quantitative stereology is method to quantify the three-dimensional microstructure by means of two dimensional sections through the solid bodies or projections onto a plane, which is applicable to any material [137]. It is important because the two-dimensional section (or projection) and the material features in a three-dimensional material are linked. The microstructure is important in controlling the properties of materials. The microstructure is required to specify and control in quantitative terms. Therefore, a correct quantitative microstructural relationship is very necessary. The quantitative analysis of a thin metal foil is presented below.

Firstly, it is desirable to specify and define the symbols. Table 2.4 lists a uniform and self-consistent set of symbols recommended for international usage [138].

Table 2.4 List of basic symbols and their definitions (adapted from [138]).

| Symbol | Dimensions* | Definition |
|---|---|---|
| $P$ | — | Number of point elements or test points |
| $P_P$ | — | Point fraction. Number of points (in areal feature) per test point |
| $P_L$ | $mm^{-1}$ | Number of points (intersections) per unit length of test line |
| $P_A$ | $mm^{-2}$ | Number of points per unit test area |
| $P_V$ | $mm^{-3}$ | Number of points per unit test volume |
| $L$ | mm | Length of lineal elements or test line |
| $L_L$ | mm/mm | Lineal fraction. Length of lineal intercepts per unit length of test line |
| $L_A$ | $mm/mm^2$ | Length of lineal elements per unit test area |
| $L_V$ | $mm/mm^3$ | Length of lineal elements per unit test volume |
| $A$ | $mm^2$ | Planar area of intercepted features or test area |
| $S$ | $mm^2$ | Surface or interface area (not necessarily planar) |
| $A_A$ | $mm^2/mm^2$ | Area fraction. Area of intercepted features per unit test area |
| $S_V$ | $mm^2/mm^3$ | Surface area per unit test volume |
| $V$ | $mm^3$ | Volume of three-dimensional features or test volume |
| $V_V$ | $mm^3/mm^3$ | Volume fraction. Volume of features per unit test volume |
| $N$ | — | Number of features (as opposed to points) |
| $N_L$ | $mm^{-1}$ | Number of interceptions of features per unit length of test line |
| $N_A$ | $mm^{-2}$ | Number of interceptions of features per unit test area |
| $N_V$ | $mm^{-3}$ | Number of features per unit test volume |
| $\bar{L}$ | mm | Average lineal intercept, $L_L/N_L$ |
| $\bar{A}$ | $mm^2$ | Average areal intercept, $A_A/N_A$ |
| $\bar{S}$ | $mm^2$ | Average surface area, $S_V/N_V$ |
| $\bar{V}$ | $mm^3$ | Average volume, $V_V/N_V$ |

* Arbitrarily shown in millimetres.

The pictures taken from thin foils by transmission electron microscopy (TEM) can be explained by the mathematics involved in the interpretation of projected images.

Projected images are the two-dimensional images or photographs taken from three-dimensional foils. The main problems however are the truncation effects at the foil surfaces and the overlapping of particles by other particles. As shown in Fig. 2.10, the dimensional ambiguities in thin foil projection that may happen [139].

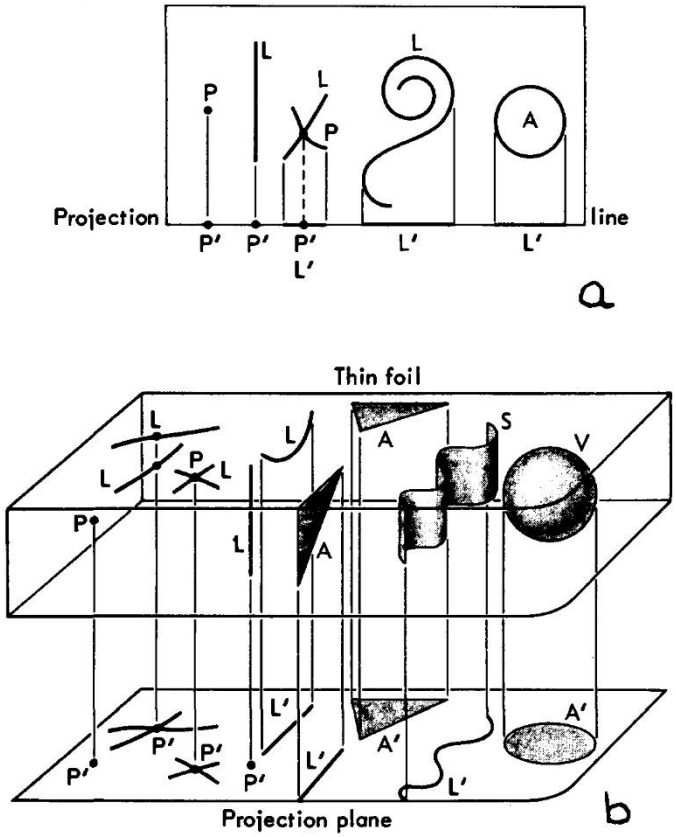


Fig. 2.10 Projections of planar figures and structural features: (a) from a plane to a projection line; (b) from a thin foil to a projection plane (adapted from [139]). (The projected quantities are identified by primes).

Then, some basic equations for projected lines, surfaces, and volumes are listed in Table 2.5 [137]. But these simple equations don't take into account the effects of truncation and overlapping.

Table 2.5 Equations for apparent projection of lines, surfaces and volumes (adapted from [137]).

| | Comments |
|---|---|
| **Lines in a Plane** | |
| $L = (\pi/2)\,\bar{L}'$ | Linear segment projected over all orientations to a projection line. |
| $L_A = (\pi/2)\,L_L'/h$ | Random system of lines in a plane (of height $h$).[a] |
| **Lines in Space** | |
| $L = (4/\pi)\,\bar{L}'$ | Linear segment projected over all orientations to a projection plane. |
| $L_V = (4/\pi)\,L_A'/t$ | Random system of lines in a foil (of thickness $t$). |
| $\bar{L} = (4/\pi)\,L_A'/N_A'$ | Linear segments of different lengths projected over all orientations to a projection plane. |
| $L_V = P_A'$ | Random lines in a foil that intersect both upper and lower surfaces at points P′. |
| **Open Surfaces in Space**[b] | |
| $S \geqq 2\bar{A}'$ | Surface projected over all orientations to a projection plane. |
| $S_V \geqq 2A_A'/t$ | Random system of surfaces in a foil (of thickness $t$). |
| **Closed Surfaces in Space**[b] | |
| $S \geqq 4\bar{A}'$ | The equality holds for convex bodies projected over all orientations to a projection plane. |
| $S_V \geqq 4A_A'/t$ | Random system of closed bodies in a foil (of thickness $t$).[c] |

[a] Negligible overlap.
[b] The inequality operates in the case of overlap.
[c] No truncation.

In order to correct for truncation and overlap effects, the concept of 'total projection' is necessary: it is the value of the projection of all elements of the structure, whether obscured or not [137]. For example, a circular perimeter of radius r in a plane has a projection length $L_2^{'} = 2r$ and a total projection $L_2^{''} = 4r$ when it is projected to a line. Similarly, a spherical surface with radius r has a total projection area $2\pi r^2$.

For the total projection of surface in space, the basic equation is

$$S = 2\overline{A^{''}(\theta, \emptyset)} \qquad \text{(Equation 2.1)}$$

which is derived by averaging the projections of an elementary unit of the surface to a plane over all angles of orientation [139].

For any shaped particles and for any degree of overlap, basing on the total projection, a derivation is presented. Fig. 2.11 shows particles in a thin foil with the truncated particles cut by the foil surfaces [137].

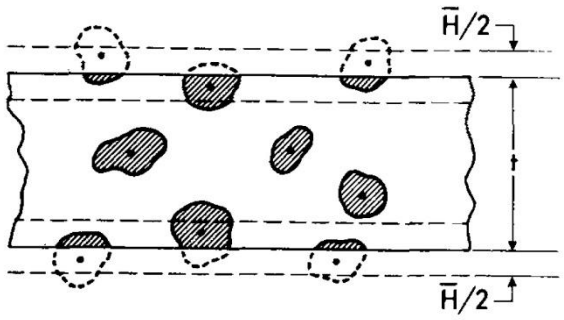


Fig. 2.11 Truncation of particles in a thin foil (adapted from [137]).

With respect to the total projection of particle surfaces, there are two contributions: particles with their centres inside the foil and those with centres outside the foil. For the total projection of truncated and overlapping particles in a foil,

$$A_A'' = (A_A'')_{flat} + (A_A'')_{curved} \qquad \text{(Equation 2.2)}$$

where, the subscripts 'flat' means the flat sectioned areas of particles on both the upper and lower foil surface; the subscripts 'curved' refers to the curved surface particles within the foil volume [137]. $(A_A'')_{flat}$ includes all the contributions of sectioned particles without considering their centre locations. Thus, the planar particle surface area which is created by sectioning the upper and lower foil surfaces is

$$(A_A'')_{flat} = 2A_A = 2V_V \qquad \text{(Equation 2.3)}$$

$(A_A'')_{curved}$ is composed of all particle surfaces within in foil volume, without considering truncation or particle center locations. Therefore, because of Equation 2.1, $(A_A'')_{curved}$ is written as

$$(A_A^{''})_{curved} = S_V t/2 \qquad \text{(Equation 2.4)}$$

Substituting Equations 2.3 and 2.4 into Equation 2.2, the volume fraction of randomly positioned and oriented particles with any shape is given by

$$V_V = \frac{A_2^{''}}{2} - \frac{S_V t}{4} \qquad \text{(Equation 2.5)}$$

Assuming the spherical particle has an uniform diameter of D, then

$$S_V = \frac{6V_V}{D} \qquad \text{(Equation 2.6)}$$

Introducing Equation 2.6 to Equation 2.5, the volume fraction of spherical particles accounting for truncation effects is

$$V_V = A_A^{''}\left(\frac{D}{2D+3t}\right) \qquad \text{(Equation 2.7)}$$

As the volume fraction of particles increases, the overlap correction is required. Fig. 2.12 shows a new particle with projected area $A_i^{'}$ added to an existing particle in a thin foil. Then the fraction of this particle obscured is given by

$$\frac{(A_i^{'})_{ob}}{A_i^{'}} = A_A^{'} \qquad \text{(Equation 2.8)}$$

i.e. the existing projected area fraction $A_A^{'}$ equals to the ratio of obscured area $(A_i^{'})_{ob}$ to the projected area $A_i^{'}$ of original particle.

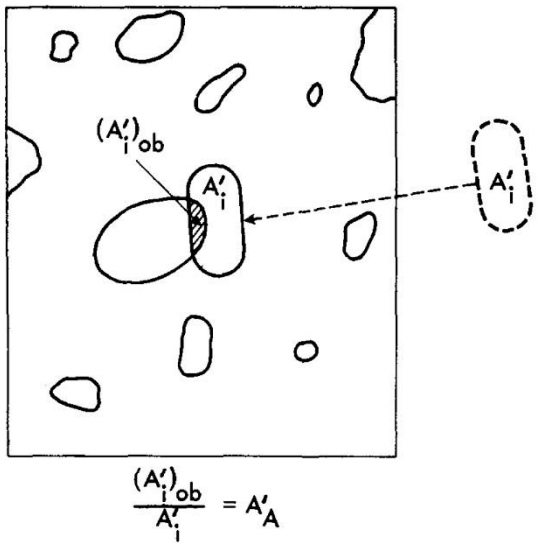


Fig. 2.12 Overlap of particles in the projection plane (adapted from [138]).

The increased apparent projected area of all particle is $\Delta A' = A'_i - (A'_i)_{ob}$. The increased total projection of the particles is $\Delta A'' = 2A'_i$. Then,

$$\frac{\Delta A'_A}{\Delta A''_A} = \frac{A'_i - (A'_i)_{ob}}{2A'_i} = \frac{1 - A'_A}{2} \qquad \text{(Equation 2.9)}$$

or, for many particles,

$$\frac{d(A'_A)}{d(A''_A)} = \frac{1 - A'_A}{2} \qquad \text{(Equation 2.10)}$$

Integration of Equation 2.10 to obtain the total projection of particles,

$$A''_A = -2\ln(1 - A'_A) \qquad \text{(Equation 2.11)}$$

Finally, substituting the Equation 2.11 to the Equation 2.7, the volume fraction after the truncation and overlap corrections can be expressed as [137]

$$V_V = -\ln(1-A_A^{'})\left(\frac{2D}{2D+3t}\right) \qquad \text{(Equation 2.12)}$$

Equation 2.12 is for the convex particles, but the derivation of the volume fraction for the rod-like particles is same. Assuming the rod-like particle has a diameter of D and length of L, then

$$S_V = \frac{2V_V}{L} + \frac{4V_V}{D} \qquad \text{(Equation 2.13)}$$

Introducing Equation 2.13 to Equation 2.5, the volume fraction of rod-shaped particles becomes

$$V_V = A_A^{''}\left(\frac{DL}{2DL+(D+2L)t}\right) \qquad \text{(Equation 2.14)}$$

Then, substituting Equation 2.11 into Equation 2.14, the volume fraction of rod-shaped precipitates after the truncation and overlap corrections is

$$V_V = -\ln(1-A_A^{'})\left(\frac{DL}{DL+(\frac{D}{2}+L)t}\right) \qquad \text{(Equation 2.15)}$$

where D is the diameter of the rod-shaped precipitates, L is the rod length, t is the foil thickness and $A_A^{'}$ is the projected area fraction of precipitates. It is noted that the average foil thickness is used to correct the average diameter of the different kinds of precipitates for truncation effects induced by the limited foil thickness and to calculate the volume fraction of precipitates.

## 2.7 Corrosion of magnesium alloys

### 2.7.1 Mechanisms

Among all the structural metals, magnesium possesses the highest reactivity. The reactivity of some metals and commercial alloys in seawater is represented in Table 2.6 [140]. The alloys close to the top are cathodic and inert, whereas those at the bottom are most anodic and extremely reactive. Magnesium is chemically active and will react with the water to form a protective film. However, this protective film cannot provide long-term protection against corrosion, and it is not thermodynamically stable in neutral and acid environments whereas it is very stable in highly alkaline environments.

Table 2.6 Galvanic Series (adapted from [140]).

| | |
|---|---|
| | Platinum |
| | Gold |
| | Graphite |
| | Titanium |
| | Silver |
| | 316 Stainless steel (passive) |
| | 304 Stainless steel (passive) |
| ↑ | Inconel (80Ni-13Cr-7Fe) (passive) |
| | Nickel (passive) |
| | Monel (70Ni-30Cu) |
| Increasingly inert (cathodic) | Copper-nickel alloys |
| | Bronzes (Cu-Sn alloys) |
| | Copper |
| | Brasses (Cu-Zn alloys) |
| | Inconel (active) |
| | Nickel (active) |
| | Tin |
| | Lead |
| Increasingly active (anodic) | 316 Stainless steel (active) |
| | 304 Stainless steel (active) |
| ↓ | Cast iron |
| | Iron and steel |
| | Aluminium alloys |
| | Cadmium |
| | Commercially pure aluminium |
| | Zinc |
| | Magnesium and magnesium alloys |

Pourbaix initially worked on the electrochemical reactivity of magnesium in aqueous

solutions [141]. The pivotal diagram (Potential- pH diagram) is illustrated in Fig. 2.13. It can clearly be seen that the dissolution of magnesium occurs below approximately pH 11.5 (depending on the ion concentrations), while the formation of $Mg(OH)_2$ happens at higher pH values (above 11.5). In the physiological environment, the dissolution of magnesium is easily aroused because the pH of blood is around 7.

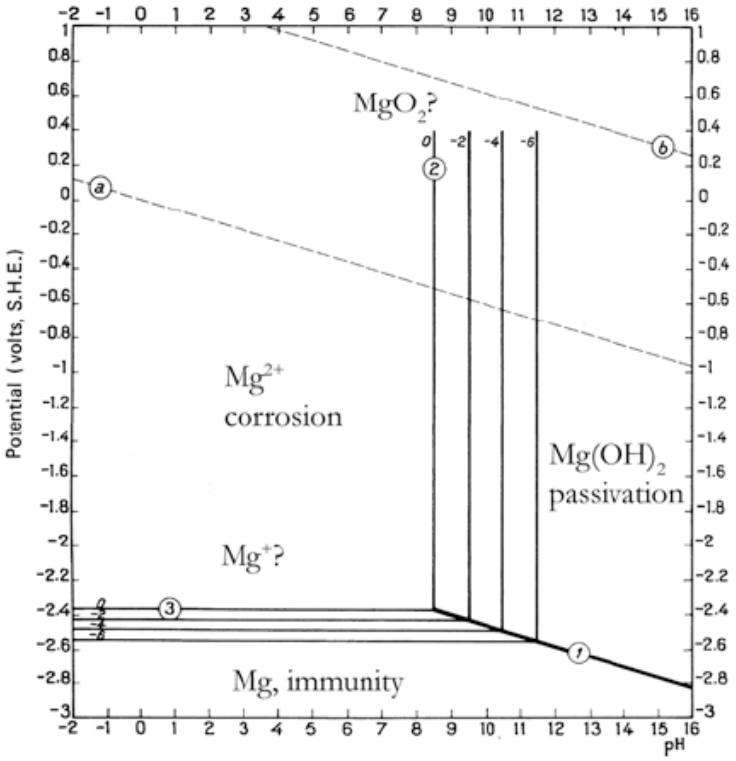


Fig. 2.13 Pourbaix's potential-pH equilibrium for magnesium (adapted from [141]): The region between the marked lines ⓐand ⓑ is water stable. The different regions are separated by the following reactions: ① $Mg + H_2O \rightarrow Mg(OH)_2 + H_2$;

② $Mg^{2+} + H_2O \rightarrow MgO + 2H^+$; ③ $Mg \rightarrow Mg^{2+} + 2e^-$.

The corrosion of magnesium in an aqueous environment can be described as follows:

Anodic reaction/ Dissolution: $Mg \rightarrow Mg^{2+} + 2e^-$ (Equation 2.16)

Cathodic reaction: $2H_2O + 2e^- \rightarrow 2OH^- + H_2$ (Equation 2.17)

Hydrolysis: $Mg^{2+} + H_2O \rightarrow MgOH^+ + H^+$ (Equation 2.18)

Product formation: $Mg^{2+} + 2OH^- \rightarrow Mg(OH)_2$ (Equation 2.19)

Obviously, the hydrolysis reaction consumes $H_2O$ and produces $H^+$, and thus reduces the pH values in the solution close to the anode. The balancing cathodic reaction results in an increase of pH, favours the precipitation of $Mg(OH)_2$ and stabilizes this passive film. With time, the cathodic reaction leads to an alkalization of the solution owing to the balance between the anodic and cathodic reactions. Each $Mg^{2+}$ formed produces two $OH^-$, and generates one $H^+$. Therefore, the overall reaction results in a pH increase. It must be mentioned that hydrogen evolves during the reaction according to the cathodic reaction. Fig. 2.14 illustrates the corrosion mechanism of magnesium in an aqueous environment. The processes of Equation 2.16 - 2.19 are vividly demonstrated in Fig. 2.14 (a). The dissolution of magnesium and the formation of hydrogen and magnesium hydroxide are the main features. The aggressive ion $Cl^-$ reacts with $Mg(OH)_2$ and forms more soluble $MgCl_2$ (see Fig. 2.14 (b)). Further corrosion of magnesium is promoted by the dissolution of $Mg(OH)_2$ due to the disappearance of the protected areas [61]. $Cl^-$ catalyses the dissolution of magnesium and directly produces $MgCl_2$, exposing the bare magnesium to the solution [142, 143] (Fig. 2.14 b)).

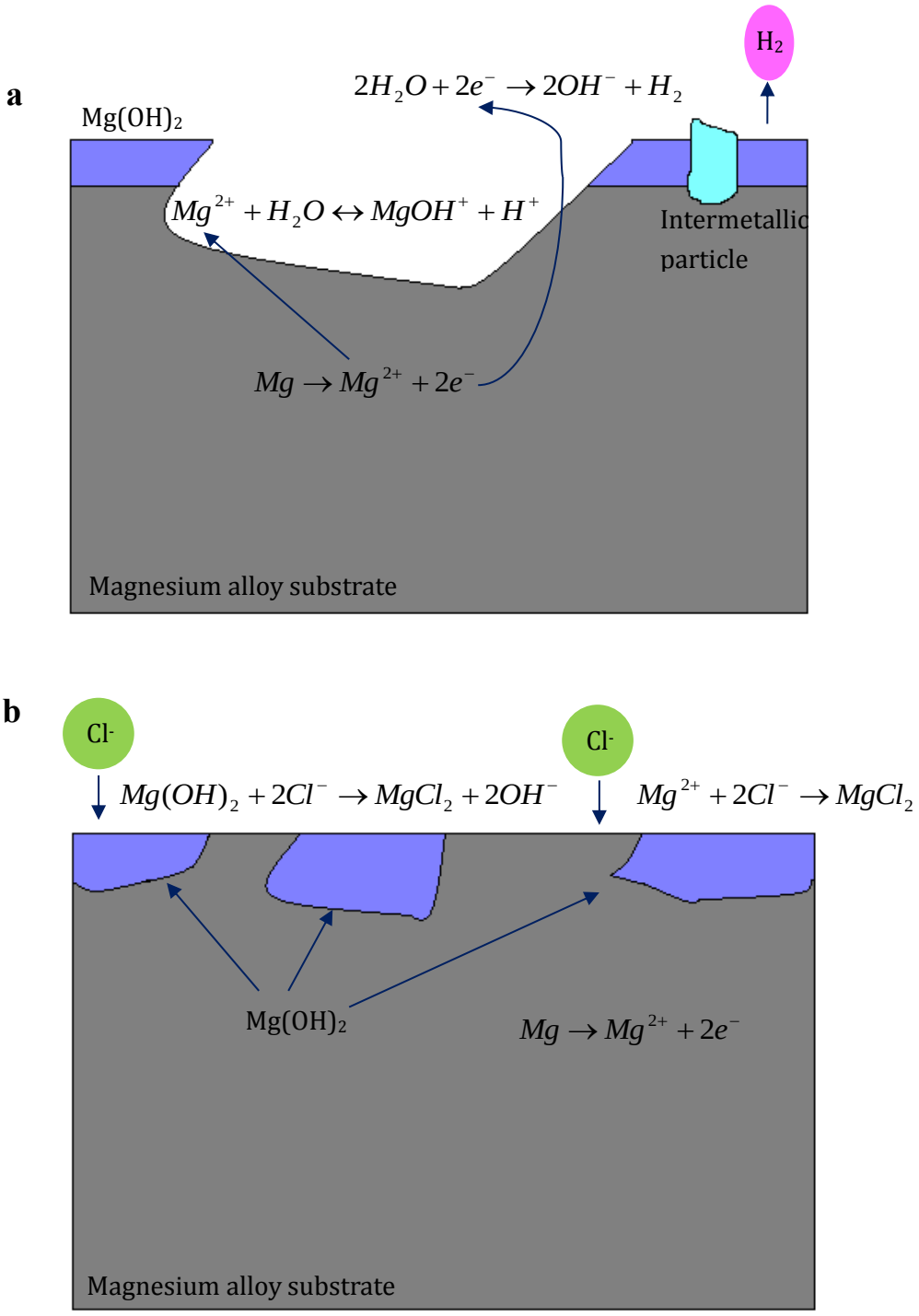


Fig. 2.14 Schematic illustration of the corrosion of magnesium in an aqueous environment:

(a) The dissolution of magnesium via the anodic reaction. The cathodic reaction increases the pH and produces $H_2$, while hydrolysis reduces the pH. Intermetallic particles act as cathodic sites and consume the electrons produced by the anodic

reaction. (b) Chlorine ions in the solution attack and dissolve the $Mg(OH)_2$ film.

### 2.7.2 Behaviour

#### 2.7.2.1 Pitting corrosion

Pitting corrosion is an extremely localized form of corrosion which results in the appearance of small holes on the surface of the metal. Specific areas of a material undergo fast corrosion while vast areas of the surface are not subject to attack [14]. The depassivation of a small area is the driving force. The majority area of the material is cathodic and the small area is anodic, which leads to extremely localized galvanic corrosion. This kind of corrosion is very insidious: it seems that it imposes very little damage on the material surface, however, it damages the deep material structure (as shown in Fig. 2.15).

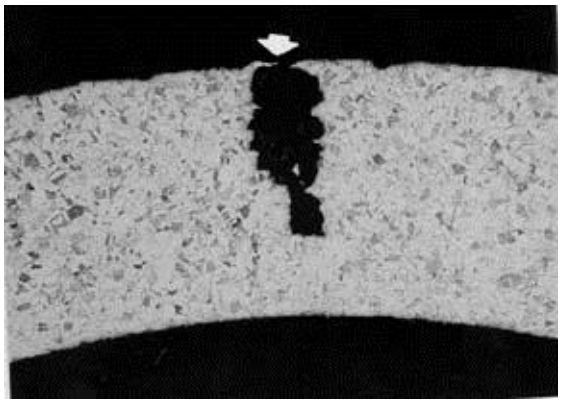

Fig. 2.15 Pitting corrosion in split tubing (adapted from [144]).

For magnesium and its alloys, pitting corrosion is common [145]. Typically, in neutral or alkaline solutions magnesium suffers from pitting corrosion [14]. Pitting corrosion crosses the passive film and breaks it, thus providing an easy site for the anodic reaction (magnesium dissolution). Generally, where these disruptions take place is close to an inclusion. As a result, pitting corrosion takes place close to the inclusions. The corrosion occurs at the interface between the inclusion and the passive film, and

then exposes the magnesium to the corrosive medium (Fig. 2.16) [146]. This brings about more intensive dissolution of the magnesium. Moreover, pitting is made worse by the $Cl^-$, because $Cl^-$ transforms $Mg(OH)_2$ to the more soluble $Mg(Cl)_2$ [143, 147]. Pitting in magnesium alloys does not follow a regular mode of development: it develops laterally and then covers the whole sample surface, rather than growing vertically more deeply.

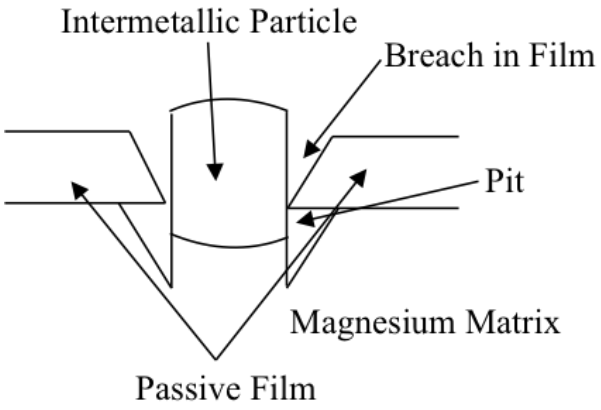


Fig. 2.16 Pitting by an intermetallic particle producing a local break in the protective film (adapted from [146]).

### 2.7.2.2 Galvanic corrosion

When two different metals with different electrochemical potentials are in electrical contact, galvanic corrosion occurs [148-150]. Galvanic corrosion is one of the main types of severe corrosion in magnesium [151]. Magnesium is easily attacked by this kind of corrosion. Galvanic corrosion can be divided into external and internal galvanic corrosion. If magnesium is in contact with a nobler metal, this noble metal acts as an external cathode: this is external galvanic corrosion. If a cathodic second phases or impurities exist in the magnesium, this is regarded as internal galvanic corrosion. Fig. 2.17 presents a schematic illustration of these two kinds of galvanic corrosion [14].

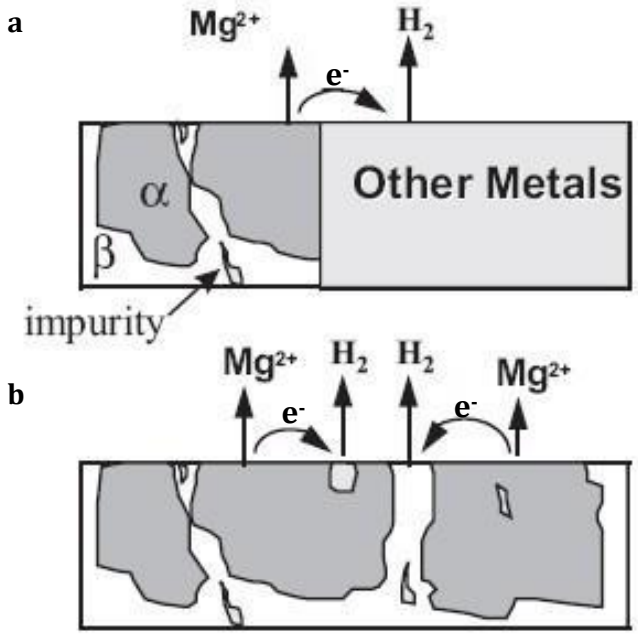


Fig. 2.17 Schematic illustration of galvanic corrosion (adapted from [14]):
(a) External galvanic corrosion; (b) Internal galvanic corrosion.

### 2.7.3 Influence of composition and microstructure

#### 2.7.3.1 Effects of alloying elements and impurities

Alloying elements play an important role in the corrosion performance of magnesium alloys. Some elements such as Al, Mn, Zn have a good effect on the corrosion performance of magnesium alloys; some elements such as Fe, Ni, Cu have an extremely detrimental influence on the corrosion resistance. Their concentration is also an important factor in deciding the corrosion behavior. Lunder et. al [152] reported that the corrosion resistance of Mg-Al alloy improved along with increasing addition of aluminium from 2 % to 4 % because a higher proportion of stable aluminum oxide existed in the film; it dropped over 4 % however. Adding manganese to Al-containing magnesium alloys can improve the corrosion resistance by converting iron and other metallic elements into relatively harmless intermetallic compounds [43]. However, some researchers think that the addition of manganese is not always beneficial to the corrosion behavior of magnesium. Some pitting corrosion

occurs around the manganese containing particles, even if they are iron-free [153]. Zinc is beneficial to the corrosion resistance, because it can increase the tolerance limit for the impurities and reduce the negative effects when impurities exceed this limit [71]. In Mg-Al-Mn-Ni alloys, the addition of 3 wt% Zn improves the tolerance limit of Ni from 10 to 20 wt.-ppm and decreases the corrosion rate even at the higher concentration of Ni [62].

The impurity elements in magnesium alloys are bad for the corrosion performance. The detrimental elements in magnesium alloys are iron (Fe), copper (Cu), nickel (Ni) and cobalt (Co). Hanawalt et.al [154] found that these detrimental elements have a significant accelerating influence on the salt water corrosion rate at a concentration of 0.2 % or lower. Purification can be employed to slow down the corrosion of magnesium alloys [6]. The solid solubility of Fe, Ni and Cu in magnesium is low and their cathodic activity is high, thus their detrimental influences on the corrosion rate of magnesium alloy are significant [151]. The corrosion resistance is dramatically reduced when the impurity concentration exceeds the tolerance limit [14]. Ingots are susceptible to hot tearing and corrosion resistance is obviously reduced when the content of Ni is higher than 0.03 %. Generally, the amount of Fe is limited to 35-50 ppm and Cu should not be over 100-300 ppm [155].

#### 2.7.3.2 Effects of microstructure

Generally, the microstructure involves the grain size, the phase constituents and their distribution. The corrosion performance of magnesium alloys is closely related to the microstructure [156, 157].

The second phase has a profound impact on the corrosion performance of magnesium alloys. Magnesium alloys with a homogeneous microstructure are desirable. A

different corrosion potential between the α-Mg and the second phase is the reason for microgalvanic corrosion. For example, in AZ alloys, the β phase ($Mg_{17}Al_{12}$) has a different corrosion potential from the α-Mg matrix. The β phase is nobler than the α-Mg matrix (see Table 2.7 [61]) and can aggravate the corrosion of magnesium due to microgalvanic effects [158]. In other words, β phase acts as a cathode, whereas α-Mg acts as an anode and is dissolved.

Table 2.7 Corrosion potentials of magnesium and second phases (after 2 hours in deaerated 5% NaCl solution saturated with $Mg(OH)_2$, pH 10.5) (adapted from [61]).

| **Metal** | **$E_{corr}$, $V_{SCE}$** |
|---|---|
| Mg | -1.65 |
| $Mg_2Si$ | -1.65 |
| $Al_6Mn$ | -1.52 |
| $Al_4Mn$ | -1.45 |
| $Al_8Mn_5$ | -1.25 |
| $Mg_{17}Al_{12}$ (β) | -1.20 |
| $Al_8Mn_5$ (Fe) | -1.20 |
| β-Mn | -1.17 |
| $Al_4RE$ | -1.15 |
| $Al_6Mn$ (Fe) | -1.10 |
| $Al_6$(MnFe) | -1.00 |
| $Al_3Fe$(Mn) | -0.95 |
| $Al_3Fe$ | -0.74 |

Some researchers believe that β phase has a dual influence: it can act as a corrosion barrier and has a positive influence on the corrosion resistance [156, 157, 159], while it causes poor corrosion resistance because of the microgalvanic coupling built up between the β phase and α-Mg [14]. The fraction and distribution of β phases are important factors in determing which effect dominates. The finely and continuously distributed β phase serves as a corrosion barrier and inhibits corrosion; otherwise, β

phase promotes corrosion. Fig. 2.18 shows the effect of a continuous β phase on the corrosion of a Mg alloy [160]. β phase acts as a corrosion barrier and restricts the corrosion development while α-Mg is dissolved preferentially. Similar results are obtained in MEZ alloy (Mg-Rare earth-Zr alloy): more continuous second phases can benefit the corrosion resistance [161].

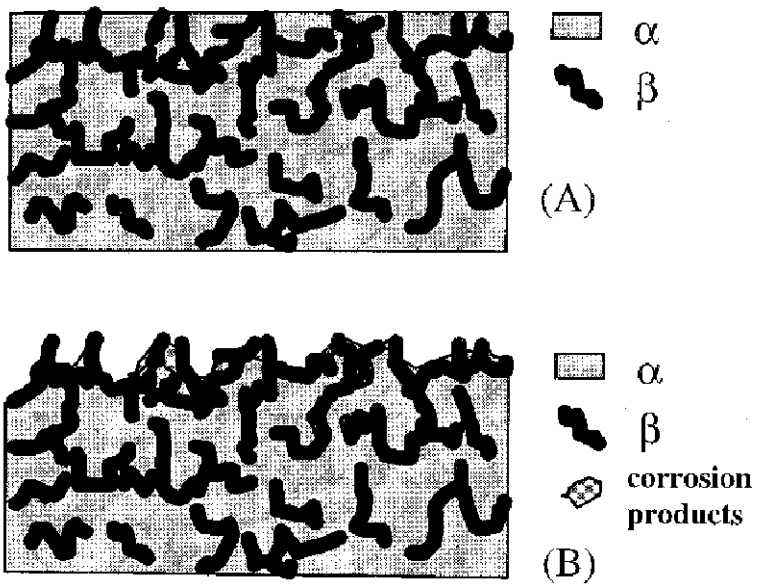


Fig. 2.18 Schematic diagram showing a corrosion surface where β phase acts as a corrosion barrier: (a) initial surface; (b) final surface (adapted from [160]).

Fig. 2.19 presents two kinds of corrosion morphology: one is where the primary α matrix is preferentially corroded, another is where β phase is undermined due to the dissolution of the eutectic α phase. In Fig. 2.19 (b), the dissolution of the primary α is illustrated on the left hand side, while the corrosion of the eutectic α phase is shown on the right hand side and thus β phase is exposed to the corrosion medium and then is corroded and drops out [160].

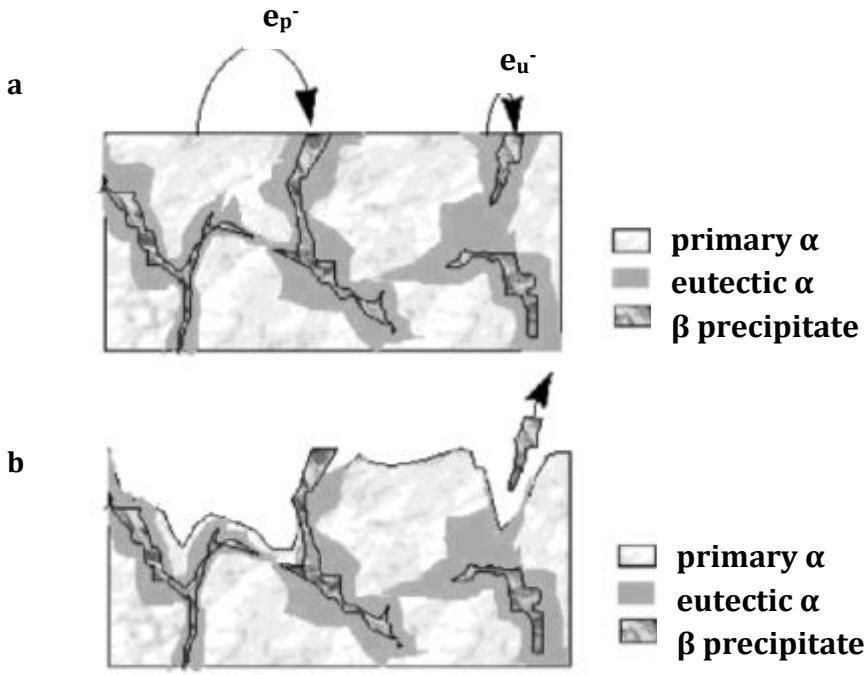


Fig. 2.19 Schematic diagram showing galvanic corrosion between α phases and β phase: (a) initial surface; (b) subsequent corrosion morphology ($e_p^-$ is the electron transport between the primary α phase and the β phase; $e_u^-$ is the electron transport between the eutectic α phase and the β phase) (adapted from [160]).

The morphology of the second phase also affects the corrosion behaviour of magnesium alloys. For example, magnesium with a coarse Chinese script $Mg_2Si$ phase shows a weaker corrosion performance than that with evenly distributed polygonal shaped $Mg_2Si$ phases [162]. The reduction and refinement of $Mg_2Si$ phases lead to better corrosion behaviour of Mg-Si(-Ca) alloys [13].

Furthermore, the corrosion behavior of magnesium alloys is closely related to the grain size. Some researches show that grain refinement is an effective way to improve the corrosion performance of magnesium alloys [143, 160, 163-165]. Song et al. [160] indicated that the skin of the die-cast AZ91D alloy exhibits better corrosion performance than the interior, because more continuous β phase formed around finer α-Mg grains. If the grains are small and the volume fraction of β phase is not too low,

then β phase forms continuously like a net, and will be difficult to undercut because corrosion development cannot easily pass through numerous β precipitates. β phase is exposed and α-Mg phase corrodes due to preferential corrosion of α-Mg phase. Eventually, the final surface of the sample has a lot of β phase and the β phase is more difficult to be corroded than α-Mg phase, so the corrosion resistance is improved [49, 160]. Normally, segregation appears at the free surface or at an internal interface, such as a grain boundary or the interface between a precipitate and the matrix. A smaller grain size minimizes the segregation and thus leads to homogeneous corrosion. Grain refinement causes a decreased corrosion rate because of the improved passive film [166-168]. A high grain boundary density promotes a better oxide film conduction rate on surfaces with low to passive corrosion rates and therefore fine a grain structure is more corrosion resistant.

Birbilis proposed that the corrosion rate increases as the logarithm of average grain size increases in pure Mg [165]. Ralston also presented a relationship between corrosion rate and grain size [169]. The relationship is as follows:

$$i_{corr} = (A) + (B) \cdot gs^{-0.5} \qquad \text{(Equation 2.5)}$$

where A is a constant and a function of the environment (because the same materials have different corrosion rates in different electrolytes for the same grain size). B is a material constant, determined by the composition and impurity level of the material. g is grain size and $i_{corr}$ is the corrosion rate.

Several researchers report that twins, texture and dislocations have influences on the corrosion performance. Aung reported that the existence of twins can accelerate the corrosion of magnesium alloys [163]. After equal channel angular extrusion (ECAE),

a higher density of dislocation and twins appeared and a more severe dissolution of the anode resulted [164]. Andrei indicated that the equilibrium potential in the vicinity of the dislocations is locally reduced, thus causing accelerated dissolution of the anode [170]. According to Xin [171] extruded AZ31 sheet showed a better corrosion resistance because of the initial basal texture. Schmutz reported that filaments of corrosion propagated at twin boundaries; this corrosion happened on a plane near the basal plane and then propagated down the prismatic planes [172].

## 2.8 In vivo and in vitro experiments

### 2.8.1 In vivo testing

The in vivo assessment of the compatibility of biomaterials and medical devices with tissue is important for the development and implementation of implants for human use. Many in vivo studies have been conducted to understand the degradation process and the associated mechanisms. Animal models are adopted in order to determine the response to the biomaterials or medical devices, such as the interactions of various cell types with the implants, endocrine factors acting on cells around the implant and interactions with blood-borne cells and proteins. In vivo studies were mainly performed on small animals, such as guinea pigs, rats and rabbits. Heublein investigated a cardiovascular stent (AE21 alloy) in pigs [45]. It has been reported that magnesium chips have been implanted into a sheep in spinal applications [173]. The first comprehensive in vivo study on magnesium alloys was carried out by Witte et al. [5] on four different magnesium alloys (AZ31, AZ91, WE43 and LAE442), and these four magnesium alloys were implanted in the femurs of guinea pigs. Although in vivo testing provides more precise information due to its being a closer environment to the human body, animal tests are not humane. Every hour, around 20,000 animals die in laboratory tests. Because of this, in vitro testing is required to minimize the requirement for animal tests.

### 2.8.2 In vitro testing

#### 2.8.2.1 Physiological solution

It is neither ethical nor economical to do in vivo tests using animals for large numbers of different alloys. In vitro tests which can imitate in vivo conditions are necessary. Compared with in vivo studies, in vitro experiments are convenient and can provide quick and reasonable feedback on efficacy. The simulated body fluid (SBF) method is more realistic because this is an aqueous solution with ion concentrations and pH value equal to those of human body fluids. Table 2.8 shows several solutions used in in vitro tests [174]. In this table, it clearly can be seen that Kokubo's SBF solution is the physiological solution closest to human blood plasma.

Table 2.8 The concentration of ions and pH values in blood plasma and different solutions (mM) (adapted from [174]).

| Ion | Blood plasma | Ringer | EBSS | HBSS | Kokubo's SBF |
|---|---|---|---|---|---|
| $Na^+$ | 142.00 | 130.00 | 143.60 | 138.00 | 142.00 |
| $K^+$ | 5.00 | 4.00 | 5.37 | 6.14 | 5.00 |
| $Ca^{2+}$ | 2.50 | 1.40 | 1.80 | 1.26 | 2.50 |
| $Mg^{2+}$ | 1.50 | - | 0.81 | 0.81 | 1.50 |
| $Cl^-$ | 103.00 | 109.00 | 125.30 | 144.8 | 147.80 |
| $HCO^{3-}$ | 27.00 | - | 26.2 | 4.2 | 4.20 |
| $HPO_4^{2-}$ | 1.00 | - | 1.00 | 0.78 | 1.00 |
| $SO_4^{2-}$ | 0.50 | - | 0.81 | 0.81 | 0.50 |
| Ca/P | 2.50 | - | 1.80 | 1.62 | 2.50 |
| Buffer | - | - | - | - | Tris |
| pH | 7.4 | 6.5 | 6.7-6.9 | 6.7-6.9 | 7.4 |

EBSS (Earle's balanced salt solution); HBSS (Hank's balanced salt solution)

#### 2.8.2.2 Measurements of degradation rates of magnesium alloys

There are several methods to measure the degradation rates of magnesium alloys: weight loss, hydrogen evolution and electrochemical techniques. For biomaterials,

especially the biodegradable magnesium alloys, the degradation performance is vital. In order to evaluate the degradation performance and thus effectively and precisely control the corrosion rate, the measurement of degradation rate should be carefully chosen.

1) Weight loss is the simplest method for degradation testing, with mass loss rates depending on the test duration. In the weight loss method, the degradation rates of the specimens are calculated as follows:

$$\text{degradation rate } (\text{mg/cm}^2/\text{day}) = \frac{\text{weight loss}}{\text{original surface area} \times \text{exposure time}}$$

(Equation 2.6)

The setup of test is extremely simple: it only requires a sample, a test solution and an accurate microbalance. The sample is placed in the corrosion medium (SBF solution) for a period of time. After that, the tested specimen is taken out and washed with a cleaning solution (such as dilute chromic acid) to remove all corrosion products and then the resultant mass change is measured. Because corrosion products directly affect the weight loss rate and thereby influence the corrosion rate, the corrosion products must be removed cleanly. This classic method has been used by a number of researchers [54, 59, 104, 175-178]. However, this simplest in vitro method has some drawbacks: (1) In order to obtain accurate results, all corrosion products should be completely removed while the un-corroded alloy cannot be damaged. This procedure cannot be precisely controlled, and some experimental errors are probably introduced into the weight loss rate. (2) The weight loss rate is an average result rather than an instantaneous value. During the corrosion, some detailed corrosion information is inaccessible such as the corrosion performance of the initial or final stage and the relative anodic and cathodic reaction kinetics.

2) Song et al. [179] developed the hydrogen evolution method, which was based on the collection of hydrogen gas during degradation of magnesium in aqueous solutions. Currently, the hydrogen evolution measurement is very popular and widely accepted by a lot of researchers [10, 42, 59, 106, 107, 180-183]. The device needed for this experiment is quite simple. An illustration of this experimental setup is introduced later in Chapter 3. The mechanism of this measurement is simple and easy to understand, and is based on the reaction below:

$$Mg + 2H_2O \rightarrow Mg(OH)_2 + H_2 \uparrow \qquad \text{(Equation 2.7)}$$

The evolution of one mole of hydrogen gas corresponds to the dissolution of one mole of magnesium metal. Thus, the volume of evolved hydrogen gas is equal to the weight loss of the alloys, and they can be converted into the same units (mg/cm$^2$/day). The corrosion rate can be measured by the increase of hydrogen gas volume. Moreover, the corrosion products do not affect the results. It is also possible to calculate the degree of alkalization, which is a problem during the degradation of magnesium alloys, because the dissolution of 1 mol Mg relates to the release of 2 mol of $OH^-$.

3) The electrochemical behaviour of metals can be investigated by many electrochemical methods, such as potentiodynamic polarization, open circuit potential evolution and electrochemical impedance spectroscopy (EIS). Electrochemical measurement is also widely used in measuring the in vitro degradation behaviour of magnesium alloys [13, 58, 184-187]. The greatest advantage of this measurement is that it can be used to obtain the real-time corrosion rate. The changes in the corrosion behaviour can be instantaneously observed. Using this method, more corrosion information can be accessed, such as the relative rates of the anodic and cathodic reactions over a range of potentials [188]. A number of investigations indicate that the corrosion rate of magnesium alloys measured by electrochemical testing agrees with

that by hydrogen evolution, and helps us to understand how corrosion takes place [160, 188, 189].

In order to obtain precise and comprehensive information concerning the bio-corrosion performance, simultaneous use of hydrogen evolution and electrochemical measurement is recommended [107, 163, 181, 190, 191] and has also been applied in this project.

## 2.9 Applications

Biomaterials have two main clinical applications: hard tissue replacement implants, such as fracture plates, screws, pins, joint replacements and dental implants; and soft tissue replacement implants, such as sutures, vascular implants, maxillofacial implants and heart assist devices. Commonly, degradable biomaterials can be used in orthopaedic surgery as indicated in Fig. 2.20 [192].

Fig. 2.20 Black areas indicate possible locations for biodegradable implants in

orthopaedic surgery (adapted from [192]).

The development of magnesium alloys would provide more possibilities for the implants in both un-loaded and loaded applications. Current studies of biomedical magnesium alloys focus on two aspects: orthopaedic implants and biodegradable stents. Fig. 2.21 a) shows a biodegradable stent which is made from WE43 alloy. It is 10~15 mm in length and 3.5 mm in diameter [45, 193]. Fig. 2.21 b) shows a cortical bone screw, machined from AZ31 and with a length of 18 mm, thread diameter of 3.5 mm, and weight of 240 mg [194]. Biodegradable magnesium screws are used in reconstruction surgery and applied to help the injury recover to the original condition in combination with plates. Fig. 2.21 c) presents a mandible fixer made of AZ31 alloy [195]. An Mg-0.8 Ca screw, ZEK100 plate and LAE442 intramedullary nail are illustrated in Fig. 2.21 d) [196].

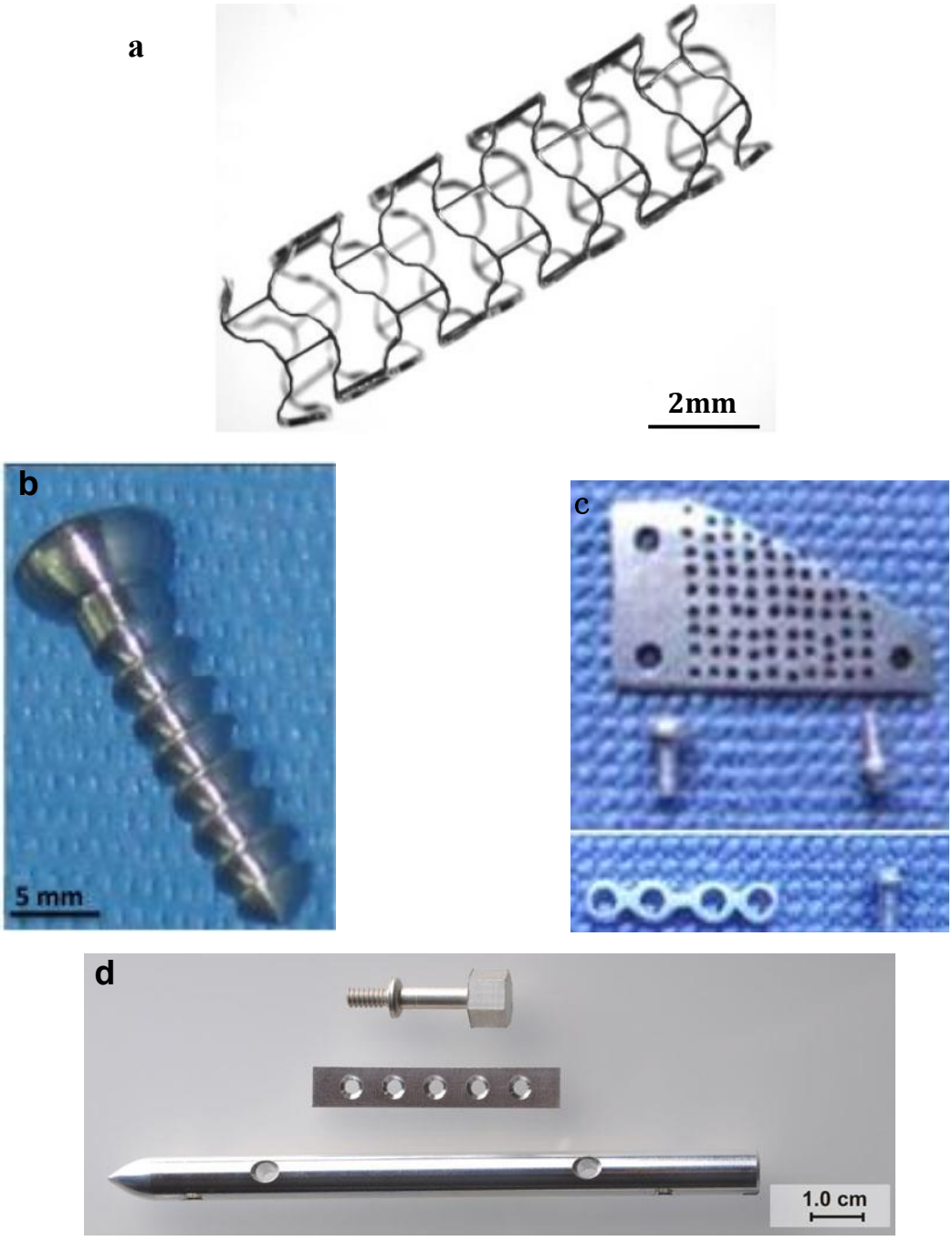


Fig. 2.21 (a) Bioabsorbable magnesium stent (BIOTRONIK, Berlin, Germany); (b) AZ31 alloy screw (cortical bone screw); (c) mandible fixer made of AZ31; (d) Mg-0.8Ca screw, ZEK100 plate, intramedullary LAE442 nail (from top to bottom).

# Chapter 3 Experimental

## 3.1 Materials

Pure magnesium (99.95 wt%, Yuhua Metallurgical and Materials Company, China), a master alloy (Mg-30 wt% Ca, Yuhua Metallurgical and Materials Company, China) and pure zinc (99.99 wt%, Sigma-Aldrich Company, UK) were used to prepare magnesium alloys. The compositions of pure magnesium and Mg-Ca master alloy provided by the supplier are summarized in Table 3.1.

Table 3.1 Chemical compositions of pure magnesium (wt%).

| **Element** | **Ca** | **Si** | **Fe** | **Ni** | **Cu** | **Al** | **Mn** | **Mg** |
|---|---|---|---|---|---|---|---|---|
| **Mg** | - | < 0.005 | < 0.004 | < 0.0007 | < 0.003 | < 0.006 | < 0.01 | > 99.95 |
| **Mg-Ca** | 31.53 | 0.025 | 0.025 | 0.00053 | 0.0012 | 0.0041 | 0.014 | Balance |

## 3.2 Preparation of magnesium alloys

### 3.2.1 Mg alloys

Magnesium alloys were identified according to the standard nomenclature. The main components were named by Z zinc and X calcium, respectively. The alloys were designed and their compositions are given in Table 3.2. The chemical compositions of the magnesium alloys were analyzed by X-ray fluorescence spectroscopy (XRF) on a Rigaku NEX-CG system.

Table 3.2 Chemical compositions of the alloys (wt%).

| Elements | Actual Composition (wt%) | |
|---|---|---|
| | **Mg-3Zn (MZ3)** | **Mg-3Zn-0.3Ca (MZX30)** |
| **Zn** | 3.08 | 2.97 |
| **Ca** | - | 0.33 |
| **Si** | <0.0001 | <0.0001 |
| **Fe** | 0.0045 | 0.0040 |
| **Ni** | 0.0006 | <0.0001 |
| **Cu** | <0.0001 | <0.0001 |
| **Mg** | Balance | Balance |

### 3.2.2 Equipment and method for preparing magnesium alloys

Alloys were cast via induction melting in an inert atmosphere using a home-made electrical induction furnace (for more details, see Appendix). Fig. 3.1 shows the vacuum melting and casting induction furnace with a tiltable heating coil and crucible. The whole procedure, including heating, melting and casting, was carried out in this induction furnace. Magnesium is chemically active and easily oxidized. Prevention of the oxidation and burning of magnesium is the main issue which has to be considered. In this study, a protective atmosphere consisting of argon was used to eliminate the oxygen in the furnace chamber and thus suppress loss of magnesium; the vacuum system also helped to reduce oxygen and inhibited burning from the safety point of view.

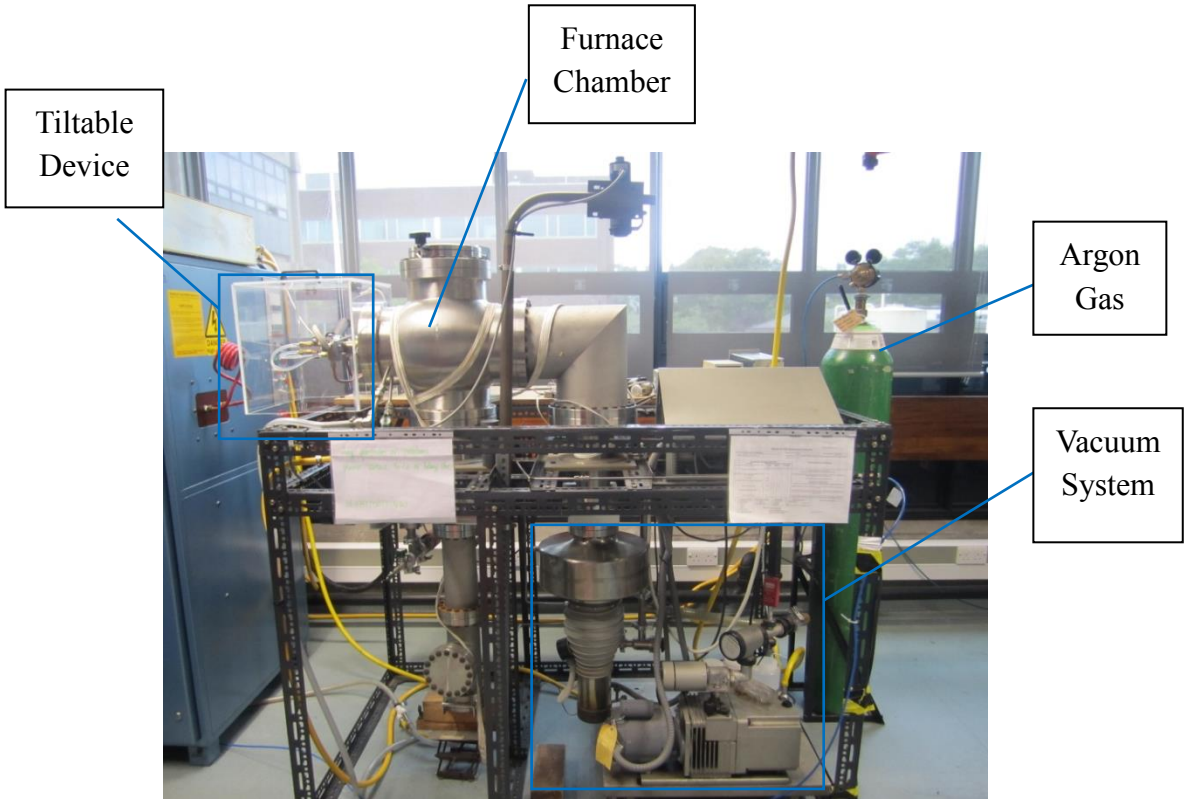


Fig. 3.1 Vacuum melting and casting induction furnace for magnesium alloys.

### 3.2.3 Melting and casting process

Magnesium alloys with nominal composition Mg-3 wt% Zn and Mg-3 wt% Zn-0.3 wt% Ca were induction melted in a mild steel crucible. The melting and casting process is briefly summarised as follows: all of the raw materials needed to be polished to remove the oxide layer on the surface. After placing the raw materials in the furnace chamber, the vacuum was established. Argon was introduced into the furnace to create the inert atmosphere required for casting magnesium. The temperature was gradually raised to 650 ℃. The crucible was tilted when the raw materials were melted and then the molten metal could be cast into a pre-positioned mild steel mould under an argon atmosphere (500~600 mbar). The rectangular ingot (100 mm × 70 mm × 35 mm) was then cooled, as shown in Fig. 3.2.

Fig. 3.2 Optical image obtained from the magnesium alloy ingot.

## 3.3 Microstructural characterisation

### 3.3.1 Metallurgical observations

The specimens were cut from the middle part of the ingot along the transverse plane, as shown in Fig. 3.3. This is to avoid shrinkage.

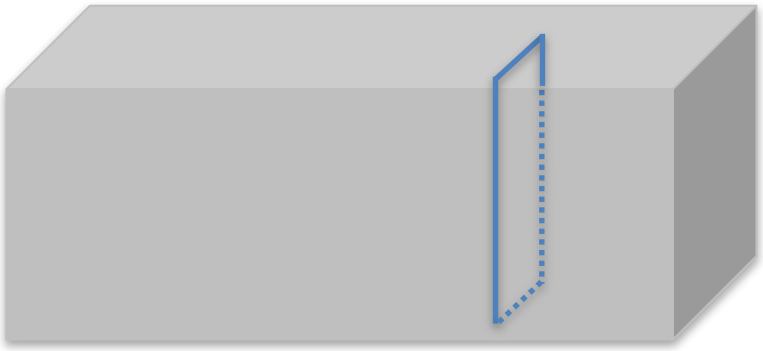

Fig. 3.3 Schematic representation of the sectioning of the specimens for microstructural characterization.

The specimens were mechanically ground using SiC papers up to #4000 on a Struers

Labopol-5, followed by polishing on the same machine. The magnesium samples were polished using 'MD Mol' cloth (Struers Ltd.) with 3 μm liquid diamond suspension (Kemet Ltd.). An 'MD Nap' polishing cloth (Struers Ltd.) with 1 μm liquid diamond suspension was then used (Metprep Ltd.). The 'MD Nap' polishing cloth was again used for the final polishing, using 0.25 μm diamond compound (Metprep Ltd.). Ethanol or water-free lubricant was used throughout the whole polishing process to prevent the oxidation of the samples. The sample was ultrasonically rinsed in the ethanol and dried in the cool air. The samples were etched using different etchants and etching times, as shown in Table 3.3. Optical observations were conducted on a microscope (Zeiss Axioskop 2) using Axio vision image capture and analysis software. The grain size was measured using the analysis software based on the Zeiss microscope. At least 20 measurements of grain size were made at a magnification of 100×. The software Image J was used to analyse the phase fractions. The reported data represent an average of at least 20 measurements.

Table 3.3 Etching methods.

| | **Sample** | **Etchant** | **Time** |
|---|---|---|---|
| **Etching Method (Metallurgical Observation for OM and SEM)** | As-cast Mg-3Zn | 50 ml Distilled water<br>150 ml Ethanol<br>1 ml Acetic acid | ~40 s |
| | As-cast Mg-3Zn-0.3Ca | 4% Nitric acid<br>96% Ethanol | ~10 s |
| | Heat-treated Mg-3Zn | 50 ml Distilled water<br>150 ml Ethanol<br>1 ml Acetic acid | ~60 s |
| | Heat-treated Mg-3Zn-0.3Ca | 4% Nitric acid<br>96% Ethanol | ~20 s |

### 3.3.2 SEM

A scanning electron microscope (SEM) equipped with Energy Dispersive X-ray (EDX) analysis is a powerful tool in the observation of microstructure and the analysis of the chemical compositions of alloys. In this study, JEOL JSM-6060LV, Philips XL30, JEOL JSM-7000F SEMs and a Philips XL-30 ESEM were employed for observing the microstructure and corrosion morphology. The first two microscopes possess thermo-electric guns, the latter two have field emission guns and are used for higher resolution observation. All EDX detectors on the SEMs were silicon lithium semiconductor detectors. INCA software was used to analyse the chemical compositions. Generally, for microstructural observation, the preparation of the SEM specimen was as for OM, as detailed in Section 3.3.1. The microstructural and corrosion morphology characterisations were performed at an operating voltage of 20 keV. The compositions of second phases were determined by EDX analysis, including spot analysis, line scans and maps.

### 3.3.3 TEM

Transmission Electron Microscope (TEM) examination was performed in a computer-controlled fully-digitized microscope (JEOL-2100HT TEM) equipped with an Oxford INCA EDX system. TEM can be used not only to determine crystal structure and to identify precipitates, but can also be applied to analyse the chemical compositions of the small precipitates. For preparation of TEM samples, thin slices of about 1 mm in thickness were cut from bulk samples using electro discharge machining (EDM, Metal Crystals and Oxides Ltd.). TEM discs 3 mm in diameter were punched from these thin slices and manually ground to 150~180 μm thick by using the finer SiC grinding paper. The foils were prepared by twin-jet electro-polishing (Struers TenuPol-3). The parameters for the electro-polishing are listed in Table 3.4. Once

removed from the jet polisher, the specimens were quickly dipped into a 20 vol. % nitric acid - 80 vol. % ethanol solution to remove a black opaque layer from the surface. Finally, the specimens were cleaned to remove the oxide layer formed quickly on the highly reactive magnesium surface using a Gatan Precision Ion Polishing system (PIPS) PIPS691 at a beam voltage of 4.0 kV and a low incidence angle of 4° for about 30 minutes for each side.

Table 3.4 Electro-polishing method.

| | **Polishing Chemical** | **Temperature** | **Voltage** | **Current** | **Time** |
|---|---|---|---|---|---|
| **Electro-polishing Method (for TEM)** | 4 vol.% Perchloric acid 95 vol.% Ethanol | -10 ℃ | 20 V | 0.6 A | Until a hole appears |

### 3.3.4 FIB/SEM

A Focused Ion Beam Scanning Electron Microscope (FIB/SEM, FEI Quanta 3D FEG) equipped with a focused gallium ion beam and a conventional field-emission gun scanning electron beam was used to serially section samples prior to reconstructing the 3D image and to prepare TEM samples in specific positions. This microscope enables TEM samples that are difficult otherwise to produce, such as a cross-section or a particular area (e.g. specified precipitate, shown in Fig. 3.4 a)). Using this microscope, the user can view the whole TEM sample making process. Firstly, the interested area was coated with tungsten in order to protect the adjacent area from ion milling. Then, the specific area was thinned to 1 μm by using the ion beam at 30 kV with a beam current from 65 nA down to 5 nA. This thin slice was cut off and mounted on an Omniprobe (tungsten needle), followed by welding it onto a copper

grid. Finally, this slice was ion beam thinned to around 200 nm and cleaned at a very low beam current. A final TEM sample is illustrated in Fig. 3.4 b).

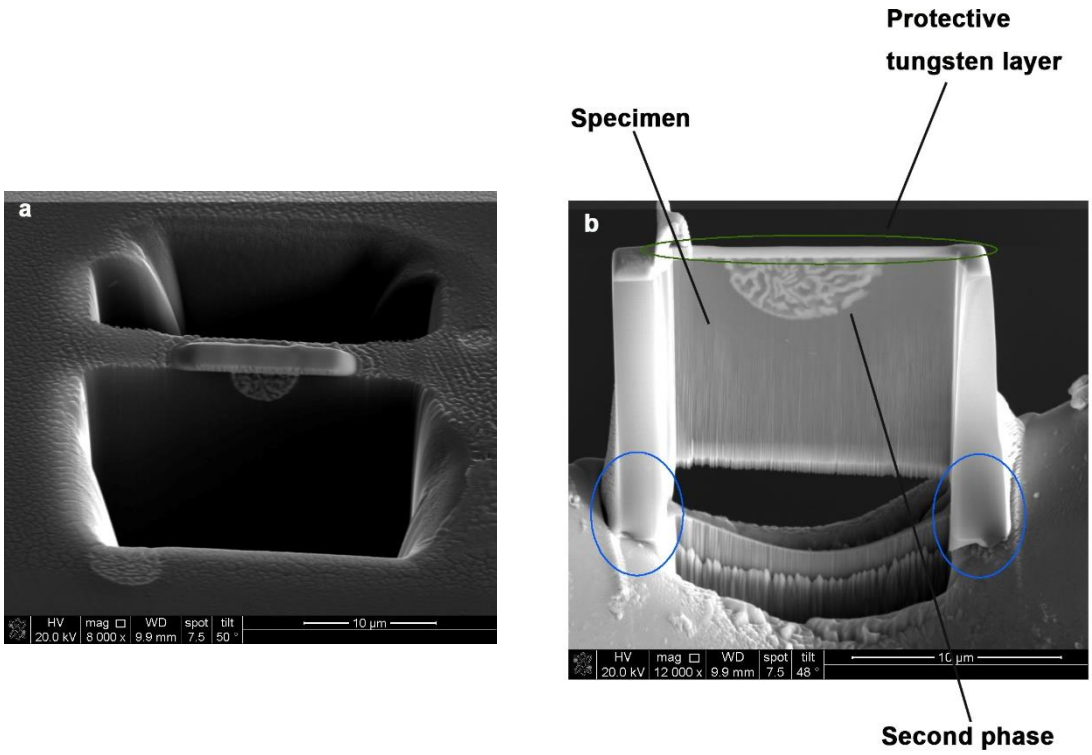


Fig. 3.4 a) Using FIB to lift out a specimen of the particular second phases in MZ3; b) final TEM sample (MZ3). The specimen is the central rectangle. The V shaped Cu grid is below the specimen. The specimen was soldered at two points as shown by the ellipses.

The software named 'Auto Slice and View' can be used to slice sequentially the sample and automatically record every image. The reconstruction of 3D image was carried out using Avizo Software.

### 3.3.5 PIPS

The Precision Ion Polishing System (PIPS) is a user-friendly and precise ion polisher which is designed to produce high quality TEM samples. Two miniature Penning Ion

Guns (PIG'S) are used at glancing angles to the specimen. The low sputtering angles minimize radiation damage and beam heating while producing specimens with exceptionally large, clean electron transparent areas. A schematic representation of the PIPS work chamber is shown in Fig. 3.5.

A Gatan PIPS was used in this study to prepare TEM samples when analysing the grain boundaries' second phases. This is because the second phases on the grain boundaries were dissolved when performing the electro-chemical polishing method. The bulk samples were sliced to 1 mm thick followed by grinding to 200~250 μm. Afterwards, the discs with 3 mm diameter were punched using a Gatan Disc Punch and then these discs were gently ground to 30 μm in thickness. Following that polishing removed the scratches on the sample surface, and then a small hole was made in the polished sample using PIPS at a beam voltage of 5 kV and an incidence angle of 8° for about 50 minutes. PIPS was also used to clean the TEM sample by removing the oxide layer.

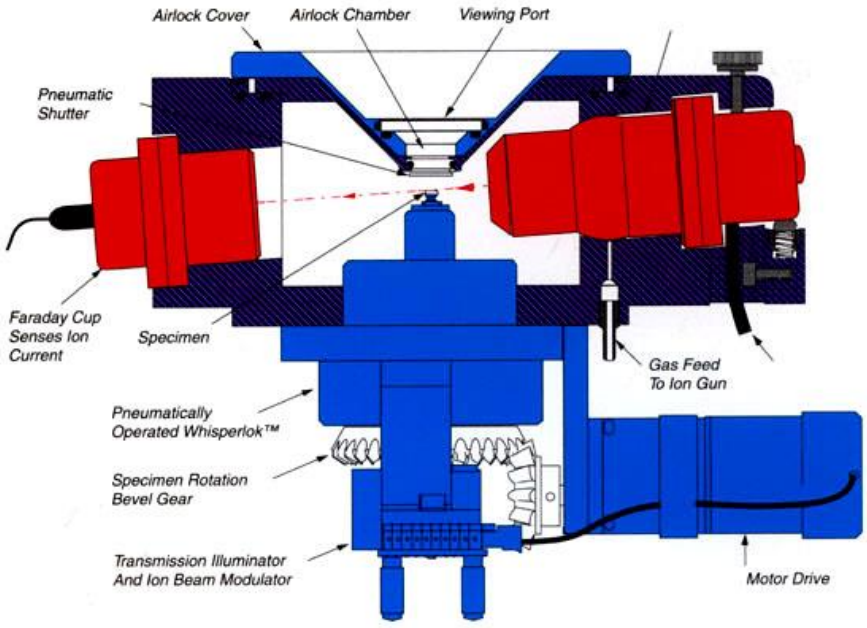


Fig. 3.5 Schematic illustration of the PIPS work chamber showing the Penning ion gun, specimen exchange mechanism, Faraday cup, airlock and specimen post

(adapted from [Gatan manu micron.ucr.edu/public/gatan/pips-691.html]).

### 3.3.6 XRD

X-ray diffraction (XRD ) is used to study crystalline and non-crystalline materials. A characteristic X-ray is directed at the sample at a constant angular velocity through increasing values and is diffracted at certain angles which contain crystallographic information. Corrosion products and coating identification were performed using Philips X-Pert Multi Purpose Diffractometer. The samples were investigated in parallel beam geometry, using Cu $K_\alpha$ radiation source. The XRD data were measured from $10^\circ$ to $90^\circ$, with a scan rate of $0.04^\circ/s$ and scan step of $0.01^\circ$.

### 3.3.7 AFM

Atomic Force Microscopy (AFM) is a high-resolution type of scanning probe microscopy, with demonstrated resolution down to a fraction of a nanometer. The instrument works by measuring the deflection produced by a sharp tip on a micron-sized cantilever as it scans across the surface of the specimen. The cantilever is typically made of silicon or silicon nitride with a tip radius of curvature of the order of nanometres. When the tip is brought proximate to a sample surface, a deflection of the cantilever is caused by the forces between the tip and the sample according to Hooke's law. Typically, the deflection is measured using a laser spot reflected from the top surface of the cantilever into an array of photodiodes. The schematic of an AFM appears as Fig. 3.6.

In this study, Multi Mode AFM (Digital Instruments, Veeco Metrology Group) was used to understand the surface characterization (roughness) of the HA coating of the magnesium alloys.

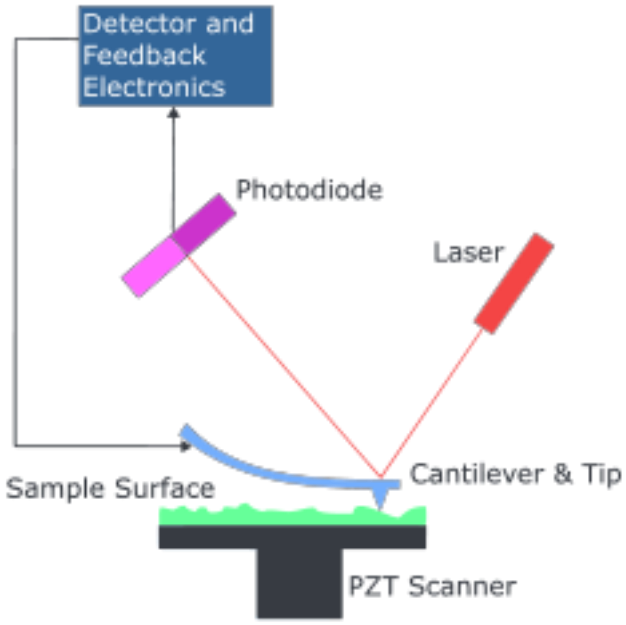


Fig. 3.6 Schematic of AFM using beam deflection detection.

### 3.3.8 Micro-CT

Micro X-Ray computed tomography (Micro-CT) is a non-destructive technique providing images of the internal structure of samples. Fig. 3.7 illustrates Micro-CT. The square pillar-like samples (1 mm × 1 mm × 10 mm) were scanned using Micro-CT tomography machines. A Nikon XTH 225 Micro X-Ray CT and Bruker Skyscan 1172 were used to examine the structure of Mg alloys before and after immersing in SBF solution. The scannings were carried out at 99 kV and 6 W.

Micro-focal spot X-Ray projections acquired at hundreds of equally angled positions around the object, are used to reconstruct a 3D database which represents the distribution map of the linear attenuation coefficients determined by the X-ray source and the atomic composition of the target material [197]. The Feldkamp-Davis-Kress (FDK) algorithm for cone beam geometry was used to reconstruct the collected projections, calculating the spatial distribution of attenuation coefficient of each voxel. Each voxel was assigned to a specific grey value which depends on the average

attenuation coefficients during reconstruction. For the 3D reconstruction, the raw data were loaded firstly in Image J software. A threshold was used to segment the different regions (magnesium matrix, second phases and corrosion sites). Then, Avizo software was used to reconstruct the 3D tomography.

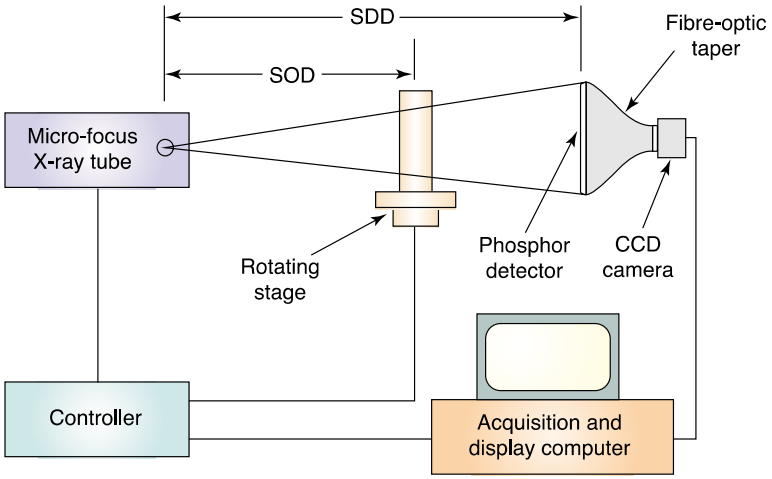


Fig. 3.7 Schematic illustration of micro X-Ray computed tomography (Micro-CT) (adapted from [197]).

## 3.4 Coating

### 3.4.6 Coating preparation

The samples were coated with a layer of HA using the potentiostatic method. A three electrode cell was used in the coating production, with a pre-treated sample as the working electrode, platinum as the counter electrode and a saturated calomel electrode (SCE) as the reference electrode, as seen in Fig. 3.8.

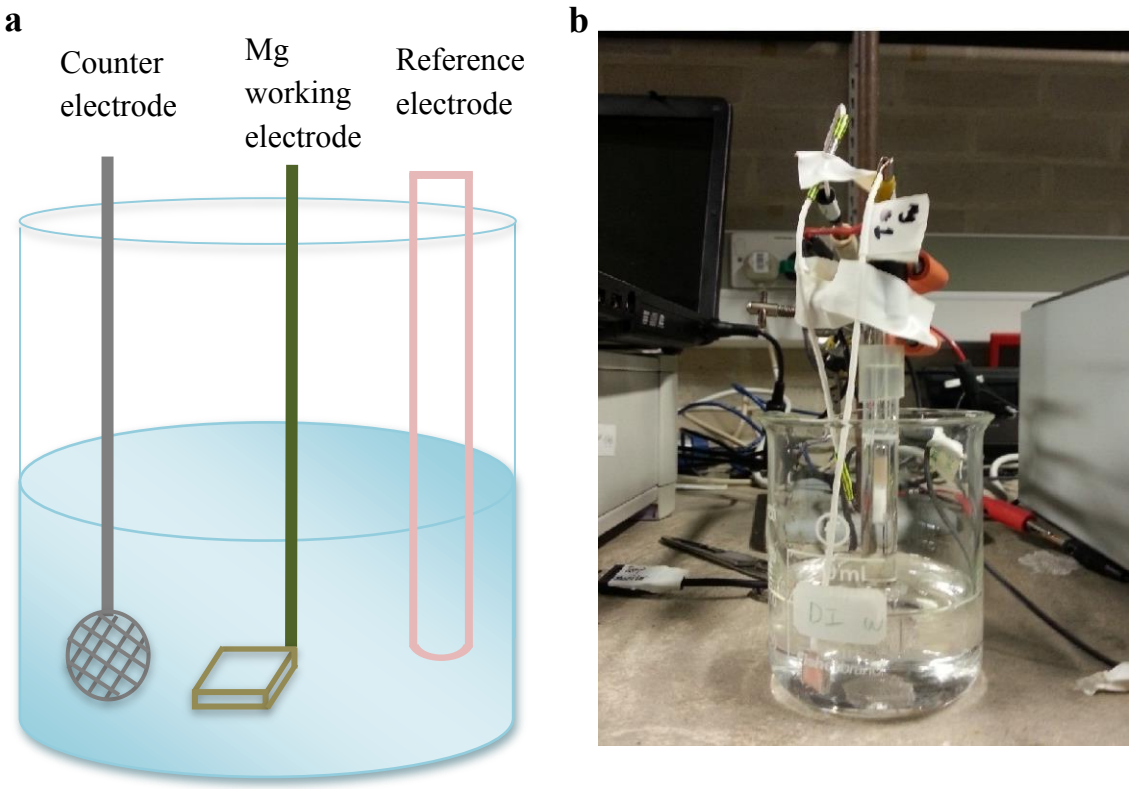


Fig. 3.8 Apparatus for the potentiostatic deposition coating:

(a) A schematic drawing shows the set-up for potentiostatic deposition;

(b) The real thing.

The sample was gradually ground to 1200 grit before the alkaline pre-treatment. As itemised in Fig. 3.9, the sample was pre-treated in 1 M NaOH for 1 h at a constant temperature of 80 ℃. Before the potentiostatic deposition, the specimen was connected to the wire in order to establish a good electrical current to the sample and then sealed by araldite. The other areas of the sample were also sealed using araldite and one area left exposed (1 $cm^2$). The potentiostatic deposition was carried out in a coating solution containing 0.06 M $NH_4H_2PO_4$ and 0.1 M $Ca(NO_3)_2$ at room temperature, the cathodic voltage was -2 V, and the duration of the coating was 30 minutes. After coating, the samples were post-treated by being immersed in 1 M NaOH for 1 h at 80 ℃.


Fig. 3.9 Coating processing route.

### 3.4.7 Sample preparation and characterization

The HA coating was observed by SEM at 20 kV (Fig. 3.10 a)). The samples were then mounted in cold resin, vertically sectioned (Fig. 3.10 b)) and polished (Fig. 3.10 c)) to investigate the cross section.

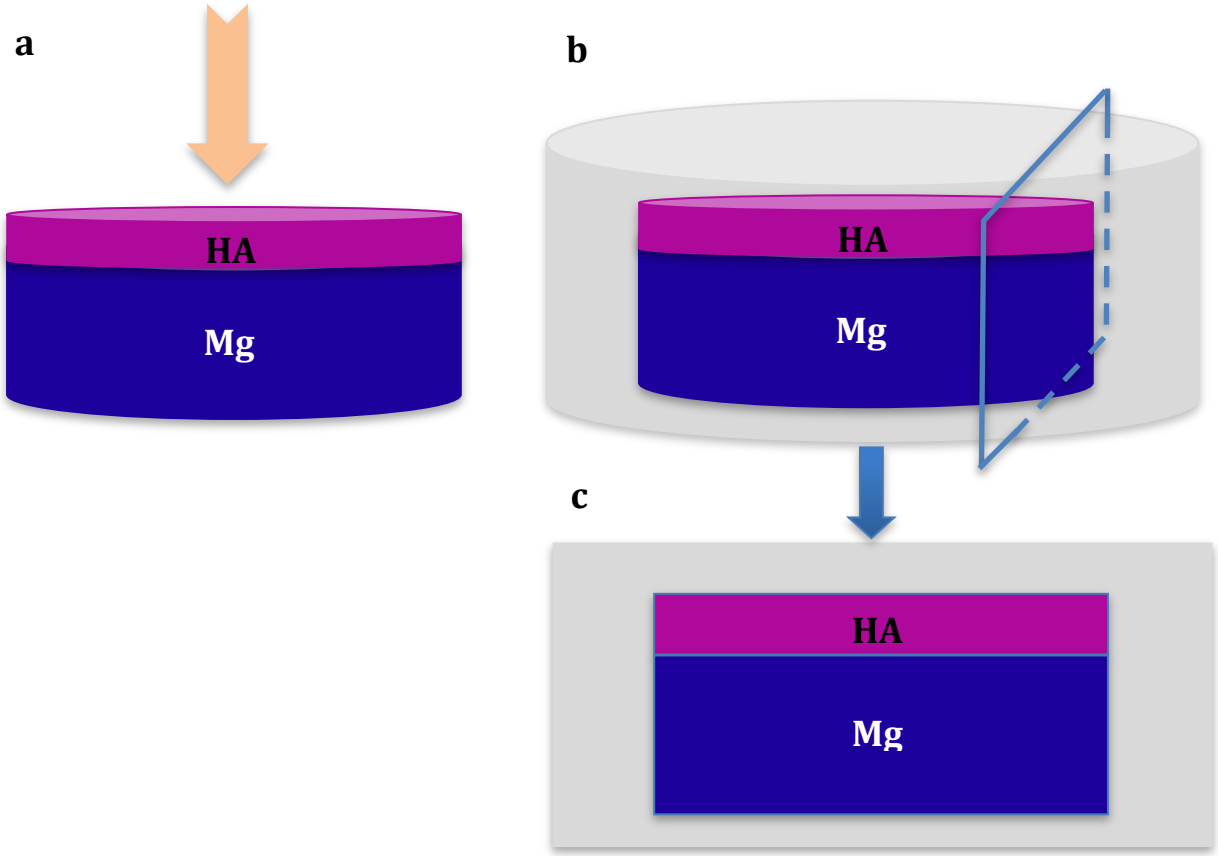


Fig. 3.10 HA-coated sample preparation for SEM analysis:

(a) A schematic drawing shows an HA coated Mg alloy. The coating was observed directly (yellow arrow) by SEM;

(b) For cross-sectional observation, the HA coated sample was mounted in resin (grey);

(c) The mounted sample was cut along the blue plane shown in (b) and polished to reveal the cross section of the sample.

### 3.5 Volume fraction of fine precipitates

In order to investigate the effect on the bio-corrosion performance of the fine precipitates produced after aging, it is necessary to measure their volume fraction by using TEM. Jain [198] provides a detailed quantitative characterization of precipitates in Mg-Zn alloys. In this study, the following equation was used to calculate the volume fraction of rod-shaped precipitates (more details, see Chapter 2):

$$f_v = -\ln(1-A_A)\left(\frac{DL}{DL+(\frac{D}{2}+L)t}\right) \qquad \text{(Equation 3.1)}$$

where D is the diameter of the rod-shaped precipitates, L is the length of the precipitates, t is the specimen thickness and $A_A$ is the projected area fraction of the precipitates.

The foil thickness was determined from approximately six measurements from six different grains for each aging condition (as detailed in Chapter 3.5.1). The average values were reported.

### 3.5.6 Thickness measurement

Several techniques are available for foil thickness measurement, such as EELS and thickness fringes. One reliable measurement is via Convergent Beam Electron Diffraction (CBED) [199, 200].

The technique uses the intensity oscillations present in convergent beam diffraction patterns. An equation deriving from the two beam dynamical theory of electron diffraction defines a relationship between $\xi_g$, t and the position of the minima in the intensity oscillations in the diffraction disc, as follows:

$$\left(\frac{s_i}{n_i}\right)^2 + \left(\frac{1}{n_i}\right)^2\left(\frac{1}{\xi_g}\right)^2 = \frac{1}{t^2} \qquad \text{(Equation 3.2)}$$

where $s_i$ is the deviation parameter of the ith minimum for the reflection **g** and can be measured directly from the spacing of the fringes in the convergent beam pattern. $n_i$ is the number of the fringes counting outwards from the mid-line. $\xi_g$ is the extinction

distance.

$s_i$ can be obtained via the following equation:

$$s_i = \frac{\lambda}{d^2}\left(\frac{\Delta\theta_i}{2\theta_B}\right) \qquad \text{(Equation 3.3)}$$

where λ is the wavelength. d is the plane spacing of the operating reflection. $\Delta\theta_i$ is the distance to the chosen minimum from the mid-line. $2\theta_B$ is the distance between the centre disc and the diffracted disc. Plotting $(s_i/n_i)^2$ against $(1/n_i)^2$, the foil thickness is given by the intercept of the resulting straight line with the $(s_i/n_i)^2$ axis if n gives a straight line. The method to obtain the specimen thickness is illustrated in Fig. 3.11. Very large d values (very low order reflections) must be avoided due to multiple scattering from systematic reflections. In this study, thickness measurements were carried out near the $[1\bar{2}10]$ zone axis using g = $\bar{2}0\bar{2}1$. An example of a thickness measurement will be shown in Chapter 4 (section 4.5.2.3).

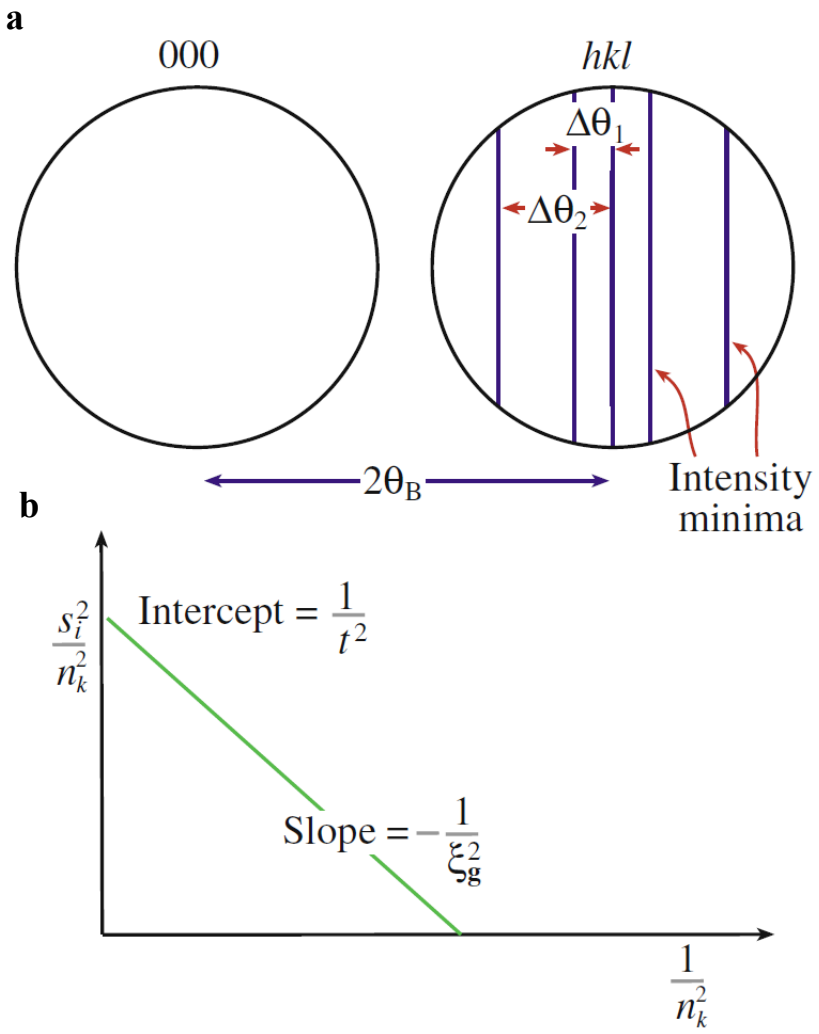


Figure 3.11 Schematic drawing presenting the foil thickness measurement using a convergent beam electron diffraction pattern centred on a Bragg position (adapted from [201]):

(a) The measurements necessary to extract the specimen thickness (t) from Kossel-Möllenstedt (K-M) fringes. From $n_i$ measurements space of $\Delta\theta_i$, determine the deviation parameters $s_i$;

(b) Plot $(s_i/n_i)^2$ versus $(1/n_i)^2$. The value of $t^{-2}$ can be determined by the extrapolation to the ordinate if the plot is a straight line.

### 3.5.7 Dimension measurements

Transmission electron microscopy (TEM) is a very useful tool to measure the dimension of the micro or nano particles on account of its high resolution. However, even the best TEM still suffers from overlapping and truncation of the precipitates. In this study, bright field images taken at magnifications of 8 K and 10 K were used to measure the projected area fraction ($A_A$). The growth axis of the precipitates is parallel to $[0001]_{Mg}$ in this study. In order to measure the true dimensions of the precipitates reducing the overlap, all the images were taken with beam directions close to $\langle 1\bar{2}10 \rangle$ or $\langle 0001 \rangle$. The foil normals of all the samples used are within 30° of $\langle 1\bar{2}10 \rangle$ and $\langle 0001 \rangle$.

## 3.6 Corrosion behaviour tests

### 3.6.6 Simulated body fluid (SBF) preparation

Kokubo [202] developed a simulated body fluid (SBF) that has inorganic ion concentrations and pH value very similar to those of human extracellular fluid. In order to research in vitro degradation rates of bio-magnesium alloys, SBF solution is indispensable. The ion concentrations and pH are defined in Table 2.6 (see Chapter 2). Table 3.5 lists the reagents and their constituents for SBF preparation. The following powder reagent grade chemicals have to be kept in a desicator. It must be stressed that these chemicals should be added sequentially into the solution after each reagent has completely dissolved. De-ionised water was used for the preparation of the SBF. The pH of the SBF was adjusted to 7.4 at 36.5 ℃ by using tris (hydroxymethyl) aminomethane and HCl. The pH meter and thermometer constantly monitored the solution. Finally, the SBF was placed in a polyethylene bottle and stored in a refrigerator at 5-10 ℃. SBF is a clear solution: it must not be used for any further testing if precipitation occurs in the solution.

Table 3.5 List of reagents in SBF (pH 7.4, 1L).

| Reagent | Amount | Source |
|---|---|---|
| **Sodium chloride (NaCl)** | 7.996 g | Scientific & Chemical Supplies Ltd., UK |
| **Sodium hydrogen carbonate ($NaHCO_3$)** | 0.350 g | Sigma-Aldrich Ltd., UK |
| **Potassium chloride (KCl)** | 0.224 g | Sigma-Aldrich Ltd., UK |
| **Di-potassium hydrogen phosphate trihydrate ($K_2HPO_4 \cdot 3H_2O$)** | 0.228 g | Sigma-Aldrich Ltd., UK |
| **Magnesium chloride hexahydrate ($MgCl_2 \cdot 6H_2O$)** | 0.305 g | Sigma-Aldrich Ltd., UK |
| **Hydrochloric acid (1 kmol/$m^3$ HCl)** | 40 ml | Sigma-Aldrich Ltd., UK |
| **Calcium chloride ($Ca_2Cl$)** | 0.278 g | Sigma-Aldrich Ltd., UK |
| **Sodium sulphate ($Na_2SO_4$)** | 0.071 g | Sigma-Aldrich Ltd., UK |
| **Tris-hydroxymethyl aminomethane ($(CH_2OH_3)CNH_2$)** | 6.057 g | Sigma-Aldrich Ltd., UK |

### 3.6.7 Immersion tests

In order to study degradation rate variations versus exposure time, the hydrogen evolution rates need to be monitored and then translated to the degradation rate. The increase in pH caused by the corrosion of magnesium in SBF affects the degradation rate of magnesium. In order to minimize the variation of the pH of the SBF during the test, on the one hand, keep the ratio of sample surface to the SBF volume large, on the other, the SBF solution was refreshed every 24 h. In the immersion test, the ratio of sample surface to the volume of the SBF was set to 1 $cm^2$:100 mL. The whole set-up for the hydrogen collection is simple, as displayed in Fig. 3.12. The temperature was kept around 37 ℃ to simulate human body temperature. After different immersion

durations, the soaked specimens were taken out and gently rinsed in the de-ionised water and dried in cool air. Then, the corrosion morphology and composition of the corrosion products could be observed using SEM.

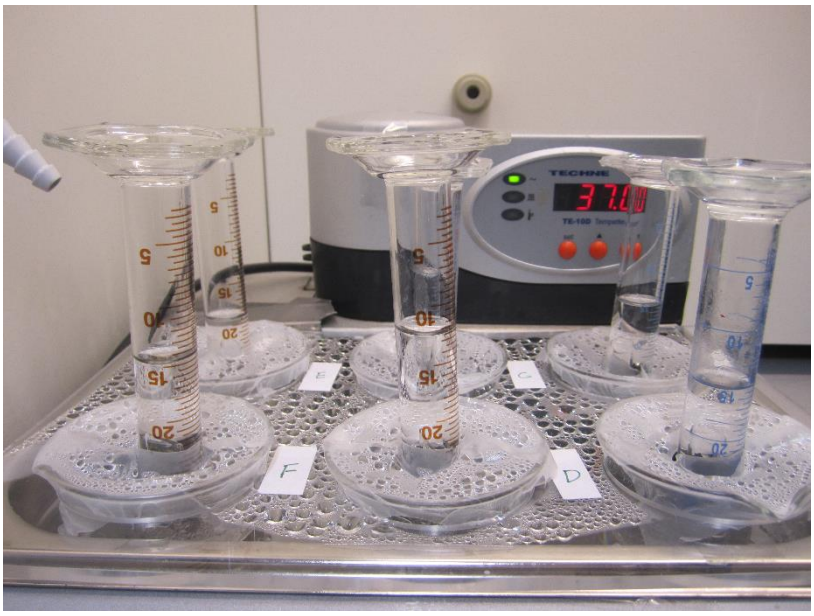

Fig. 3.12 Apparatus for hydrogen evolution test.

The set-up for measuring the $H_2$ evolved was detailed in Fig. 3.13. The funnel was placed upside down over the sample, and a measuring cylinder was positioned above the funnel. Hydrogen bubbles generated from the soaked sample were collected into a measuring cylinder. The amount of hydrogen can be measured from the height difference of the SBF solution in the measuring cylinder. Thus, the degradation rate of magnesium can by monitored over time via the emitted hydrogen.

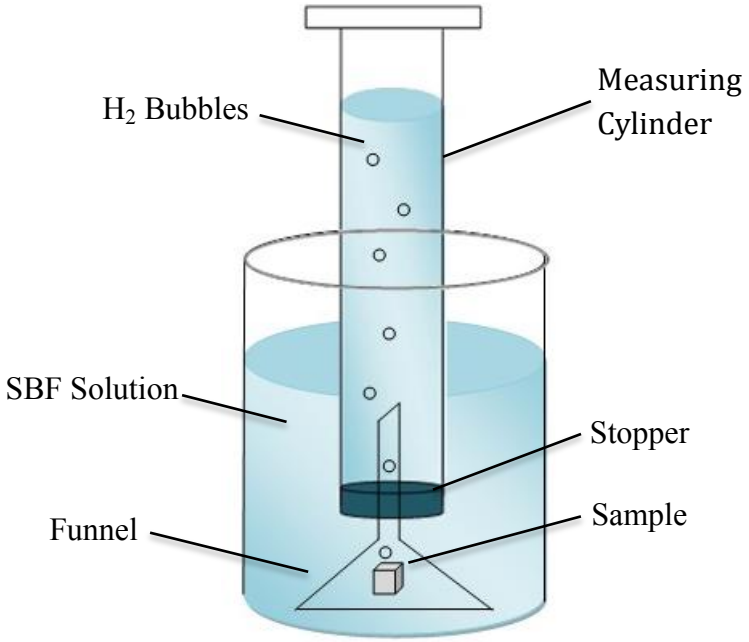


Fig. 3.13 Schematic illustration of measurement of evolved hydrogen volume.

Samples with dimensions of 10 mm ×10 mm × 2 mm were ground up to #4000 using SiC papers and then polished to a mirror-like surface. The bottom side of the immersed sample was sealed by waterproof nail enamel to prevent corrosion on this side, because even on the bottom side in contact with the beaker, corrosion also took place. Before immersion, all the samples were ultrasonically cleaned in the ethanol followed by cool air drying. An average of three measurements was taken for each group. After immersion, the specimens were taken out, rinsed gently in the de-sioned water and dried with cool air. A solution of 180 g/L $CrO_3$ was used to clean carefully the tested samples to remove the corrosion products with minimal damage to the sample.

The average degradation rate (mg/cm$^2$/day) of magnesium alloys was calculated from the collected hydrogen volume. After a certain immersion period, the total amount of measured $H_2$ can be translated to weight loss, according to the relationship between evolved hydrogen gas and dissolved magnesium (1 mL evolved $H_2$ =0.001083 g degraded magnesium).

### 3.6.8 Electrochemical measurements

Electrochemical testing was employed to study the main features of the corrosion of the magnesium alloy in SBF solution. The whole test was carried out in a water bath maintained at 37 ℃, as illustrated in Fig. 3.14. A three-electrode cell is used for the electrochemical test, as illustrated in Fig. 3.15. The standard three-electrode configuration includes saturated calomel as a reference electrode, platinum as a counter electrode and the magnesium sample as the working electrode.

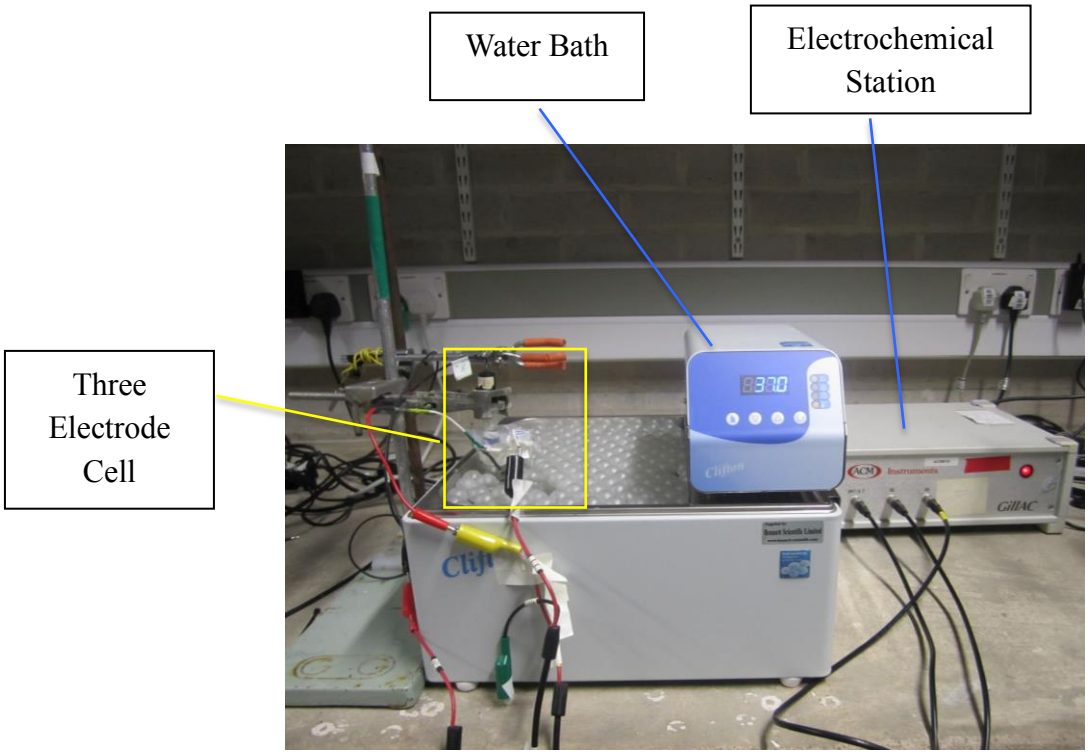


Fig. 3.14 Electrochemical test (temperature: 37 ℃; solution: SBF).

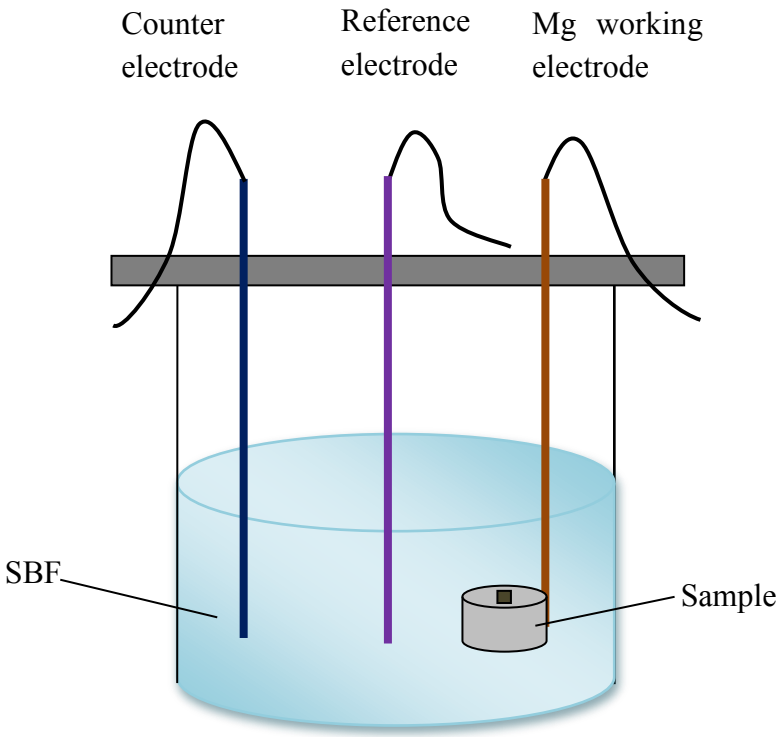


Fig. 3.15 Schematic illustration of electrochemical test.

The electrochemical measurements were carried out at a scanning rate of 1 mV/s using an electrochemical station (ACM INSTRUMENT Gill AC). The tests were performed in 100 mL of SBF solution under 37 ℃. Variations in the open circuit potential (OCP) were recorded with immersion times up to 60 minutes. Then the potentiodynamic tests were commenced. Tests were performed three times to confirm the reproducibility of the results.

Samples (10 mm ×10 mm ×2 mm) were obtained and soldered to a wire that provides an electrical connection. The exposed end of the wire was firstly fixed on the back side of the sample by using silver paint (Agar). Solder was then used to fasten them tightly together. Following that the sample was mounted in cold resin (Metprep) to isolate the corrosion medium, leaving an exposed area of 1 $cm^2$ as working electrode (see Fig. 3.16). Before the electrochemical tests, the specimens were gradually ground

to # 4000, then polished to 1 μm, ultrasonically rinsed in the ethanol and finally dried in cool air.

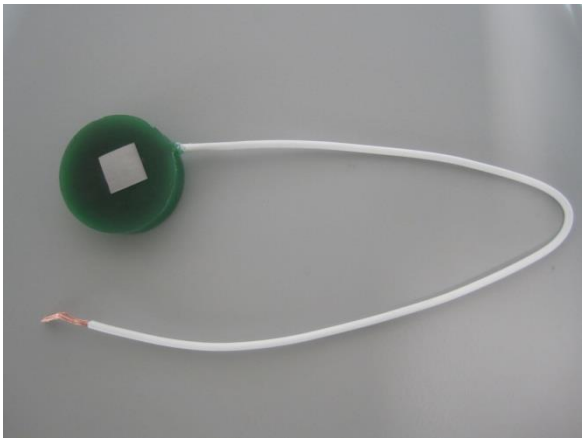

Fig. 3.16 Sample mounted in epoxy resin with an electrical connection for the electrochemical test.

### 3.7 Heat treatment

Mg-3Zn and Mg-3Zn-0.3Ca alloys were embedded in graphite powder to prevent severe oxidation during the solution treatment. For the Mg-3Zn alloys, solution treatment (T4) was carried out at 310 ℃ for 24 h followed by quenching in water. The solution treated samples were then aged at 160 ℃ for 10 h, 25 h, 50 h, 96 h and 144 h. For the Mg-3Zn-0.3Ca alloys, samples were solution treated at 310 ℃, 360 ℃, 400 ℃, 420 ℃ and 450 ℃ for different durations to produce different volume fractions of the second phase.

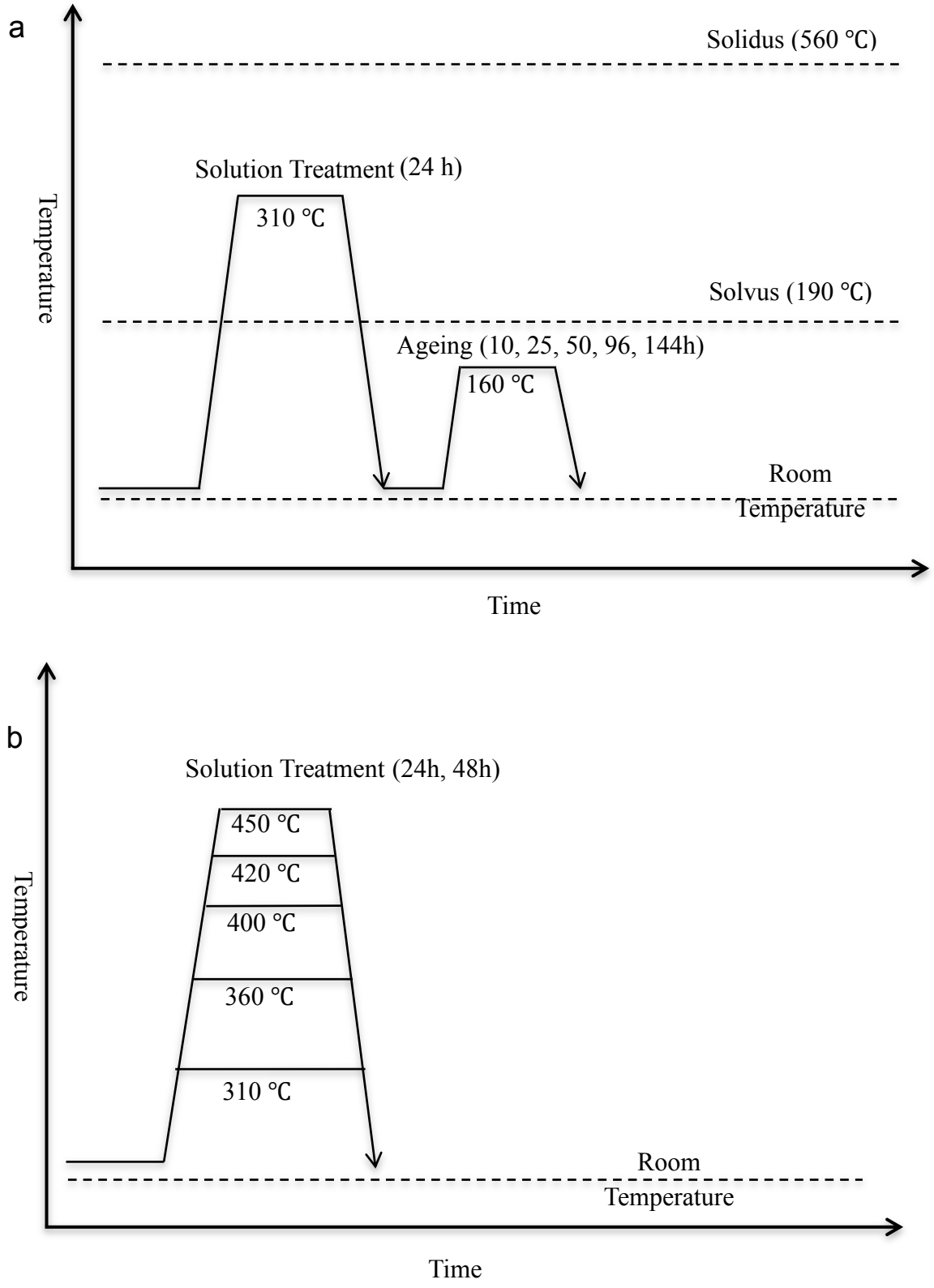


Fig. 3.17 Schematic diagrams showing the heat treatment procedure:

(a) Heat treatments for Mg-3Zn. After each heat treatment, the specimen was quenched into water;

(b) Heat treatments for Mg-3Zn-0.3Ca. Solution treatments were followed by water quenching.

### 3.8 Hardness tests

All specimens were ground using a series of waterproof silicon carbide papers #400, #800, #1200, #2400 and # 4000, followed by diamond paste polishing to 1 μm to produce a mirror-like surface. Hardness testing was performed on the polished surface using a Mitutoyo MVK-H1 micro-hardness tester fitted with a Vickers indenter with a load of 100 g for 10 s.

# Chapter 4 Microstructure of Mg-3Zn (-0.3Ca) alloys

## 4.1 Microstructure of as-cast MZ3 and MZX30

### 4.1.1 Optical microstructure

Fig. 4.1 shows the general microstructure of pure Mg, as-cast MZ3 and as-cast MZX30. As can be seen in Fig. 4.1 a), pure Mg is a single phase (α-Mg) with a large grain size (203 ± 11 μm). Figs. 4.1 b) and c) show dendrites in the as-cast MZ3 and MZX30. The grain size was reduced by the addition of alloying elements, as detailed in Table 4.1. The grain size of MZX30 further reduces after the addition of Ca as compared with MZ3.

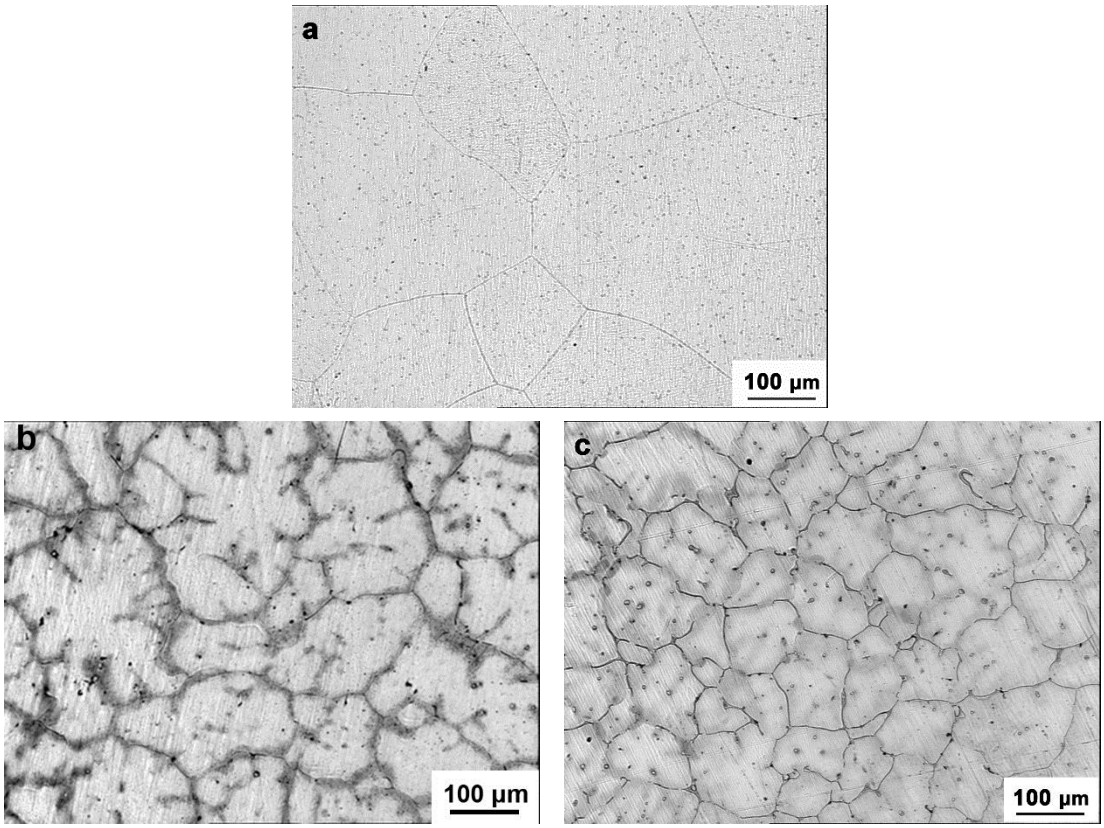


Fig. 4.1 Optical micrographs of pure Mg and as-cast Mg alloys: (a) pure Mg; (b) MZ3; (c) MZX30.

Table 4.1 summarizes the microstructure of the as-cast MZ3 and MZX30. The grain size is reduced from 141 ± 8 μm to 97 ± 6 μm by the addition of Ca. Also, the volume fraction of second phases is significantly increased by adding Ca: 0.6 ± 0.1 % in MZ3 and 2.4 ± 0.4 % in MZX30.

Table 4.1 Microstructure characteristics of the as-cast Mg alloys.

| **Alloys** | **Average grain size (μm)** | **Volume fraction of second phase (%)** |
|---|---|---|
| **MZ3** | 141 ± 8 | 0.6 ± 0.1 |
| **MZX30** | 97 ± 6 | 2.4 ± 0.4 |

### 4.1.2 SEM observation and EDS analysis

Fig. 4.2 shows that when Ca is added, the morphology and distribution of the second phases are changed greatly compared with those in the as-cast MZ3. In the as-cast MZ3, the spherical second phases are distributed mainly within grains, as shown in Figs. 4.2 a) and b). As can be seen from Fig. 4.2 c) and d), the as-cast microstructure of MZX30 consisted of α-Mg grains, spherical phases and a network of second phase along the grain boundaries.

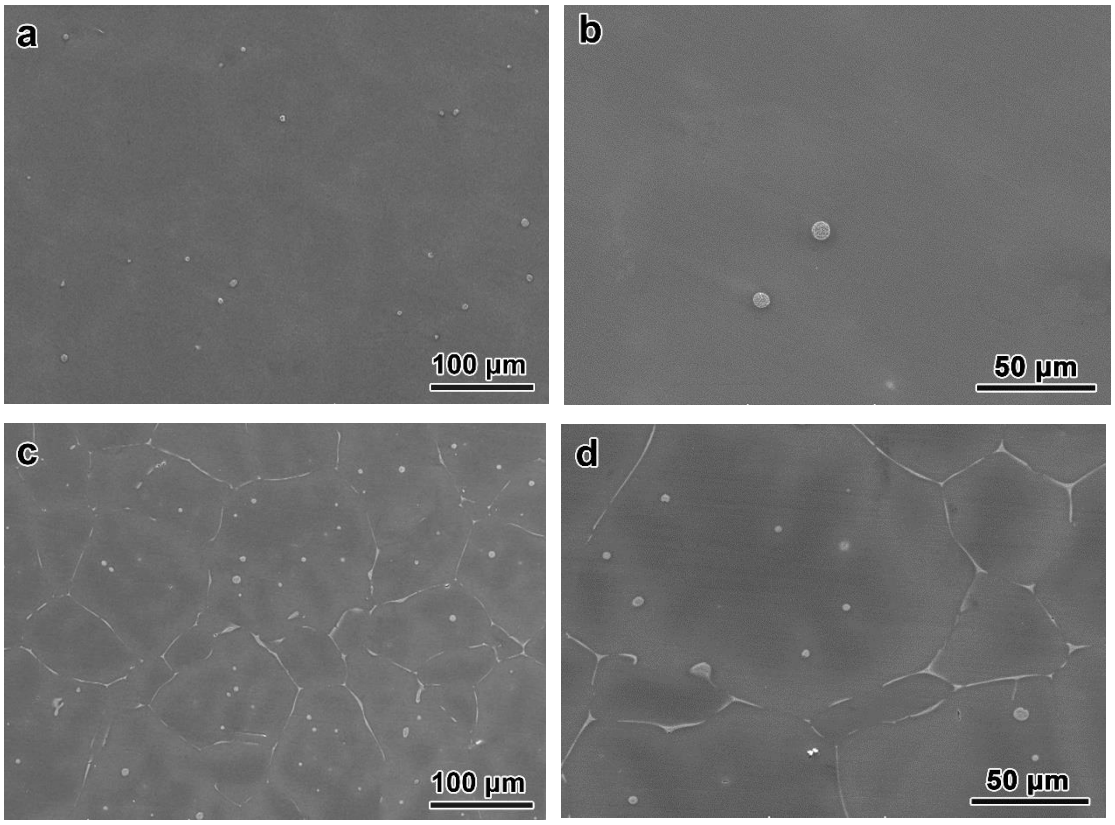


Fig. 4.2 SEM micrographs of the as-cast Mg alloys: (a) and (b) MZ3; (c) and (d) MZX30.

In the as-cast MZ3, the spherical second phases have an average diameter of 5 μm and show an internal lamellar morphology (Fig. 4.3). In the high magnification image (Fig. 4.3 b)), in the net-like phase, the bright and dark areas arranged alternately: the darker area is the α-Mg.

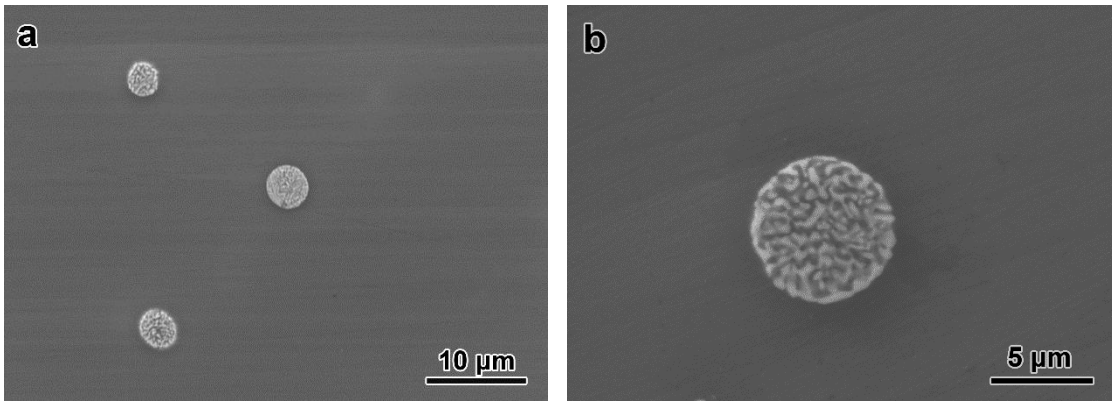


Fig. 4.3 (a) SEM micrograph of as-cast MZ3; (b) high magnification SEM morphology of the spherical product.

According to the Mg-Zn binary phase diagram [203] (see Chapter 2), this spherical product is likely to be a mixture of α-Mg + MgZn. As shown by EDX (Fig. 4.4) of the bright area, it contains 63.9 at% Mg and 36.1 at% Zn. However, the concentration of Mg is higher than that of the expected MgZn phase (50 at% Mg). It is possible that the small amount of magnesium could be due to the poor spatial resolution of EDS measurements in the SEM. The identity of the second phase was confirmed subsequently by TEM (for more details see section 4.3).

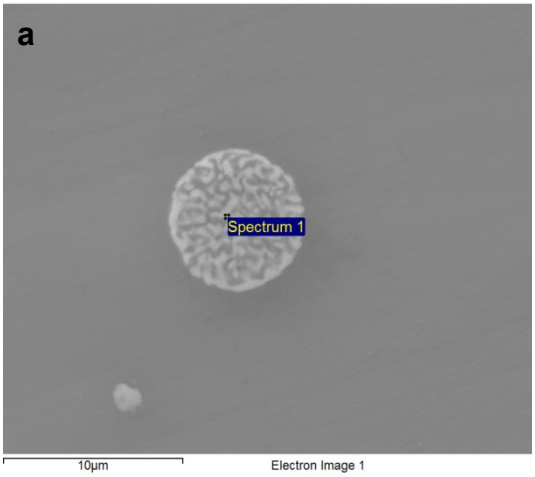


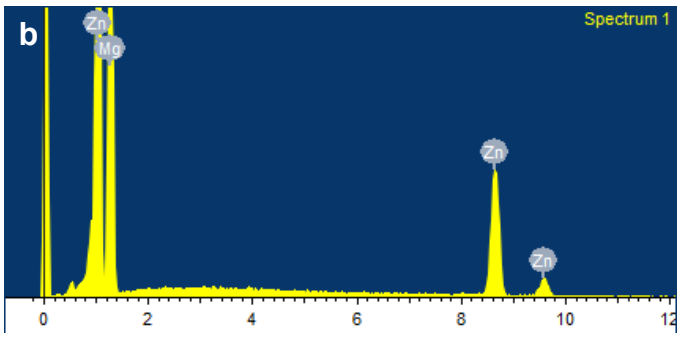


| Element | wt% | | at% | |
|---|---|---|---|---|
| **Mg** | 39.7 | ± 2.3 | 63.9 | ± 2.1 |
| **Zn** | 60.3 | ± 2.3 | 36.1 | ± 2.1 |

Fig. 4.4 EDX of spherical product in as-cast MZ3: (a) image of spherical product; (b) EDX analysis of bright phase in the spherical product.

Fig. 4.5 illustrates the microstructure of the as-cast MZX30. The second phases is mainly formed along the grain boundary. The minority spherically shaped precipitates are distributed mainly inside the grains and have an average size of 5 µm.

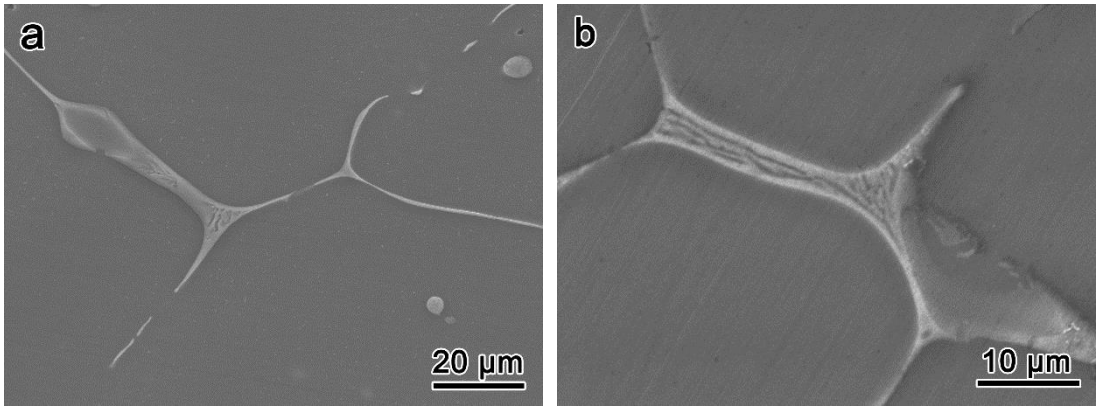


Fig. 4.5 (a) SEM microstructure of as-cast MZX30; (b) eutectic morphology of grain boundary precipitation.

As can be seen from Fig. 4.6, both the spherical and strip shaped second phases contain Mg, Zn and Ca. The chemical compositions of both second phases are shown in Table 4.2, as measured by EDX. This second phase is probably $Ca_2Mg_6Zn_3$ and which locates at the grain boundary and inside the grains. The crystal structure of this phase was further confirmed by TEM (see section 4.3).

Table 4.2 Composition of precipitates in as-cast MZX30 (at%).

| Phase | Mg | Zn | Ca |
|---|---|---|---|
| **Spherical** | 66.5 ± 2.0 | 8.6 ± 0.8 | 24.9 ± 1.4 |
| **Strip-like** | 67.7 ± 1.3 | 8.9 ± 1.0 | 23.4 ± 0.9 |

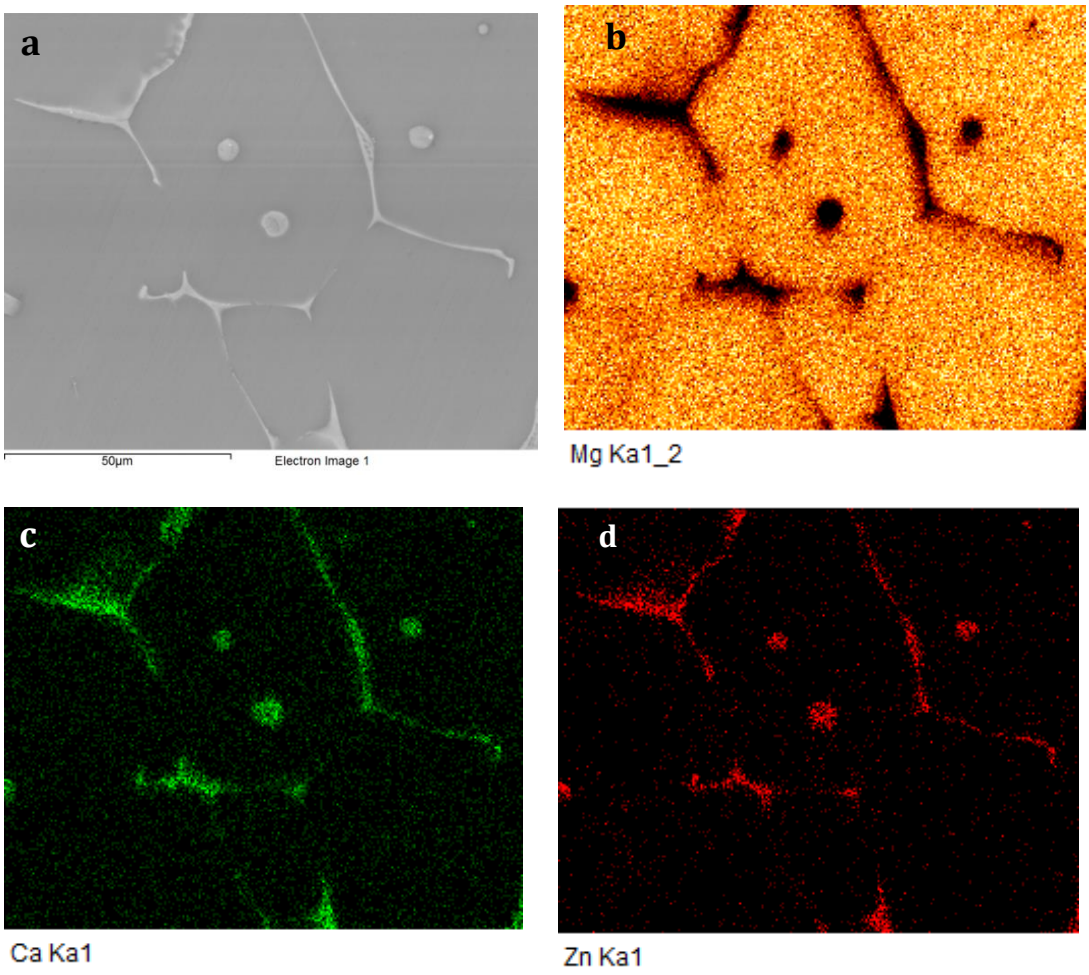


Fig. 4.6 Element distribution maps showing second phases in as-cast MZX30.

## 4.2 Hardness of as-cast Mg alloys

It can clearly be seen that the hardness increases (see Fig. 4.7) from 38.2 ± 1.8 HV for Mg to 48.8 ± 1.8 HV for MZ3 and 55.5 ± 2.9 HV for MZX30.

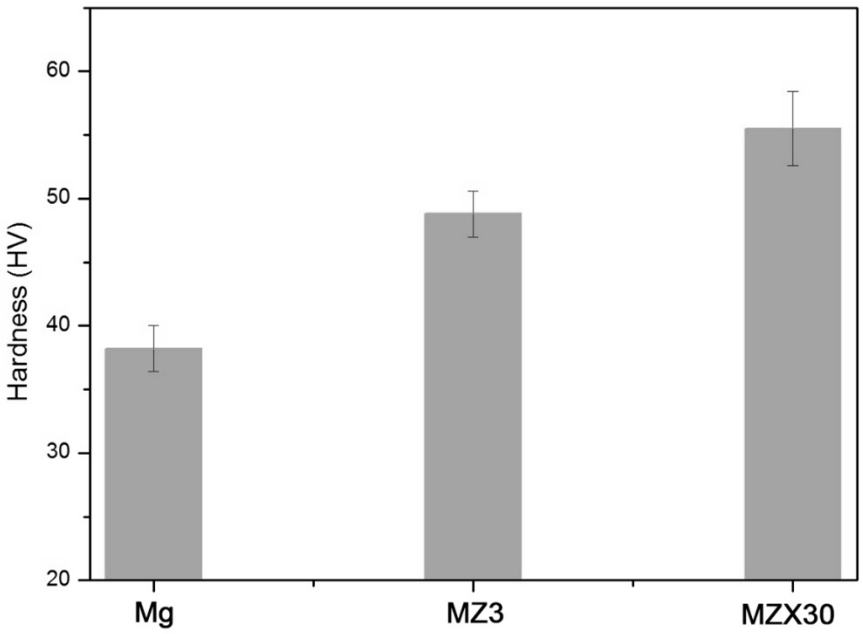


Fig. 4.7 Micro-hardness of Mg and Mg alloys.

## 4.3 Identification of second phase in the as-cast MZ3 and MZX30

### 4.3.1 Second phase in as-cast MZ3

TEM was used to confirm the structure of the second phase in the as-cast MZ3. The morphology and chemical composition of the second phase are identified (Fig. 4.8). As shown in Fig. 4.8 a), the globular particle has alternating bright and dark regions. An EDX spectrum recorded from a dark region (Fig. 4.8 b)) shows a significant Zn $L_\alpha$ and $K_\alpha$ peaks and Mg $K_\alpha$ peak.

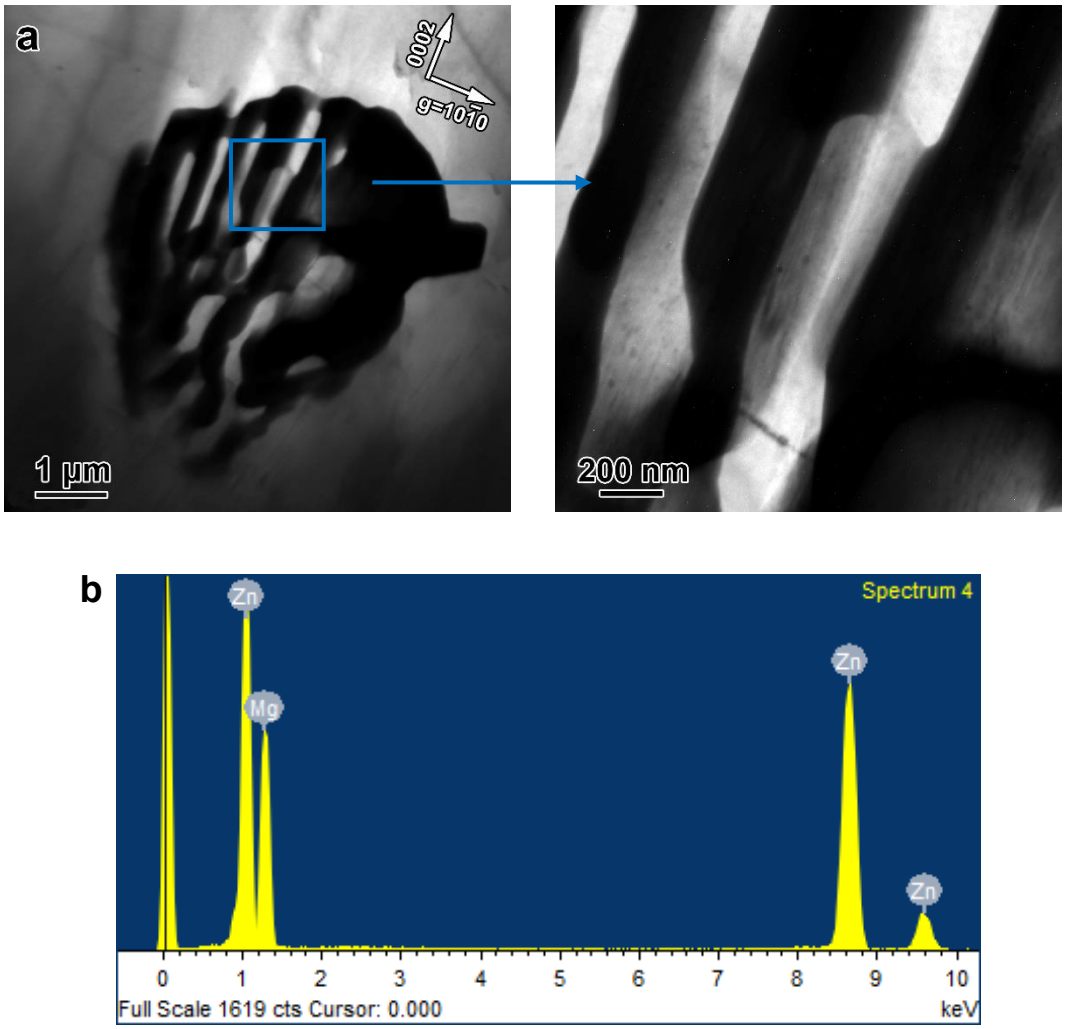


Fig. 4.8 (a) TEM BF images showing a coarse particle in the as-cast MZ3. The electron beam direction is close to [1$\bar{2}$10] of Mg; (b) EDX spectrum obtained from dark region of the particle.

The bright region shows a contrast similar to that of the surrounding α-Mg matrix, and EDX microanalysis reveals that this bright region was indeed α-Mg (Table 4.3). An average of 20 measurements is carried out. The composition of the dark region is 49.0 ± 3.7 at% Mg and 51.0 ± 3.7 at% Zn (Table 4.2). The atomic ratio of Mg to Zn is thus around 1:1.

Table 4.3 Composition of different areas in a coarse particle (at%).

| | Mg | Zn |
|---|---|---|
| **Dark region** | 49.0 ± 3.7 | 51.0 ± 3.7 |
| **Bright region** | 95.1 ± 3.2 | 4.9 ± 3.2 |
| **Matrix** | 97.6 ± 0.7 | 2.4 ± 0.7 |

The crystal structure of the second phase in the as-cast MZ3 is confirmed by systematic tilting experiments (Fig. 4.9). The electron diffraction patterns of the second phase can be identified as MgZn with a rhombohedral structure (a= 2.6 nm and c=1.8 nm). These results are consistent with those reported by Khan [123]. Both chemical composition and diffraction patterns confirm that the second phase in the MZ3 is MgZn.

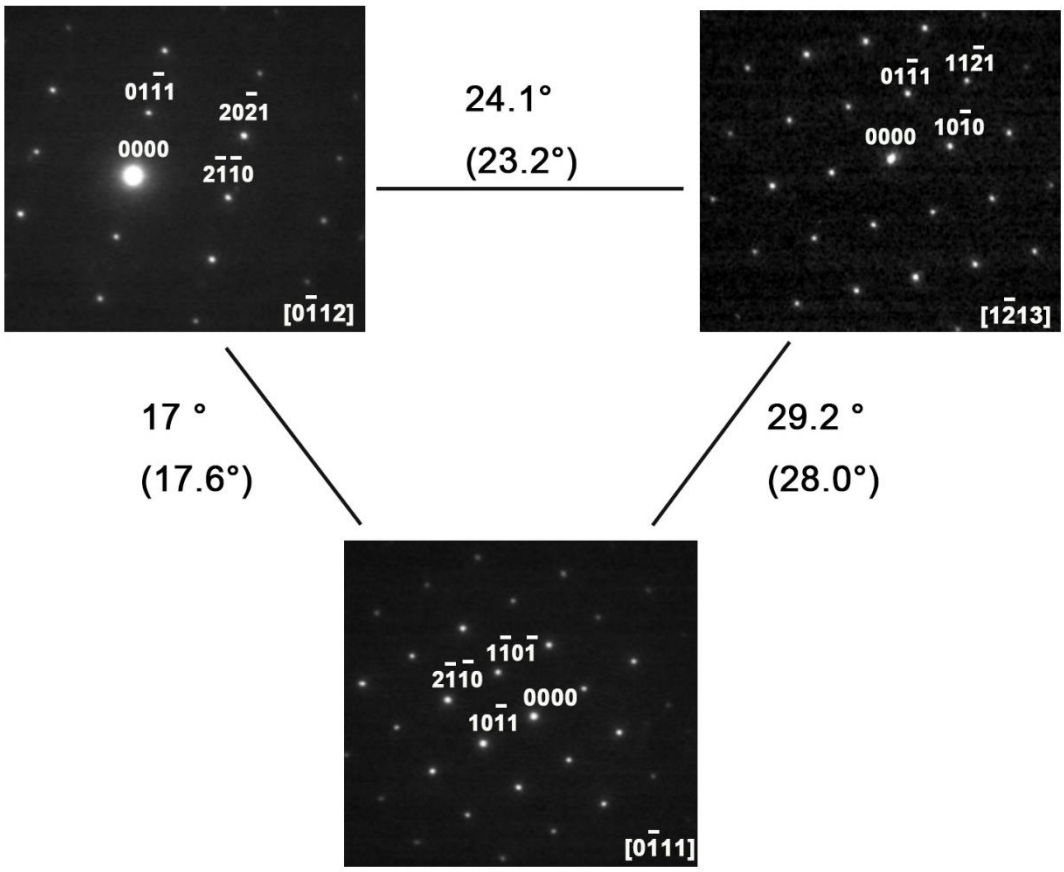


Fig. 4.9 TEM crystallographic analysis showing the MgZn phase to have a rhombohedral structure. The values without brackets are theoretical values and the

actual tilt angles are shown in brackets.

### 4.3.2 Second phases in as-cast MZX30

There are two types of precipitate in the as-cast MZX30: the first is coarse and globular, the second is strip-like (see Figs. 4.10 and 4.12). As shown in Fig. 4.10 a), the globular particles have alternating bright and dark regions. The SADP obtained from the dark region (Fig. 4.10 b)) shows six-fold symmetry. The possible crystal structures with a six- or three-fold symmetry are cubic, hexagonal, or trigonal [204]. The crystal structure of this second phase is thus narrowed down to these three crystal systems. An EDX spectrum recorded from the dark region shows a prominent Mg peak, together with significant Zn and Ca peaks (Fig. 4.10 c)). The concentrations of Mg, Ca and Zn in the dark region are 60.2 $\pm$ 3.7 at%, 15.8 $\pm$ 1.5 at%, 24.0 $\pm$ 2.3 at%, respectively. The atomic ratios of Ca, Mg and Zn are thus about 2:6:3. This composition is very close to $Ca_2Mg_6Zn_3$ [205]. This compound was found in JCPDS as card number 00-012-0266.

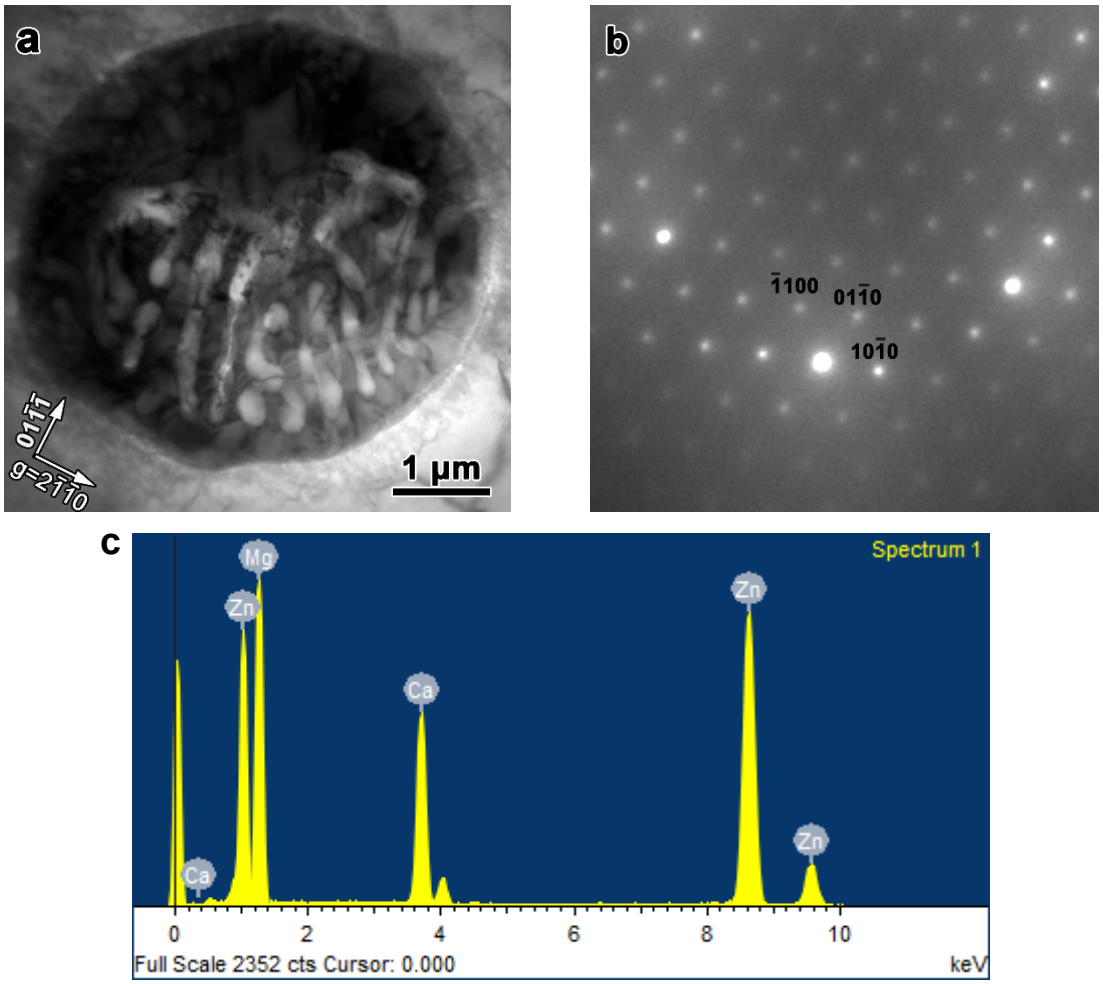


Fig. 4.10 (a) TEM BF image of a coarse globular-shaped precipitate in as-cast MZX30 with beam direction close to $[2\bar{1}\bar{1}0]$ of Mg; (b) SADP recorded from a [0001] zone axis of the dark region in such coarse globular precipitate; (c) EDX spectrum from a dark region of the precipitate in (a).

The crystal structure of $Ca_2Mg_6Zn_3$ is further confirmed by systematic large angle tilting (Fig. 4.11). Electron diffraction patterns recorded from the dark region can be indexed as $Ca_2Mg_6Zn_3$ phase with a trigonal structure (a=0.97 nm, c=1.00 nm), which is consistent with the results given by Jardim [205].

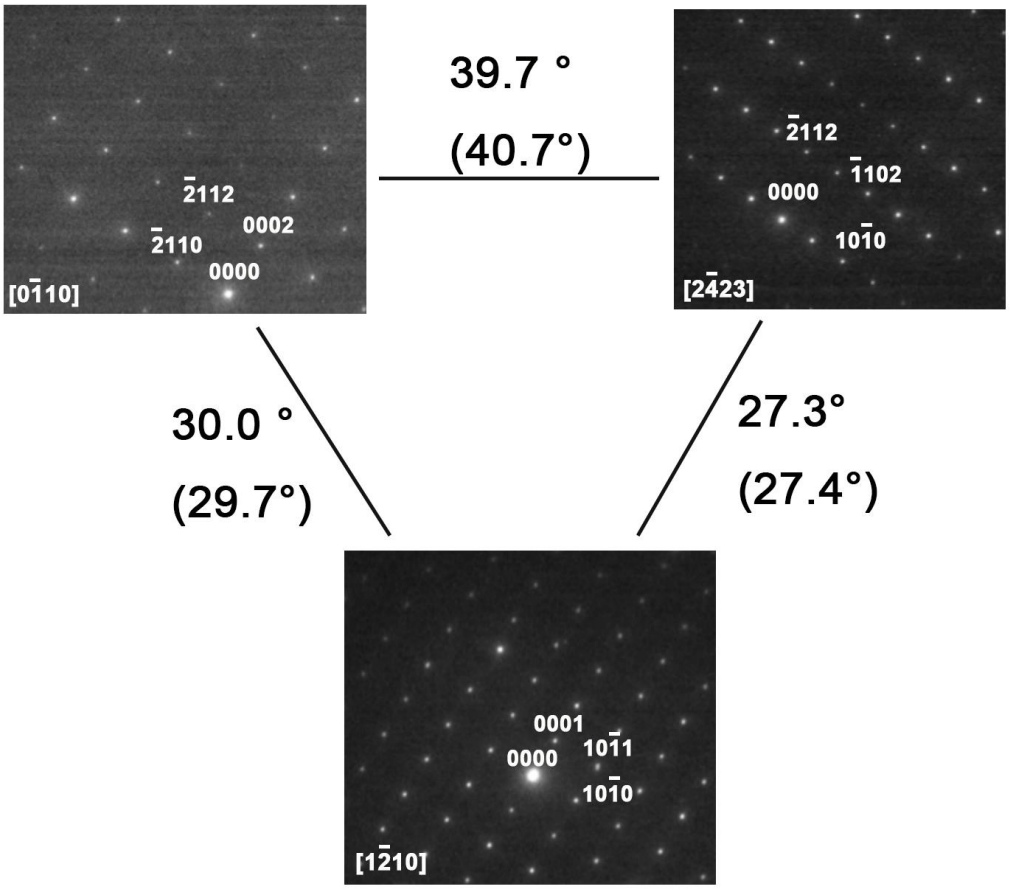


Fig. 4.11 TEM crystallographic analysis of $Ca_2Mg_6Zn_3$ phase (a=0.97 nm, c=1.00 nm). The values without brackets are theoretical tilt angles; the actual tilt angles are shown in brackets.

The other precipitates are in the strips at the grain boundaries (Fig. 4.12 a)). An EDX spectrum recorded from the particles is provided in Fig. 4.12 b), indicating significant Mg, Zn and Ca peaks. The particle contains 58.3 ± 3.0 at% Mg, 16.8 ± 1.2 at% Ca, 24.9 ± 2.4 at% Zn. The crystal structure of the network is confirmed by systematic tilting (Fig. 4.13). This particle also is $Ca_2Mg_6Zn_3$, which has a trigonal structure with space group $P\bar{3}1c$ and lattice parameters a=0.97 nm and c=1.00 nm, i.e. identical to that in the globular precipitate.

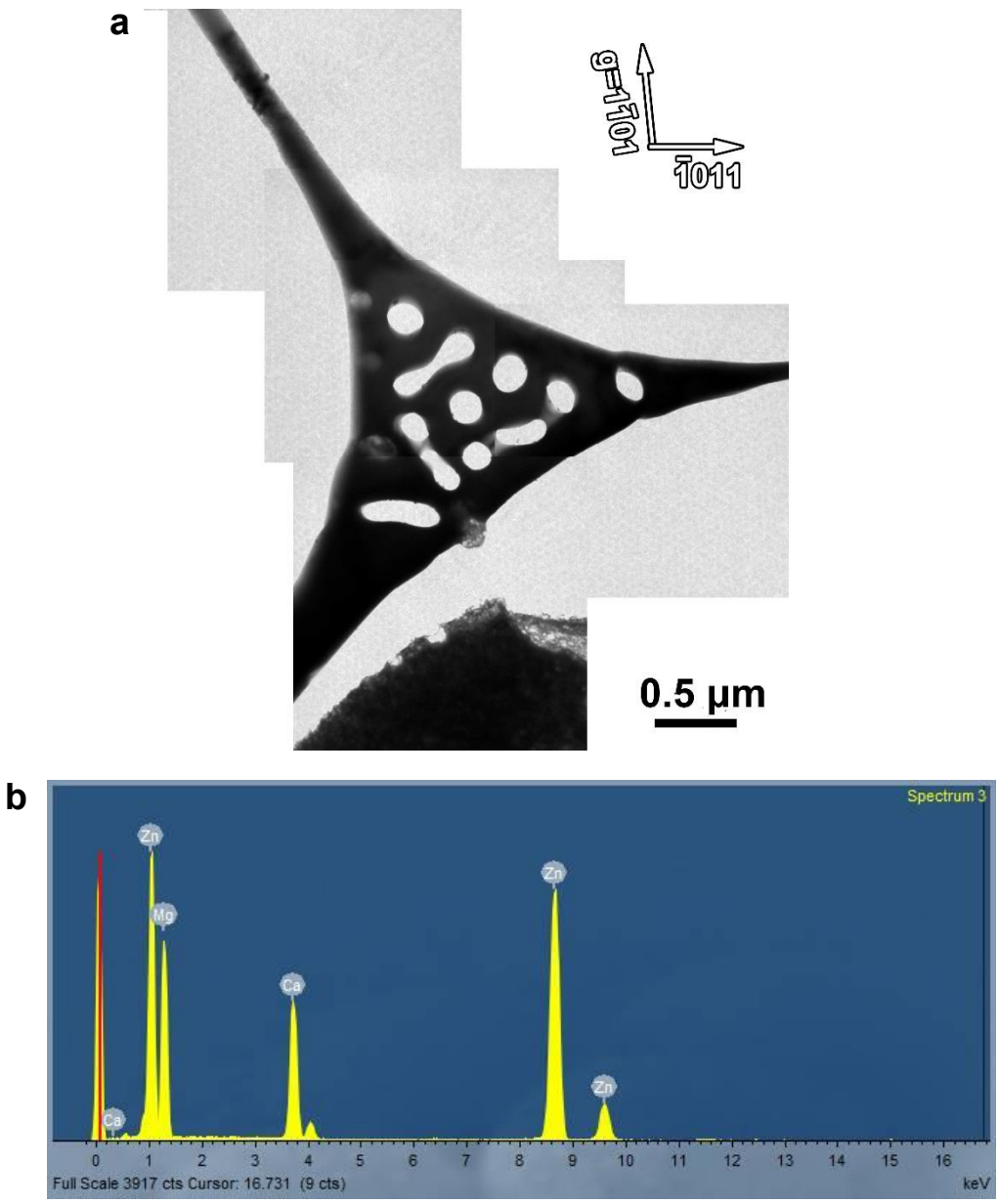


Fig. 4.12 (a) TEM BF image showing a coarse particle located at a grain boundary in MZX30. The beam direction is close to $[01\bar{1}1]$ of Mg; (b) EDX spectrum obtained from the particle (dark region).

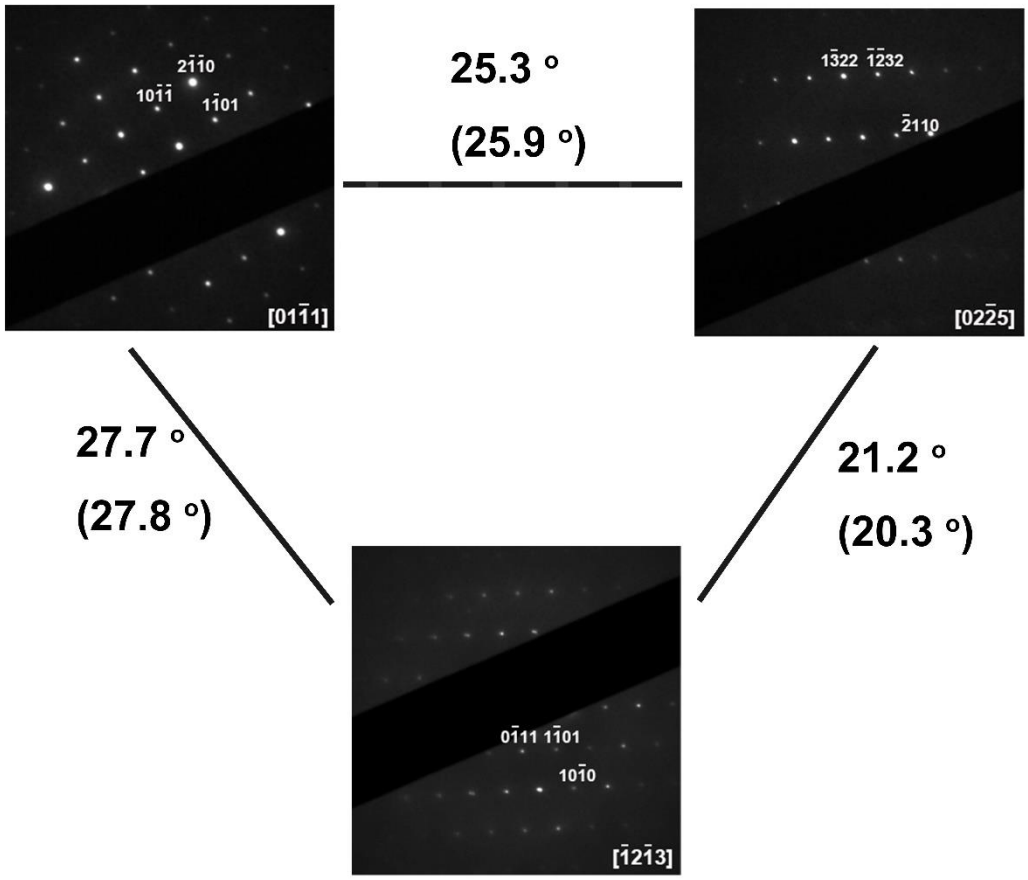


Fig. 4.13 TEM crystallographic analysis confirming trigonal $Ca_2Mg_6Zn_3$ phase. The values without brackets are theoretical values and the actual tilt angles are shown in brackets.

## 4.4 3D microstructure analysis

### 4.4.1 Eutectic product in as-cast MZ3

A more complete understanding of the morphology of the second phases is achieved using FIB tomography. Fig. 4.14 shows some of the images during slicing of the as-cast MZ3. A side view of the milled site is shown: the sample has been tilted by 52° with regard to the incident beam where the ion beam was normal to the specimen surface. Prior to the 3D reconstruction, the 2D images are segmented and then aligned. Segmentation is the process of dividing an image into different subregions (also called segments). In this study, the segments are the different phases. A

segmentation assigns to each pixel of the image a label describing to which phase the pixel belong, i.e. MgZn or α-Mg. The 'Multi-Thresholding' module in the Avizo software was used to separate the different segments. The 'Align slices' module is used for aligning 2D slices of a 3D image stack. As shown in Fig. 4.14, it is clear that one phase (MgZn) has lighter contrast with a surrounding darker contrast (Mg matrix).

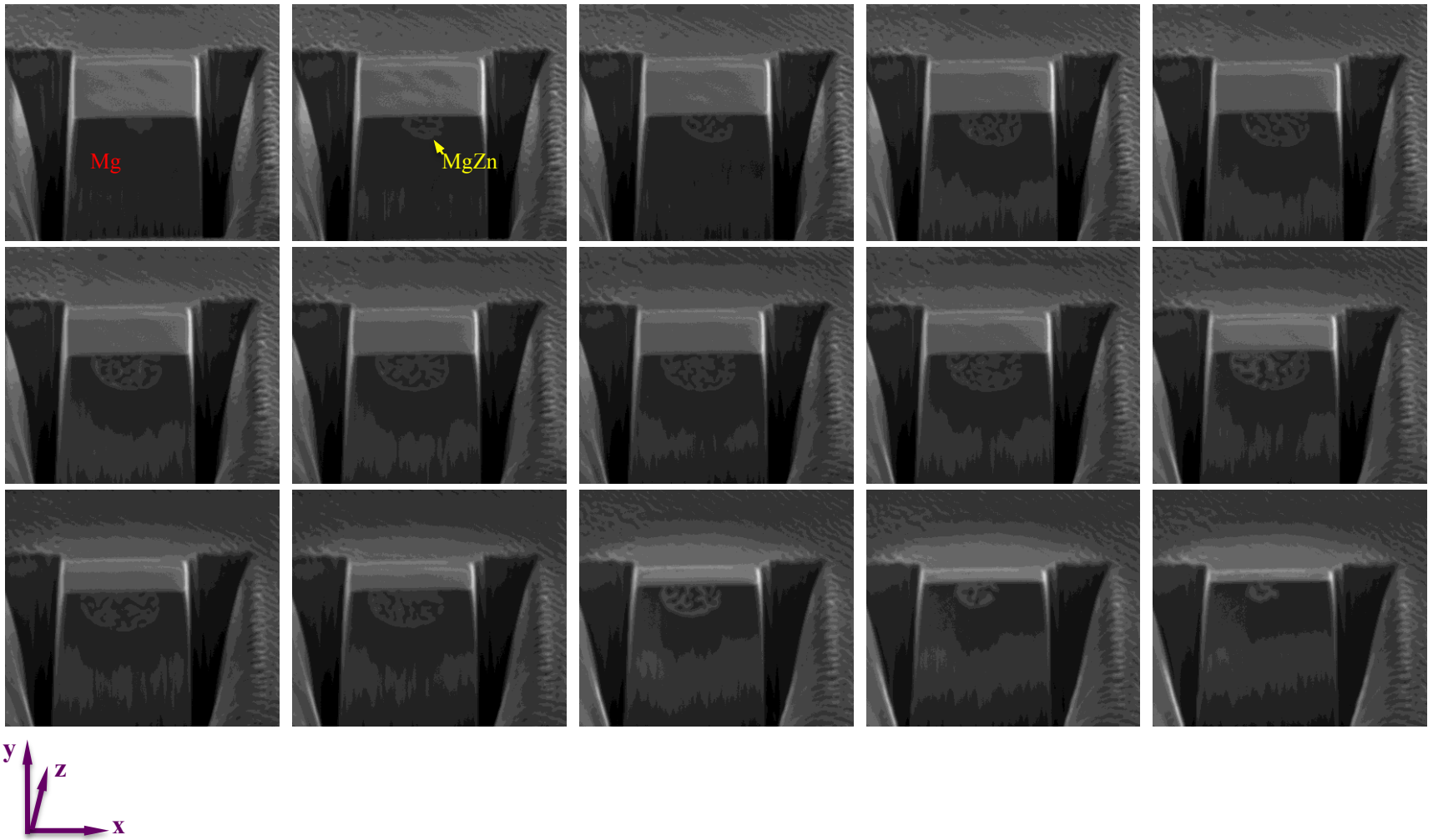


Fig. 4.14 Series of FIB images (a part) obtained sequentially. The slicing/view function on FIB/SEM allows the visualization of the second phases in three dimensions.

3D microstructures are computationally reconstructed from a set of sections which are digitized from the 2D SE images, as shown in Fig. 4.15. 3D FIB tomography reveals the inner microstructure of the eutectic products. The spherical product consists of lamellar MgZn and α-Mg. The size of the products is nearly 5 μm. The α-Mg phase (indicated by the green colour) encloses the MgZn phase (indicated by the red colour).

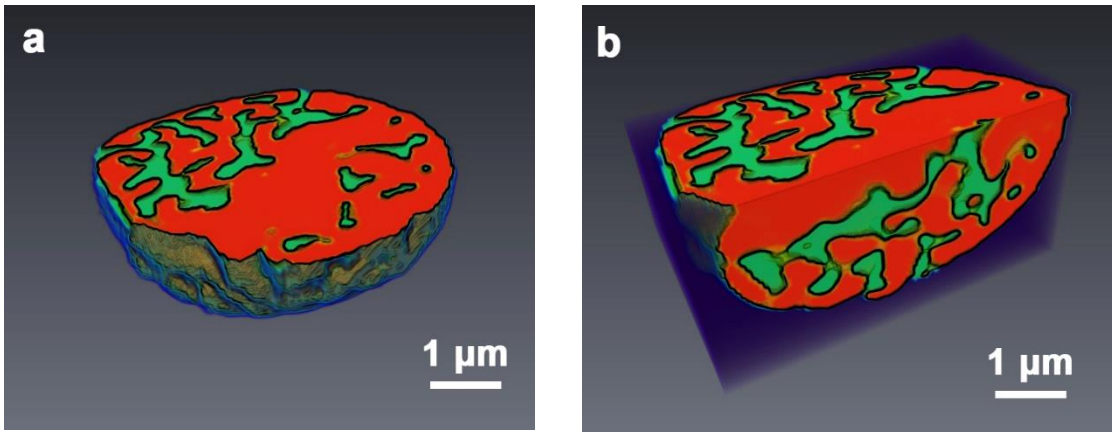


Fig. 4.15 3D reconstruction of the globular-shaped particle in as-cast MZ3: MgZn phase (red region), α-Mg (green region) and Mg matrix surrounding the particle (blue region).

### 4.4.2 3D characterisation of second phases in as-cast MZX30

Fig. 4.16 shows 2D horizontal and vertical slices of as-cast MZX30 obtained by X-Ray MicroCT. Fig. 4.16 shows that the different phases present different contrast: $(\alpha\text{-Mg} + Ca_2Mg_6Zn_3)_{eutectic}$ (white) and the Mg matrix (dark). The net-like structure of the $(\alpha\text{-Mg} + Ca_2Mg_6Zn_3)_{eutectic}$ phases is clearly observed. Before the 3D reconstruction, segmentation is applied to every 2D image to clearly identify different phases. Good segmentation is a prerequisite of a good reconstruction. A 'Threshold Tool' in Avizo was used to vary the threshold to select the region of the second phases. The segmentation process is achieved by both threshold and personal judgment.

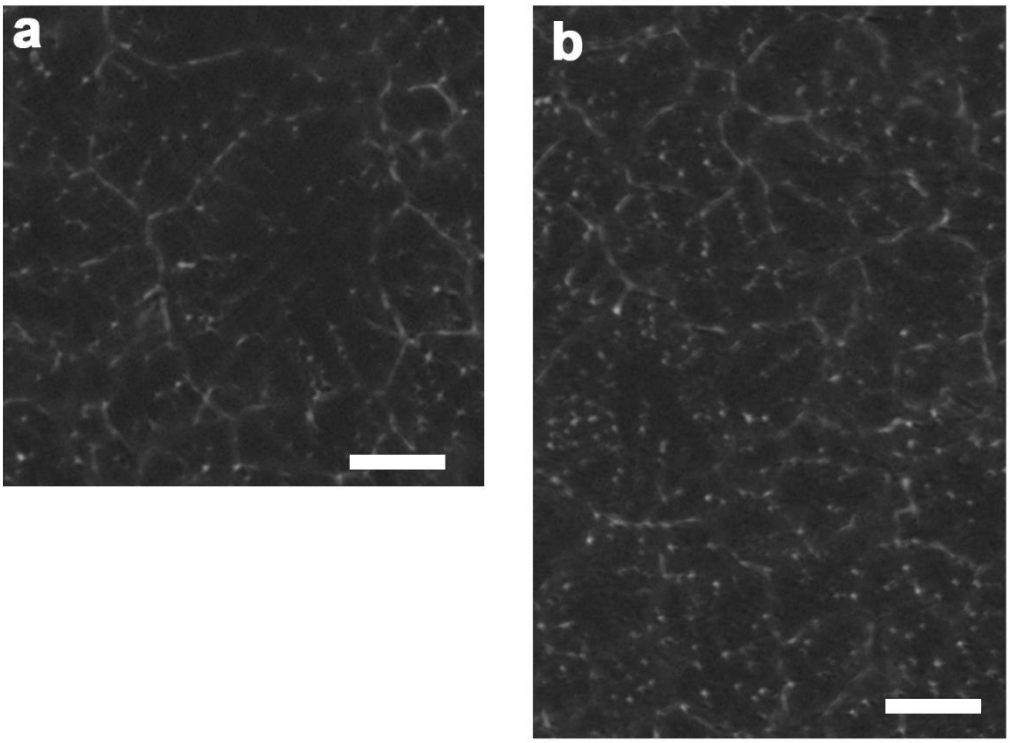


Fig. 4.16 2D reconstructed cross sections of as-cast MZX30: (a) horizontal view; (b) vertical view (second phases: bright; Mg matrix: dark). Scale bar = 150 μm.

MicroCT allows the 3D reconstruction of a sample from a sequential assembly of 2D projections. Fig. 4.17 is the 3D reconstructed microstructure of as-cast MZX30. The dendritic α-Mg phase surrounds the eutectic phases (blue).

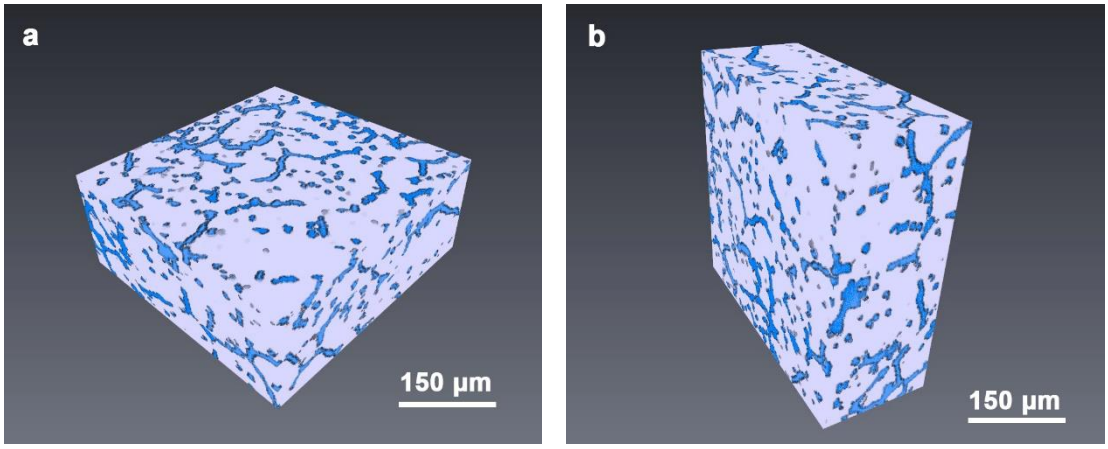


Fig. 4.17 3D reconstruction of ($\alpha$-Mg + $Ca_2Mg_6Zn_3$)$_{eutectic}$ (blue) + Mg (white) in as-

cast MZX30.

Fig. 4.18 reveals the 3D distribution of the second phases in the as-cast MZX30. A transparency and blue is assigned to the Mg matrix and second phases, respectively. Fig. 4.18 a) and b) demonstrate that the eutectic product encloses the Mg matrix in a type of network. The inner connectivity of $(\alpha\text{-Mg} + Ca_2Mg_6Zn_3)_{eutectic}$ phases is evident (Fig. 4.18 c)). The disconnected spherical precipitates are distributed within the net-like structure, as shown in Fig. 4.18 d).

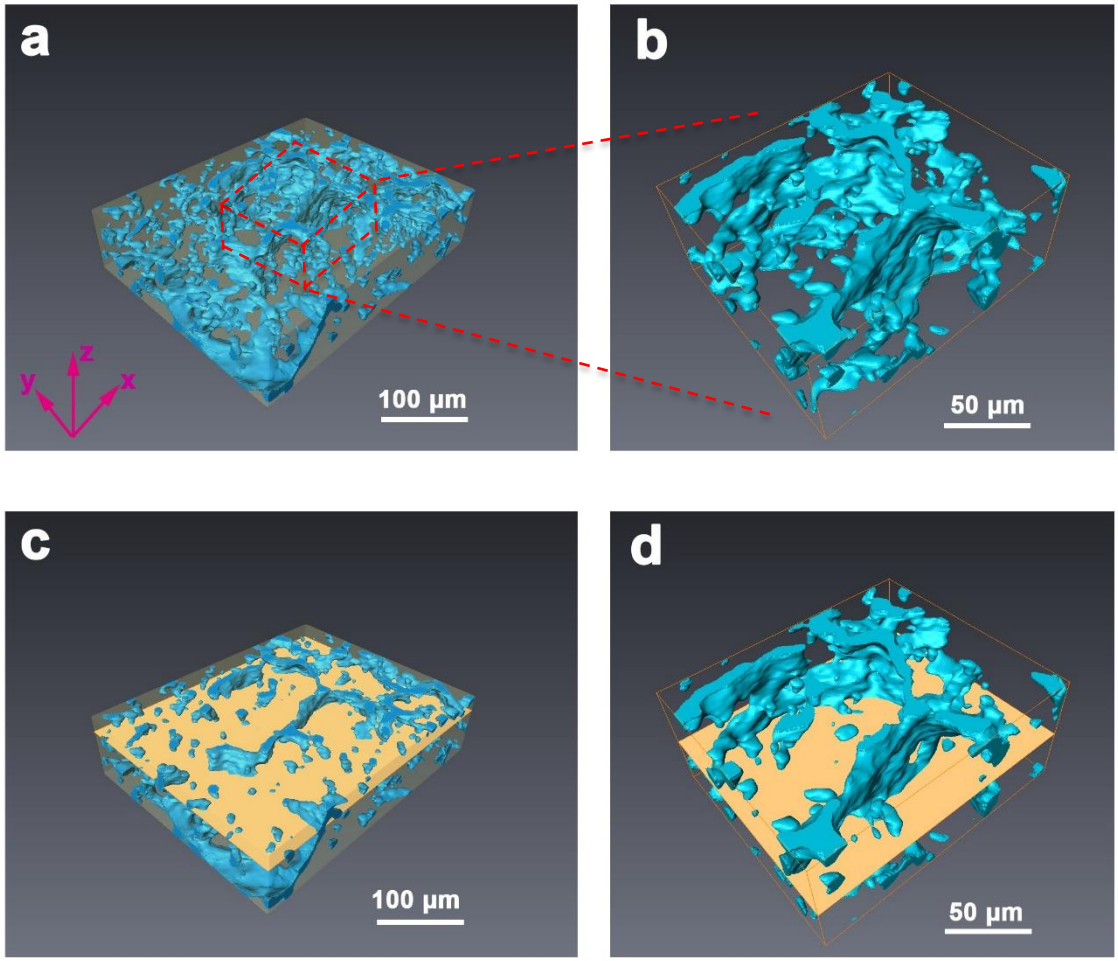


Fig. 4.18 (a) Surface rendered 3D reconstruction of the $(\alpha\text{-Mg} + Ca_2Mg_6Zn_3)_{eutectic}$ phases (blue) in as-cast MZX30; (b) is a high magnifications of (a); (c) 3D reconstruction of (a) with a cutting plane (yellow); (d) 3D reconstruction of (b) with a cutting plane (yellow).

## 4.5 Microstructural characterisation and hardness of heat-treated MZ3

### 4.5.1 Solution treated MZ3

The solution treatment temperature was chosen to be 310 ℃ based on the Mg-Zn binary phase diagram and other literature [104, 129, 203]. At this temperature, the MgZn second phase can be dissolved into the Mg matrix, but no grain boundary melting takes place. Optical images of MZ3 after solution treatment are shown in Fig. 4.19. After exposure at 310 ℃ for 24 h, the grains of MZ3 grow to 232 ± 12 μm and the dendrite structure disappeared (Fig.4.19 b)).

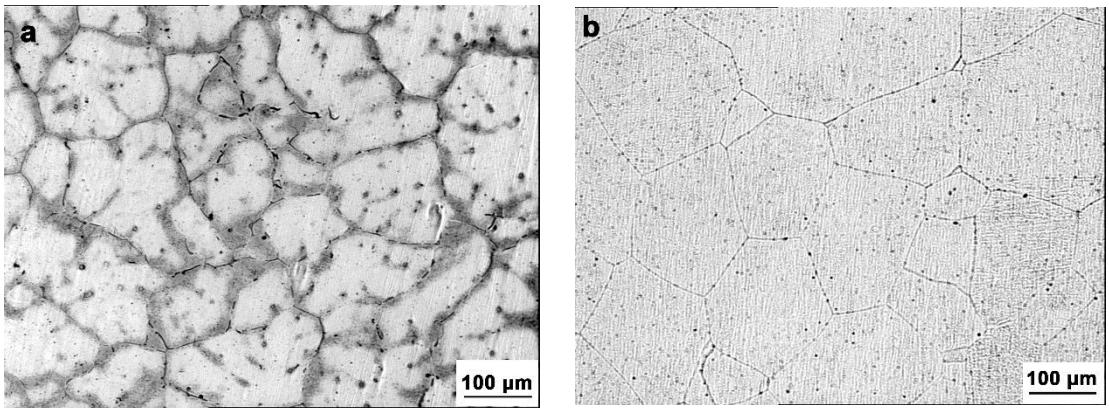


Fig. 4.19 Optical microstructures: (a) as-cast MZ3; (b) after 310 ℃/24 h.

As can be seen from Fig. 4.20, the spherical second phase (MgZn) has largely dissolved into the Mg matrix upon the solution treatment (310 ℃/ 24 h).

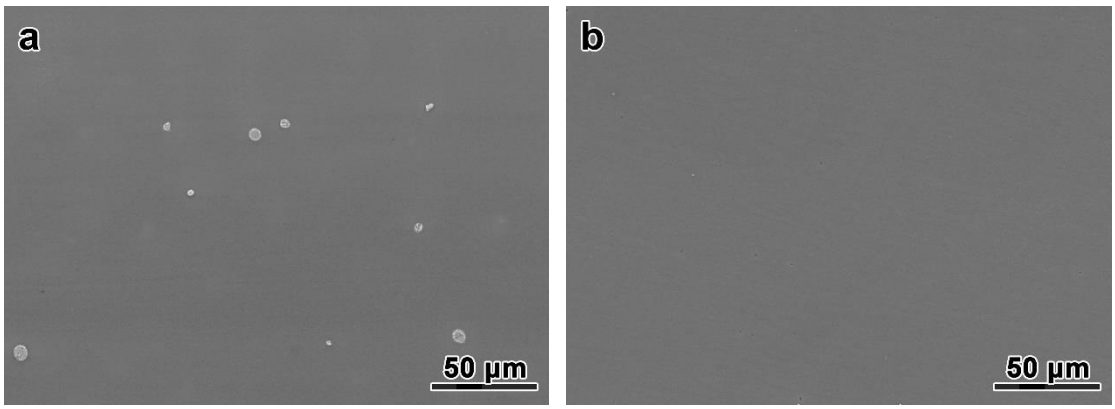


Fig. 4.20 SEM micrographs of MZ3: (a) as-cast; (b) after 310 ℃/ 24 h.

### 4.5.2 Aged MZ3

#### 4.5.2.1 Hardness

After ageing, the hardness increases as compared with the as-cast sample (48.8 ± 1.8 HV) and solution-treated sample (52.9 ± 2.3 HV). The MZ3 thus age-hardens, as shown in Fig. 4.21. An age-hardening behaviour can be seen. The peak hardness is achieved at 160 ℃ and 96 h (66.5 ± 3.2 HV) and then the hardness decreases. Ageing increases the peak hardness by 28 %. The maximum increment in hardness is similar with the value reported in the literature [132, 206, 207]: 23 % in Mg-9 wt% Zn, 25 % in Mg-2.8 at% Zn and 31 % in Mg-2.4 at% Zn, respectively.

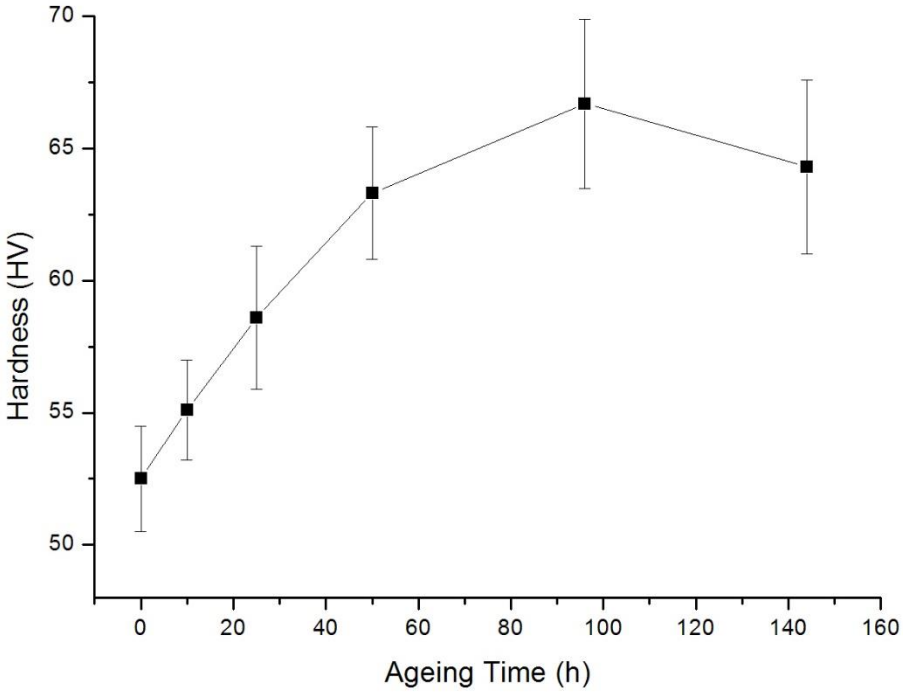


Fig. 4.21 Hardness of aged MZ3 as a function of ageing time at 160 ℃.

#### 4.5.2.2 Precipitates in aged MZ3

As shown in Fig. 4.22, only a small number of precipitates have formed after aging at 160 ℃ for 10 h. The precipitate presents a near circular cross section when viewing

along [0001] (Fig. 4.22 a)). In the $[2\bar{1}\bar{1}0]$ micrograph, Fig. 4.22 b), the precipitates (indicated by the arrow) have long axes parallel to [0001] and a small size. This rod-shaped precipitate is reported to be $\beta_1'$ in the literature (base-centred monoclinic structure, a=2.596 nm, b=1.428 nm, c=0.524 nm, γ=102.5°) [134, 207, 208].

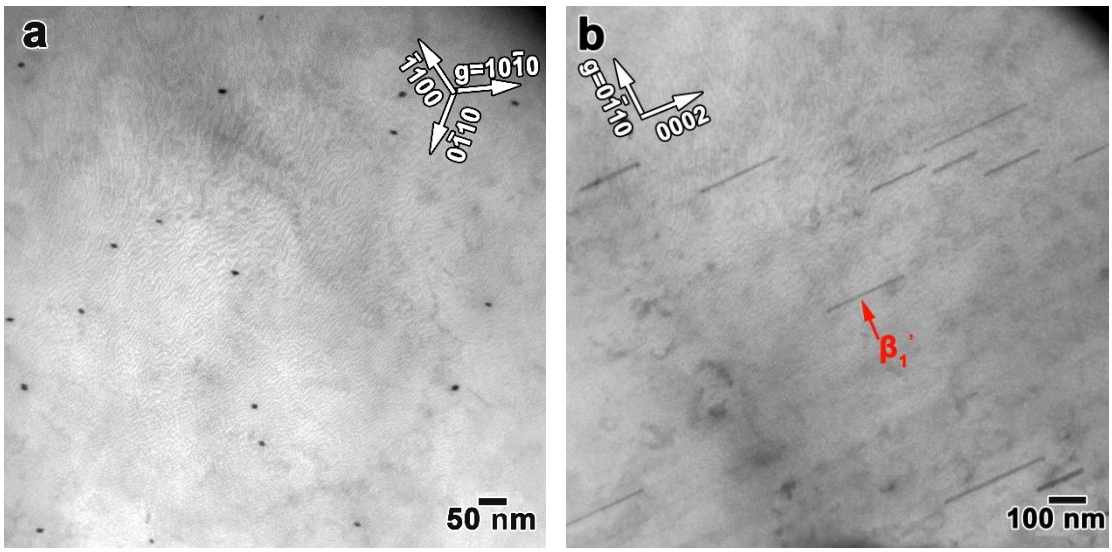


Fig. 4.22 TEM micrographs of MZ3 after ageing at 160 ℃ for 10 h: (a) BD~[0001]; (b) BD~$[2\bar{1}\bar{1}0]$.

After ageing at 160 ℃ for 25 h, more rod-shaped precipitates formed, as shown in Fig. 4.23 a) and b). The average length of the precipitates is now around 170 nm.

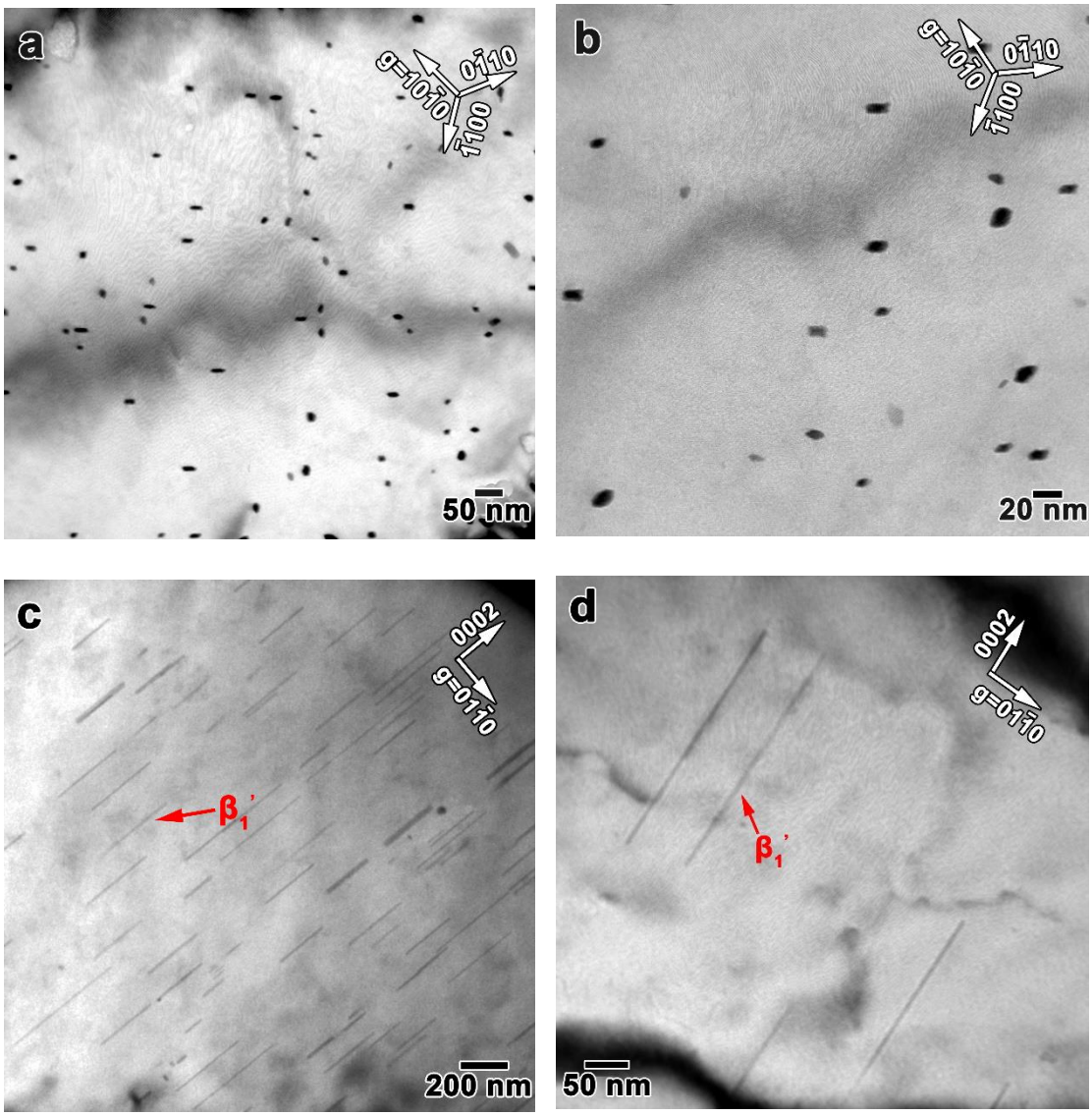


Fig. 4.23 TEM micrographs showing precipitates in samples aged at 160 ℃ for 25 h: (a) and (b) rod-shaped precipitates with nearly round cross section, BD~[0001]; (c) and (d) rod-shaped precipitates, BD~[$2\bar{1}\bar{1}0$].

Prolonging the aging time, $\beta_2'$ also precipitates. The [0001] $\beta_1'$ rod precipitates and the coarse (0001) $\beta_2'$ plates after 160 ℃/ 50 h are shown in Fig. 4.24 a) and b). In previous studies [134, 209], $\beta_2'$ has been reported to have a hexagonal structure with lattice parameters a=0.523 nm, c=0.858 nm, which is similar to $MgZn_2$. It is evident

that the number density of the precipitates is higher than for 160 °C/ 10 h and 160 °C/ 25 h (Figs. 4.24 a) and c)). Fig. 4.24 b) exhibits some [0001] $\beta_1'$ rods. An example is indicated by the red arrow. There is a very small number of (0001) $\beta_2'$ plates such as the one indicated by the blue arrow. The face of the $\beta_2'$ plate is parallel to (0001). In the $[2\bar{1}\bar{1}0]$ images (Figs. 4.24 c) and d)), the $\beta_1'$ rods lie along [0001] and the $\beta_2'$ plates are edge-on.

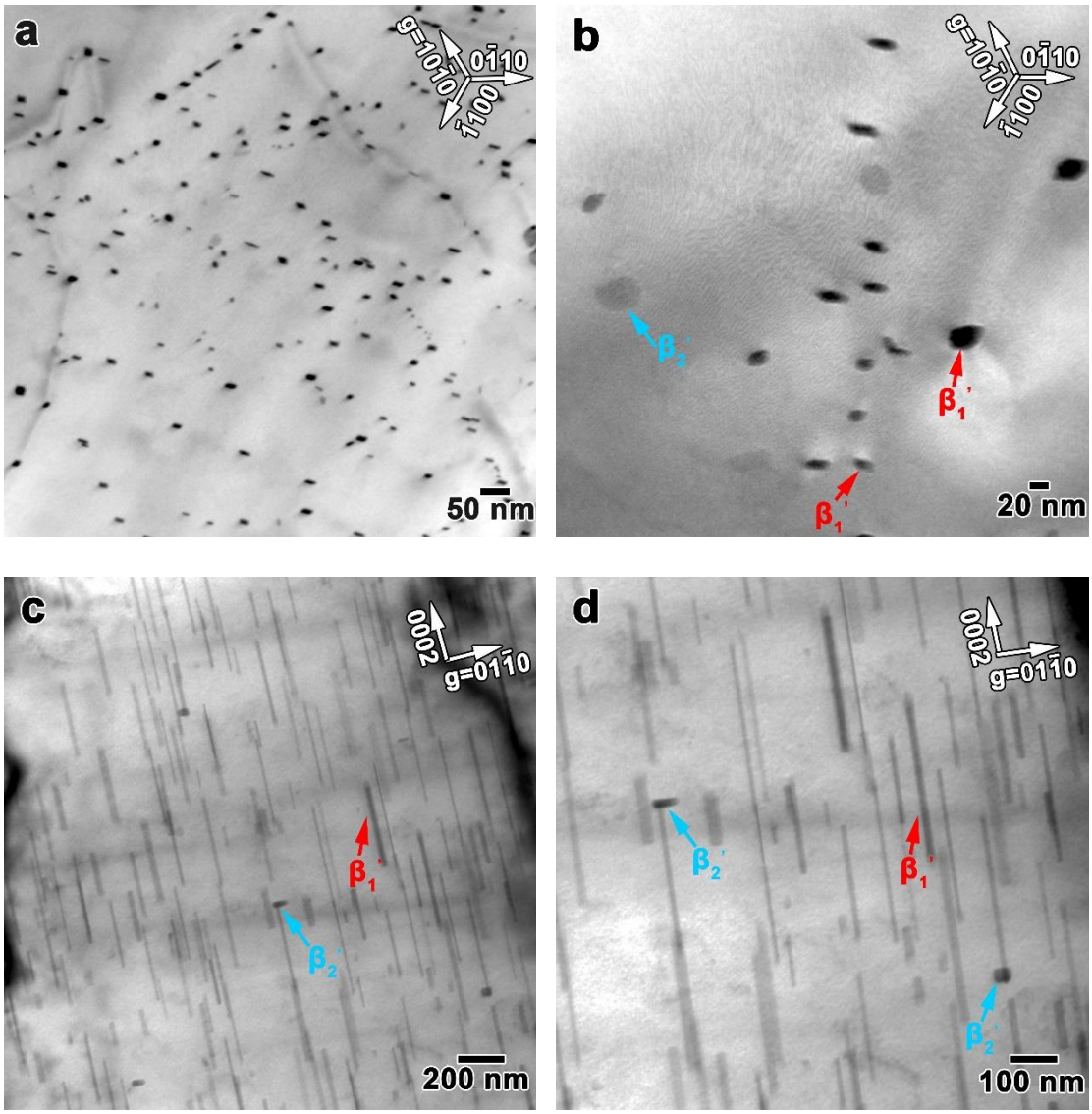


Fig. 4.24 TEM BF images of precipitates produced during aging at 160 °C for 50 h: (a) and (b) rods ($\beta_1'$) and coarse plates ($\beta_2'$), BD~[0001]; (c) and (d) BD~$[2\bar{1}\bar{1}0]$.

Fig. 4.25 shows the TEM microstructure of the sample aged at 160 ℃ for 96 h which is close to the peak age. It is the rod-like $\beta_1'$ precipitates which confer the optimal strengthening [132]. After ageing for 96 h, the microstructure still consists mainly of $\beta_1'$ rods with a small fraction of $\beta_2'$ discs lying on the basal plane. The number density of precipitates increases with ageing time, as shown in Fig. 4.25 a) and c). The $\beta_1'$ precipitates lay on $(2\bar{1}\bar{1}0)$ of the Mg matrix, with a growth direction of [0001] (Fig. 4.25 d)).

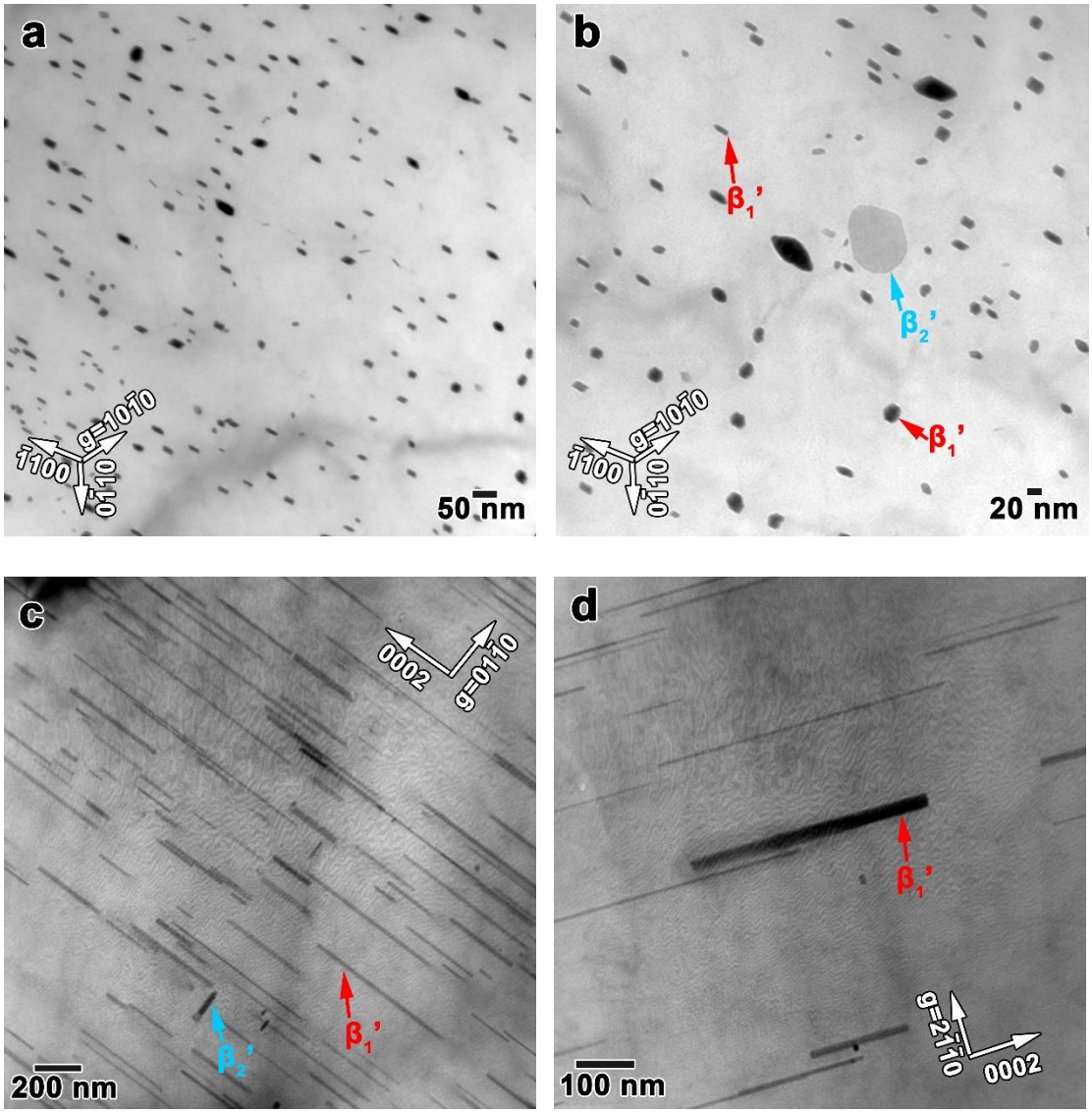


Fig. 4.25 TEM BF images of MZ3 after 160 ℃/96 h: (a) and (b) BD~[0001]; (c) BD~$[2\bar{1}\bar{1}0]$; (d) BD~$[01\bar{1}0]$.

As shown in Fig. 4.26, both the size and density of the precipitates are greatly increased by 160 ℃/ 144 h. The coarsening of the $\beta_2'$ is obvious, as shown in Fig. 4.26 b). The largest volume fraction of precipitates is achieved in the 144 h aged sample.

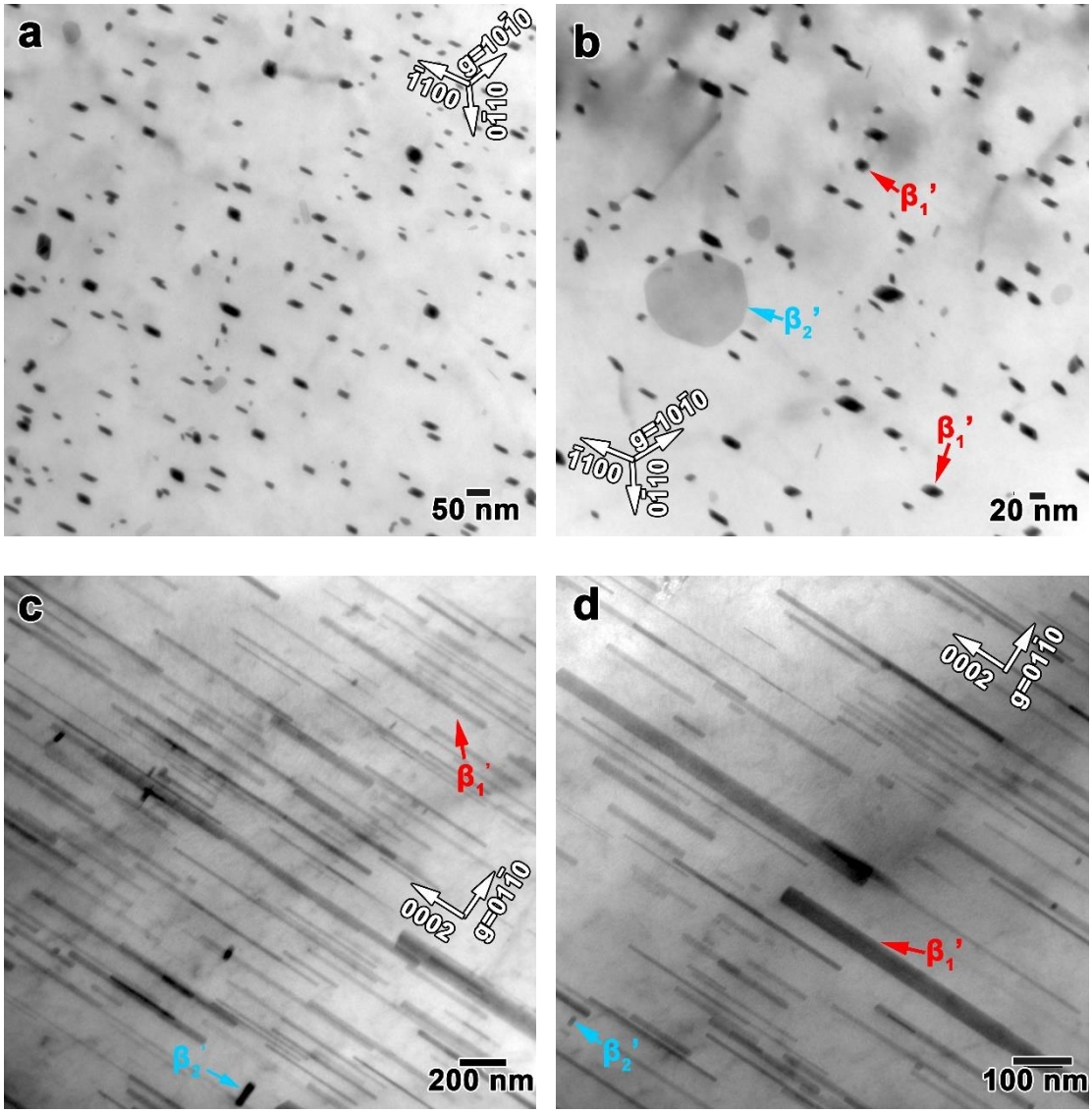


Fig. 4.26 TEM BF images recorded in 160 ℃/144 h MZ3: (a) and (b) BD~[0001]; (c) and (d) BD~[$2\bar{1}\bar{1}0$].

### 4.5.2.3 Volume fraction of fine precipitates

A quantitative estimate of the $\beta_1'$ precipitate volume is required. Quantitative

stereology was used to quantify the volume fraction of precipitates in the thin metal foil. After truncation and overlap corrections, the volume fraction of fine precipitates ($f_v$) was determined by the equation below (for more details, see Chapter 2 Section 2.6).

$$f_v = -\ln(1-A_A)\left(\frac{DL}{DL+(\frac{D}{2}+L)t}\right) \qquad \text{(Equation 4.1)}$$

(D: diameter of rod-shaped precipitates; L: length of precipitates; t: specimen thickness; $A_A$: projected area fraction of precipitates)

In order to measure the dimensions of the rod-like precipitates, they were observed along <0001> and $< 2\bar{1}\bar{1}0 >$ matrix zone axes, as shown in Fig. 4.27. In the [0001] TEM micrograph (Fig. 4.27 a)), it is assumed that precipitate has an approximately circular section. In the $< 2\bar{1}\bar{1}0 >$ images (Fig. 4.27 b)), the average rod length is measured. The projected area fraction of precipitates is obtained using Image J. The reported data represent an average of at least 300 measurements for each condition.

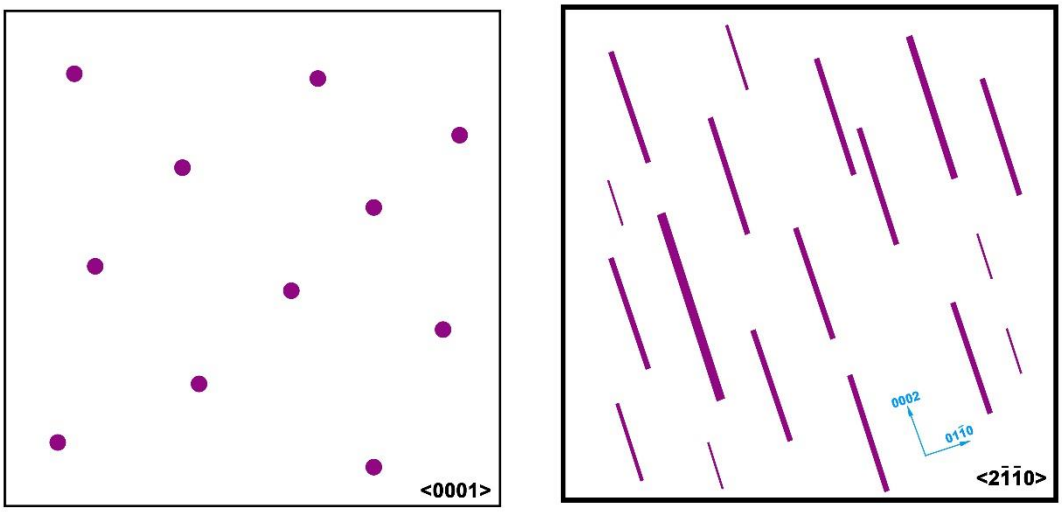


Fig. 4.27 Schematic illustration of the dimension measurements of fine precipitates: (a) average diameter calculated from [0001] matrix zone axis; (b) average rod length calculated from $< 2\bar{1}\bar{1}0 >$ matrix zone axis.

The measurement of the foil thickness is required for the quantification of volume fraction. Moreover, the average foil thickness determined for each ageing condition is used to correct the average precipitate dimensions for truncation effects caused by the limited foil thickness. An example of a thickness measurement using CBED is illustrated in Tables 4.4, 4.5 and Fig. 4.28. Fig. 4.28 a) is a CBED pattern taken close to $[1\bar{2}10]$ using $g = \bar{2}0\bar{2}1$ in a 160℃/ 10 h aged MZ3. The inter-planar spacing of $d_{\bar{2}0\bar{2}1}$ is 0.134 nm. $s_1$, $s_2$ and $s_3$ are calculated from Equation 3.3 (Chapter 3) and given in Table 4.4. Generally, the integer 1 is assigned to the first fringe. For $n_i = 1, 2, 3$, the corresponding values of $s_i^2/n_i^2$ are calculated and given in Table 4.4. But these data do not plot as a straight line against $1/n_i^2$. Then, the integer 2 is assigned to the first fringe. For $n_i = 2, 3, 4$, the values of $s_i^2/n_i^2$ are obtained and shown in Table 4.5. It can be seen that these data are monotonously decreasing and a straight line for $s_i^2/n_i^2$ against $1/n_i^2$ is obtained (Fig. 4.28 b)). The intercept of the straight line with the ordinate is $1/t^2$ ($3.31 \times 10^{-5}$), and thus the foil thickness (t) is 173.8 nm. In the current study, the thickness of the measured area was generally between 130 nm and 200 nm.

Table 4.4 CBED data for thickness determination.

| $s_i$ ($nm^{-1}$) | $n_i$ | $s_i^2/n_i^2$ ($nm^{-2}$) |
|---|---|---|
| 0.0068 | 1 | $4.64 \times 10^{-5}$ |
| 0.0144 | 2 | $5.17 \times 10^{-5}$ |
| 0.0211 | 3 | $4.99 \times 10^{-5}$ |

Table 4.5 Alternative CBED data for thickness determination.

| $s_i$ ($nm^{-1}$) | $n_i$ | $s_i^2/n_i^2$ ($nm^{-2}$) |
|---|---|---|
| 0.0068 | 2 | $1.16 \times 10^{-5}$ |
| 0.0144 | 3 | $2.30 \times 10^{-5}$ |
| 0.0211 | 4 | $2.81 \times 10^{-5}$ |

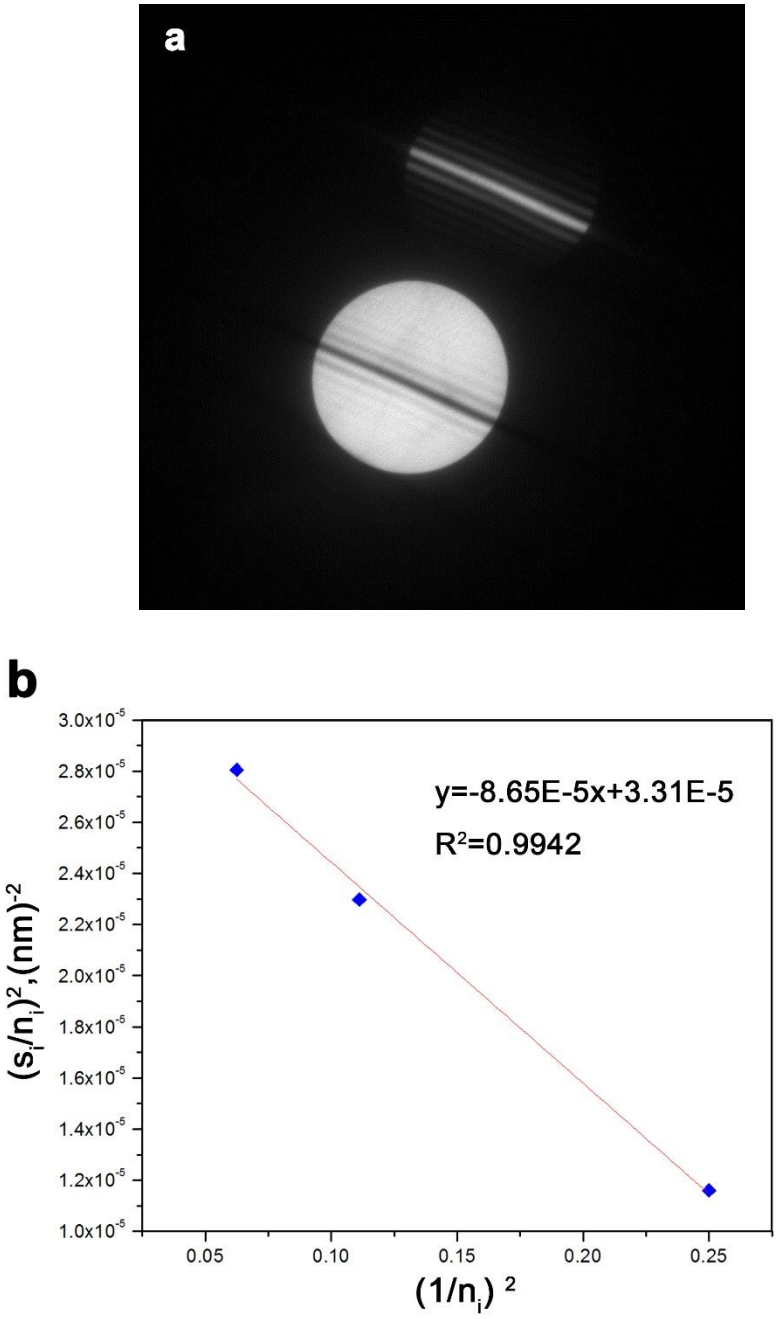


Fig. 4.28 (a) CBED pattern taken close to $[1\bar{2}10]$ using $g = \bar{2}0\bar{2}1$ in a 160℃/ 10 h aged MZ3; (b) $s_i^2/n_i^2$ was plotted as a function of $1/n_i^2$; the intercept of the straight line with the $s_i^2/n_i^2$ axis is $1/t^2$.

The foil thickness, the size of the rod-shape precipitates and the relative volume fraction after different ageing times at 160 ℃ were measured and are presented in Table 4.6. Qualitatively, the length and diameter of the precipitates are shown to

increase with ageing time.

Table 4.6 Rod-shaped precipitate dimensions and volume fraction in aged MZ3 measured from TEM micrographs.

| Ageing Time (h) | Particle Dimensions (nm) | | Foil Thickness (t) | Projected Area Fraction (%) | Volume Fraction (%) |
|---|---|---|---|---|---|
| | Length (l) | Diameter (D) | | | |
| **10** | 106.1 | 8.5 | 188.8 | 0.9 | 0.04 ± 0.02 |
| **25** | 172.9 | 12.1 | 198.2 | 1.6 | 0.09 ± 0.03 |
| **50** | 250.9 | 20.2 | 140.4 | 12.3 | 1.61 ± 0.14 |
| **96** | 291.3 | 22.5 | 172.7 | 16.1 | 1.96 ± 0.13 |
| **144** | 367.2 | 25.5 | 150.5 | 19.7 | 3.03 ± 0.17 |

As illustrated in Fig. 4.29, with increasing ageing time the volume fraction of precipitates increases monotonically. The volume fraction at 160 ℃/ 10 h is only about 0.04 ± 0.02 %. The largest volume fraction of precipitates is obtained in the 144 h aged alloy (3.03 ± 0.17 %).

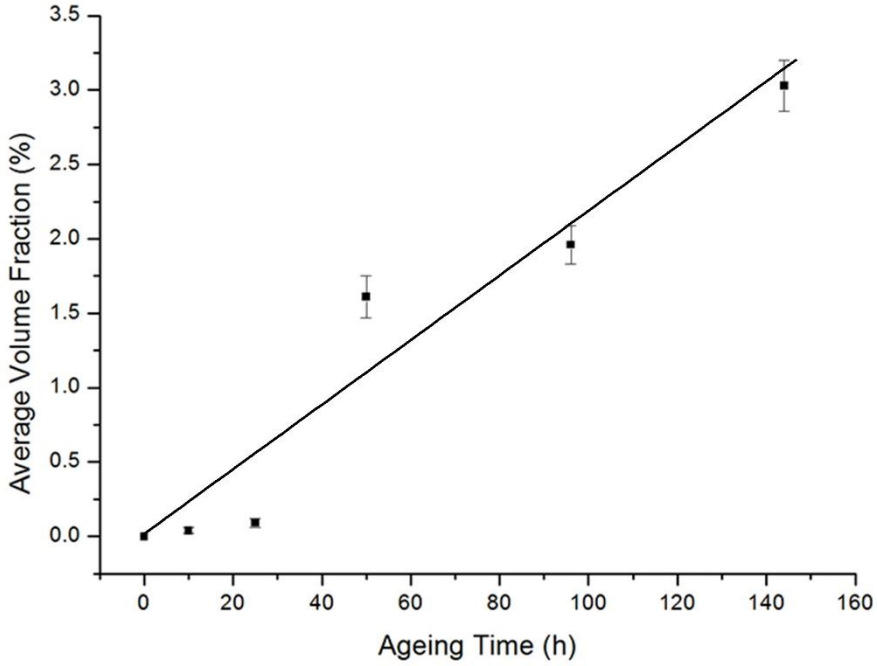


Fig. 4.29 The evolution with ageing time of the rod-shaped precipitate volume fraction for samples aged at 160 ℃.

## 4.6 Microstructural characterisation and hardness of solution-treated MZX30

### 4.6.1 Hardness

The hardness evolves with different solution treatments as shown in Fig. 4.3.

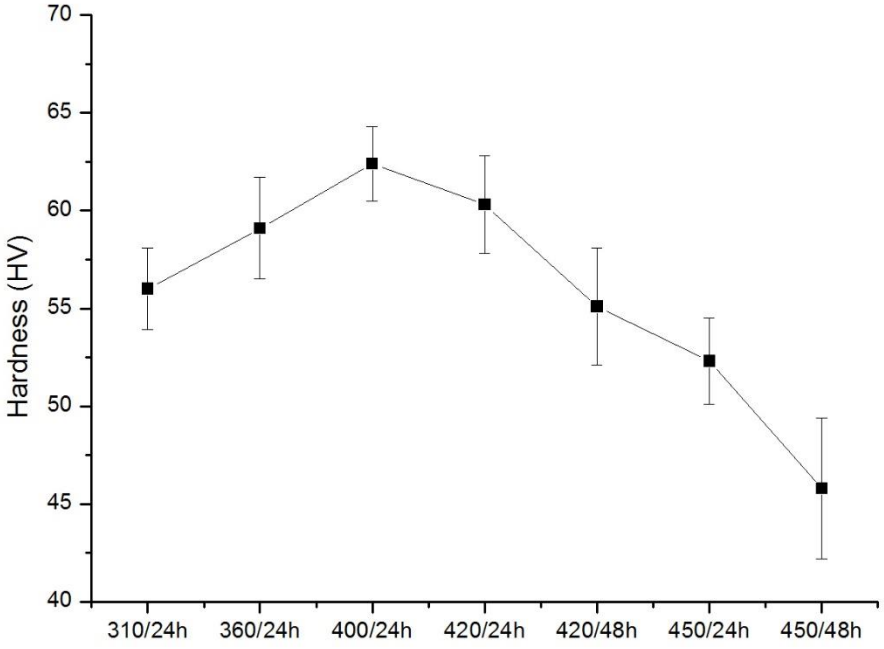


Fig. 4.30 Micro-hardness of solution-treated MZX30.

### 4.6.2 Microstructures

Fig. 4.31 shows the microstructure of MZX30 after different solution treatments. In the as-cast sample, shown in Fig. 4.31 a), the dendrite structure is evident and the grain size is relatively small. After 310 ℃/24 h, the grain size has increased (Fig. 4.31 b)). After 360 ℃/24 h, the dendrites have disappeared (Fig. 4.31 c)). The grain size at 400 ℃/24 h has increased further (Fig. 4.31 d)). In Figs. 4.31 e) – h), the grain size increases greatly as temperature increases. The amount of second phase located at the grain boundaries and spherical second phase is gradually reduced. The smallest volume fraction of second phases is 0.06 % in 450 ℃/48 h sample.

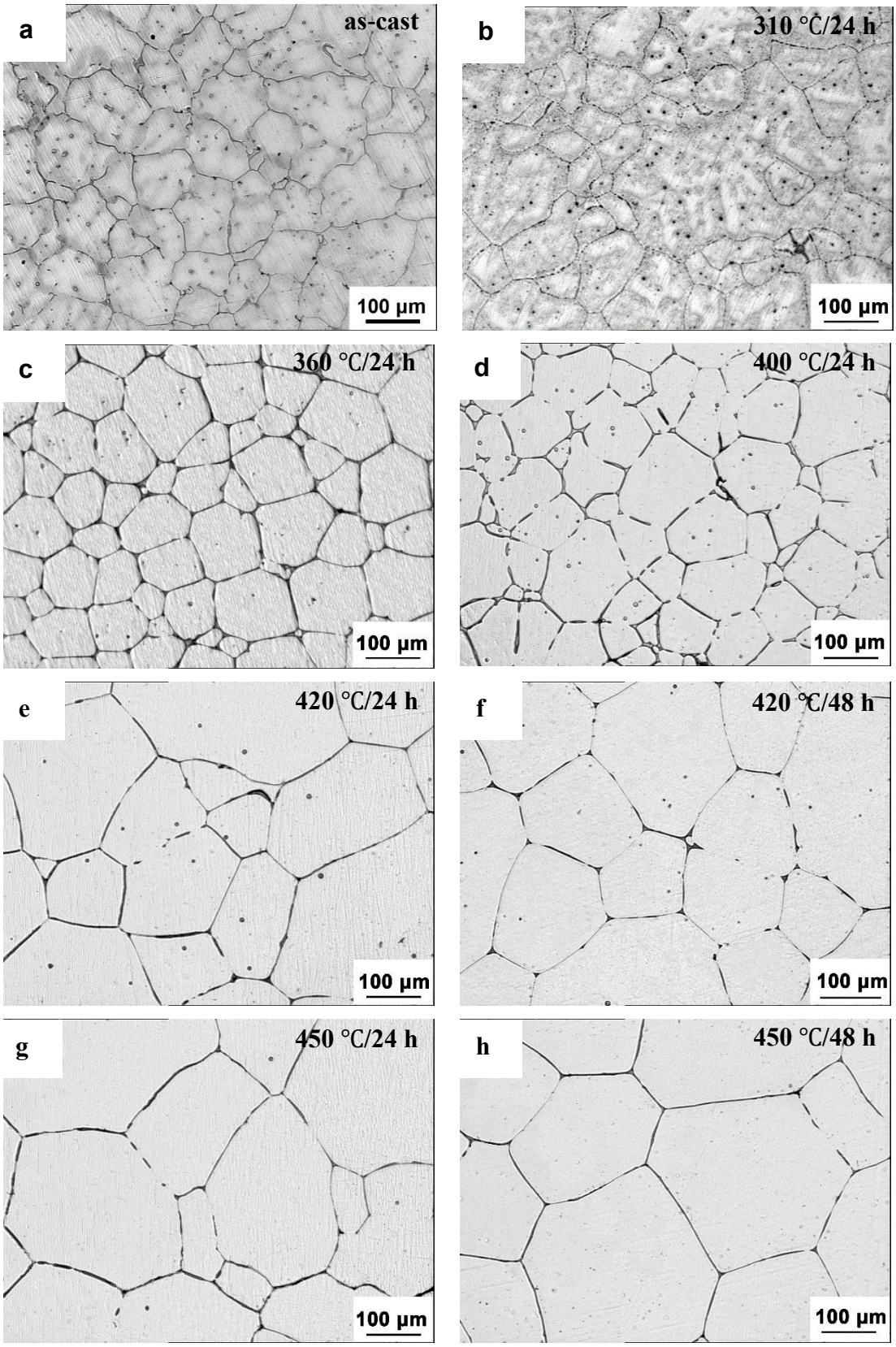


Fig. 4.31 Optical micrographs obtained from the as-cast sample (a) and the solution-treated samples (b) - (h).

SEM micrographs of the as-cast and solution-treated MZX30 are shown in Fig. 4.32. Fig. 4.32 a) illustrates a continuous network of second phases and randomly distributed spherical second phases in the as-cast sample. After 310 ℃/ 24 h, the grains grow and second phases dissolve into the Mg matrix (Fig. 4.32 b)). As shown in Fig. 4.32 c), 360 ℃/ 24 h MZX30 exhibits a relatively small amount of second phases; in particular the second phases located along the grain boundaries start to disconnect. Increasing the temperature (400 ℃/24 h), the intragranular spherical phases are greatly reduced, while the second phases present along the grain boundaries become thinner and more discontinuous (Fig. 4.32 d)). In Fig. 4.32 e), MZX30 after 420 ℃/ 24 h shows a little second phase. In comparison with 400 ℃/24h, the volume fraction of second phases (420 ℃/ 24 h) is considerably decreased ($0.7 \pm 0.3$ %). After 420 ℃/ 48 h, the dissolution of second phases is more obvious than that of 420 ℃/ 24 h, as shown in Fig. 4.32 f). In Fig. 4.32 g) and h), the second phase is mostly dissolved and the microstructure consists of α-Mg solid solution.

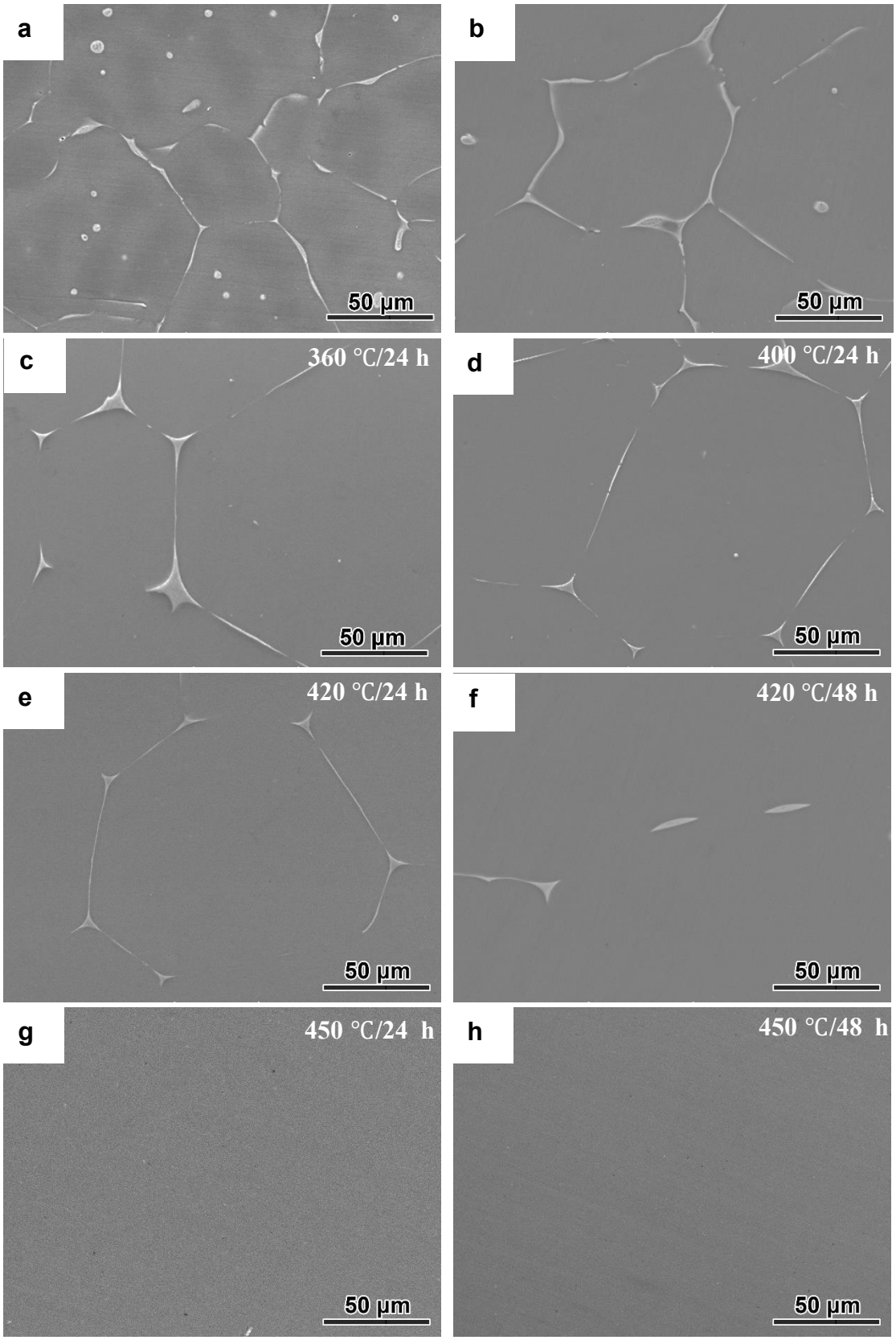


Fig. 4.32 SEM micrographs of as-cast and solution-treated MZX30: (a) as-cast; (b) 310 ℃/24 h; (c) 360 ℃/ 24h; (d) 400 ℃/24 h; (e) 420 ℃/24h; (f) 420 ℃/ 48h; (g) 450 ℃/ 24h; (h) 450 ℃/ 48h.

Table 4.7 details the microstructural characteristics of MZX30 after solution treatment. The largest volume fraction of second phases (2.4 ± 0.4 %) and smallest grain size (97 ± 6 μm) are obtained in the as-cast sample. As the temperature and time increases, the volume fraction of second phase decreases gradually and the grain size increases gradually. The volume fraction decreases to (1.7 ± 0.2) % and the grain size increases to (114 ± 7) μm in the 310 ℃/ 24 h sample. 450 ℃/ 48h MZX30 has the lowest secondary phase volume fraction (0.06 ± 0.01 %), while the grain size is the largest (214 ± 10 μm).

Table 4.7 Microstructural characteristics of MZX30.

| **Condition** | **Mg-3Zn-0.3Ca** | |
|---|---|---|
| | **Secondary Phase Volume Fraction (%)** | **Grain Size (μm)** |
| **as-cast** | 2.4 ± 0.4 | 97 ± 6 |
| **310 ℃/24 h** | 1.7 ± 0.2 | 114 ± 7 |
| **360 ℃/24 h** | 1.5 ± 0.1 | 129 ± 9 |
| **400 ℃/24 h** | 1.3 ± 0.3 | 151 ± 5 |
| **420 ℃/24 h** | 0.7 ± 0.3 | 166 ± 8 |
| **420 ℃/48 h** | 0.2 ± 0.1 | 180 ± 7 |
| **450 ℃/24 h** | 0.08 ± 0.03 | 193 ± 9 |
| **450 ℃/48 h** | 0.06 ± 0.01 | 214 ± 10 |

## 4.7 Discussion

### 4.7.1 Microstructure of as-cast MZ3 and MZX30

#### 4.7.1.1 Grain refinement effect of Ca and Zn

The microstructures of pure Mg, as-cast MZ3 and MZX30 are shown in Fig. 4.1. It is evident that the grain size of MZ3 and MZX30 is less than for Mg. After addition of Ca, the grain size of the Mg alloy reduces further. The refinement efficiency of the elements can be determined by their growth restriction factor [210-212]. The growth restriction factor (GRF) Q is a measure of the segregating power of an element during solidification.

$$\text{Growth restriction factor} = \sum_i m_i C_{0,i}(k_i\text{-}1) \qquad \text{(Equation 4.2)}$$

where $m_i$ is the slope of the liquidus line (assumed to be straight), $k_i$ is the distribution coefficient and $C_{0,i}$ is the initial concentration of element i [213].

Table 4.8 indicates some GRF values for various alloying elements in Mg alloys which are determined from binary phase diagrams [214]. The GRF values of Zn and Ca are 5.31 and 11.94, as detailed in Table 4.8. They are higher than for elements (Al, Sr and Y, etc). Zn and Ca play an important role in controlling the growth of the nucleated grains and in subsequent nucleation. Ca has a significantly high GRF, which means the growth restricting effect of Ca on the solid-liquid interface of the new grains is strong, thus preventing new grains from growing into the melt. This is consistent with the literature where Lee et al. [214] reported that Ca segregation to the boundaries restricted grain growth and thus caused refinement. Zn and Ca segregate strongly in the melt and cause intense constitutional supercooling in a diffusion layer ahead of the advancing solid/liquid interface, consequently promoting nucleation and restricting grain growth.

Table 4.8 Slope of the liquidus line (m), equilibrium distribution coefficient (k) and GRF values (m(k-1)) for various alloying elements in Mg alloys (adapted from [214]).

| Element | m | k | GRF |
|---|---|---|---|
| **Zr** | 6.90 | 6.55 | 38.29 |
| **Ca** | -12.67 | 0.06 | 11.94 |
| **Zn** | -6.04 | 0.12 | 5.31 |
| **Al** | -6.87 | 0.37 | 4.32 |
| **Sr** | -3.53 | 0.006 | 3.51 |
| **Yb** | -3.07 | 0.17 | 2.53 |
| **Y** | -3.40 | 0.50 | 1.70 |
| **Sn** | -2.41 | 0.39 | 1.47 |

As illustrated in Fig. 4.7, the hardness increases after the addition of Zn and Ca. The increased hardness has a close relationship with the refined microstructure via the Hall-Petch equation

$$\sigma = \sigma_0 + kd^{-1/2} \qquad \text{(Equation 4.3)}$$

where σ is yield stress, d is grain size, k is the strengthening coefficient (a constant unique to each material) and $\sigma_0$ is a material constant. There is a reciprocal relationship between the grain size and hardness: the decrease in grain size strengthens the alloy. This is directly related to grain boundary strengthening. Moreover, the solid solution strengthening makes contribution. When Zn and Ca solute atoms are introduced, local stress fields are formed and then interact with the dislocations to impede their motion, thus resulting in an increase in the yield stress of Mg.

#### 4.7.1.2 3D tomography of second phases in the as-cast MZ3 and MZX30

FIB tomography is a destructive technique, but it can provide higher spatial resolution (many orders of magnitude) than X-ray tomography. The 2D images can be clearly segmented and thus the phases' contours can be clearly distinguished. The high resolution of the FIB tomographic method permits a detailed representation of the 3D features. As shown in Figs. 4.2 a), b) and 4.3, the spherical product is distributed mainly intragranularly in the as-cast MZ3. Fig. 4.15 shows the 3D tomography of the spherical phases (around 5 μm) achieved using FIB tomography. Each phase is assigned a different colour. 3D tomography is directly evident that is unobtainable in the 2D images, revealing the inner structure of the (α-Mg+MgZn) product. The 3D images exhibit a lamellar character and display a fair degree of interconnection.

MicroCT tomography requires a simple sample preparation, which allows samples for unbiased comparisons without sample preparation errors. Structural measurements using this assessment contribute to understanding the 3D structure and connectivity of materials. As can be seen from Figs. 4.2 c), d), and 4.5, (α-Mg + $Ca_2Mg_6Zn_3$) phases possess two different morphologies in the as-cast MZX30: one is spherical and the other is network. Fig. 4.18 shows a 3D reconstruction with a selective transparency applied to the Mg matrix and blue applied to the (α-Mg + $Ca_2Mg_6Zn_3$) phases. All 3D reconstruction can be viewed from any angle, or along any desired cutting plane, as shown in Fig. 4.18 c) and d). The dendritic α-Mg encloses the (α-Mg + $Ca_2Mg_6Zn_3$) structure. The isolated blue volumes (spherical phases in 2D) are randomly distributed within the blue volume networks (strip-like phases in 2D). 3D examination reveals a relatively large amount of (α-Mg + $Ca_2Mg_6Zn_3$) phases beneath the MZX30 surface. This causes a relatively large corrosion reaction volume beneath the alloy surface (more details in Chapter 5).

### 4.7.2 Aged MZ3

As mentioned in Chapter 2 (Section 2.5.1), Mg-Zn alloys have a precipitation sequence as follows:

$$\text{SSSS} \rightarrow \text{GP zones} \rightarrow \text{transitional phase} \rightarrow \text{equilibrium phase}$$

The activation energy barrier for nucleation is lower in such a sequence, especially for the GP zones, compared with the direct precipitation of the equilibrium phase. Thus, the nucleation rate is increased and a fine precipitate distribution is formed.

As indicated in Figs. 4.22 – 4.26, precipitation at 160 ℃ involves the formation of $\beta_1'$ and $\beta_2'$ transitional phases. The precipitate morphology and habit in aged MZ3 are shown in a schematic representation in Fig. 4.33. The purple rod-like precipitate is $\beta_1'$ (rods $\perp \{0001\}_{Mg}$;) and the blue plate precipitates are $\beta_2'$ (plates $\parallel \{0001\}_{Mg}$).

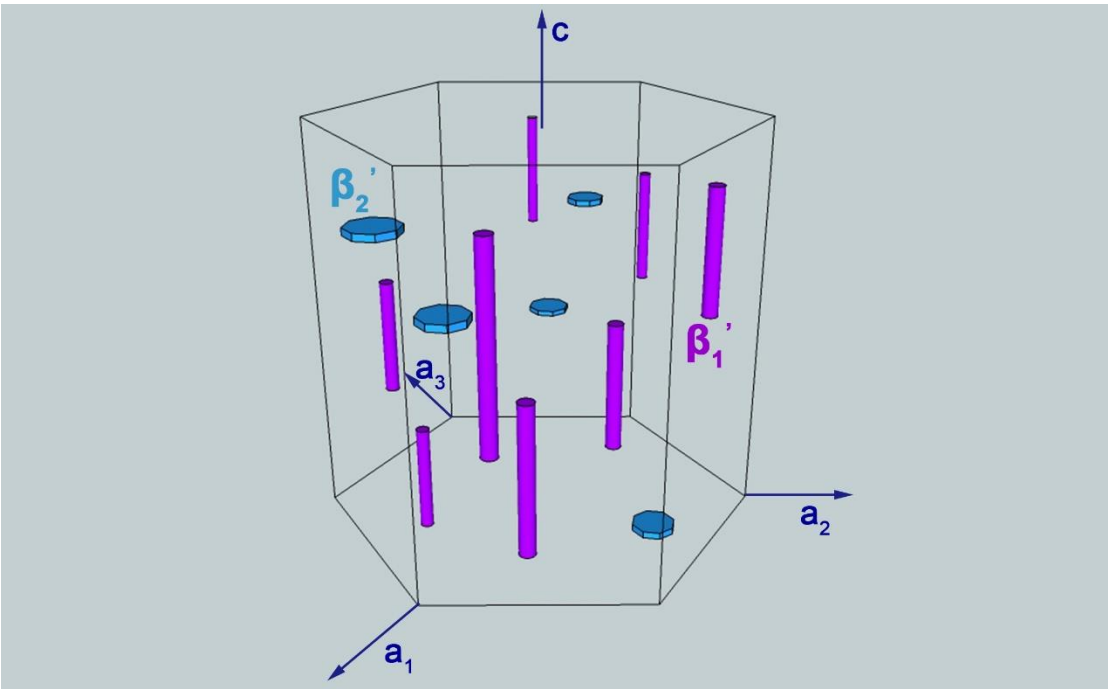


Fig. 4.33 Schematic representation of the precipitate morphology and habit in aged MZ3.

$\beta_1'$ is a transitional phase rather than an ordered GP zone, because the GP zones are formed below 100 ℃ in the Mg-Zn system [129, 215, 216]. The $\beta_1'$ precipitates at an ageing temperature above 149 ℃. The length to width ratio of rod-shaped $\beta_1'$ is high. This is reasonable on the basis of different growth rates of the $\beta_1'$/Mg interface in different directions in the Mg matrix. $[001]_{\beta_1'}$ is parallel to $[0001]_{\mathrm{Mg}}$. A good match in spacing exists along $[001]_{\beta_1'}$ with $[0001]_{\mathrm{Mg}}$. In this direction, the interface between $\beta_1'$ and matrix is a well-ordered dislocated boundary. The lattice matching between the $\beta_1'$ and the matrix along the c axis of the matrix is better than along the a axes; the interface of $\beta_1'$ with the matrix across (0001) must be disordered. Thus, growth is easier along the c axis. $\beta_1'$ starts to form as rods in the early stages of precipitation; the continued lengthening is maintained by the tips' point effect on diffusion, thus a very long rod is exhibited.

The crystal structures of the plate-shaped $\beta_2'$ and the Mg matrix are hexagonal and they have a common [0001] zone axis. The orientation relationship of $\beta_2'$ with the Mg matrix is $(0001)_{\beta_2'} \parallel (0001)_{\mathrm{Mg}}$ and $[11\bar{2}0]_{\beta_2'} \parallel [10\bar{1}0]_{\mathrm{Mg}}$ [134, 207].

The decomposition of the supersaturated solid solution of Zn in Mg produces age hardening. The age hardening response of MZ3 at 160 ℃ is illustrated in Fig. 4.21. Hardening is mainly ascribed to the energy increment due to the disturbance by the atomic arrangement of the particles to dislocations passing through the particles [217]. The age hardening involves two precipitates: rods ($\beta_1'$) and coarse plates $\beta_2'$ [208]. The rod-like $\beta_1'$ precipitates are primarily responsible for the age-hardening. It is clear that peak hardness is achieved at 96 h (Fig. 4.21), because of the dense dispersion of rod-shaped $\beta_1'$. After ageing for 144 h, the hardness decreases due to the transformation of $\beta_1'$ to disc-shaped $\beta_2'$. $\beta_2'$ precipitates are easily bypassed by dislocations and provide less obstruction to the movement of dislocations [207].

### 4.7.3 Solution-treated MZX30

The microstructural evolution of solution-treated MZX30 is illustrated in Figs. 4.31 and 4.32. The grain size and volume fraction of the second phases after different solution treatments are summarized in Table 4.6. As shown in Fig. 4.32, the morphology and quantity of (α-Mg + $Ca_2Mg_6Zn_3$) are greatly changed after different solution treatments. At 360 ℃/ 24 h, the networks along the grain boundaries start to disconnect. The network second phases become thinner after 400 ℃/24 h. At 420 ℃/48 h, the strip-like second phases are changed to the fragmented and discontinuous islands (Fig. 4.32 f)). At 450 ℃/24 h and 450 ℃/48 h, the (α-Mg + $Ca_2Mg_6Zn_3$) phases dissolve completely and the average grain size grows to about 200 μm.

The solution treatment is controlled by two factors, the diffusion coefficient of atoms and vacancy concentration in the alloys. Both of them are enhanced at high temperature. The grain boundaries and phase interfaces are distorted regions with high imperfection and a high diffusion rate. It is easier and quicker for the Zn and Ca atoms diffuse along the grain boundaries and phase interfaces. The Zn and Ca atoms diffuse along the interfaces and enter the Mg crystal lattice and thus the $Ca_2Mg_6Zn_3$ phases decompose locally and become thinner. At higher temperature/time, the networks transform to a favoured shape in order to reduce the interface energy. The second phases become smaller and finally dissolve completely.

The hardness of the solution-treated MZX30 is shown in Fig. 4.30. The hardness increases after 310 ℃/ 24 h, 360 ℃/ 24 h and 400 ℃/ 24 h, because of solid solution strengthening due to the dissolution of the second phases. Then, the hardness decreases after 420 ℃/ 24h due to the increase of the average grain size.

## 4.8 Conclusions

1. In the as-cast Mg-3Zn (MZ3), the spherical (α-Mg + MgZn) eutectic products are mainly distributed within the grains. MgZn has a rhombohedral structure (a= 2.6 nm and c=1.8 nm). As-cast Mg-3Zn-0.3Ca (MZX30) consists of α-Mg and (α-Mg + $Ca_2Mg_6Zn_3$) phases (globular and strip shaped). $Ca_2Mg_6Zn_3$ has a trigonal structure (a =0.97 nm, c=1.00 nm).

2. 3D tomography of (α-Mg + MgZn) phases is obtained via FIB/SEM. The lamellar structure of the (α-Mg + MgZn) phases is internally observed. MicroCT tomography of the as-cast MZX30 shows that the dendritic α-Mg encloses a relatively large amount of (α-Mg + $Ca_2Mg_6Zn_3$) phase mixture beneath the MZX30 surface.

3. Quantitative TEM analysis is used to characterize the precipitation in the Mg-3 Zn alloy with different ageing times at 160 ℃. There is a monotonoic relationship between the ageing time and the volume fraction of the fine precipitates.

4. The hardness of MZ3 is improved by ageing and the peak hardness is achieved at 160 ℃/ 96 h because of dense dispersion of rod-shaped $\beta_1'$.

5. After different solution treatments, MZX30 shows different microstructures. As the temperature and time increase, the volume fraction of the second phases decreases gradually and the grain size increases. The hardness increases with increasing temperature (up to 400 ℃) and then decreases.

6. During the solution treatments of MZX30, the strip-like (α-Mg + $Ca_2Mg_6Zn_3$) phases are transformed from a network-like shape to being disconnected and

isolated, to reduce the interface energy. At 450 ℃, the second phases have completely dissolved.

# Chapter 5 Degradation of Mg-3Zn(-0.3Ca) alloys in SBF

## 5.1 Initial corrosion of as-cast MZ3 and MZX30 in SBF

### 5.1.1 As-cast MZ3

SEM micrographs of as-cast MZ3 before immersion are shown in Figs. 5.1 a) and b). The hardness mark is used as an identification to easily track the interesting area. In Fig. 5.1 a), the (α-Mg+MgZn) phases disperse randomly within the as-cast MZ3. The morphology of the spherical ( α -Mg + MgZn) phases is shown in the high magnification image (Fig. 5.1 b)). Corrosion morphologies of as-cast MZ3 after 10 min soaking are presented in Figs. 5.1 c) and d). It is visible that the spherical phases are closely surrounded by the white circular and radially extended corrosion products indicated by green arrows (Fig. 5.1 c)). In Fig. 5.1 d), the second phases are surrounded by a blue dotted circle, while the spherical corrosion product is indicated by a red dotted circle.

Interestingly, Figs. 5.1 e) and f) show a volcano-shaped corrosion morphology after exposure to SBF for 10 min. A volcano-shaped corrosion area of about 40 μm is evident. During the immersion, streams of $H_2$ bubbles evolve from the sample surface. Clusters of corrosion products are observed around the hydrogen bubbles. Fig. 5.1 f) shows that the volcano-shaped corrosion centre contains a bright particle of about 7 μm in diameter, as indicated by the red arrow.

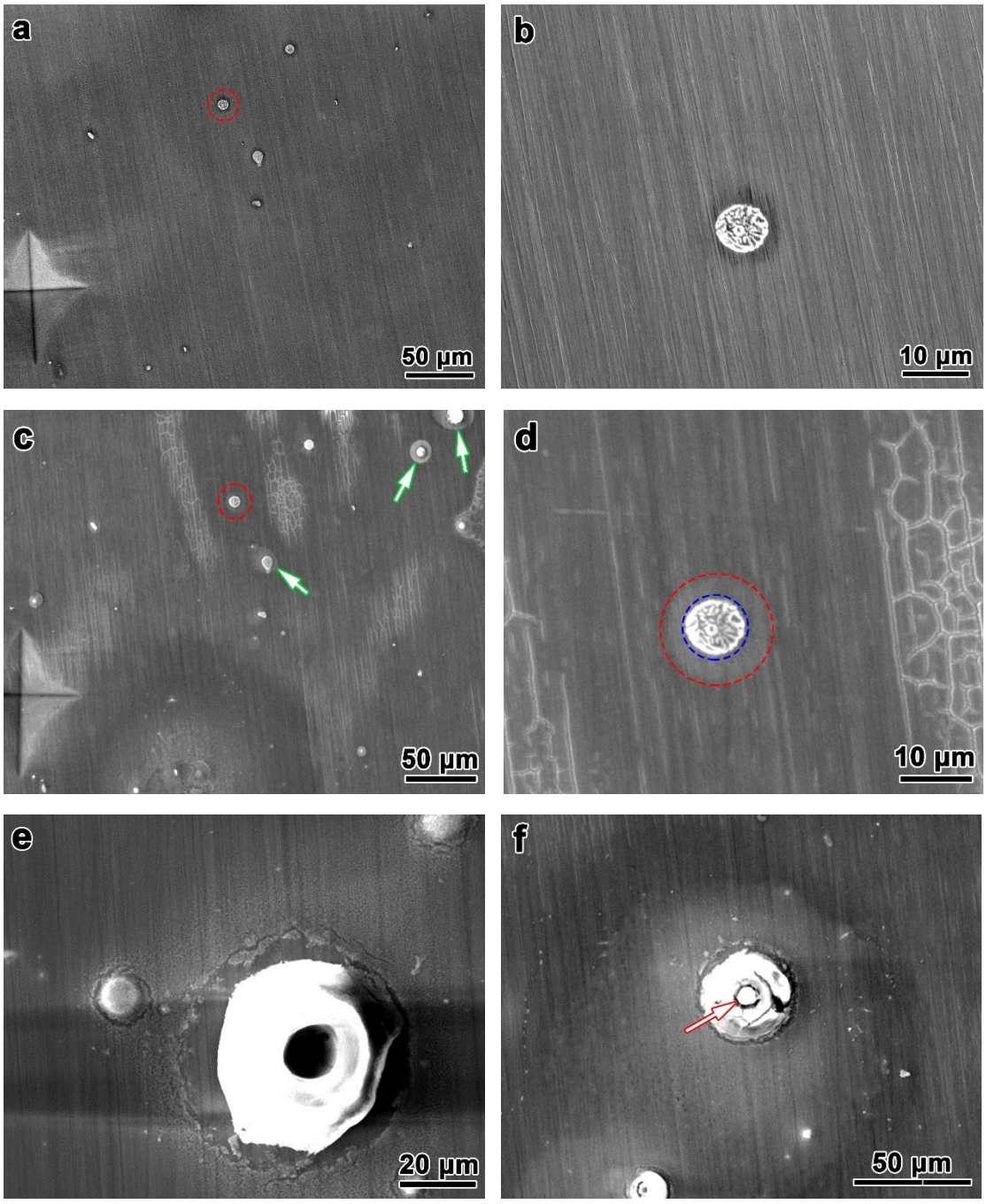


Fig. 5.1 (a) and (b) SEM micrographs of as-cast MZ3 before immersion: (b) is a high magnification of circle in (a); (c) and (d) SEM images after 10 min immersion in SBF (pH: 7.4) at 37 ℃: (d) is a high magnification of circle in (c); (e) and (f) volcano-shaped corrosion morphology.

It would be expected that Mg and Mg alloys be vulnerable to general corrosive attack because they are highly reactive. But, this is not the case. Corrosive attack on magnesium is local rather than general although Mg is highly reactive. After a longer

immersion time, localized corrosion in Mg is more obvious. The corrosion morphology for as-cast MZ3 immersed in SBF for 1 h is shown in Figs. 5.2 a) and b). After 1 h immersion, the volcano-shaped corrosion morphology at the localized corrosion sites indicated by green arrows and an irregular square corrosion layer indicated by purple arrows are visible in Figs. 5.2 a) and b). These volcano-shaped blisters often have holes in the centre. The spherical corrosion morphology suggests that $H_2$ bubbles form at the corrosion sites. After removal of the corrosion products, a non-uniform corrosion morphology is revealed (Figs. 5.2 c) and d)). The corrosion of MZ3 initiates in the Mg matrix only, while the (α-Mg+MgZn) phases are un-attacked. As shown in Fig. 5.2 d), the pits are adjacent to (α-Mg+MgZn) phases (indicated by blue arrow). The localized corrosion has occurred in the Mg matrix rather than in the second phases.

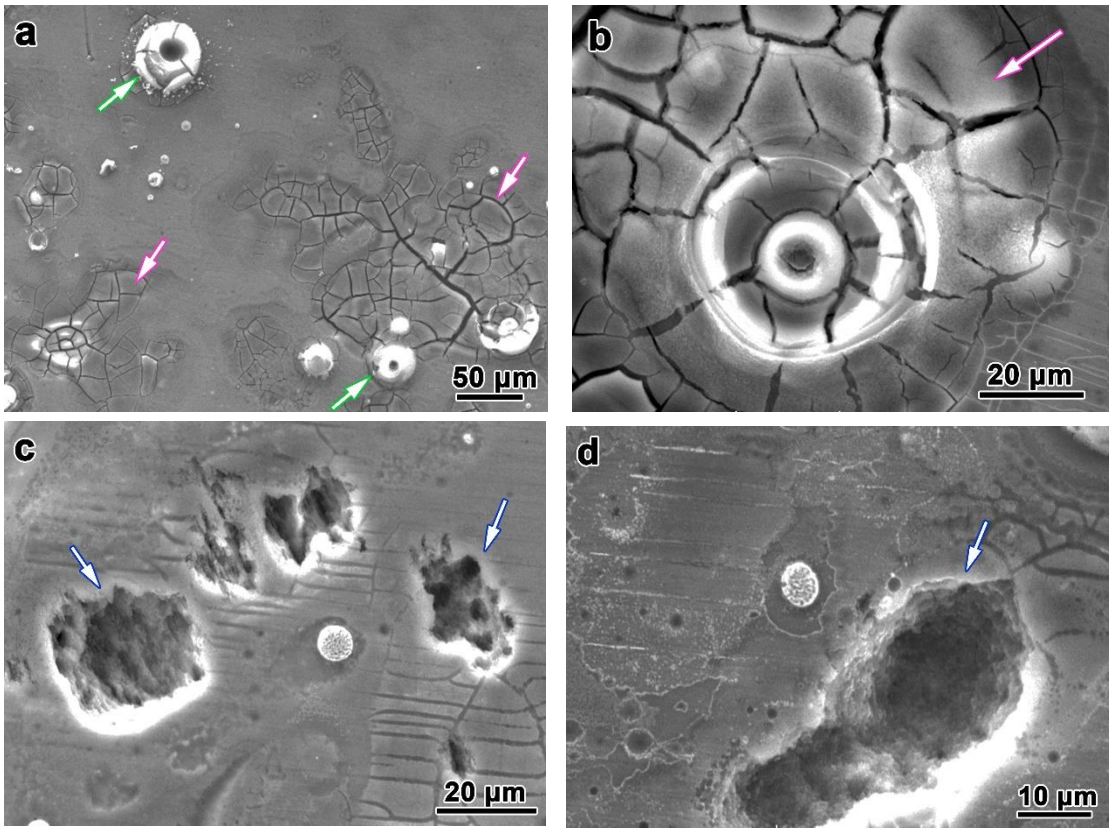


Fig. 5.2 (a) and (b) SEM images of as-cast MZ3 exposed to SBF for 1 h; (c) and (d) SEM micrographs of corroded MZ3 after removal of corrosion products.

Fig. 5.3 shows the elemental distribution at a localized corrosion site in as-cast MZ3 after 1 h immersion, suggesting enrichment of O, P and Ca. The cluster of corrosion products is because the increase of local pH around the corroded site promotes their formation. The water reduction at the cathodic particle results in a locally increased pH.

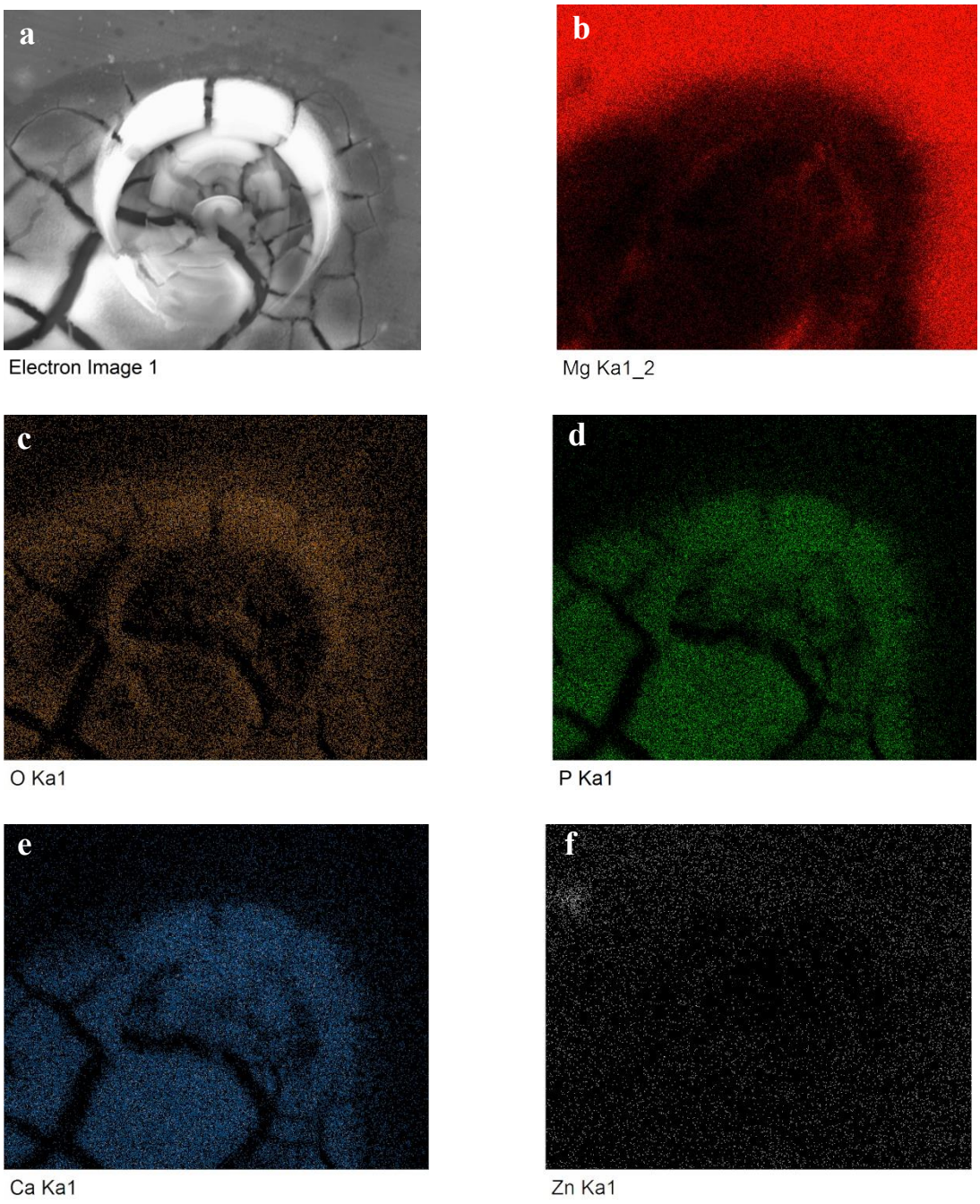


Fig. 5.3 SEM image and elemental maps of as-cast MZ3 after exposure to SBF for 1h.

### 5.1.2 As-cast MZX30

Low and high magnification SEM micrographs of as-cast MZX30 are shown in Figs. 5.4 a) and b), respectively. The as-cast MZX30 consists of spherical and strip-like (α-Mg+$Ca_2Mg_6Zn_3$) phases. After exposure to SBF for 10 min, the peculiar corrosion structure rising out of the surface is observed (Figs. 5.4 c) and d)), as indicated by the green arrows. At corresponding higher magnification (Fig. 5.4 d), the volcano-like corrosion features are very similar to that of as-cast MZ3. It is clearly evident that localized corrosion occurs in the area where clusters of (α-Mg+$Ca_2Mg_6Zn_3$) phases are present.

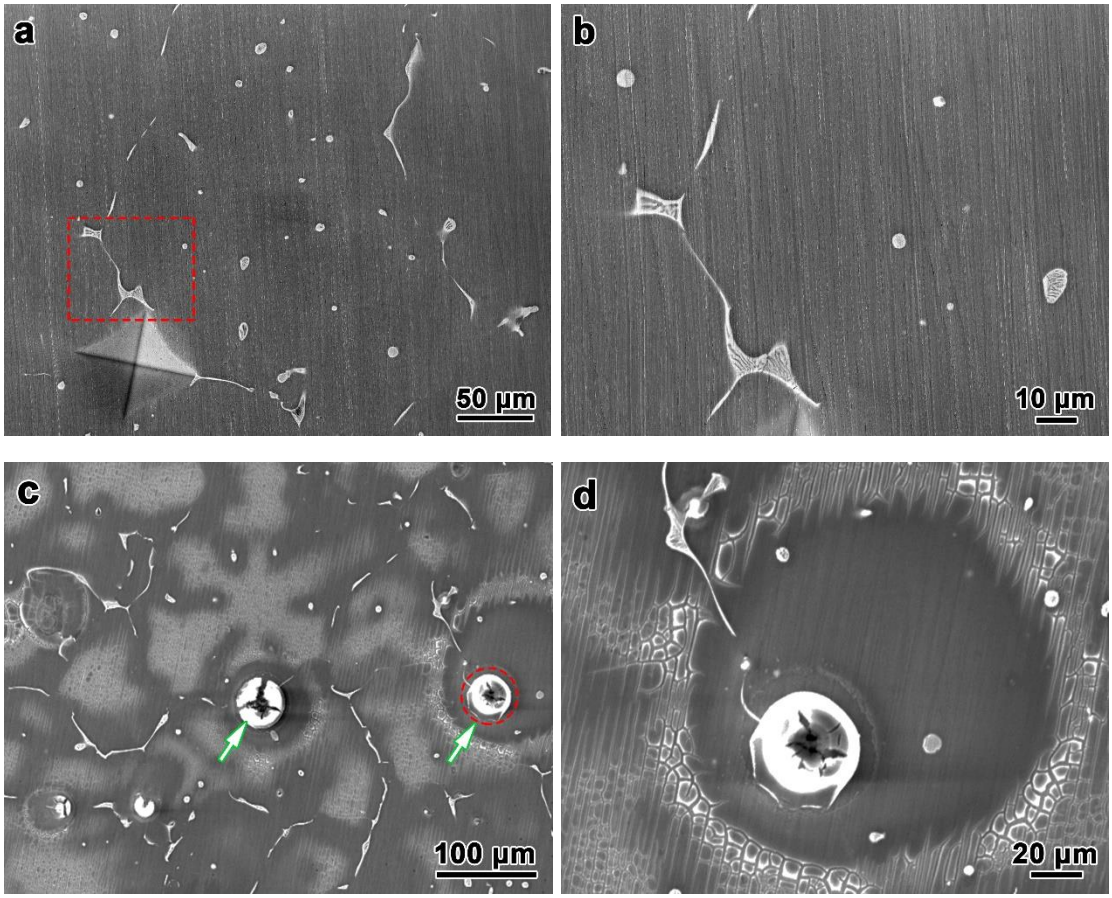


Fig. 5.4 (a) and (b) SEM micrographs of as-cast MZX30 before immersion: (b) is a high magnification of the square in (a); (c) and (d) SEM images after 10 min immersion: (d) is a high magnification of the circled area in (c).

After a prolonged immersion time (1 h), it is clear that some bumps indicated by green arrows appear on the surface which correspond to the site where hydrogen bubbles formed, as shown in Figs. 5.5 a) and b). This corrosion morphology is the same as in as-cast MZ3. A particle is observed in the centre of the corrosion area which is surrounded by the corrosion products, as indicated by the red arrow (Fig. 5.5 b)). Fig. 5.5 c) and d) show the corrosion morphology after corrosion product removal. It can clearly be seen that corrosion attacks the Mg matrix and causes pits (marked by blue arrows). As shown in Fig. 5.5 d), significant dissolution of the Mg matrix occurs around the second phases (indicated by the dotted lines).

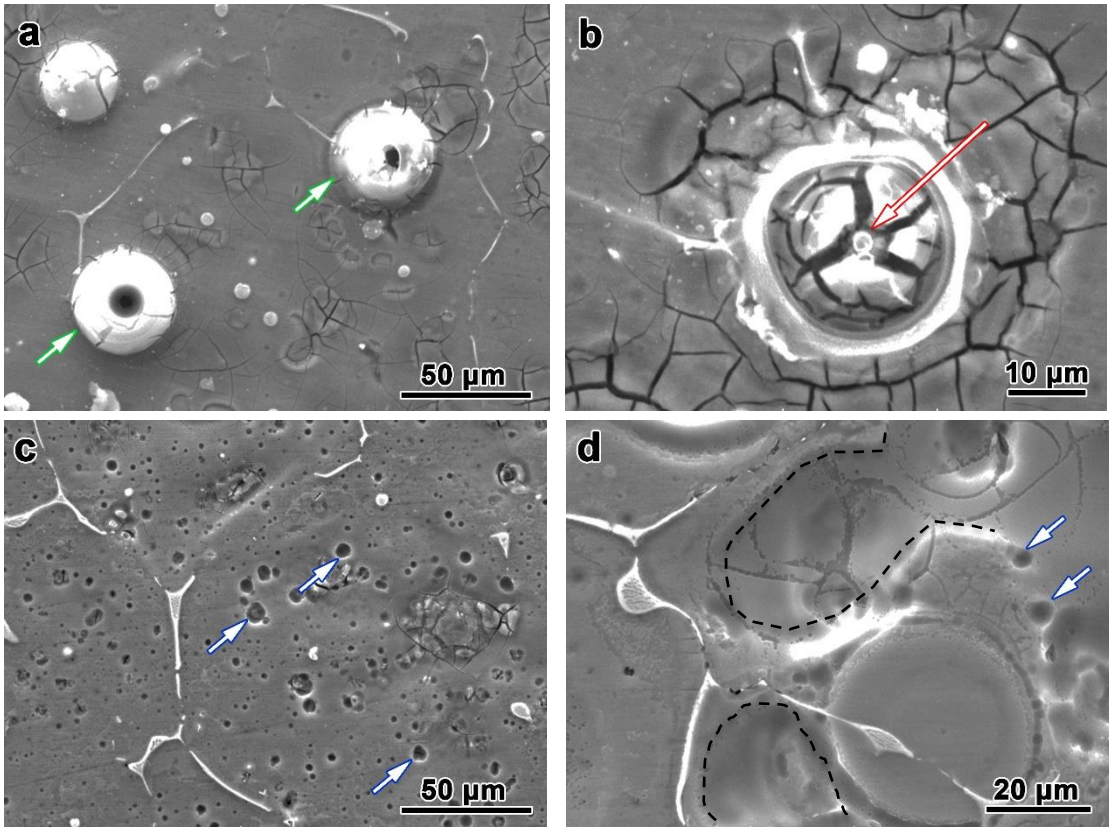


Fig. 5.5 (a) and (b) SEM images show as-cast MZX30 exposed in SBF for 1 h; (c) and (d) corrosion morphology after corrosion product removal.

An SEM image and elemental maps of the 1h-immersed as-cast MZX30 are displayed in Fig. 5.6. The EDX results reveal the O, P and Ca elements enriched at the spherical corrosion site, especially at the periphery of the spherical corrosion structure.

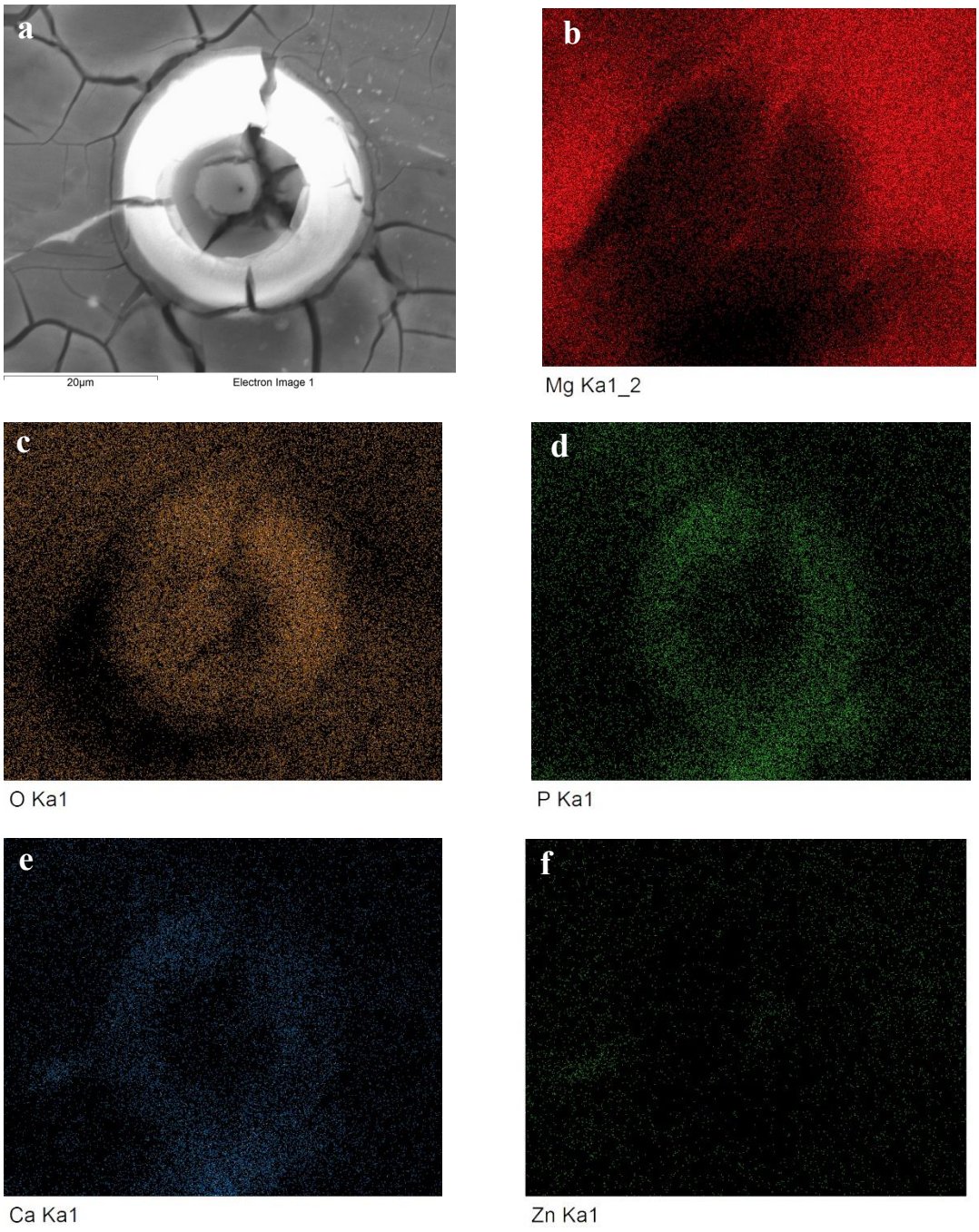


Fig. 5.6 SEM image and elemental maps of the corroded as-cast MZX30 after exposure to SBF for 1 h.

## 5.2 Degradation of as-cast MZ3 and MZX30 in SBF

### 5.2.1 Degradation rate measurement

The amount of hydrogen evolution during 10 days in SBF is illustrated in Fig. 5.7. The degradation rates of all samples increase during the whole immersion period.

Between Mg, as-cast MZ3 and MZX30, Mg presents the best corrosion resistance (degradation rate: 2.08 ± 0.11 mL/cm$^2$/day), over the whole immersion period. As shown in Fig. 5.7, MZ3 and MZX30 display a similar degree of degradation, 3.50 ± 0.20 mL/cm$^2$/day and 3.33 ± 0.02 mL/cm$^2$/day, respectively. It can be seen that Mg has a better corrosion resistance than that of as-cast MZ3 or MZX30, because there is galvanic corrosion in the Mg alloys.

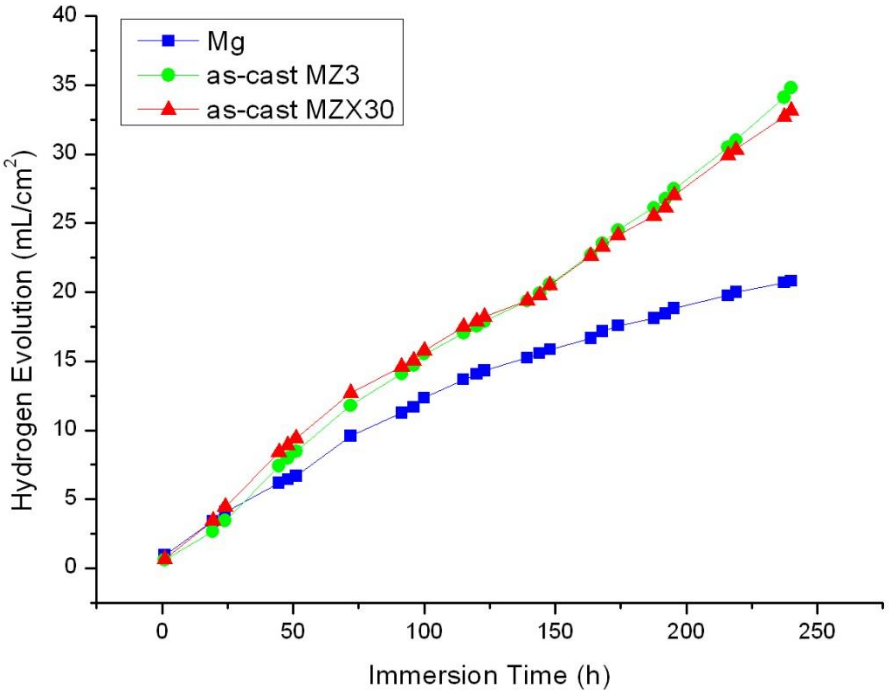


Fig. 5.7 Hydrogen evolution from Mg, as-cast MZ3 and MZX30 in SBF at 37 ℃.

### 5.2.2 Corrosion product analysis

As shown in Fig. 5.8, all the samples have rough surfaces and are covered by corrosion products. The appearance of cracks is due to the dehydration of the corroded layer during drying. The EDX data was acquired from the square in Figs. 5.8 a), c) and e). As shown in the EDX spectra (Figs. 5.8 b), d) and f)), the Mg surface is rich in O, Mg, P and Ca, while the MZ3 and MZX30 surface layers are mainly composed of O, Mg, P, Ca and Zn (originating from the Mg substrates). The relatively

weaker Mg peaks for Mg indicates a thicker coverage, which is also related to the better corrosion resistance of Mg due to the better corrosion layer protection.

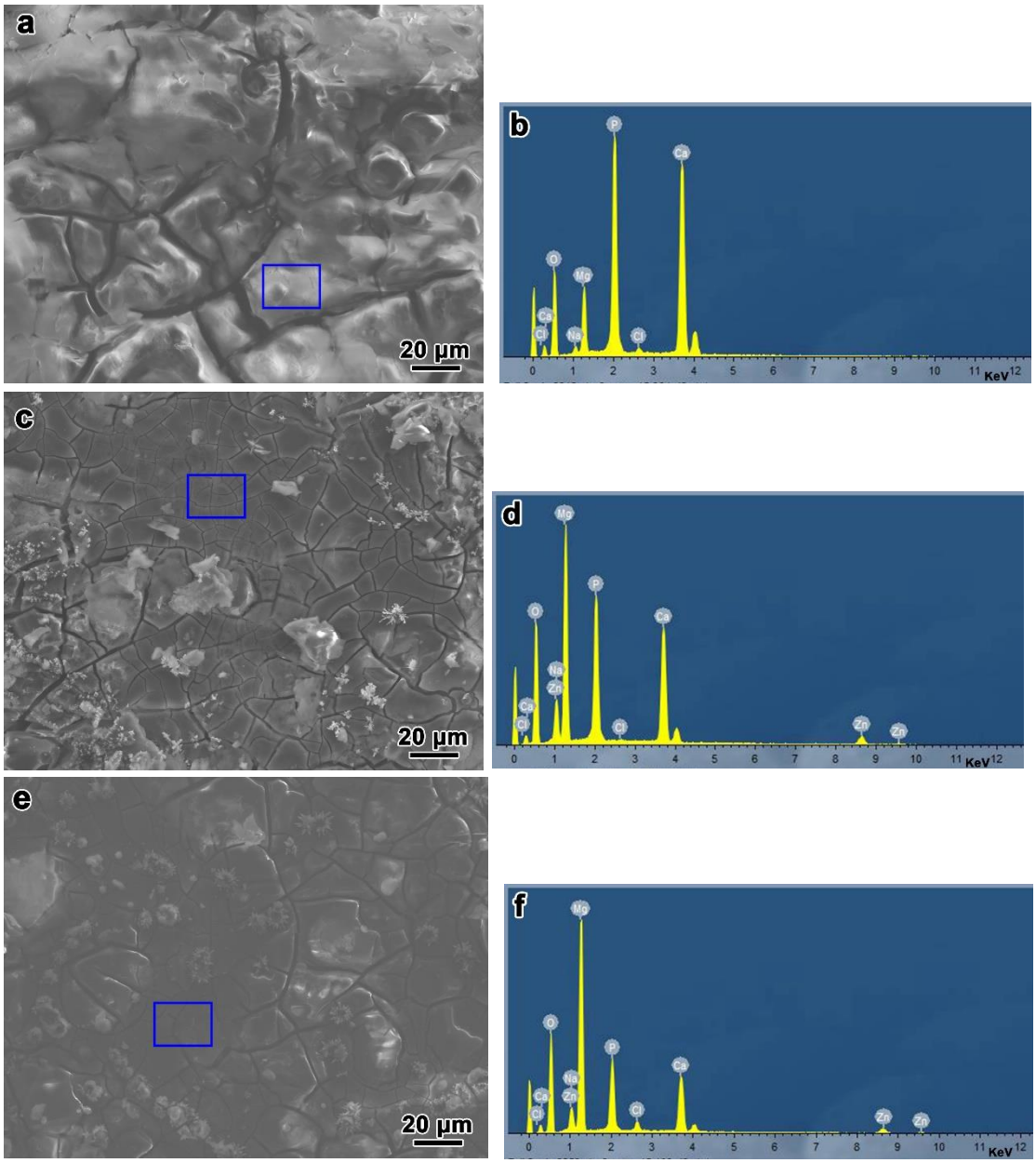


Fig. 5.8 Surface morphologies after 10 days' immersion in SBF of (a) Mg, (c) as-cast MZ3 and (e) as-cast MZX30; corresponding EDX analysis of the rectangular areas in the SEM images (b), (d) and (f).

XRD analysis of the samples after 10 days' immersion is shown in Fig. 5.9. It clearly can be seen that the corrosion products are magnesium brucite ($Mg(OH)_2$) (PDF reference code: 00-044-1482), hydroxyapatite (HA, $Ca_5(PO_4)_3(OH)$) (PDF reference

code: 00-024-0033) and magnesium phosphate tribasic ($Mg_3(PO_4)_2$) (PDF reference code: 00-043-0500) (and the Mg matrix). The corrosion products are biocompatible: the hydroxyapatite is an essential component of human bone and the deposition of hydroxyapatite particles on an Mg substrate can accelerate the healing of bone tissue [86, 87]; magnesium phosphate also has favourable biocompatibility.

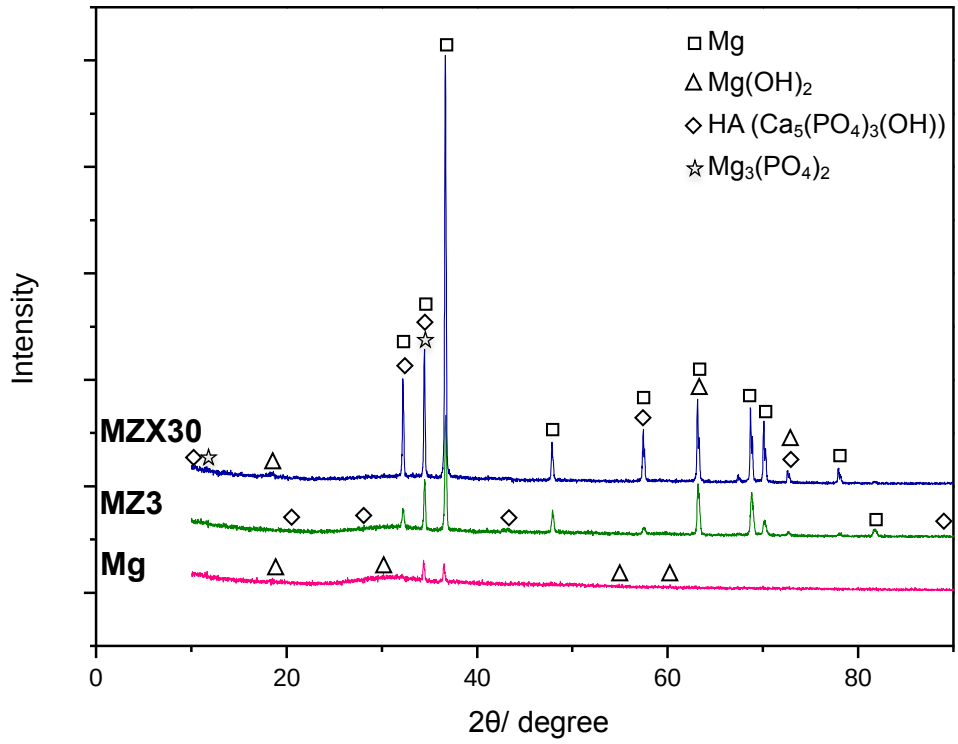


Fig. 5.9 XRD spectrA of Mg, as-cast MZ3 and MZX30 after 10 days' immersion.

### 5.2.3 Corrosion morphology

Fig. 5.10 shows the surface morphologies of as-cast MZ3 and MZX30 after 10 days' immersion. For Mg, the corrosion morphology is smoother than that of as-cast Mg alloys, as shown in Figs. 5.10 a) and b). Notably, both the as-cast MZ3 and MZX30 display a significant partial dissolution, as illustrated by the large cavities in Figs. 5.10 c) and e). Some Mg matrix surrounding second phases is preferentially attacked and undermined and then the second phase is peeled from the surface thus forming

pits (as indicated by the blue box). In as-cast MZ3, the surrounding α-Mg is corroded and the preferential corrosion sites are adjacent to the (α-Mg+MgZn) product (Fig. 5.10 d)), leaving a narrow and black trench. Fig. 5.10 e) shows severe localized corrosion. The Mg matrix is significantly dissolved after 10 days' immersion. The (α-Mg+$Ca_2Mg_6Zn_3$) phases survive as indicated by the arrows in Figs. 5.10 e) and f).

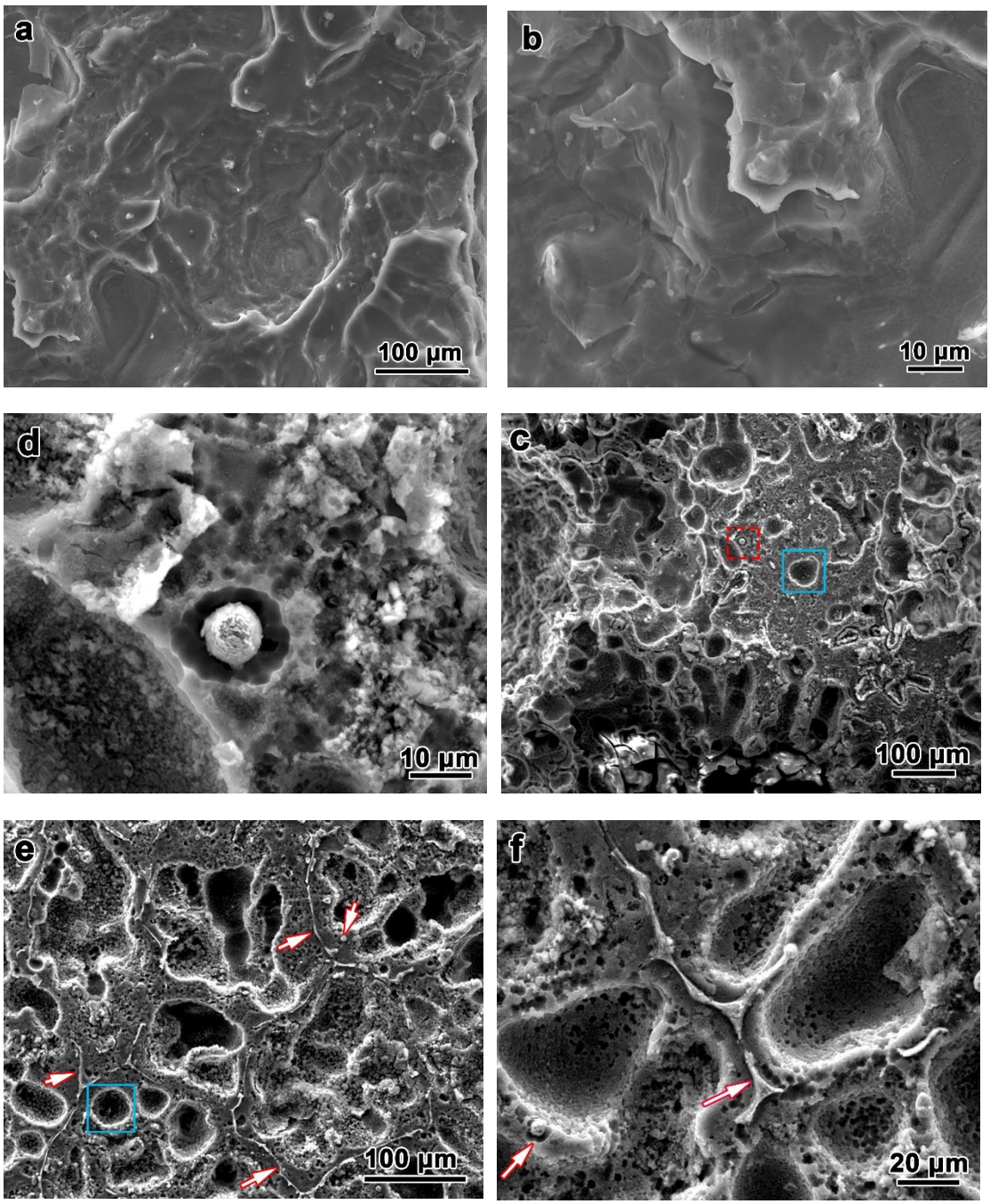


Fig. 5.10 Surface morphologies after 10 days' immersion (after removal of corrosion products): (a) and (b) Mg; (c) and (d) as-cast MZ3, (d) is a high magnification of red

box in (c); (e) and (f) as-cast MZX30.

## 5.3 3D tomographic observation of corroded as-cast MZ3 and MZX30

### 5.3.1 As-cast MZ3

A Micro X-Ray CT is used to visualize the 3D morphology of corroded as-cast MZ3. Fig. 5.11 illustrates the 3D reconstructions measured from 1 h - corroded as-cast MZ3. As shown in Fig. 5.11 a), the localized corrosion is initiated in the Mg matrix (blue), and extended into the sample as indicated by the purple arrow. Fig. 5.11 b) shows respective views along specific cutting planes. In Fig. 5.11 b), the black regions represent the corroded Mg matrix (indicated by the purple arrow), while the remaining region of uncorroded matrix is evident. From the sections, it can be seen that corrosion of the Mg matrix occurs on the sites adjacent to the (α-Mg+MgZn) phases and develops deeply.

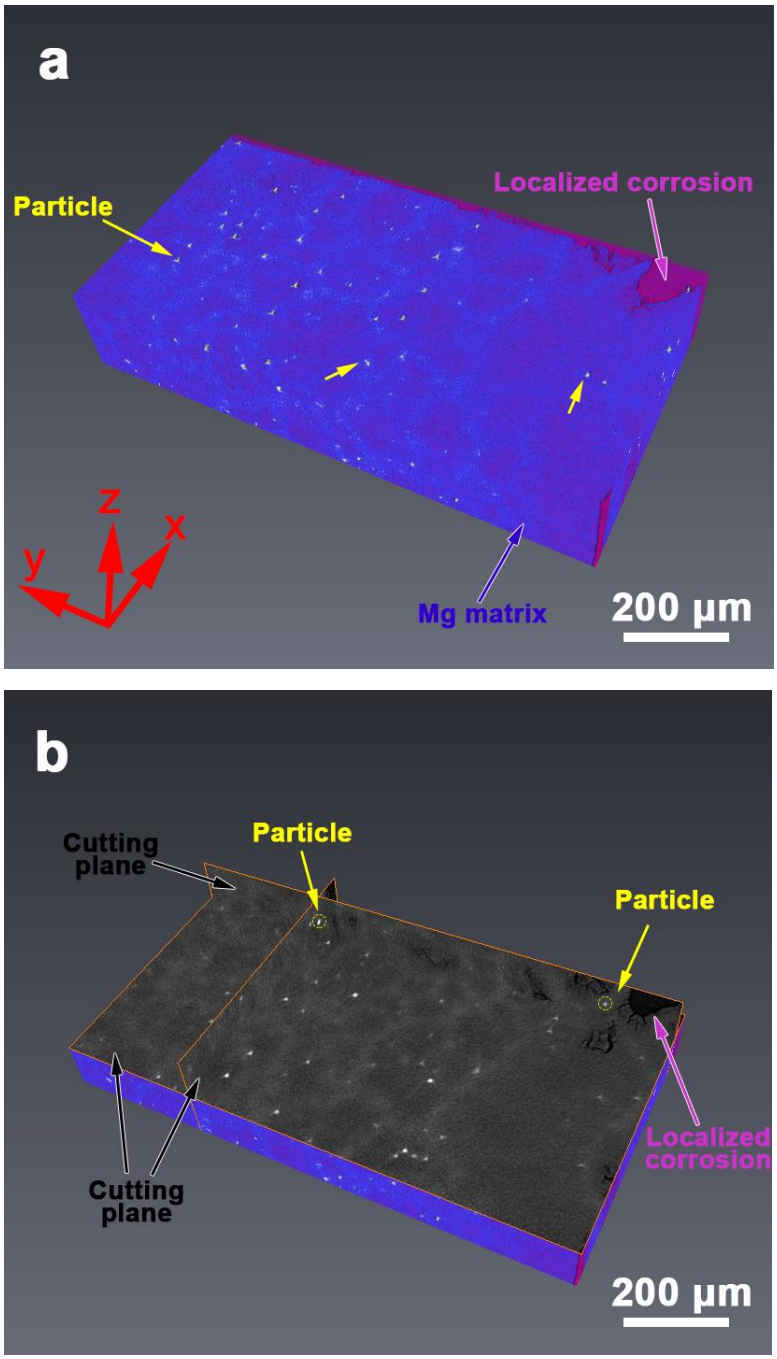


Fig. 5.11 (a) 3D reconstruction of as-cast MZ3 after 1 h immersion containing corrosion sites (in SBF and at 37 ℃). Blue refers to the Mg matrix, purple to the corroded region. White is the particle, indicated by yellow arrows. (b) The grey planes represent a specific serial of cutting planes through specimen.

### 5.3.2 As-cast MZX30

Fig. 5.12 shows the 3D reconstructions of corroded as-cast MZX30. Individual features are assigned a colour: red, blue, and white to the corroded region, Mg matrix and second phases, respectively. In Fig. 5.12 a), the morphology of the red volume clearly outlines the interfaces between the corroded region and the second phases (white), indicating that corrosion propagates preferentially. The corrosion penetrates into the interior of the sample, as indicated by the black region (Fig. 5.12 b)). It is evident that the curved regions of the corrosion front are near the ( α -Mg+$Ca_2Mg_6Zn_3$) phases, while the Mg matrix is attacked during immersion.

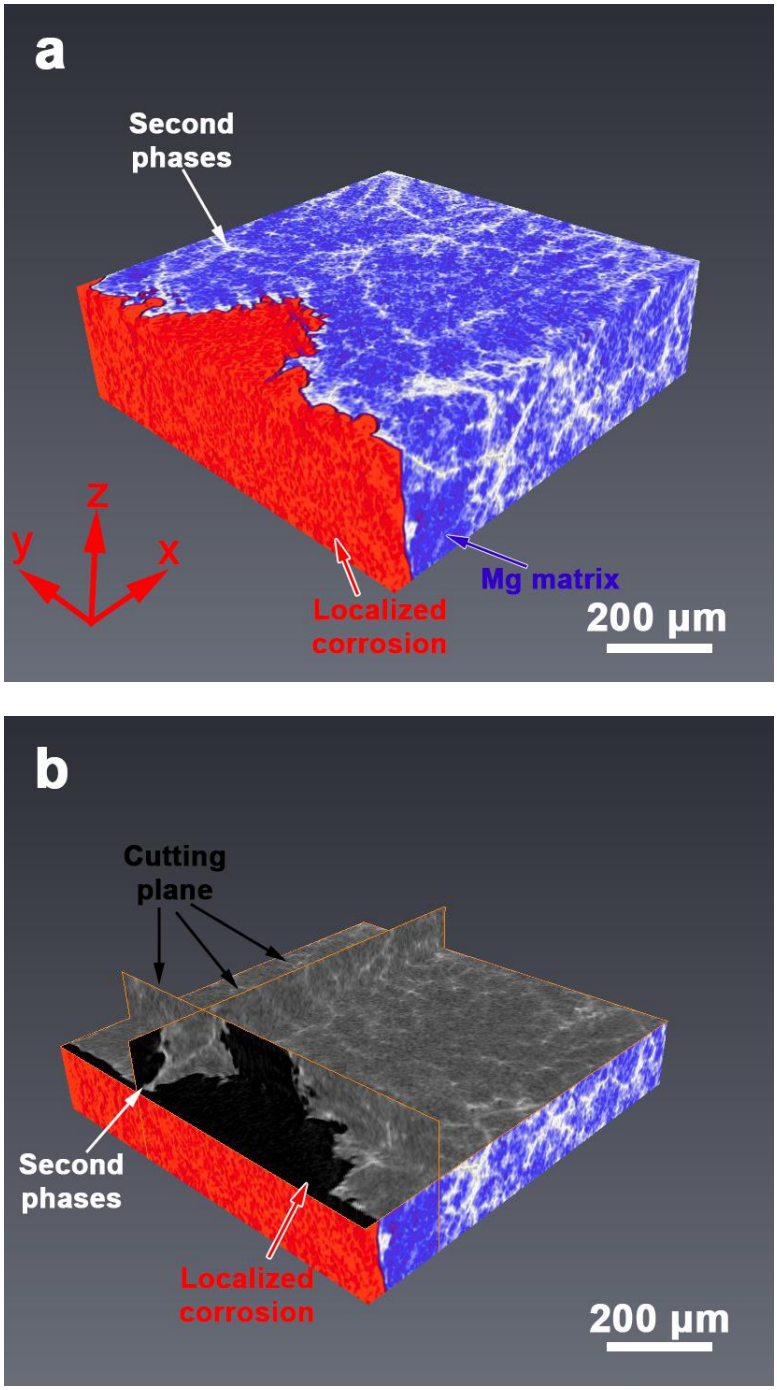


Fig. 5.12 (a) 3D reconstruction of as-cast MZX30 after 1 h immersion showing corrosion sites (in SBF and at 37 ℃). Blue is the Mg matrix. Red is the corroded region. White is the particle. (b) The grey planes represent a specific serial of cutting planes through specimen.

## 5.4 Bio-corrosion of aged MZ3 in SBF

### 5.4.1 Degradation rate measurement

The bio-corrosion rates of the aged samples are higher than that of 310 ℃/ 24 h solution-treated sample (3.05 ± 0.20 mL/cm$^2$/day). The variation of degradation rate with immersion time for aged samples is presented in Fig. 5.13. The bio-corrosion rate of the aged samples increases with increasing aging time. The degradation rate of the 10 h aged sample is slightly higher than that of the 25 h aged sample: 3.16 ± 0.14 and 3.23 ± 0.20 mL/cm$^2$/day, respectively. After aging for 50 h, the bio-corrosion rate shifts to a higher value (3.51 ± 0.10 mL/cm$^2$/day). The 96 h aged sample suffers more severe corrosion with a degradation rate of 4.08 ± 0.11 mL/cm$^2$/day. The sample with 144 h aging time shows the highest degradation rate, 4.65 ± 0.06 mL/cm$^2$/day, indicating the worst bio-corrosion resistance.

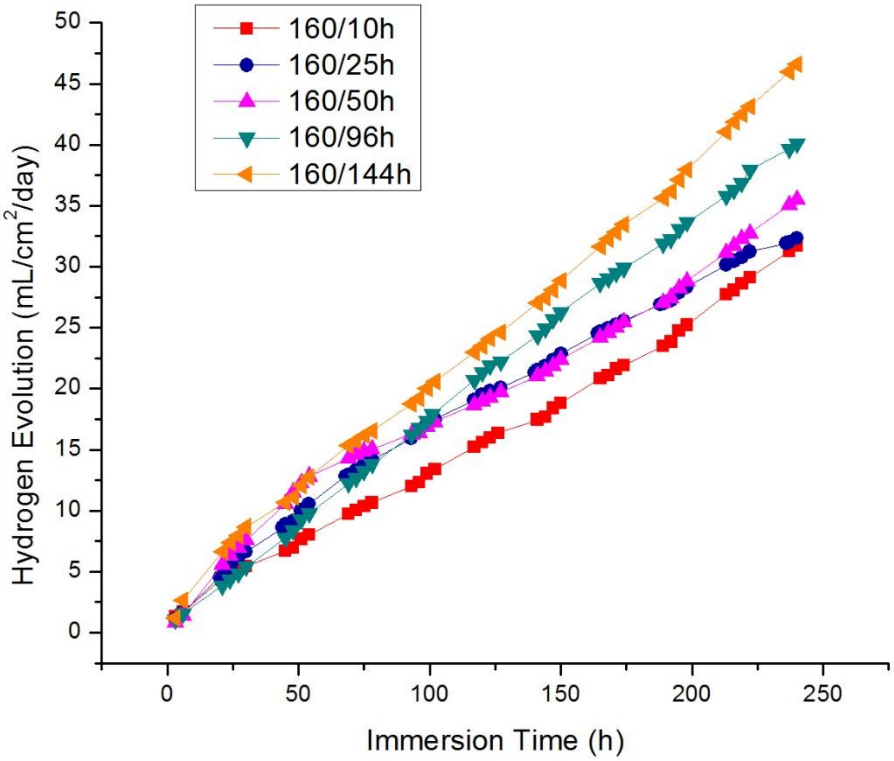


Fig. 5.13 Degradation rate of aged MZ3 immersed in SBF for 10 days at 37 ℃ as a function of ageing time at 160 ℃.

### 5.4.2 Corrosion morphology

Fig. 5.14 shows the surface morphology of the aged samples after exposure in SBF for 10 days. The surfaces are decorated with pits (as indicated by green arrows). Occasionally shallow corrosion pits can be observed in the 10 h aged-sample, while serious corrosion occurs all over the surfaces of the other samples. With prolonged aging time, the corrosion morphology becomes more faceted as indicated by the red double arrows, especially in the samples aged for 50 h, 96 h and 144 h, as shown in Figs. 5.14 c), d) and e). The rod-like precipitates are formed along a specific orientation during ageing: [0001]. The precipitates present different orientations in different grains and this results in differently orientated corrosion morphologies (see Fig. 5.14 f)).

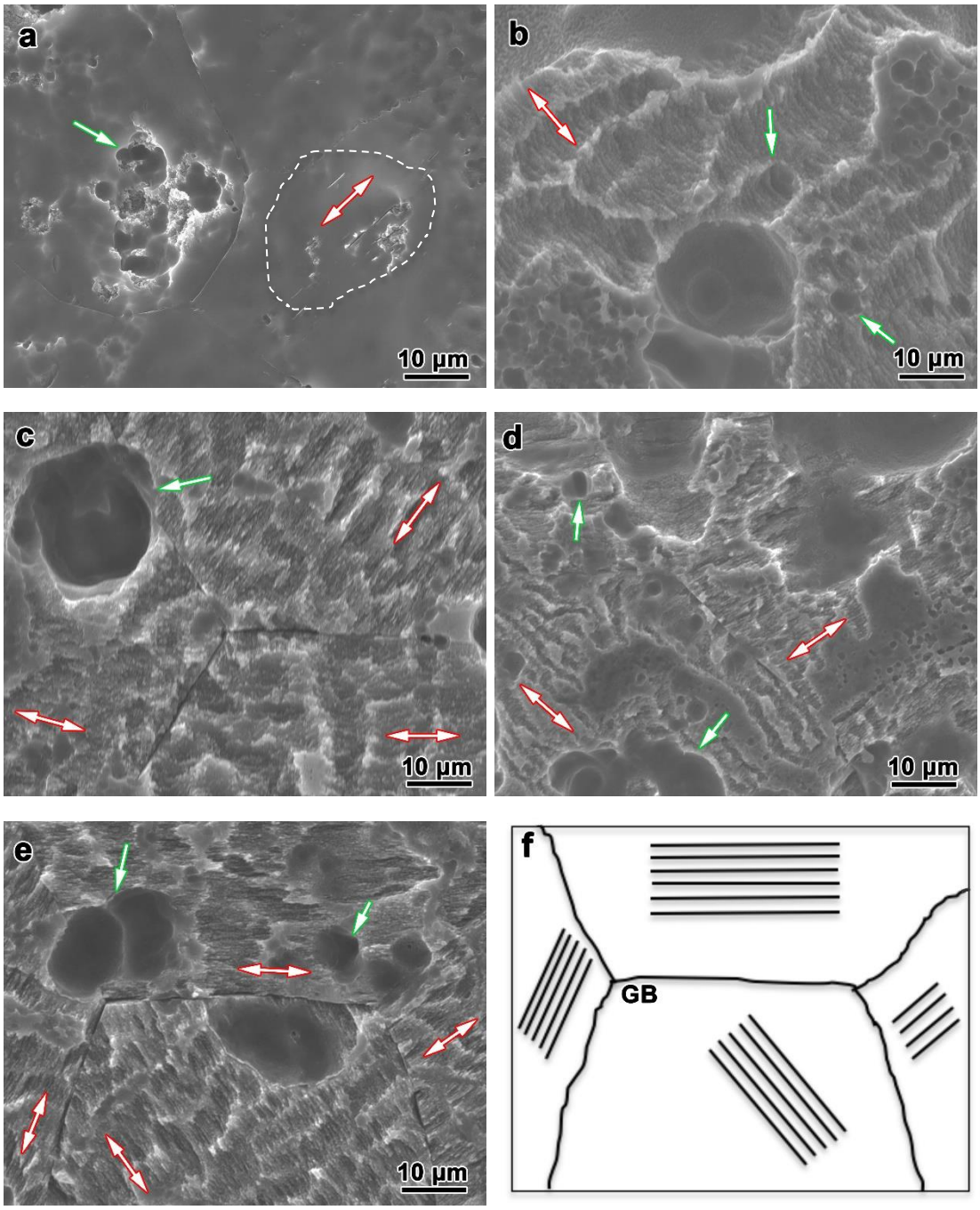


Fig. 5.14 SEM micrographs showing the surface morphology after immersion in SBF for 10 days at 37 ℃ of samples aged for (a) 10 h; (b) 25 h; (c) 50 h; (d) 96h and (e) 144 h. (f) is a schematic drawing of differently orientated corrosion morphologies (as illustrated in (e)).

### 5.4.3 Electrochemical tests

Fig. 5.15 shows the open circuit potential ($E_{ocp}$) - time curves for MZ3 immersed in SBF for 3600 s. As can be seen in Fig. 5.15, there is a tendency for the potential to fluctuate: the potential of the samples shifts in a nobler direction smoothly and gradually during the test and at the end of immersion, the potential tends to become constant. The increase in the open circuit potential is attributed to the gradually improved protection introduced by the corrosion product layer. The open circuit potential of the solution treated sample (310 ℃/24 h) is obviously more positive than that of the other samples. Furthermore, $E_{ocp}$ shifts towards more negative values with increasing ageing time.

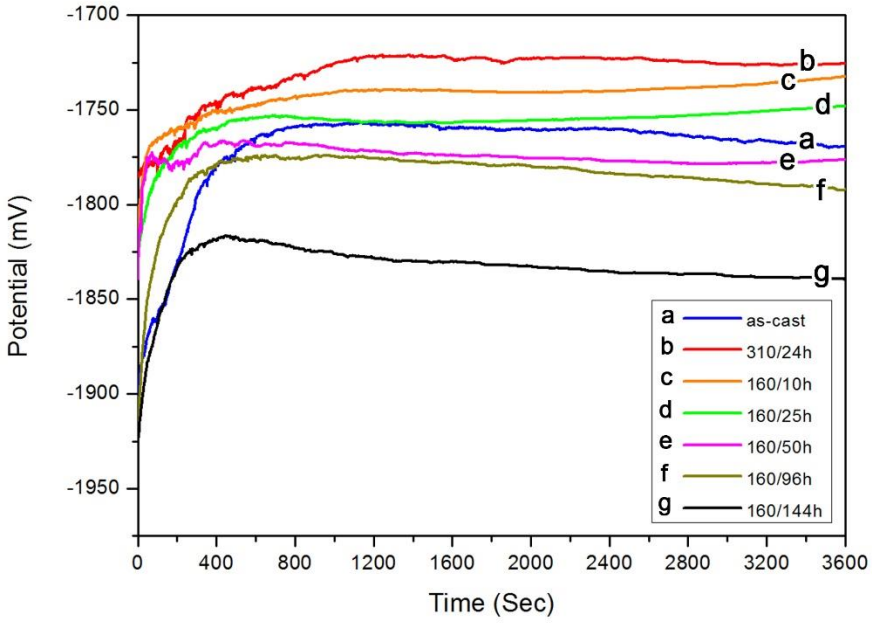


Fig. 5.15 The open circuit potential measured from MZ3 samples in SBF at 37 ℃.

The polarization curves appear in Fig. 5.16. Solution treatment (310 ℃/ 24 h ) gives rise to a shift in the polarization curve to a more positive potential and a lower cathodic current density. The improvement in the $E_{corr}$ of the solution-treated sample can be attributed to the dissolution of the (α-Mg +MgZn) eutectic phases, thus reducing the susceptibility to galvanic corrosion. $E_{corr}$ of aged samples decreases with

ageing time, from -1732.0 mV at 160 ℃/10 h to -1837.2 mV at 160 ℃/144 h. The cathodic current density of aged MZ3 tends to increase with ageing time: thus the sample after 144 h ageing has the highest cathodic current density. Generally, the cathodic polarization curve represents the hydrogen evolution reaction. The influence of heat treatment on the cathodic hydrogen evolution is clear.

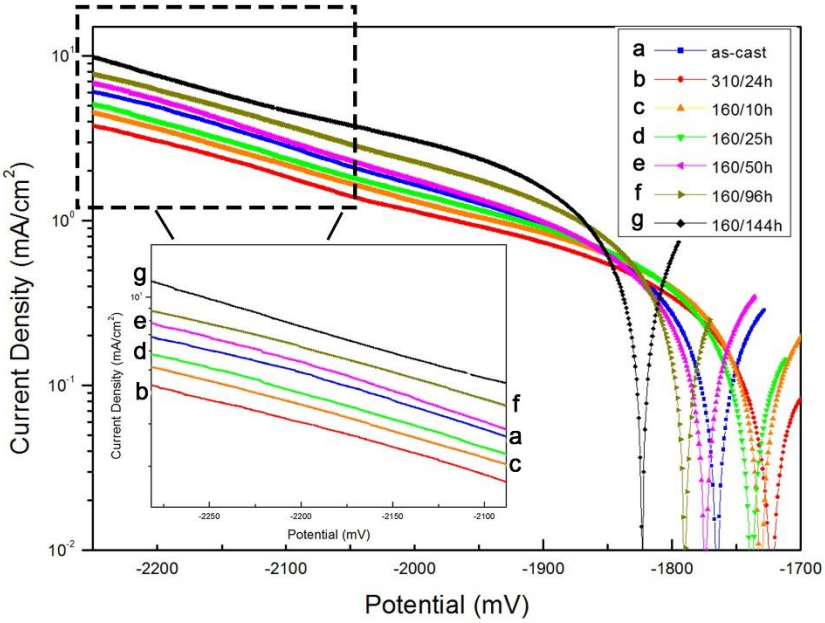


Fig. 5.16 Polarization curves obtained from MZ3 samples in SBF at 37 ℃. The inset is an enlarged view of the area highlighted in the dashed square showing the different current densities.

## 5.5 Bio-corrosion of solution-treated MZX30 in SBF

### 5.5.1 Degradation rate measurement

The degradation rates of MZX30 change after solution treatments, as shown in Fig. 5.17. In order to display the data clearly, the tolerances are not given in the figure (the maximum tolerance is ± 0.12). After solution treatment, the corrosion resistance is improved as compared with as-cast sample. It is found that the degradation rate of solution-treated MZX30 decreases in the order 310 ℃/24 h > 360 ℃/24 h > 450 ℃/48 h > 400 ℃/24 h > 450 ℃/24 h > 420 ℃/48 h> 420 ℃/24 h. The best corrosion

resistance is achieved in the 420℃/24 h, viz. 1.61 ± 0.09 mL/cm$^2$/day.

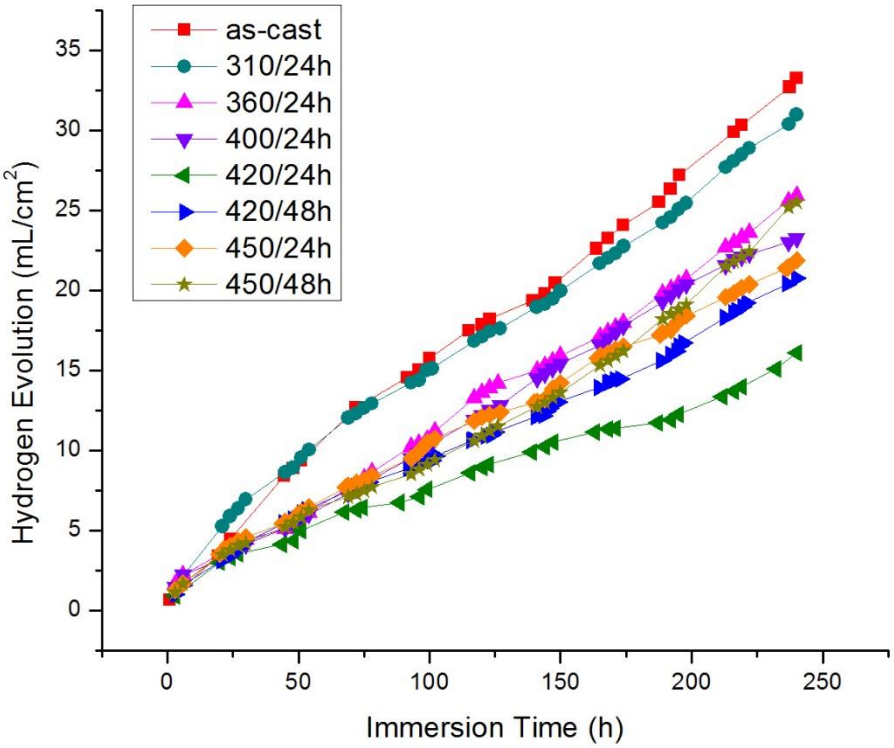


Fig. 5.17 Volume of hydrogen evolved for as-cast and solution treated MZX30 samples during 240 h immersion in SBF at 37 ℃.

### 5.5.2 Corrosion morphology

Fig. 5.18 shows the corrosion morphologies of MZX30 after 10 days' immersion. As can be seen in Fig. 5.18 a), the as-cast sample suffered obvious local corrosion attack (pitting), as indicated by the arrows. After solution treatment, MZX30 shows a smoother corroded surface with fewer pits, as can be seen in Figs. 5.18 b), c) and d). The 310 ℃/24 h treated sample displays less eutectic product and therefore the micro-galvanic corrosion weakens (Fig. 5.18 b)). The sample after 420 ℃/24 h exhibits a lower density and depth of corrosion pits (Fig. 5.18 e)) and shows the best corrosion resistance. In the 420 ℃/48 h, 450 ℃/24 h and 450 ℃/48 h samples (Figs. 5.18 f), g)

and h)), a number of tiny corrosion pits on the alloy surface are visible and more corrosion occurs of the Mg matrix.

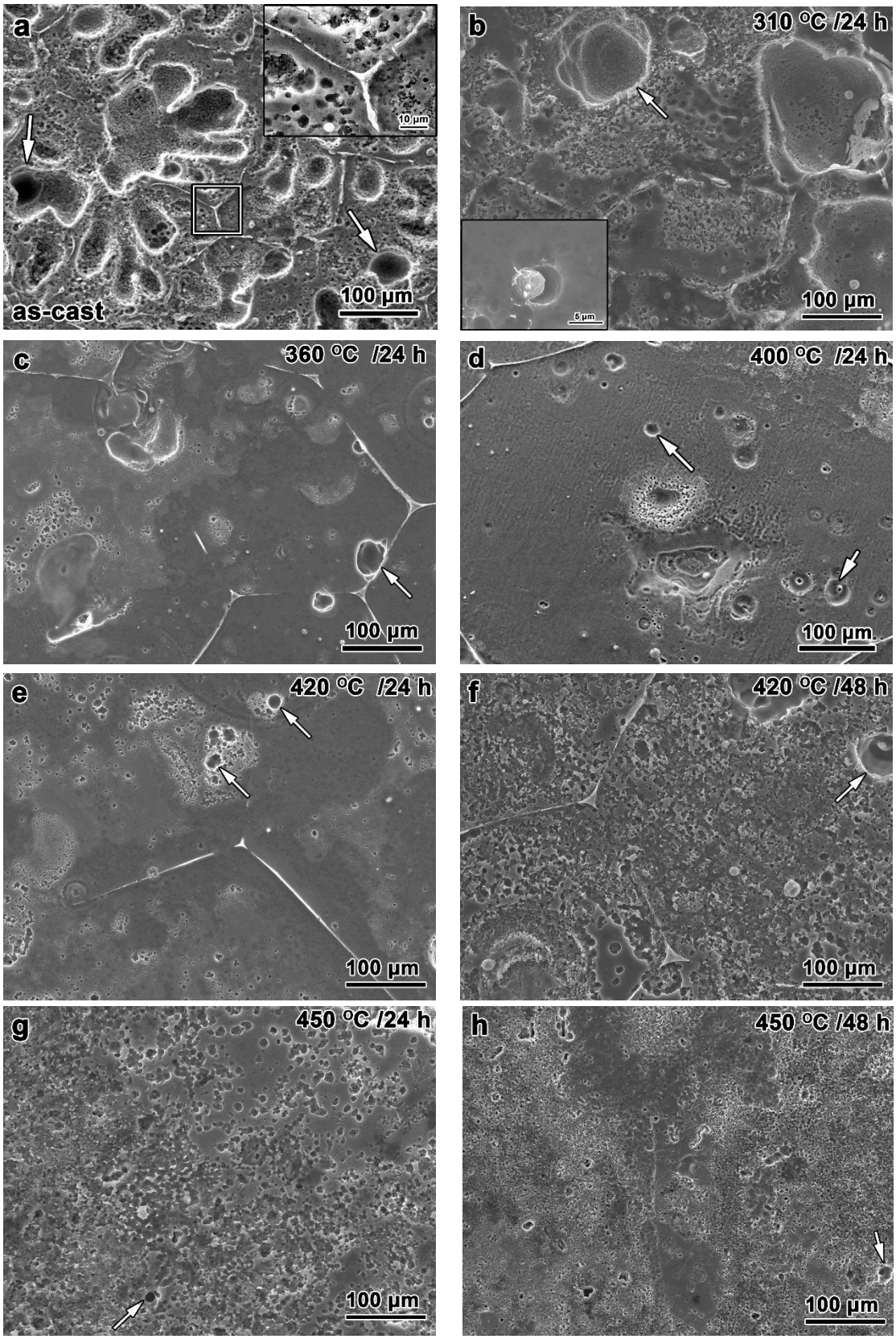

Fig. 5.18 SEM micrographs showing the corroded samples after 10 days' immersion and corrosion product removal.

### 5.5.3 Electrochemical tests

Fig. 5.19 shows the evolution of the open circuit potential ($E_{ocp}$) for MZX30 exposed to SBF solution for 3600 s. Each measurement series started immediately after immersion of the MZX30 sample in the SBF and reflects the initiation and propagation of corrosion. The curves display a similar tendency over the potential range: a sharp rise initially and then a very slow increase indicating the stable growth of a protective surface film. There was a significant positive shift in the magnitude of the $E_{ocp}$ in the solution-treated MZX30 samples. The 420 ℃/24 h treated sample has a more positive $E_{ocp}$ than the other samples.

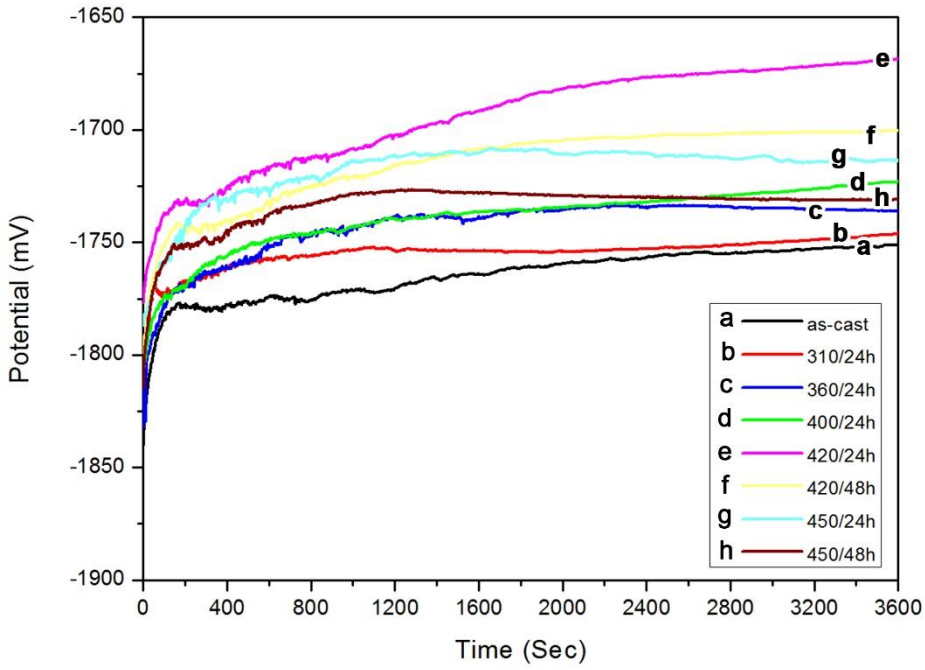


Fig. 5.19 Open circuit potential measurement of MZX30 in SBF at 37 ℃

Fig. 5.20 presents polarization curves for MZX30 in SBF at 37 ℃. The as-cast sample shows more negative value of $E_{corr}$ (-1751.4 mV) and a higher cathodic current

density. Noticeably, the cathodic currents from the polarization curves are lower for all solution-treated samples as compared with the as-cast sample. The highest $E_{corr}$ is achieved at 420 ℃/24 h treated sample (-1668.6 mV). The 420 ℃/24 h has the lowest cathodic current density, which suggests that the cathodic reaction resistance is improved by solution treatment. Generally, the cathodic polarization curve is assumed to represent the hydrogen evolution from magnesium: a lower polarization current indicates a lower hydrogen evolution rate. The ($\alpha$-Mg + $Ca_2Mg_6Zn_3$) product acts as a cathode during the micro-galvanic corrosion. More second phases thus cause more severe corrosion. This is consistent with the fact that the as-cast sample with the largest volume fraction of second phase shows the highest hydrogen evolution rate. The solution treatment leads to a reduction of the amount of second phase and thus reduces the corrosion rate.

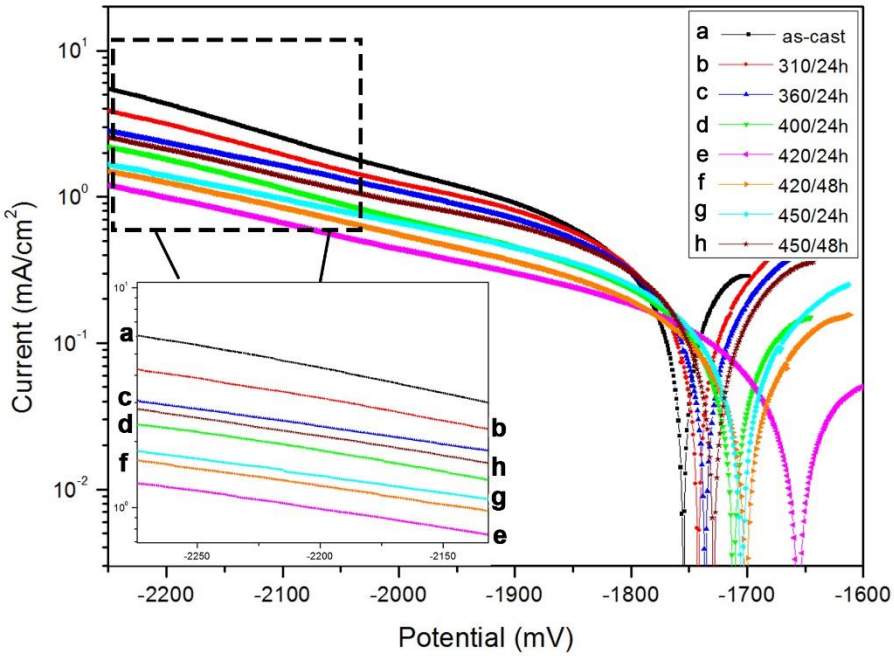


Fig. 5.20 Polarization curves of MZX30 in SBF at 37 ℃.

## 5.6 Discussion

### 5.6.1 Bio-corrosion of as-cast MZ3 and MZX30 in SBF

#### 5.6.1.1 Initial corrosion

After exposure of as-cast MZ3 and MZX30 to SBF, a volcano-like structure surrounding the second phases is formed. It is clearly evident that the localized corrosion occurs, as shown in Figs. 5.1 e) and f), 5.2, 5.4 c) and d) and 5.5. The Mg dissolution is accompanied by $H_2$ evolution. The $H_2$ evolution occurs in the form of bubbles. The steams of $H_2$ bubbles form at local sites on the Mg alloy surface where electrochemical reactions are taking place, leading to the peculiar structure with a round shape and often with a hole in the centre (Figs. 5.1 e), 5.2 a) and 5.5 a)). $H_2$ evolution is always from cathodic sites, thus the second phases within the spherical structure are the water reduction areas which act as cathodes.

Fig. 5.21 presents schematically the genesis of the volcano-like corrosion morphology in MZ3 and MZX30, showing the micro-galvanic corrosion process suffered by Mg alloys. The Mg dissolution results in the formation of Mg oxide products ($Mg(OH)_2$) on the Mg surface, according to the reaction 5.1 to 5.3.

Anodic reaction: $Mg \rightarrow Mg^{2+} + 2e^-$ (Equation 5.1)

Cathodic reaction: $2H_2O + 2e^- \rightarrow H_2 + 2OH^-$ (Equation 5.2)

Product formation: $Mg^{2+} + 2OH^- \rightarrow Mg(OH)_2$ (Equation 5.3)

According to the cathodic reaction, presented in Equation 5.2, the local pH increases because of the local generation of $OH^-$ ions. Consequently, corrosion products (such as $Mg(OH)_2$) are easily formed at areas adjacent to the second phases. The volcanic-like structure adjacent to the cathodic centre (second phases) is accumulated by the $Mg(OH)_2$. The formation of $Mg(OH)_2$ is stimulated by the cathodic water reduction

releasing $OH^-$ and by anodic Mg corrosion releasing $Mg^{2+}$.

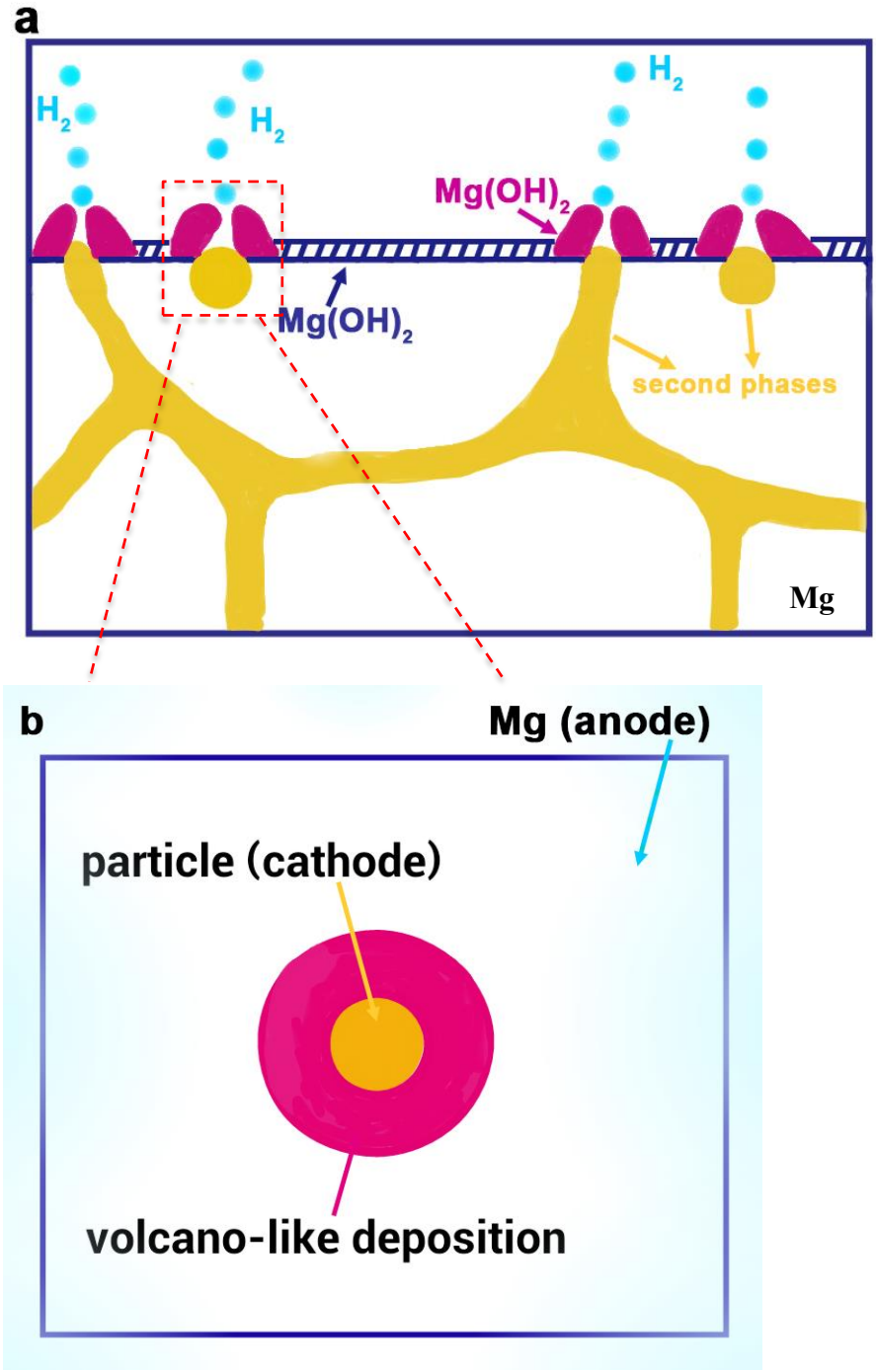


Fig. 5.21 Schematic of volcano-like corrosion mechanism of MZ3 and MZX30 exposed to SBF.

Besides the formation of $Mg(OH)_2$, other corrosion products are generated during exposure to the complex electrolyte (SBF). The corresponding EDX maps reveal

enrichment of O, Ca, P and Mg (Figs. 5.3 and 5.6). This is consistent with other studies [218, 219]. The presence of $OH^-$ near the Mg surface promotes the transformation of $HPO_4^{2-}$ in SBF solution into $PO_4^{3-}$. It is expected that $Ca^{2+}$ and $PO_4^{3-}$ ions diffuse from SBF solution towards the Mg surface and are incorporated in the corrosion layer $Mg(OH)_2$ as corrosion products. The solubility product constant of $Ca_5(PO_4)_3(OH)$ and $Mg_3(PO_4)_2$ is smaller than for $Mg(OH)_2$ [220]. Thermodynamically, $Ca_5(PO_4)_3(OH)$ and $Mg_3(PO_4)_2$ are more stable than $Mg(OH)_2$. Thus, the final products are $Mg(OH)_2$, $Ca_5(PO_4)_3(OH)$ and $Mg_3(PO_4)_2$ [218].

#### 5.6.1.2 Corrosion after 10 days' immersion

After 10 days' immersion, localized corrosion attack is obvious, as shown in Fig. 5.9. The aggressive $Cl^-$ ions in SBF promote destruction of the corrosion layer. Some protective film is dissolved and then fresh Mg substrate is exposed to the solution. Then, the reactions 5.1 to 5.3 will occur continually and result in deep dissolution. The corrosion continually attacks the area adjacent to the cathodic second phases, resulting in trenching of the Mg matrix around the particles. The microgalvanic corrosion is schematically illustrated in Fig. 5.22. Fig. 5.22 a) shows the particle (cathode) and Mg matrix (anode) with different potentials forming a galvanic couple. The local corrosion is initiated by the dissolution of the Mg matrix in the vicinity of the particles. With the process of corrosion, some small discontinuous particles may fall out by undermining [160]. Fig. 5.22 b) shows the final corrosion morphology.

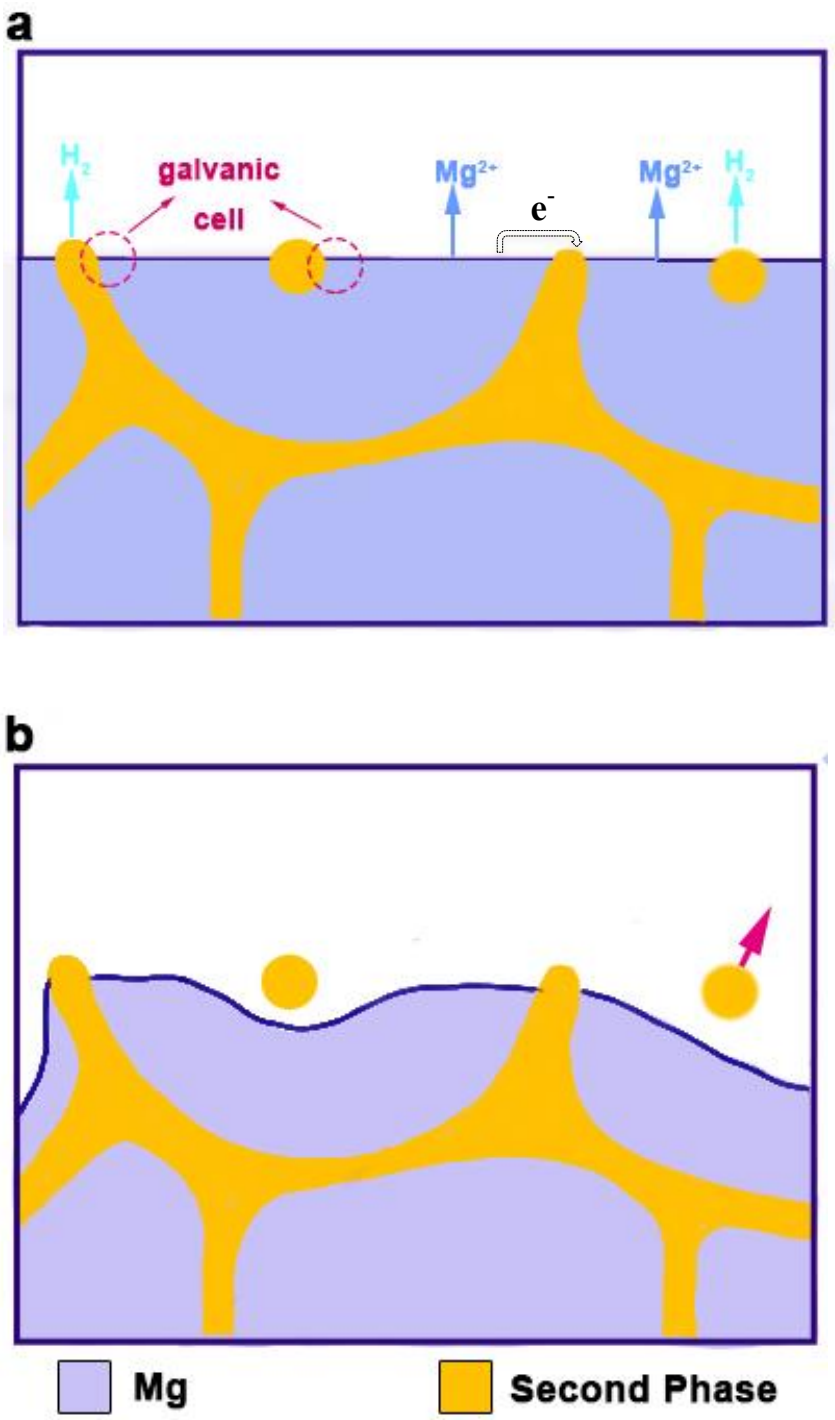


Fig. 5.22 Schematic of galvanic corrosion between the anodic Mg matrix and the cathodic second phases.

### 5.6.2 3D tomography study of corroded as-cast MZ3 and MZX30

The 3D observations allow the visualization of the relationship between corrosion

attack and alloy microstructure. Black corrosion areas adjacent to the particles are evident, as shown in Figs. 5.11 b) and 5.12 b), indicating that corrosion occurs at the cathodic constituents and that the surrounding Mg matrix is dissolved. It is consistent with the 2D observations (Figs. 5.2 c) and d), 5.5 c) and d) and 5.10). In Fig. 5.12 b), a number of (α-Mg + $Ca_2Mg_6Zn_3$) second phases is buried beneath the MZX30 sample surface, and the Mg matrix at the periphery of second phases is attacked during immersion. Song proposed that β phase in AZ91 alloy can act as a galvanic cathode or barrier: finely and continuously distributed β phase serves as a corrosion barrier and inhibits corrosion; otherwise, β phase promotes corrosion [14, 160]. In as-cast MZ3 and MZX30, the second phases act as micro-galvanic cathodes rather than as a corrosion barrier. The (α-Mg + MgZn) phases are distributed randomly within Mg and with a small size (~5 μm), which cannot prevent corrosion. For as-cast MZX30, (α-Mg + $Ca_2Mg_6Zn_3$) phases with net-work and spherical shapes are largely distributed across the Mg matrix resulting in many micro-galvanic couples. Consequently, the dissolution of Mg is promoted.

### 5.6.3 Relationship between the microstructural characterisation and degradation rate in aged MZ3

The degradation rate of MZ3 after different heat treatments is associated with the microstructure. In the as-cast sample, spherical eutectic nodules (α-Mg + MgZn) are dispersed. After solution treatment (310 ℃/ 24 h) the second phases dissolve. The corrosion resistance of the solution-treated sample is thus higher than that of the as-cast sample. This is because micro-galvanic coupling has built up between the second phase and the matrix. The dissolution of the eutectic product during the solution treatment is evidently beneficial to the corrosion resistance.

The corrosion rate and corrosion morphology of MZ3 change with ageing time. The corrosion rate of aged MZ3 increases compared with that in the solution-treated sample. Noticeably, the parallel corrosion trenches with particular orientation are

evident, as illustrated in Fig. 5.14. A similar corrosion morphology has been observed in other aged Mg alloys [221, 222]. The proposed corrosion mechanism in the aged MZ3 is shown schematically in Fig. 5.23. The precipitates formed along a specific orientation during the ageing. In MZ3, a large number of rod-like $\beta_1'$ precipitates grow along $[0001]_{Mg}$. In this corrosion mechanism, only $\beta_1'$ is considered because few $\beta_2'$ are observed in aged samples which therefore can only have a minimal influence on the corrosion. When the samples are immersed in SBF, micro-galvanic corrosion cells form between the fine precipitates and the Mg matrix; hence, the Mg matrix dissolves and the fine precipitates are undermined and fall from the surface which then forms these parallel filament-like trenches with different orientations in different grains.

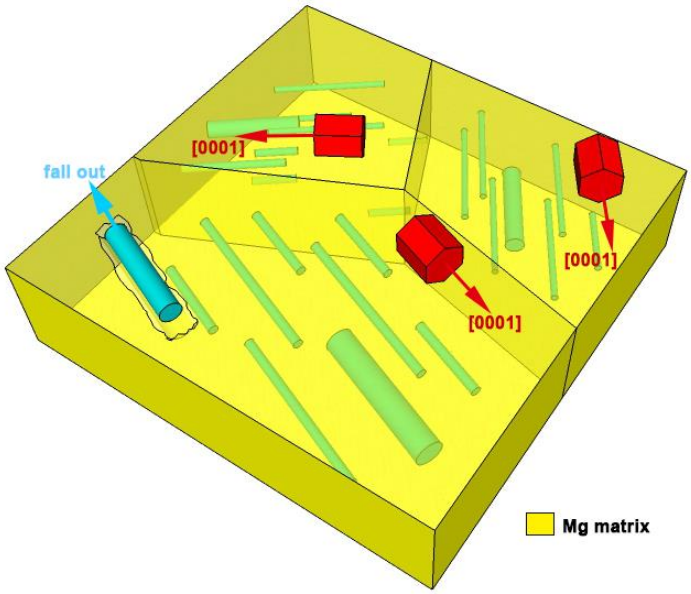


Fig. 5.23 A schematic drawing of the precipitates and the observed corrosion morphology in the aged MZ3. A hexagon is included in each grain to indicate the crystallographic orientation and rods are used to represent the fine precipitates.

Upon ageing, fine precipitates form and the quantity increases with increasing ageing time (as indicated in Fig. 4.29, see Chapter 4). The degradation rate of the aged samples is sensitive to the volume fraction of fine precipitates. In Fig. 5.24, a linear regression suggests that as the precipitate volume fraction increases the degradation

rate increases. This is again attributed to micro-galvanic couples between the fine precipitates and the matrix. The fine precipitates are nobler than the α-Mg. Therefore, the fine precipitates act as micro-cathodes while the surrounding α-Mg matrix acts as the anode. Furthermore, the precipitates are enriched in Zn after ageing. The Mg matrix therefore becomes depleted of Zn because of the precipitation and thus is more easily attacked.

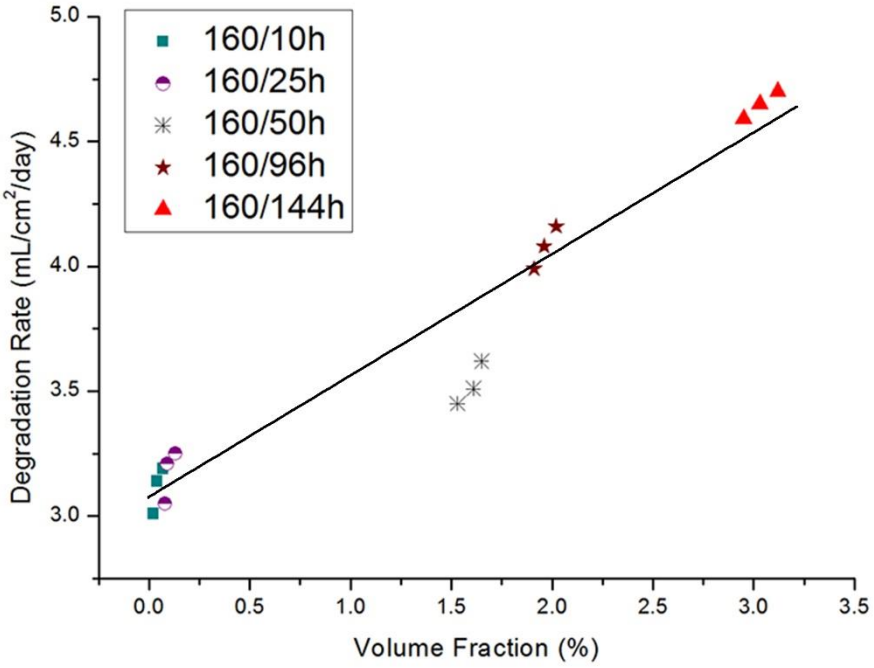


Fig. 5.24 The relationship between the volume fraction of fine precipitates and the degradation rate in the aged MZ3.

### 5.6.4 Relationship between microstructure and degradation rate in heat-treated MZX30

Fig. 5.18 presents the corrosion morphologies of the as-cast and solution-treated MZX30 alloys. The microstructure of the as-cast MZX30 displays more (α-Mg+$Ca_2Mg_6Zn_3$) and therefore micro-galvanic corrosion is common. The MZX30 after solution treatment presents a smoother corrosion morphology, indicating less corrosion. The volume fraction of second phases and the grain size in the alloy change

with solution treatment, as summarised in Table 4.7 (see Chapter 4). Fig. 5.25 illustrates the variation of the degradation rate with second phase volume fraction and grain size. Each data point presents a measurement of the volume fraction of second phase, grain size and the corresponding degradation rate. Fig. 5.25 a) is a plot which combines the effect of both the grain size and the second phase volume fraction. Tracking the curve in Fig. 5.25 b), the bio-corrosion rate decreases as second phase volume fraction decreases, from the as-cast sample to the 420 ℃/24 h sample. The highest corrosion rate is observed in the as-cast MZX30 with a relatively high amount of second phase, $2.4 \pm 0.4$ %. The 420 ℃/24 h sample has the lowest bio-corrosion rate (1.61 mL/cm$^2$/day) on account of the low second phase fraction (0.73 %). With increasing treating temperature and processing time (420 ℃/48 h, 450 ℃/24 h and 450 ℃/48 h), the degradation rate increases. The dependence of average degradation rate on grain size is displayed as a valley shaped relationship (Fig. 5.25 c)). It is noted that bio-corrosion rate increases with increasing grain size at the higher treatment temperatures (after 420 ℃/24 h).

The bio-corrosion rate of this alloy is a function of its grain size and the volume fraction of second phase. The amount of secondary phase has been reported to have a marked impact on the corrosion rate. $i_{corr}$ increases with an increased density of intermetallic particles [223]. Obviously, the grain boundary secondary phase observed in the current alloys also causes severe galvanic corrosion attack. A homogeneous microstructure without secondary phase is beneficial to corrosion resistance [223].

Grain boundaries possess unique structural characteristics with distinct physical and chemical properties and affect the corrosion performance of materials. Grain refinement introduces more grain boundaries. It is expected that more grain boundaries will cause to deteriorate the corrosion resistance, because grain boundaries are more chemically active and constitute local galvanic couples between the anodic grain boundary and the cathodic grain interior. However, the bio-corrosion rate increases with increasing grain size in the alloy at the higher treatment temperatures

(after 420 ℃/24 h). It has also been reported [165, 224, 225] that small grain size is beneficial to the corrosion resistance. There are several reasons why this could occur. Firstly, the corrosion behaviour is more homogeneous in a fine-grained microstructure because segregation is minimized. Secondly, Mg has a Pilling-Bedworth ratio (the ratio of molar volume of the elementary unit cell of magnesium oxide to that of Mg) lower than 1 (0.81), unlike aluminium (1.2) and stainless steel (2). The formation of oxide leads to a free volume mismatch between the oxide and Mg substrate and therefore increases the tendency for oxide film cracking [226]. A fine grain structure with increased grain boundary area reduces the structural discontinuity between the oxide layer and Mg and compensates the mismatch, thus decreases the degree of oxide cracking [165, 223, 227]. It might therefore be expected that a fine grain structure is more corrosion resistant in Mg alloys.

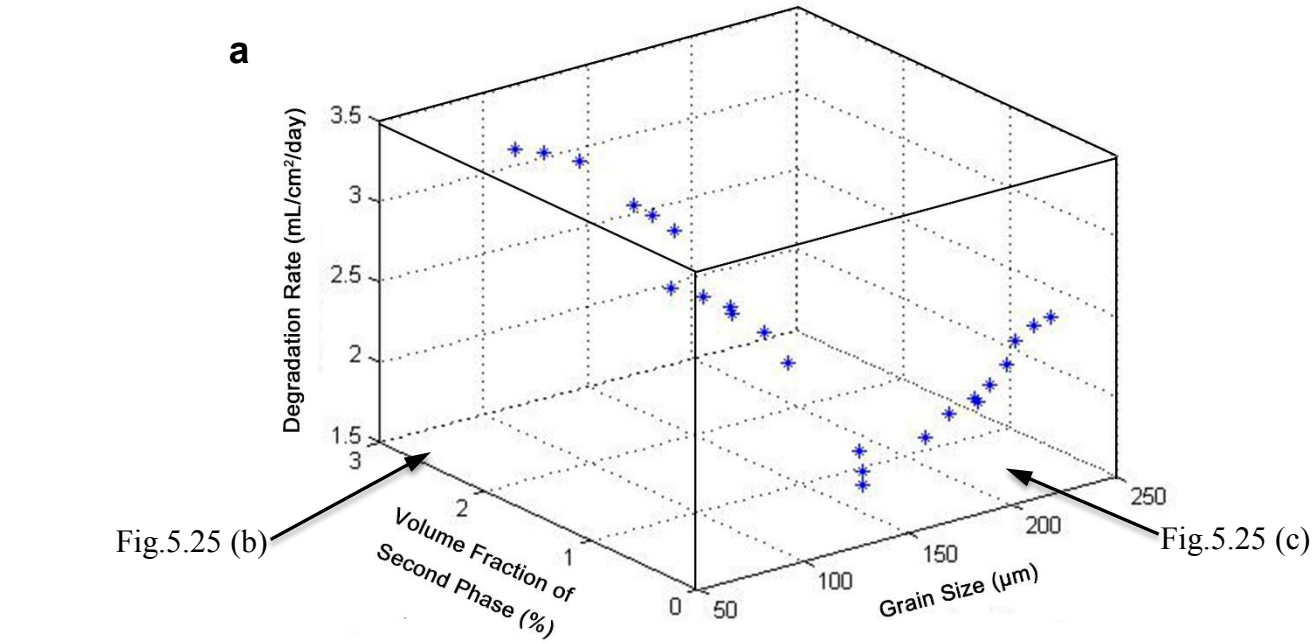
a
Degradation Rate (mL/cm²/day)
3.5
3
2.5
2
1.5
3
2
1
0
Volume Fraction of Second Phase (%)
50
100
150
200
250
Grain Size (μm)
Fig.5.25 (b)
Fig.5.25 (c)

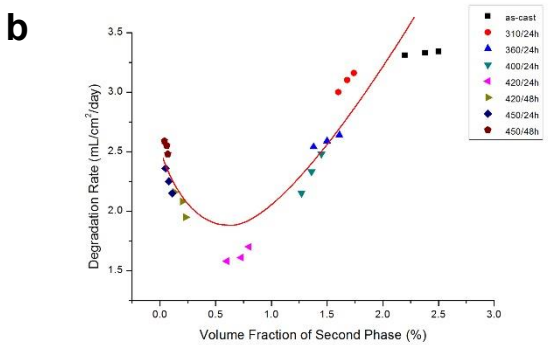
b
Degradation Rate (mL/cm²/day)
Volume Fraction of Second Phase (%)
as-cast
310/24h
360/24h
400/24h
420/24h
420/48h
450/24h
450/48h

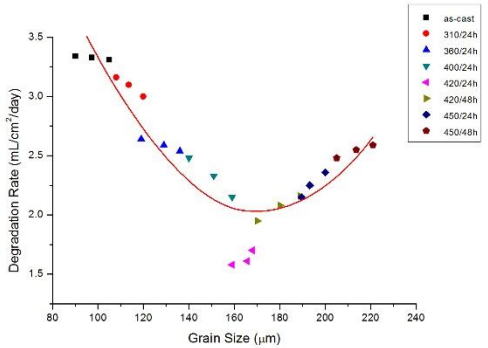
c
Degradation Rate (mL/cm²/day)
Grain Size (μm)
as-cast
310/24h
360/24h
400/24h
420/24h
420/48h
450/24h
450/48h

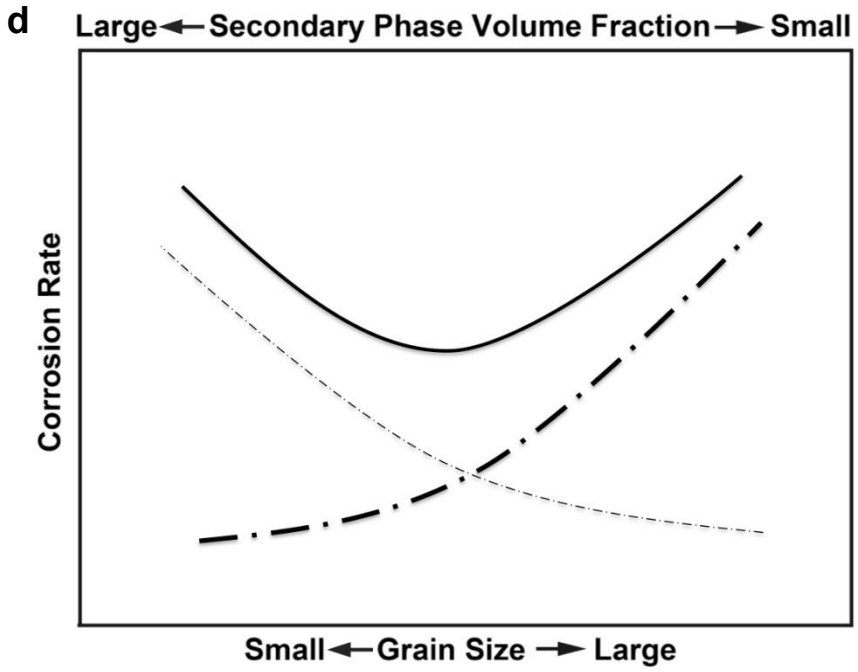


Fig. 5.25 (a) Degradation rate of the MZX30 samples in SBF against the second phase volume fraction and the grain size after different heat treatments; (b) and (c) The projected traces indicating the relationship between the volume fraction of second phase and degradation rate, and the relationship between the grain size and degradation rate, respectively; (d) Schematic drawing showing that the corrosion rate decreases with decreasing secondary phase content (thin chain-dashed curve) and increases with grain size (thick chain-dashed curve) and the overall effect on the corrosion rate (indicated by the solid curve).

As shown schematically in Fig. 5.25 d), when the grain size and the second phase volume faction are both taken into consideration, the combined effect could be like that indicated by the solid curve. Although the as-cast sample has the smallest grain size in the current study, the second phase volume fraction is the largest which has clearly overshadowed the beneficial effect of fine grain size on the corrosion performance. While the high temperature solution treated sample has the lowest secondary phase volume fraction, the large grain size of the alloy dominates, such that the corrosion rate is high. The best corrosion performance can be obtained with a

balanced grain size and secondary phase volume fraction.

## 5.7 Conclusions

1. The localized corrosion is observed in both as-cast MZ3 and MZX30. There are prominent volcano-shaped corrosion pits indicated by the accumulation of corrosion products locally. The volcano-shaped structure is formed around central second phases which act as cathodes.

2. Corrosion initiates in the anodically active Mg matrix in both as-cast MZ3 and MZX30. A micro-galvanic cell is built up between the second phases and Mg matrix and thus promotes the dissolution of Mg.

3. The corrosion resistance of the solution-treated MZ3 is better than that of other MZ3 specimens. The absence of (α-Mg + MgZn) phases reduces micro-galvanic corrosion. Nano-scale precipitates formed during ageing decrease the corrosion resistance. The increase in bio-corrosion rate with ageing time appears to be monotonic. With increasing ageing time, Mg alloys display worse corrosion resistance because of the fine precipitates.

4. A specific corrosion morphology occurs in aged MZ3: parallel filament-like trenches which mirror the growth direction of the precipitates. The size, distribution and volume fraction of the precipitates are important parameters that should be considered in order to tailor the microstructure and performance of magnesium alloys for different bio-medical applications.

5. The degradation rate of MZX30 changes with the heat treatment parameters. The volume fraction of second phases and grain size are both key factors controlling the bio-corrosion rate of the alloy. The sample with the smallest grain size but the

largest second phase volume fraction has the largest corrosion rate, because the second phase causes the galvanic corrosion which overshadows the beneficial effect of fine grain size. The sample with the lowest second phase volume fraction but the largest grain size also has a high corrosion rate is because the large grain size dominates (corrosion rate increases as grain size). The minimum corrosion rate was observed in the alloy heat-treated at 420 $^{o}$C for 24 h which has a balanced second phase volume fraction and grain size.

# Chapter 6 Surface modification of Mg-3Zn(-0.3Ca) alloys

## 6.1 Morphology of HA coating

The SEM micrographs of the hydroxyapatite (HA) coated samples before and after alkaline treatment are shown in Fig. 6.1. The morphology of the coated sample surfaces after potentiostatic deposition are displayed in Figs. 6.1 a), c), e) and g) (left hand). All the as-deposited samples show dandelion-like aggregates of plate-like crystals (marked by circles). After the final alkaline treatment, all the coated samples still show these dandelion-like features, as illustrated in Figs. 6.1 b), d), f) and h). At high magnification, a similar morphology is observed in both the as-deposited and post-treated samples (Figs. 6.1 g) and h)). This is because the nucleation and growth of HA depends on the increased supersaturation during the alkaline treatment. Consequently, the dandelion-like features are inherited. The HA coating is not greatly compact and presents a uniform morphology with radiating plate-shaped crystals. This loose morphology is beneficial to the bone tissue, allowing it to infiltrate the implant. It is helpful to the bone healing because the inorganic apatite in bone has a plate-like morphology [228].

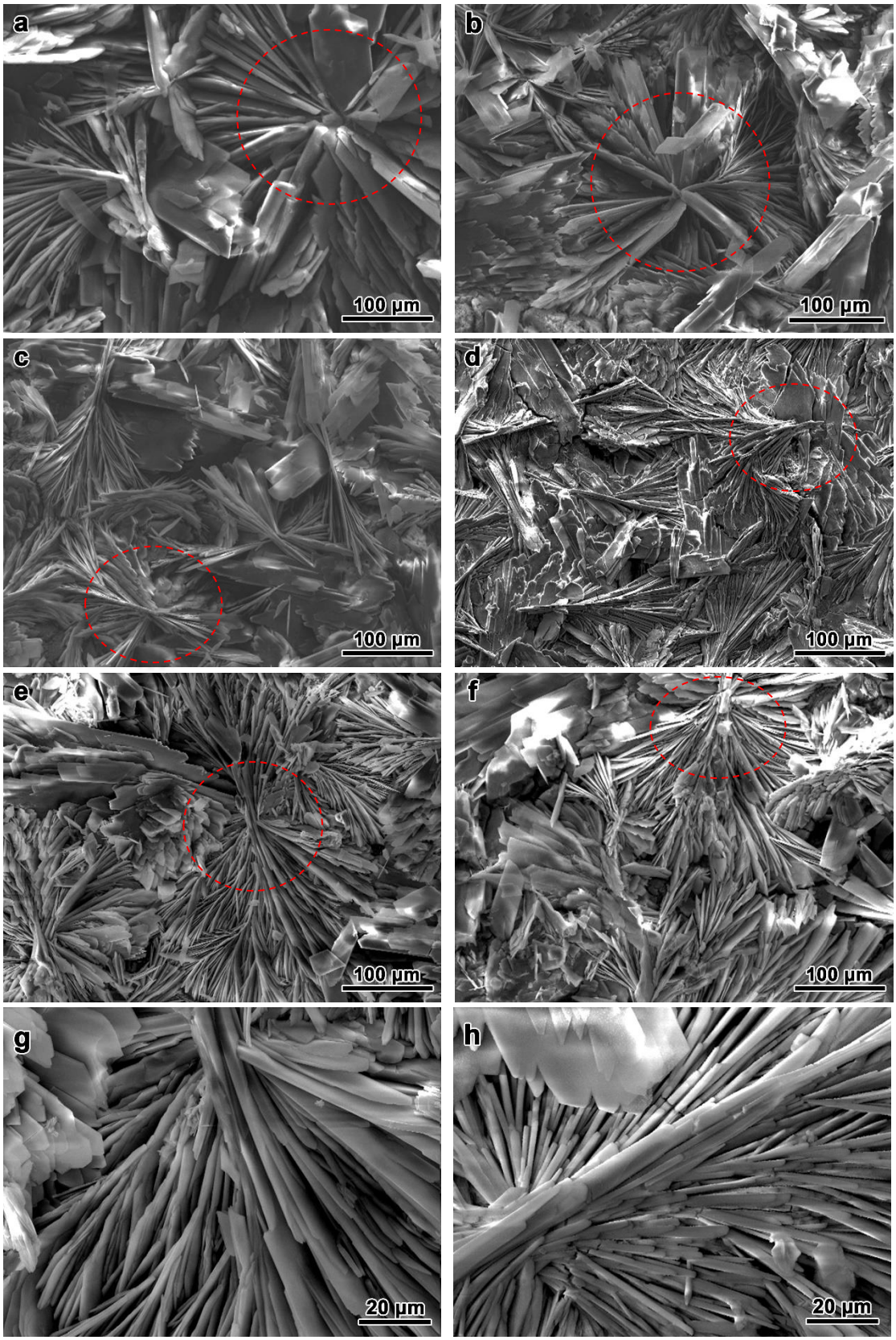


Fig. 6.1 SEM images of HA coated samples: (a) and (b) Mg; (c) and (d) as-cast MZ3; (e) and (f) as-cast MZX30; (g) and (h) the high magnification of flake-like features. (a), (c), (e) and (g) images (left hand) show the morphology of the as-deposited

samples (before final alkaline treatment). (b), (d), (f) and (h) (right hand) show the morphology of the post-treated samples.

## 6.2 Composition of HA coating

The surface compositions of the as-deposited and post-treated samples obtained by EDX are summarized in Table 6.1. The average Ca/P ratio of the as-deposited samples are 1.06, 0.96 and 1.00, which are very close to the theoretical value 1 of dicalcium phosphate dehydrate DCPD ($CaHPO_4 \cdot 2H_2O$). Thus, the as-deposited coating may indeed be DCPD which is a precursor to hydroxyapatite HA. In Table 6.1, the calculated Ca/P ratios of post-treated samples are about 1.62, 1.67 and 1.63, respectively. Theoretically, the Ca/P of hydroxyapatite HA ($Ca_5(PO_4)_3 \cdot (OH)$) is 1.67. The coating is thus probably HA after the post alkaline treatment.

Table 6.1 Surface composition of as-deposited and post-treated samples.

| Specimen | | Ca/P atom ratio |
|---|---|---|
| **As-deposited** | **Mg** | $1.06 \pm 0.08$ |
| | **MZ3** | $0.96 \pm 0.07$ |
| | **MZX30** | $1.00 \pm 0.04$ |
| **Post-treated** | **Mg** | $1.62 \pm 0.09$ |
| | **MZ3** | $1.67 \pm 0.06$ |
| | **MZX30** | $1.63 \pm 0.08$ |

Fig. 6.2 shows a SEM image and EDX linear analysis of a cross-section through post-treated Mg. The elemental distribution across the HA coating illustrates that Ca, P and O are strongly located in the coating layer.

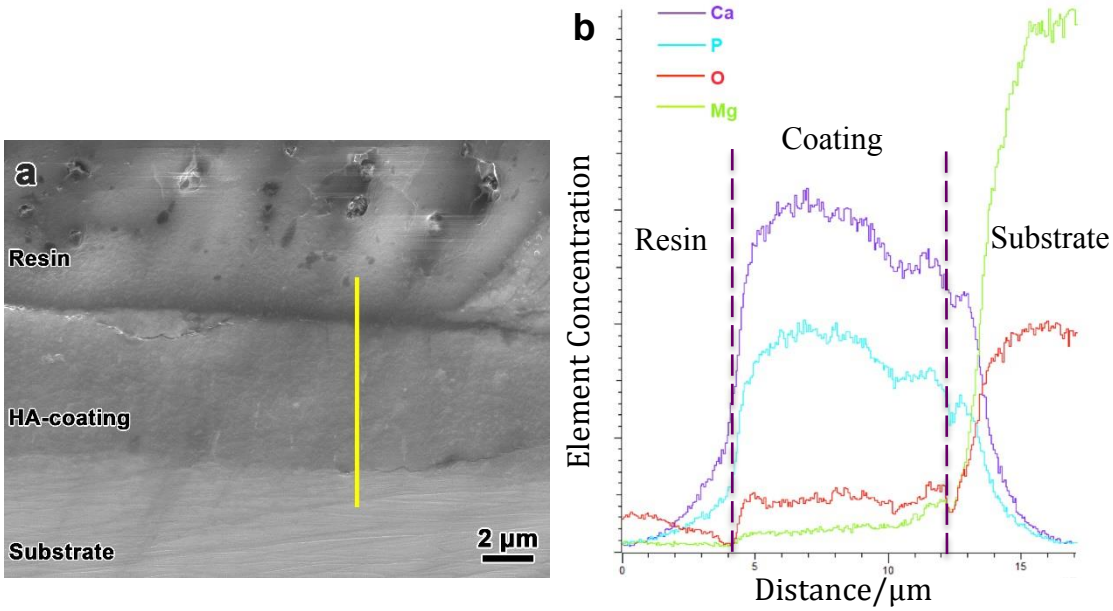


Fig. 6.2 SEM image and EDX traces across a cross-section through post-treated Mg.

Fig. 6.3 shows the X-ray spectra for the as-deposited and post-treated samples. Obviously, the main peaks are ascribed to the DCPD in Fig. 6.3 a) and HA in Fig. 6.3 b), individually. Thus, it is clear that after alkaline treatment, DCPD ($CaHPO_4 \cdot 2H_2O$) (PDF reference code: 00-009-0077) converts to HA ($Ca_5(PO_4)_3 \cdot (OH)$) (PDF reference code: 00-024-0033). The crystal structures of DCPD and HA are hexagonal and monoclinic, respectively. The crystallographic parameters of the crystals are detailed in Table. 6.2.

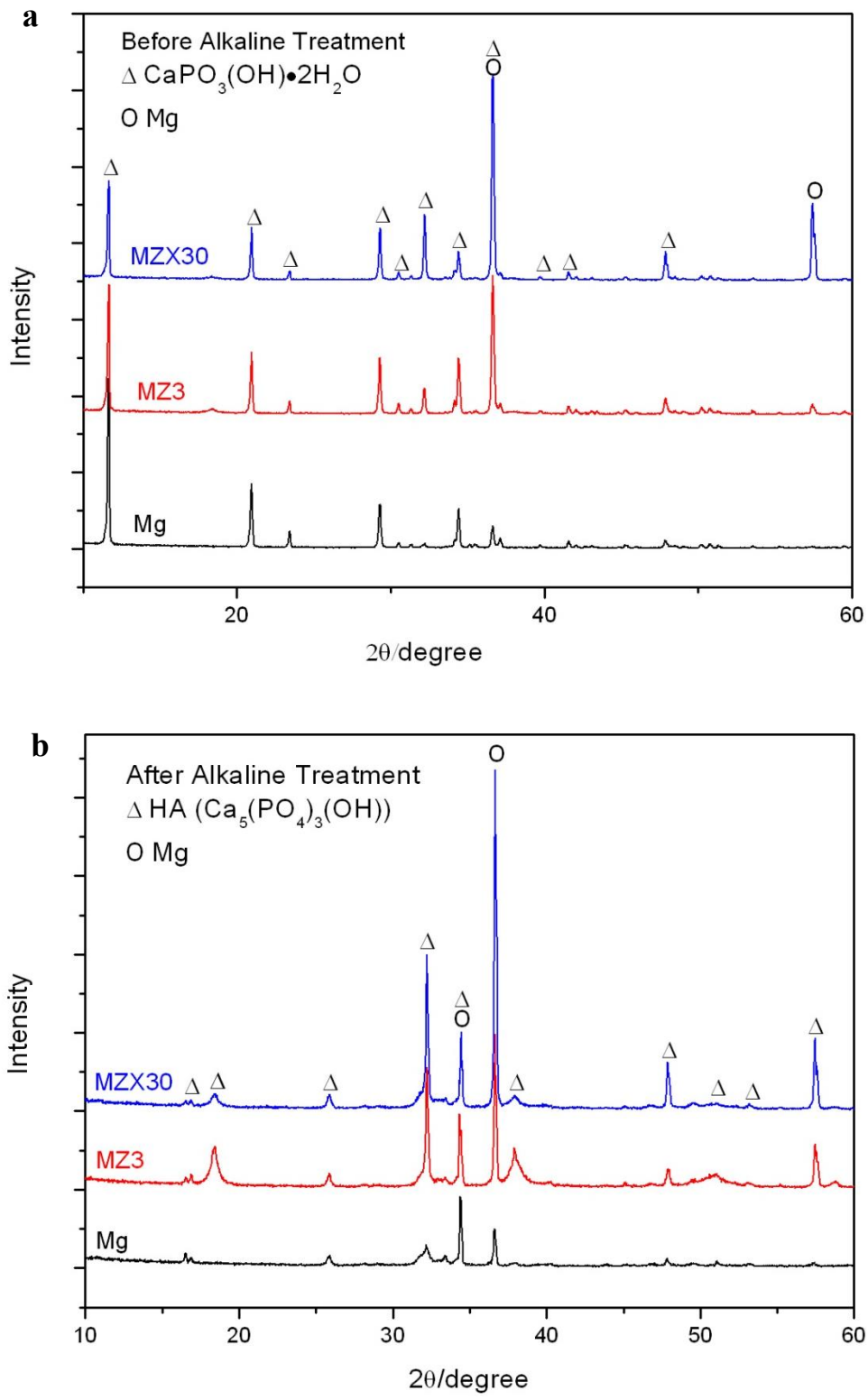


Fig. 6.3 X-ray spectra of coated samples (a) before and (b) after alkaline treatment.

Table 6.2 Crystallographic parameters of coating crystals.

| Compound | Space group | Lattice parameter (Å) | | | | | |
|---|---|---|---|---|---|---|---|
| | | a | b | c | α | β | γ |
| **$CaHPO_4 \cdot 2H_2O$ (DCPD)** | Cc | 6.3630 | 15.1900 | 5.8150 | 90 | 118 | 90 |
| **$Ca_5(PO_4)_3 \cdot (OH)$ (HA)** | P63/m | 9.4320 | 9.4320 | 6.8810 | 90 | 90 | 120 |

### 6.3 Surface characterisation

The thickness of the HA-coating is evident from the cross-section morphology (Fig. 6.4). The coating thickness of Mg, MZ3 and MZX30 is around 10 μm, 8 μm and 7 μm, respectively.

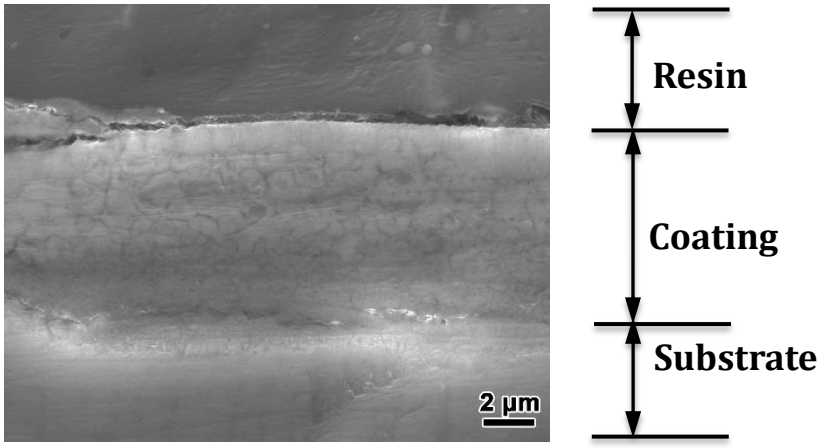


Fig. 6.4 SEM cross-section of HA-coated sample.

The crystal size of the HA is calculated using Scherrer's formula:

$$\tau_{hkl} = \frac{0.9\lambda}{B\cos\theta} \qquad \text{(Equation 6.1)}$$

where λ is the X-ray wavelength, B is the full-width half maximum (FWHM) and θ is the Bragg angle. In this study, λ is equal to 0.1548 nm because Cu $K_\alpha$ radiation is

used. The (002) HA peak at $2\theta = 26°$ is chosen to calculate the average crystal size of the post-treated samples, as reported widely in the literature [229, 230]. AFM contact mode is used to analyse the roughness of the HA coating and the results are detailed in Table 6.3.

Table 6.3 Surface characterisation of HA-coated Mg, MZ3 and MZX30.

| | **Thickness (μm)** | **Roughness (μm)** | **Crystal Size (nm)** |
|---|---|---|---|
| **HA-coated Mg** | ~ 10 | 0.64 ± 0.16 | 55 ± 13 |
| **HA-coated MZ3** | ~ 8 | 0.51 ± 0.08 | 70 ± 18 |
| **HA-coated MZX30** | ~ 7 | 0.57 ± 0.12 | 68 ± 15 |

## 6.4 Degradation of HA-coated alloys in SBF

### 6.4.1 Degradation rate measurement

The hydrogen evolution of both the HA-coated and uncoated samples after 10 days' immersion is illustrated in Fig. 6.5. The corrosion rate of all samples increases with increasing immersion time. It is evident that the corrosion rate of HA-coated Mg is lower than that of Mg: 2.10 ± 0.10 and 1.94 ± 0.09 mL/cm$^2$/day in Mg with and without coating. However, the corrosion rates of HA-coated MZ3 and MZX30 (3.61 ± 0.16 and 3.83 ± 0.12 mL/cm$^2$/day) are higher than those of the uncoated samples (3.48 ± 0.15 and 3.35 ± 0.04 mL/cm$^2$/day), implying that the HA coating does not protect the Mg alloys here.

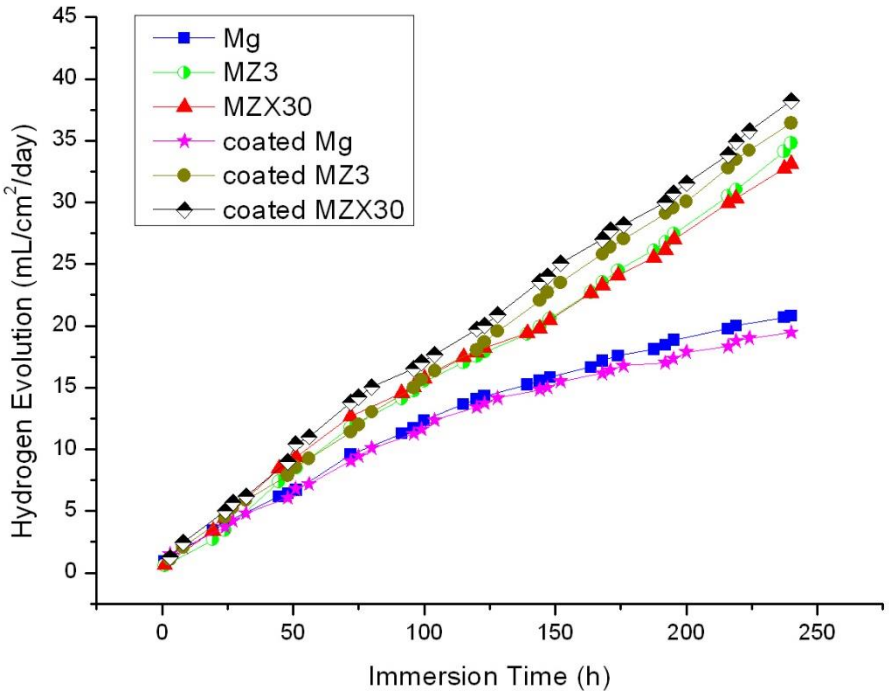


Fig. 6.5 Hydrogen evolution of uncoated and HA-coated Mg, MZ3 and MZX30 in SBF at 37 ℃.

### 6.4.2 Surface morphology after 10 days' immersion

The surface SEM morphologies of the HA-coated samples after 10 days of immersion in SBF are illustrated in Fig. 6.6. As shown in Figs. 6.6 a), c) and e), the shapes of the HA crystals after immersion are not noticeably different from those of the un-corroded crystals. The morphologies of the corroded HA-coated sample are not uniform and parts of the flaky HA coating are dissolved during the immersion. The coatings in some areas are peeled from the substrates (indicated by yellow arrows). It suggests that the adhesion of the HA coating is weakened during the immersion. In Figs. 6.6 b), d) and f), circular corrosion morphology is evident (marked by red arrows), indicating that pitting corrosion occurs.

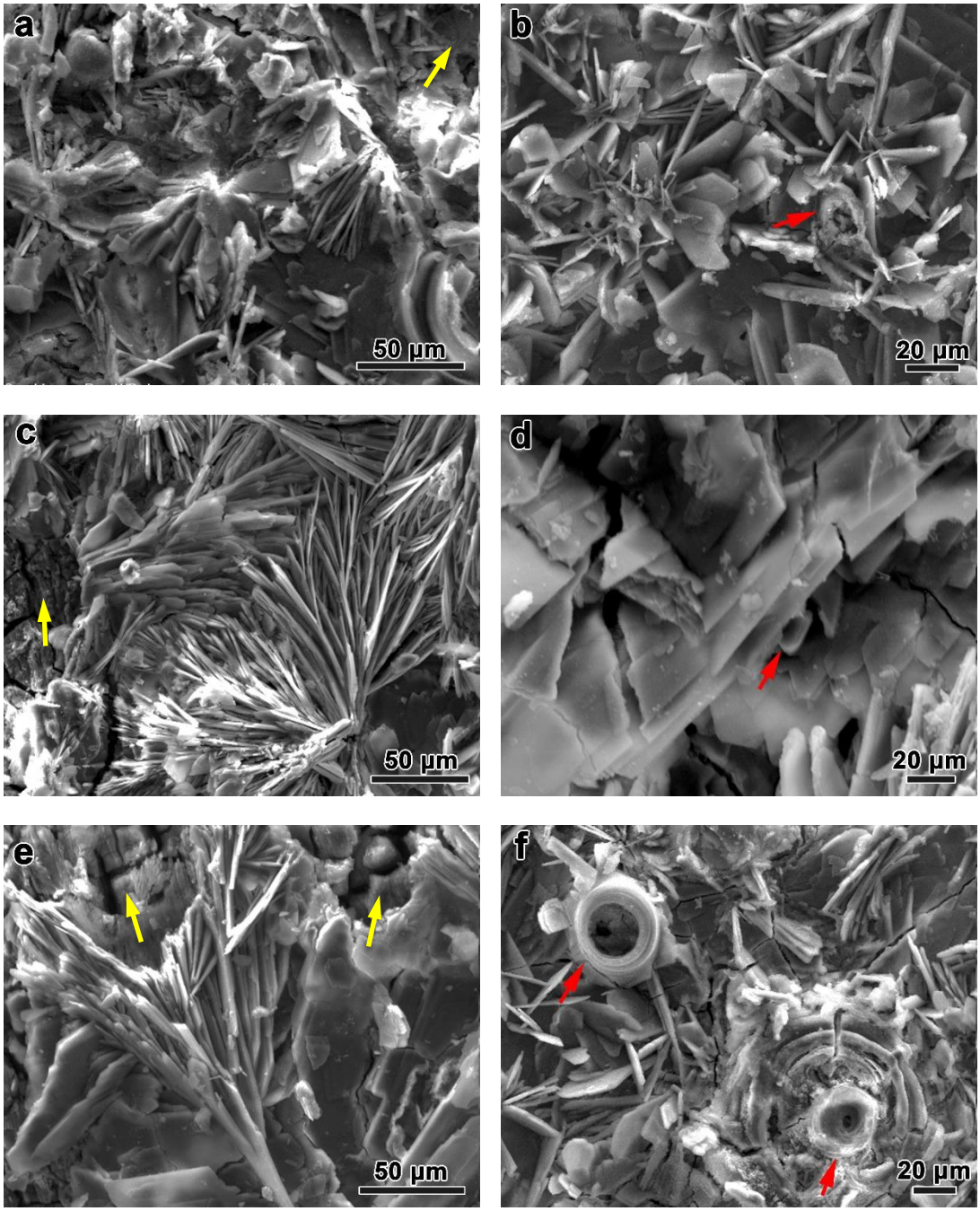


Fig. 6.6 Surface morphology of HA-coated samples after 10 days' immersion in SBF at 37 ℃: (a) and (b) Mg; (c) and (d) MZ3; (e) and (f) MZX30.

The XRD patterns from the HA-coated samples after 10 days' immersion in SBF are shown in Fig. 6.7. The resulting corrosion products are mainly octacalcium phosphate OCP ($Ca_8H_2(PO_4)_6 \cdot 5H_2O$) (PDF reference code: 00-0261-1056). OCP is an inorganic biomineral which is important in bone growth and involved in the formation

of tooth enamel, dentine and bone in living organisms [231, 232], suggesting that the corrosion products are bio-friendly.

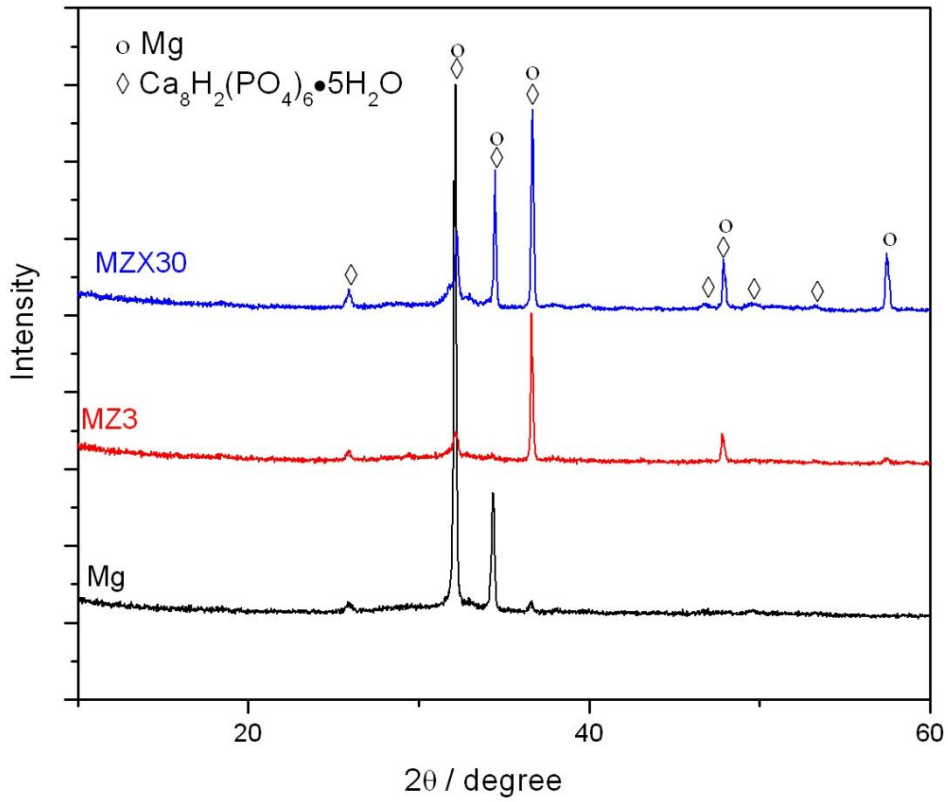


Fig. 6.7 XRD patterns from HA-coated specimens after 10 days' immersion.

## 6.5 Electrochemical tests

Potentiodynamic polarization curves acquired from bare and HA-coated samples in SBF at 37 ℃ are shown in Fig. 6.8. The HA-coated Mg reveals a shift in the corrosion potential ($E_{corr}$) towards more noble values, and the corrosion current density ($I_{corr}$) is lower than for the uncoated Mg (Fig. 6.8 a)). As shown in Figs. 6.8 b) and c), HA-coated MZ3 and MZX30 exhibit slightly higher corrosion potentials ($E_{corr}$) than the un-coated samples. It can be seen that the anodic and cathodic reactions are faster in the HA-coated MZ3 and MZX30. It is evident that $I_{corr}$ of HA-coated MZ3 and MZX30 is higher than in the uncoated samples. It is consistent with the results

obtained in the $H_2$ evolution tests: the corrosion rate of HA-coated MZ3 and MZX30 is higher than that of bare alloys.

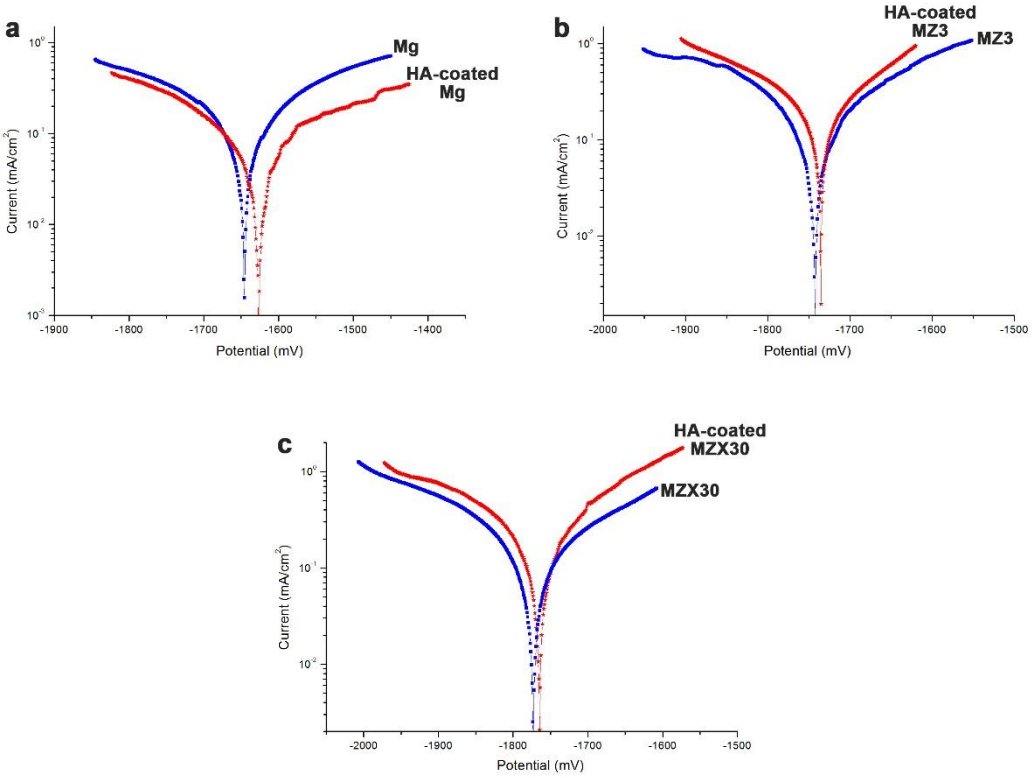


Fig. 6.8 Potentiodynamic polarization curves of samples with and without coating in SBF at 37 ℃: (a) Mg and HA-coated Mg; (b) MZ3 and HA-coated MZ3; (c) MZX30 and HA-coated MZX30.

## 6.6 Discussion

### 6.6.1 Formation of HA coating

In Fig. 6.9, a schematic illustration is used to show the formation of the HA coating on Mg alloys. The electrodeposition reactions consist of the following steps:

1. Oxido-reduction reaction (Fig. 6.9 a):

$$O_2 + H_2O + 4e^- \rightarrow 4(OH)^- \qquad \text{(Reaction 6.2)}$$

$$2H_20 + 2e^- \rightarrow H_2 + 2(OH)^- \qquad \text{(Reaction 6.3)}$$

During the process of potentiostatic deposition many $OH^-$ ions are produced from the reduction of $H_2O$. The pH at the interface between the substrate and the electrolyte is suddenly increased. The increased pH triggers the deposition of the Ca-P phase.

2. The enrichment of $OH^-$ ions promotes $H_2PO_4^-$ and $HPO_4^{2-}$ to convert into $PO_4^{3-}$ via the following reaction (Fig. 6.10 b):

$$H_2PO_4^- + OH^- \rightarrow HPO_4^{2-} + H_2O \qquad \text{(Reaction 6.4)}$$

$$HPO_4^{2-} + OH^- \rightarrow PO_4^{3-} + H_2O \qquad \text{(Reaction 6.5)}$$

3. Then, DCPD ($CaHPO_4 \cdot 2H_2O$) can be deposited upon the Mg surface via the following reaction (Fig. 6.10 c):

$$Ca^{2+} + 2HPO_4^{2-} + 2H_2O \rightarrow CaHPO_4 \cdot 2H_2O \qquad \text{(Reaction 6.6)}$$

4. The driving force for growth of HA ($Ca_5(PO_4)_3 \cdot (OH)$) is the degree of supersaturation during the alkaline treatment. HA is the most stable calcium phosphate and possess the lowest solubility. Finally, DCPD is transformed into HA after alkaline treatment (Fig. 6.10 c) and d)).

$$5CaHPO_4 \cdot 2H_2O + 6OH^- \rightarrow Ca_5(PO_4)_3 \cdot (OH) + 2PO_4^{3-} + 15H_2O \qquad \text{(Reaction 6.7)}$$

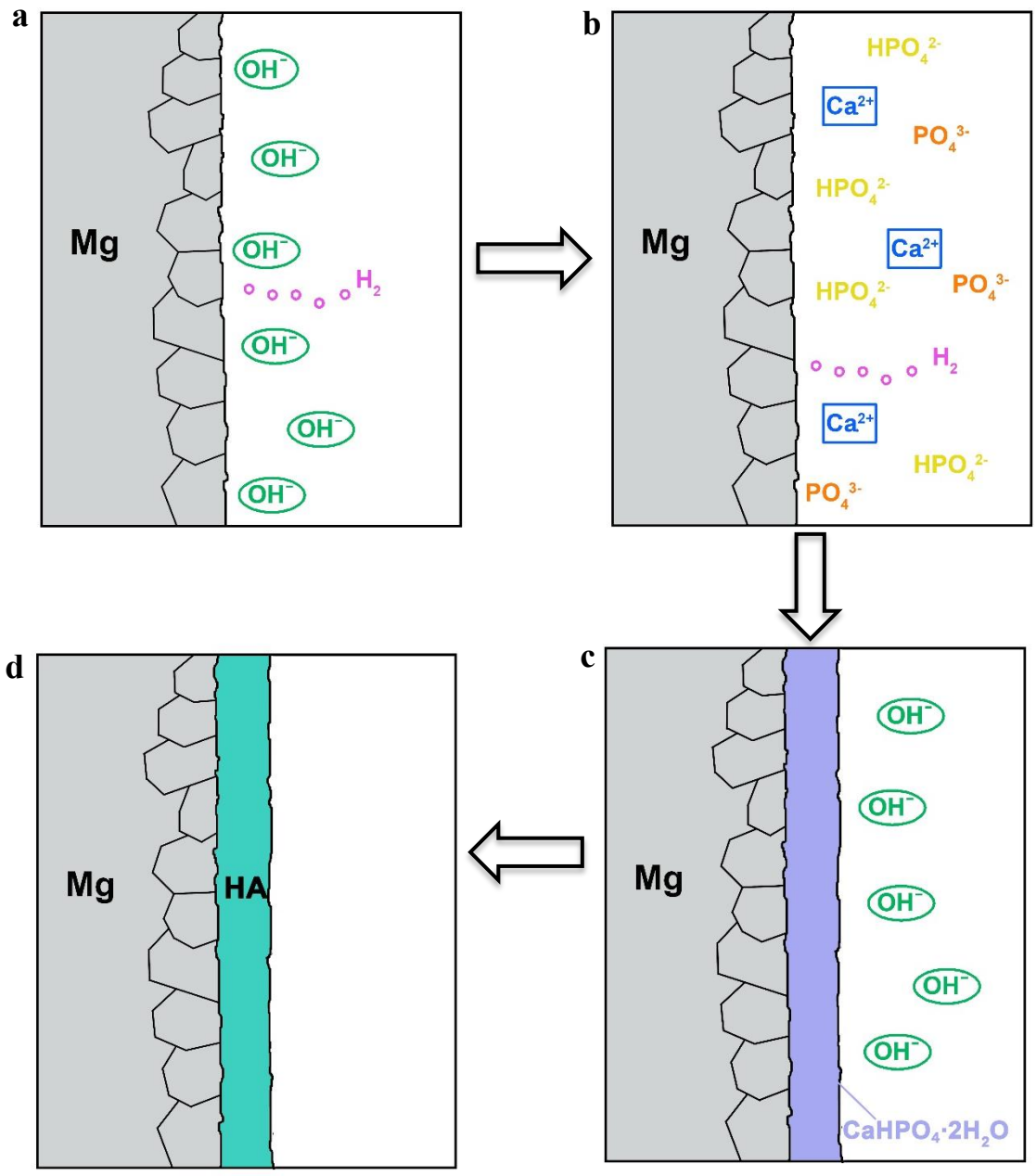


Fig. 6.9 Schematic illustration of the formation of HA coating on Mg alloys: (a) The reduction of $H_2O$ produces many $OH^-$, and then the deposition of Ca-P phase is triggered; (b) The enrichment of $OH^-$ promotes the transformation of $HPO_4^{2-}$ and $PO_4^{3-}$; (c) The DCPD deposits on the Mg surface. The alkaline treatment provides the degree of supersaturation; (d) HA forms finally by converting the DCPD.

### 6.6.2 Influence of HA coating on corrosion behaviour

An ideal corrosion-resistant coating prevents the direct electrolyte contact and electron transit and thus provides strong protection. However, Mg with a HA coating can only be protected to some extent. It is evident that HA-coated Mg has a relatively higher corrosion resistance than Mg (Figs. 6.5 and 6.8 a)). However, an HA coating cannot provide sufficient protection against corrosion attack during long time immersion. The corrosion rates of HA-coated MZ3 and MZX30 are higher than those of the bare alloys after 10 days' soaking (Figs. 6.5, 6.8 b) and c)). This is because the loose structure and fragile nature of HA decrease the corrosion resistance [233]. The coating is not so compact and uniform across the whole cross-section, as shown in Fig. 6.10, which makes it easier for SBF to penetrate into the coating and makes the Mg substrate vulnerable to corrosion. Fig. 6.10 a) displays a porous structure along the transverse direction in some areas (indicated by the arrows). A narrow flaw (marked by an arrow) is observed in Fig. 6.10 b), indicating low adhesion.

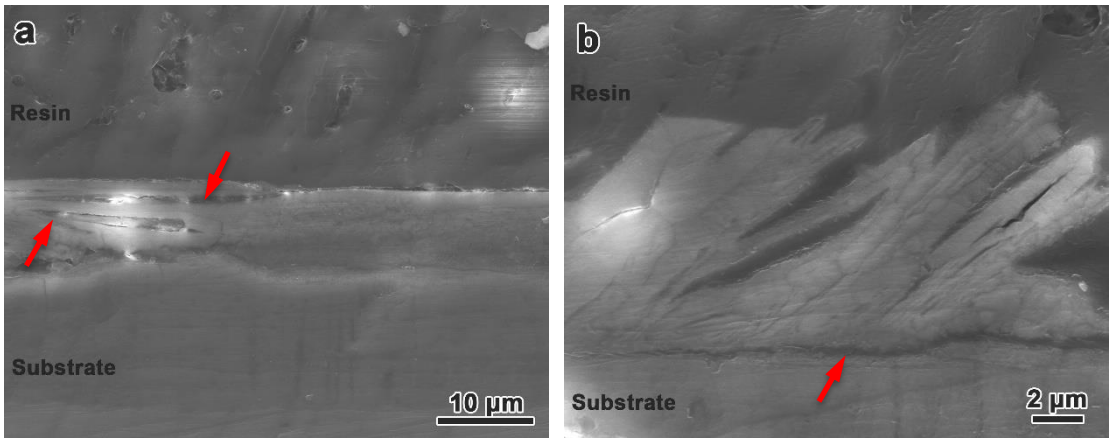


Fig. 6.10 SEM cross-section of HA-coated samples.

A pictorial model is presented which explains the corrosion of HA-coated Mg alloys after long time exposure to SBF (Fig. 6.11). The porous nature of the HA coating needs to be considered. Initially, the HA coating offers corrosion resistance (Fig. 6.11 a)). With prolonged immersion time, the corrosion pits initiate in some areas after breaking down of the coating. Then, the fresh Mg substrate is exposed to the SBF and thus the corrosion rate is accelerated (Fig. 6.11 b)). With immersion, corrosion of the HA-coated samples occurs widely and the coating detaches in some regions. The corrosion propagates into the Mg substrate along a 'through-hole', as illustrated in Fig. 6.11 c). Especially, when the region contains Mg matrix and second phases and is exposed to SBF, the substrate suffers serious corrosion attack because of galvanic corrosion. Thus the corrosion rate of the HA-coated Mg alloys is higher than that of bare ones, but, the corrosion rate of Mg with coating is lower than that of Mg.

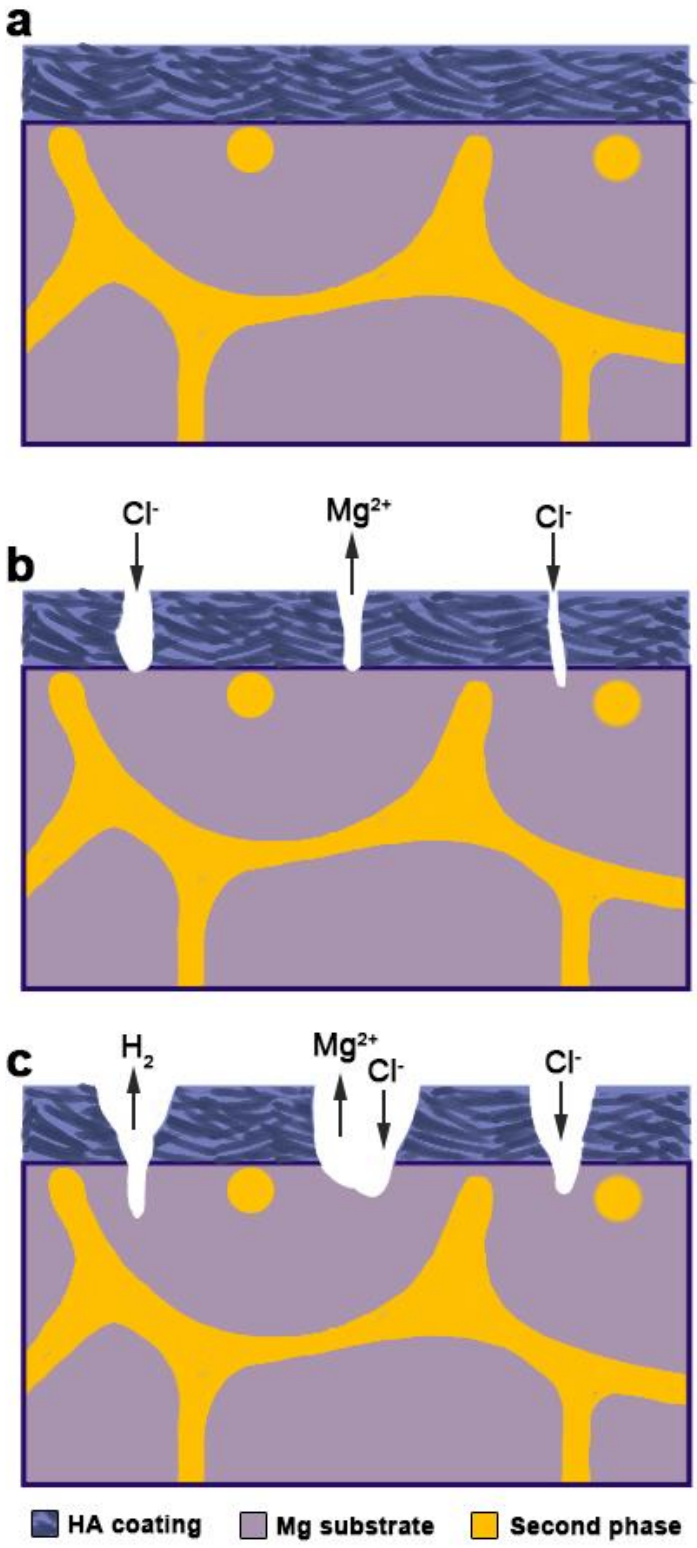


Fig. 6. 11 Schematic diagram of the degradation of an HA-coated Mg alloy: (a) Initially, the HA coating protects the Mg substrate; (b) The corrosion pits initiate in some areas after breaking down of the coating; (c) The corrosion propagates deeply into the Mg substrates.

## 6.7 Conclusions

An HA ($Ca_5(PO_4)_3\cdot(OH)$) coating is formed on Mg alloys consisting of dandelion-like aggregates of flake crystals with uniform morphology. Pitting corrosion on the HA-coated alloys occurs after long time immersion. The corrosion resistance of Mg is improved by the HA coating, while the corrosion resistance of HA-coated Mg alloy is lower than bare alloys. The loose structure of the HA coating prevents its protection of the Mg substrate. The coated Mg alloys suffers intensive corrosion due to galvanic corrosion after break down of the HA coating during immersion.

# Chapter 7 Conclusions and suggestions for future work

## 7.1 Conclusions

**Microstructures of Mg-3Zn and Mg-3Zn-0.3Ca:**

1. In the as-cast Mg-3Zn (MZ3), the spherical (α-Mg + MgZn) eutectic products are mainly distributed within the grains. MgZn has a rhombohedral structure (a= 2.6 nm and c=1.8 nm). As-cast Mg-3Zn-0.3Ca (MZX30) consists of α-Mg and (α-Mg + $Ca_2Mg_6Zn_3$) phases (globular and strip shaped). $Ca_2Mg_6Zn_3$ has a trigonal structure (a =0.97 nm, c=1.00 nm).

2. The lamellar structure of the (α-Mg + MgZn) phases is internally observed using a 3D tomography obtained via FIB/SEM. MicroCT tomography of the as-cast MZX30 shows that the dendritic α-Mg encloses a relatively large amount of (α-Mg + $Ca_2Mg_6Zn_3$) phase mixture beneath the MZX30 surface.

3. Quantitative TEM analysis is used to characterize the precipitation in the MZ3 with different ageing times at 160 ℃. There is a monotonoic relationship between the ageing time and the volume fraction of the fine precipitates. The largest volume fraction of fine precipitates is obtained at 160 ℃/ 144 h.

4. After different solution treatments, MZX30 shows different microstructures. As the temperature and time increase, the volume fraction of the second phases decreases gradually and the grain size increases. The quantitative microstructural characterisation is summarized.

**Bio-corrosion of Mg-3Zn and Mg-3Zn-0.3Ca:**

5. The localized corrosion is observed in both as-cast MZ3 and MZX30. There are prominent volcano-shaped corrosion pits indicated by the accumulation of corrosion products locally. The volcano-shaped structure is formed around central second phases which act as cathodes. Corrosion initiates in the anodically active magnesium matrix in both as-cast MZ3 and MZX30. A micro-galvanic cell is built up between the second phases and magnesium matrix and thus promotes the dissolution of magnesium.

6. The corrosion resistance of the solution-treated MZ3 is better than that of other MZ3 specimens. The absence of (α-Mg + MgZn) phases reduces micro-galvanic corrosion. Nano-scale precipitates formed during ageing decrease the corrosion resistance. The increase in bio-corrosion rate with ageing time appears to be monotonic. With increasing ageing time, magnesium alloys display worse corrosion resistance because of the precipitates.

7. A specific corrosion morphology occurs in aged MZ3: parallel filament-like trenches which mirror the growth direction of the precipitates. The size, distribution and volume fraction of the precipitates are important parameters that should be considered in order to tailor the microstructure and performance of magnesium alloys for different bio-medical applications.

8. The degradation rate of MZX30 changes with the heat treatment parameters. The grain size and volume fraction of second phases are both key factors for controlling the bio-corrosion rate of the alloy. The minimum corrosion rate was observed in the alloy heat-treated at 420 $^{o}$C for 24 hours which has a balanced second phase volume fraction and grain size.

**Surface modification of Mg-3Zn and Mg-3Zn-0.3Ca:**

9. An HA ($Ca_5(PO_4)_3 \cdot (OH)$) coating is formed on Mg alloys consisting of dandelion-like aggregates of flake crystals with uniform morphology. Pitting corrosion on the HA-coated alloys occurs after long time immersion. The corrosion resistance of Mg is improved by the HA coating, while the corrosion resistance of HA-coated Mg alloy is lower than bare alloys. The loose structure of the HA coating prevents its protection of the Mg substrate. The coated Mg alloys suffers intensive corrosion due to galvanic corrosion after break down of the HA coating during immersion.

## 7.2 Suggestions for future work

1. In the future, it is of interest to further study the microstructure and degradation behaviour of Mg-Zn(-Ca) alloys with different Zn and Ca contents and ultimately to optimise the degradation rate and mechanical performance of the alloy system.

2. It is also of interest to study more systematically the role of fine precipitates with different types/shapes/sizes on the bio-corrosion performance of magnesium alloys. Although the grain size and second phase volume fraction shows an interesting synergetic effect, it is important to further the study to understand the physical mechanisms involved and desirable to be able to predict the appropriate degradation rate based on the microstructural characteristics.

# Appendix: Design and construction of a vacuum melting and casting furnace for magnesium alloys

The present device relates to an electric induction furnace having a tiltable induction heating coil and crucible inside a vacuum chamber.

Generally, fluxes and cover gases are used for magnesium melting and casting processes, but these methods have severe drawbacks. The mechanical properties and corrosion performance are reduced when a flux covering is used, because flux inclusions are generated. The shrinkage and pores appear to be associated with these oxide inclusions. The flux reacts with molten magnesium, producing a corrosive gas which can cause instrument damage and deteriorate the working environment. At high temperature, chloride and villiaumite are highly volatile and generate toxic gases such as HF and $Cl_2$. A ($SF_6$+$CO_2$) mixture is used as a shielding gas for magnesium melting and is effective. By adding $SF_6$ gas, a thin and compact protective film is generated thereby protecting the molten magnesium. But $SF_6$ is both expensive and hazardous and therefore not ideally suitable for large-scale production. Also $SF_6$ gas poses a greenhouse threat. Applying fluxes and cover gases cannot completely prevent atmospheric oxidation. It is therefore desirable to design an apparatus which will permit vacuum melting and casting under a continuous vacuum throughout the operation.

The conventional vacuum induction furnace is not energy saving. Tilting the whole apparatus is difficult as it is cumbersome and generally requires the use of an excessively long electric cable and water hoses to allow for movement of the furnace between the melting and pouring positions. In addition, tilting the whole furnace is difficult: strong lift and motive power are demanded. Increasing forces on the

induction coils, water hoses and other unions can result in damage. An extremely heavy furnace frame with appropriate safety devices must be created to ensure the stability of so large a furnace. Currently available induction furnaces waste more energy and cost. A labour-saving and improved vacuum induction furnace is needed.

## 1. Summary

The present device aims to overcome or minimize the shortcomings discussed above by providing an improved vacuum induction furnace which includes a tiltable crucible and an induction heating coil in a stationary vacuum chamber, tilting of the coil and crucible being stably achieved via an exterior device which can carry both electricity and cooling water but also prevent the passage of gas from the atmosphere into the chamber.

Broadly stated, this vacuum casting apparatus is for melting a metal charge and casting molten metal under a vacuum. The melting, pouring and solidification can be performed in a vacuum, and under shielding gas. A tiltable crucible is surrounded by an induction coil housed in a stationary furnace chamber. A rotatable device includes a rotary feedthrough cylinder within a tubular flange on one wall of the furnace. The electric heating elements are coils which are made of hollow copper tubes. Flexible electric power cables are attached to terminal blocks connected to a power supply, to provide electricity to the coil. Flexible hoses provide water to the heating coil, leading water from the terminal blocks to the copper tube. Electricity is conducted through the conductive cables, while cooling water is connected to the heating coils through the flexible hose. The rotary feedthrough cylinder is made of a non-conductive material (Tufnol) to insulate the power leads. Furthermore, the total system can be operated easily because the each elements are spatially fixed relative to one another.

Brief description of the drawings.

Fig. 1 A vacuum melting and casting induction furnace.

Fig. 2 An enlarged view of the rotatable feedthrough device of the furnace.

Fig. 3 A perspective view showing a major subassembly of the present invention.

Fig. 4 A section taken along line 1-1 of Fig. 3.

Fig. 5 An enlarged side elevation of the tilting mechanism in the present invention

Fig. 6 A longitudinal sectional view showing the means for conducting electricity and cooling water to and from the heating coil along with the means for tilting the combined assembly.

Fig. 7 A technical drawing of vacuum melting and casting furnace for this study.

## 2. Detailed description of the device

Figs. 1 and 2 show a vacuum induction furnace for magnesium alloy melting and casting. In Fig. 1, a rotary pump (2) and diffusion pump (3) are used for establishing a vacuum in the furnace chamber. In Fig. 2, a tiltable device (4) is illustrated.

As shown in Figs. 3 and 4, the vacuum induction furnace consists mainly of a vacuum chamber (1), a rotatable mount (4) and tiltable coil and crucible (5). The crucible can be tilted together with the induction coil (5) surrounding it. The crucible is tightly surrounded by a suitable refractory material (not shown here) and no moving is allowed. The vacuum chamber is constructed by welding together sections of non-magnetic stainless steel. A cover (6) is placed over and clamped down against a gasket by using a latch located at the chamber when charged and ready for use. A viewing window (7) of heat resistant glass is installed on the cover so that the interior of the furnace can be viewed. A K-type thermocouple is provided for measuring the temperature of the metal. This thermocouple is inserted into the furnace chamber and thus the temperature of metals can be measured.

Fig. 3 illustrates flexible conductive power cables (8) and flexible hoses (9), such that both electricity and cooling water can be supplied to heating coils (5). By using these flexible cables and hoses, the rotation of the whole device (4) can be easily achieved. Moreover, there is no excess stress or movement for the coils (5) and other elements when the crucible and coil (5) are tilted.

Referring to Fig. 2, Fig. 4 and Fig. 5, the tiltable device (4) is mounted on the flange (10) of the vacuum chamber. The tiltable device (4) is mainly contained in a rotatable feedthrough cylinder (11), a hollow tubular flange (12) and two O-rings (13), (14). The rotatable feedthrough cylinder (11) is within a hollow tubular flange (12) and thus cylinder (11) can be moved relative to tubular flange (12). The cylinder (11) is approximately aligned with the tubular flange (12). The outside end (15) of the cylinder extends out of the flange (12) and the inside end (16) of the cylinder extends past the inside surface of the furnace flange (10). The cylinder (11) is made of insulating material (Tufnol) to provide thermal and electrical insulation.

In Fig. 5, one O-ring (13) is disposed between the exterior of the flange (10) and the tubular flange (12). Another O-ring (14) is mounted between the cylinder (11) and the tubular flange (12). These two O-rings (13 and 14) allow for tilting the crucible and coil (5), whilst preventing air leakage, thereby keeping a vacuum in the furnace chamber.

Referring particularly to Fig. 6, the mounting of feedthrough cylinder (11) within the tubular flange (12) is described in more detail. Copper tubes (17) pass through the feedthrough cylinder (11). There are two holes (18) (only seen in Fig. 6) in the cylinder (11). The holes are provided to allow passage of copper tube (17) into the interior of the vacuum chamber. The outside ends (19) of the holes are sealed by super glue to prevent air leakage. In this way, the interior of the furnace is completely sealed from the outside and the vacuum inside the furnace chamber is maintained during the

melting and casting process.

As illustrated in Figs. 4, 5 and 6, the current and cooling water which pass through the induction heating coils (5) are conducted through the copper tubes (17). Flexible high current electric power cables (8) and flexible hoses (9) are placed between copper tubes (17) and the terminal blocks (20 and 21). The terminal blocks (20) and (21) form a connection between the furnace and both the electricity and the cooling water supply. The two outer copper tubes (22) come from the power supply and are connected to terminal blocks (20) and (21) (Fig. 2). Current flows along the outer copper tubes (22) through the copper terminal blocks (20) to the copper tube (17 a) which is placed within the feedthrough cylinder (11), and then through heating coil (5). Cooling water passes through the outer copper tubes (22), through terminal blocks (20), through copper tube (17 a) inside the access cylinder (11) and finally arrives at the induction heating coil (5); heated cooling water is carried away through the copper tube (17 b), through terminal block (21) and comes back to the outer copper tubes (22) and the power supply. In general, the terminal blocks are used to allow the passage of cooling water and electricity from the outer copper tubes (22) to the heating coil (5). Insulating material (23) is placed around flange (12) and provides electrical insulation between flange (12) and the terminal blocks (20) and (21). The copper clamps (24) and (25) are used to provide a fixed junction for flexible cables (8) and hoses (9) between copper tubes (17) and the terminal blocks (20) and (21). Fixtures (26) and (27) are disposed between the flexible hose (9) and copper tubes (17) and prevent water leakage.

A gas-tight seal is provided between the outermost stationary flanges (10) and (12) and the rotatable feedthrough cylinder (11) by O-rings (13), (14). The cylinder (11), copper tubes (17), crucible and coil (5), flexible power cables (8) and flexible hoses (9) are held firmly together so that they can be rotated as a unit when handle (28) is rotated. When current and cooling water have been passing through the induction

heating coil (5) for a suitable time, the metal charge in the crucible will become molten. After all the metal is melted, the handle (28) can be moved so that the tiltable device (4), copper tubes (17), crucible and coil (5) are rotated. Molten metal flows out the crucible into a mould aligned therewith. The feedthrough cyliner (11), tubular flange (12) and tubes (17) are on coaxial tiltable mounts. Between these elements, O-rings or gaskets are placed and used for a tight seal.

It can be seen that the present device provides an improved induction vacuum furnace which contains a tiltable device in order to pour molten metal into a mould. The furnace vacuum chamber is stationary and only the crucible and heating coils need to rotate. No auxiliary power is required to tilt the crucible because the tilt of the crucible can be achieved by the insulated handle at the exterior of the furnace chamber. The handle is connected to the rotatable feedthrough cylinder and thus the coaxial tiltable mounts can be moved along with the handle. The current and cooling water flow stably to the induction heating coil but the passage of air through any joints between the rotary feedthrough is prevented. When pouring, only the crucible, which has a relatively low weight and is being tightly held within the induction coil, and access cylinder move smoothly about the crucible tilt axis.

Fig. 1

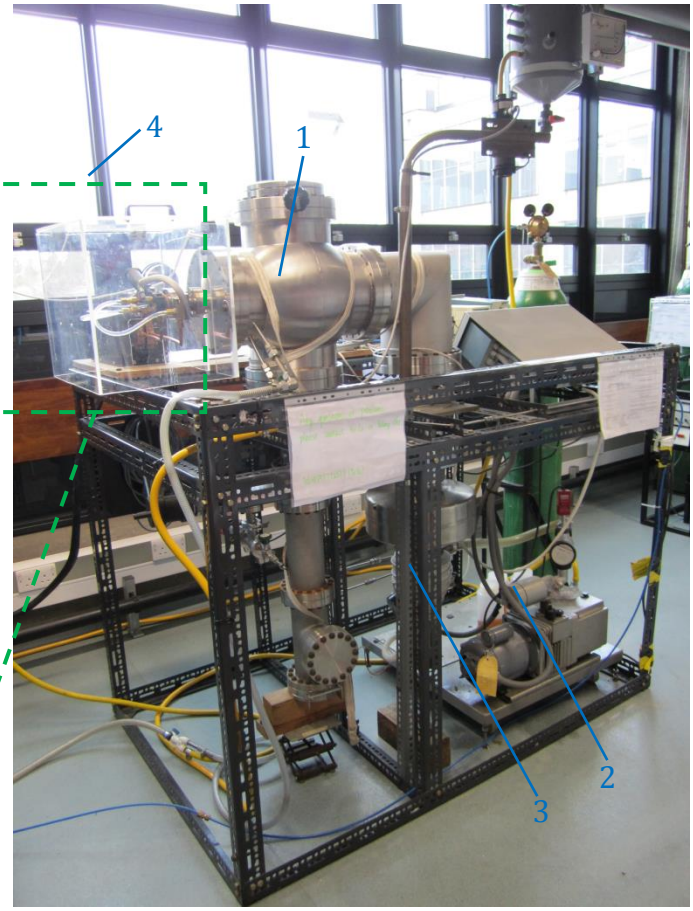


Fig. 2

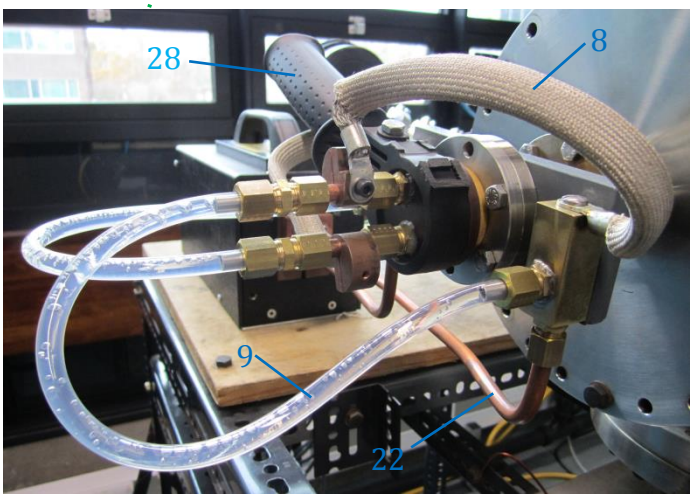


Fig. 1 A vacuum melting and casting induction furnace.

Fig. 2 An enlarged view of the rotatable feedthrough device of the furnace.

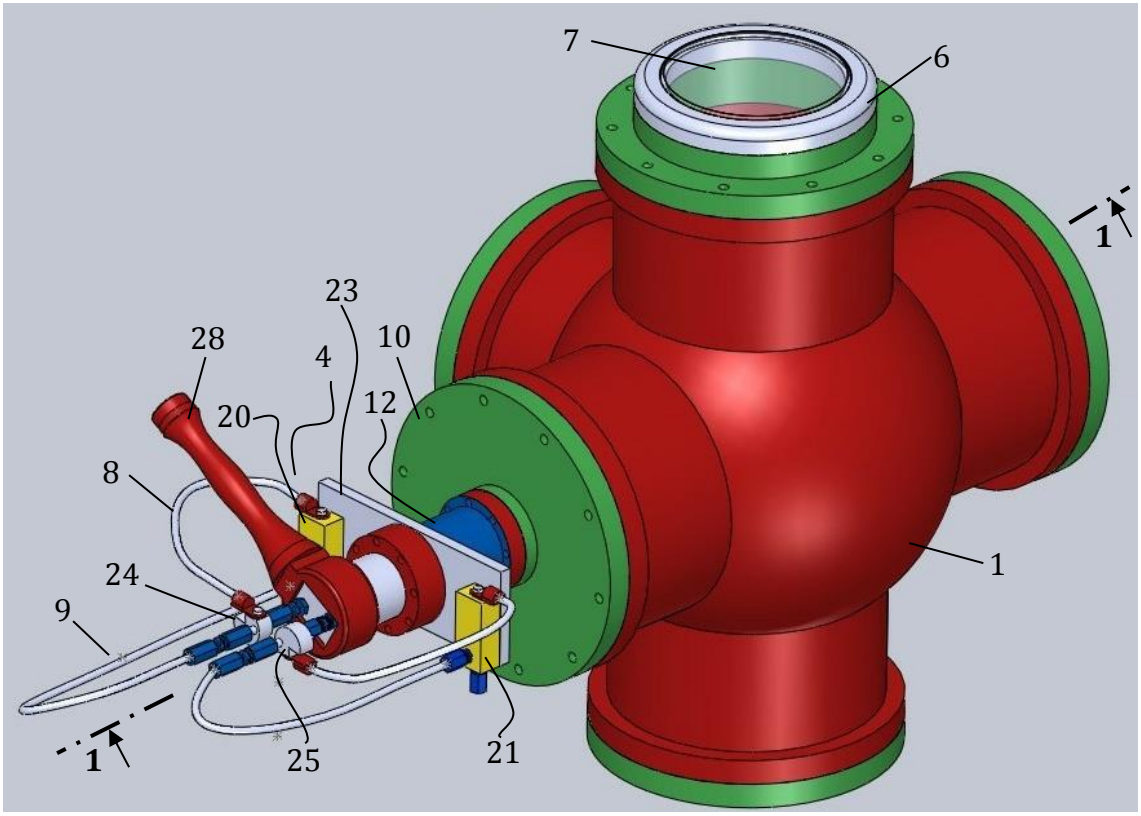


Fig. 3 A perspective view showing a major subassembly of the present invention.

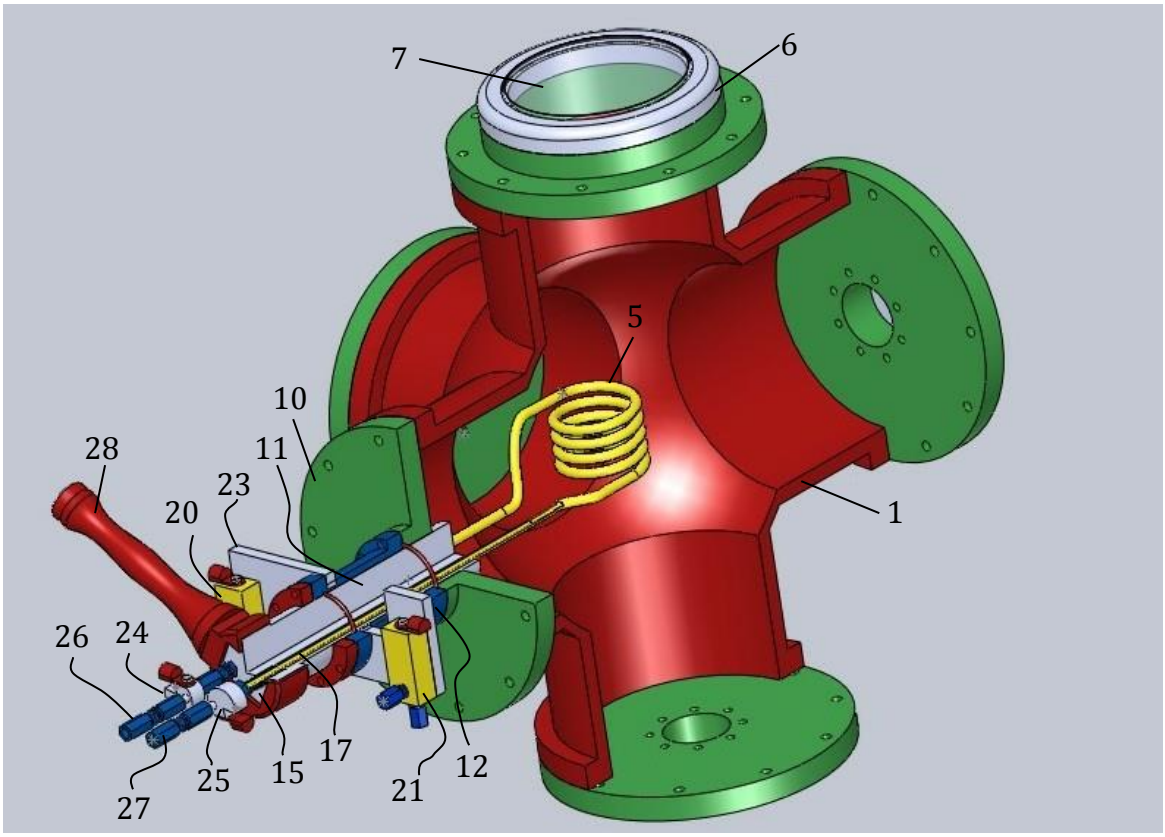


Fig. 4 A section taken along line 1-1 of Fig. 3.

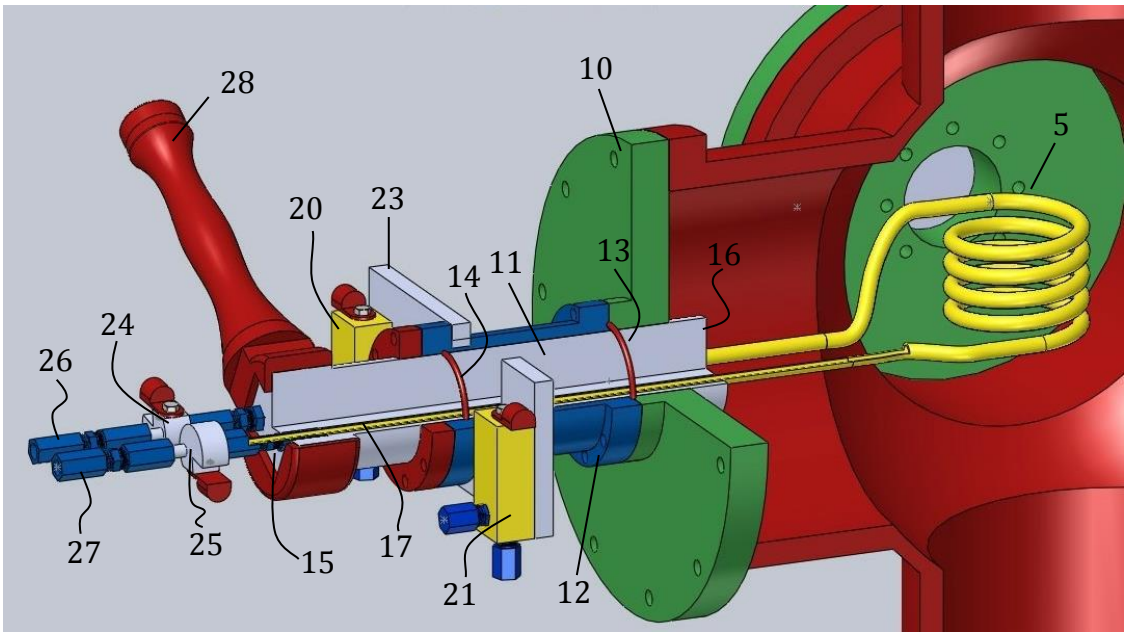


Fig. 5 An enlarged side elevation of the tilting mechanism in the present invention.

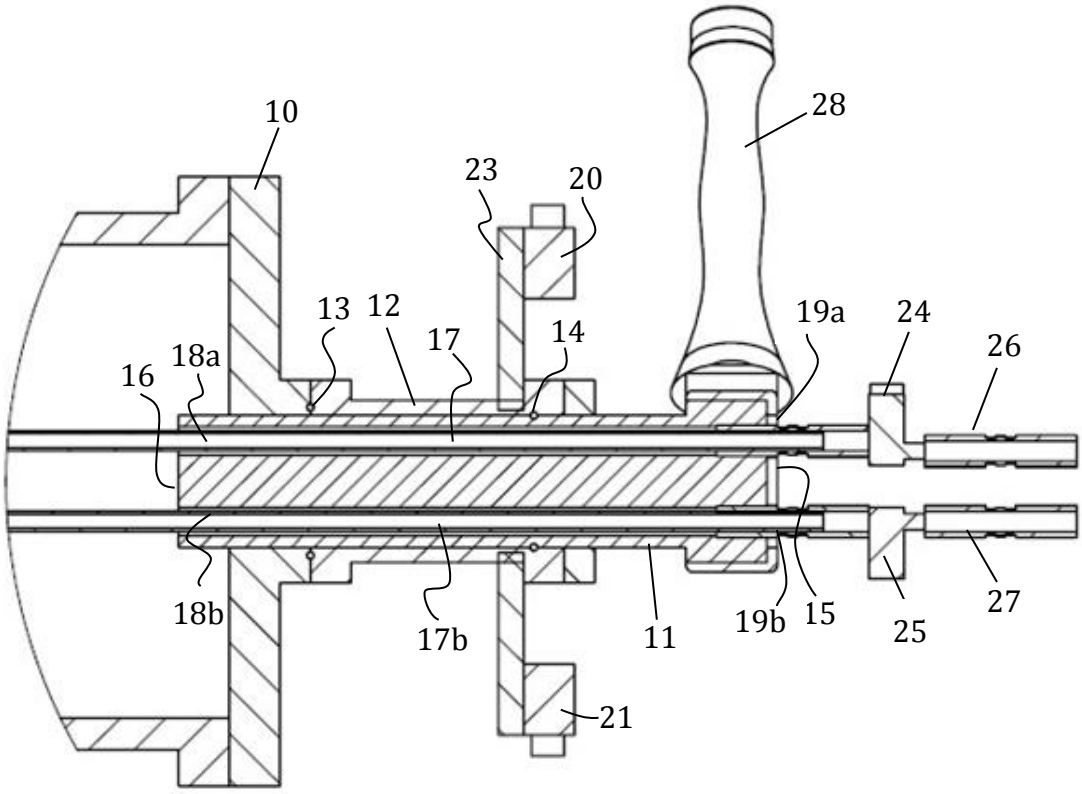


Fig. 6 A longitudinal sectional view showing the means for conducting electricity and cooling water to and from the heating coil with the means for tilting the combined assembly.

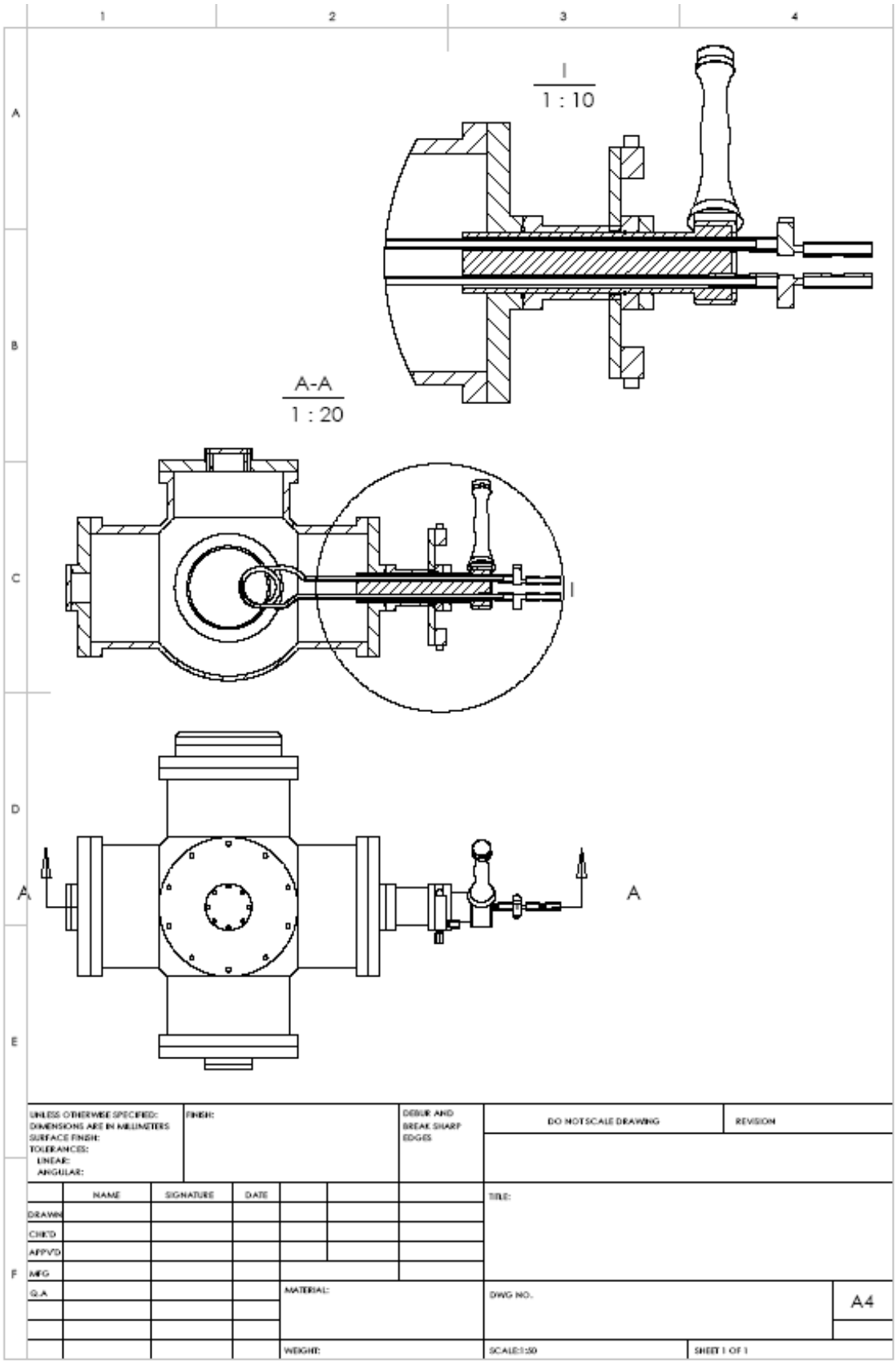


Fig. 7 A technical drawing of vacuum melting and casting furnace for this study.

## References


[1] B.D. Ratner, A.S. Hoffman, F.J. Schoen, and J.E. Lemons, *Biomaterial sciences: An introduction to materials in medicine.* 1996, San Diego: Academic Press. p. 1.

[2] B. Denkena and A. Lucas, *Biocompatible magnesium alloys as absorbable implant materials - adjusted surface and subsurface properties by machining processes.* Cirp Annals - Manufacturing Technology, 2007. **56**(1): p. 113-116.

[3] P. Zartner, R. Cesnjevar, H. Singer, and M. Weyand, *First successful implantation of a biodegradable metal stent into the left pulmonary artery of a preterm baby.* Catheterization and Cardiovascular Interventions, 2005. **66**(4): p. 590-594.

[4] F. Witte, J. Fischer, J. Nellesen, H.A. Crostack, V. Kaese, A. Pisch, F. Beckmann, and H. Windhagen, *In vitro and in vivo corrosion measurements of magnesium alloys.* Biomaterials, 2006. **27**(7): p. 1013-1018.

[5] F. Witte, V. Kaese, H. Haferkamp, E. Switzer, A. Meyer-Lindenberg, C.J. Wirth, and H. Windhagen, *In vivo corrosion of four magnesium alloys and the associated bone response.* Biomaterials, 2005. **26**(17): p. 3557-3563.

[6] G.L. Song, *Control of biodegradation of biocompatable magnesium alloys.* Corrosion Science, 2007. **49**(4): p. 1696-1701.

[7] G. Mani, M.D. Feldman, D. Patel, and C.M. Agrawal, *Coronary stents: A materials perspective.* Biomaterials, 2007. **28**(9): p. 1689-1710.

[8] H. Tapiero and K.D. Tew, *Trace elements in human physiology and pathology: zinc and metallothioneins.* Biomedicine & Pharmacotherapy, 2003. **57**(9): p. 399-411.

[9] P.D. Saltman and L.G. Strause, *The role of trace minerals in osteoporosis.* Journal of the American College of Nutrition, 1993. **12**(4): p. 384-389.

[10] Z.J. Li, X.N. Gu, S.Q. Lou, and Y.F. Zheng, *The development of binary Mg-Ca alloys for use as biodegradable materials within bone.* Biomaterials, 2008. **29**(10): p. 1329-1344.

[11] Y.W. Song, E.H. Han, D.Y. Shan, C.D. Yim, and B.S. You, *The role of second phases in the corrosion behavior of Mg-5Zn alloy.* Corrosion Science, 2012. **60**: p. 238-245.

[12] H.R. Bakhsheshi-Rad, M.R. Abdul-Kadir, M.H. Idris, and S. Farahany, *Relationship between the corrosion behavior and the thermal characteristics and microstructure of Mg-0.5Ca-xZn alloys.* Corrosion Science, 2012. **64**: p. 184-197.

[13] E.L. Zhang, L. Yang, J.W. Xu, and H.Y. Chen, *Microstructure, mechanical properties and bio-corrosion properties of Mg-Si(-Ca, Zn) alloy for biomedical application.* Acta Biomaterialia, 2010. **6**(5): p. 1756-1762.

[14] G.L. Song and A. Atrens, *Corrosion mechanisms of magnesium alloys.* Advanced Engineering Materials, 1999. **1**(1): p. 11-33.

[15] M.C. Zhao, M. Liu, G.L. Song, and A. Atrens, *Influence of the beta-phase*

*morphology on the corrosion of the Mg alloy AZ91.* Corrosion Science, 2008. **50**(7): p. 1939-1953.

[16] G.L. Song, A.L. Bowles, and D.H. StJohn, *Corrosion resistance of aged die cast magnesium alloy AZ91D.* Materials Science and Engineering A - Structural Materials Properties Microstructure and Processing, 2004. **366**(1): p. 74-86.

[17] C.S. Roberts, *Magnesium and its alloys*, ed. J.H. Hollomon1960, New York, USA: John Wiley & Sons. p. 5.

[18] H.E. Friedrich, *Magnesium technology: metallurgy, design data, automotive applications*, ed. B.L. Mordike2006, Germany: Springer-Verlag. p.147.

[19] C.J.P. Ball, *The History of Magnesium.* Journal of the Institute of Metals, 1956. **84**(11): p. 399-411.

[20] X.N. Gu, W.R. Zhou, Y.F. Zheng, Y. Liu, and Y.X. Li, *Degradation and cytotoxicity of lotus-type porous pure magnesium as potential tissue engineering scaffold material.* Materials Letters, 2010. **64**(17): p. 1871-1874.

[21] X.N. Gu, N. Li, W.R. Zhou, Y.F. Zheng, X. Zhao, Q.Z. Cai, and L.Q. Ruan, *Corrosion resistance and surface biocompatibility of a microarc oxidation coating on a Mg-Ca alloy.* Acta Biomaterialia, 2011. **7**(4): p. 1880-1889.

[22] X.N. Gu, W.R. Zhou, Y.F. Zheng, Y. Cheng, S.C. Wei, S.P. Zhong, T.F. Xi, and L.J. Chen, *Corrosion fatigue behaviors of two biomedical Mg alloys-AZ91D and WE43 - in simulated body fluid.* Acta Biomaterialia, 2010. **6**(12): p. 4605-4613.

[23] M.P. Staiger, A.M. Pietak, J. Huadmai, and G. Dias, *Magnesium and its alloys as orthopedic biomaterials: A review.* Biomaterials, 2006. **27**(9): p. 1728-1734.

[24] J.S. Temenoff and A.G. Mikos, *Biomaterials: The intersection of biology and materials sceince.* 2008, USA: Pearson Education. p. 2.

[25] B.D. Ratner and S.J. Bryant, *Biomaterials: Where we have been and where we are going.* Annual Review of Biomedical Engineering, 2004. **6**: p. 41-75.

[26] J.B. Park, *Biomaterials science and engineering.* 1984, New York: Plenum Press. p. 6.

[27] B.D. Ratner, *Biomaterials science: An introduction to materials in medicine*. 2nd ed.. 2004, San Diego: Elsevier Academic Press. p. 10-19.

[28] S.H. Teoh, *Engineering materials for biomedical applications*, ed. S.H. Teoh, et al.2004, Singapore: Word Scientific. p. 1-3.

[29] http://ocw.mit.edu/index.htm. *Massachusetts Institute of Technology (MIT) Open Course Ware (OCW)*

[30] J.S. Temenoff and A.G. Mikos, *The intersection of biology and materials science* ed. M.J. Horton and H. Stark2008, USA: Pearson Education. p. 3.

[31] M.S. Znamenskii, *Metallic osteosynthesis by means of an apparatus made of resorbing metal.* Khirurgiia, 1945. **12**: p. 60-63.

[32] Y. Xin, T. Hu, and P.K. Chu, *In vitro studies of biomedical magnesium alloys in a simulated physiological environment: A review.* Acta Biomaterialia, 2011.

**7**(4): p. 1452-1459.

[33] H.S. Brar, M.O. Platt, M. Sarntinoranont, P.I. Martin, and M.V. Manuel, *Magnesium as a biodegradable and bioabsorbable material for medical implants.* JOM, 2009. **61**(9): p. 31-34.

[34] A.C. Hanzi, I. Gerber, M. Schinhammer, J.F. Loffler, and P.J. Uggowitzer, *On the in vitro and in vivo degradation performance and biological response of new biodegradable Mg-Y-Zn alloys.* Acta Biomaterialia, 2010. **6**(5): p. 1824-1833.

[35] Y.C. Li, C.S. Wong, C. Wen, and P.D. Hodgson, *Biodegradable Mg-Zr-Ca alloys for bone implant materials.* Materials Technology, 2012. **27**(1): p. 49-51.

[36] F. Witte, N. Hort, C. Vogt, S. Cohen, K.U. Kainer, R. Willumeit, and F. Feyerabend, *Degradable biomaterials based on magnesium corrosion.* Current Opinion in Solid State & Materials Science, 2008. **12**(5-6): p. 63-72.

[37] J.B. Park and J.D. Bronzino, *Biomaterials: Principles and Applications*2000, Florida: CRC Press. p. 4.

[38] T. Okuma, *Magnesium and bone strength.* Nutrition, 2001. **17**(7-8): p. 679-680.

[39] A. Hartwig, *Role of magnesium in genomic stability.* Mutation Research-Fundamental and Molecular Mechanisms of Mutagenesis, 2001. **475**(1-2): p. 113-121.

[40] H. Rubin, *Magnesium: the missing element in molecular views of cell proliferation control.* Bioessays, 2005. **27**(3): p. 311-320.

[41] L.P. Xu, G.N. Yu, E. Zhang, F. Pan, and K. Yang, *In vivo corrosion behavior of Mg-Mn-Zn alloy for bone implant application.* Journal of Biomedical Materials Research Part A, 2007. **83A**(3): p. 703-711.

[42] X.N. Gu, Y.F. Zheng, Y. Cheng, S.P. Zhong, and T.F. Xi, *In vitro corrosion and biocompatibility of binary magnesium alloys.* Biomaterials, 2009. **30**(4): p. 484-498.

[43] N.E.L. Saris, E. Mervaala, H. Karppanen, J.A. Khawaja, and A. Lewenstam, *Magnesium - An update on physiological, clinical and analytical aspects.* Clinica Chimica Acta, 2000. **294**(1-2): p. 1-26.

[44] F. Witte, H. Ulrich, M. Rudert, and E. Willbold, *Biodegradable magnesium scaffolds: Part I: Appropriate inflammatory response.* Journal of Biomedical Materials Research Part A, 2007. **81A**(3): p. 748-756.

[45] B. Heublein, R. Rohde, V. Kaese, M. Niemeyer, W. Hartung, and A. Haverich, *Biocorrosion of magnesium alloys: a new principle in cardiovascular implant technology?* Heart, 2003. **89**(6): p. 651-656.

[46] P. Zartner, M. Buettner, H. Singer, and M. Sigler, *First biodegradable metal stent in a child with congenital heart disease: Evaluation of macro and histopathology.* Catheterization and Cardiovascular Interventions, 2007. **69**(3): p. 443-446.

[47] R.W. Revie and H.H. Uhlig, *Corrosion and corrosion control (Fourth edition),* 2008, Hoboken, New Jersey: John Wiley & Sons. p. 399.

[48] I.J. Polmear, *Light alloys: metallurgy of the light metals.* 1995, London, UK: J.Wiley &Sons.

[49] G.L. Song, *Recent progress in corrosion and protection of magnesium alloys.* Advanced Engineering Materials, 2005. **7**(7): p. 563-586.

[50] C.E. Wen, M. Mabuchi, Y. Yamada, K. Shimojima, Y. Chino, and T. Asahina, *Processing of biocompatible porous Ti and Mg.* Scripta Materialia, 2001. **45**(10): p. 1147-1153.

[51] L.E. Claes, *Mechanical characterization of biodegradable implants.* Clinical Materials, 1992. **10**(1-2): p. 41-46.

[52] T.P. Ruedi, R.E. Buckley, and C.G. Moran, *AO principles of fracture management.* 2007, Switzerland: Thieme New York.

[53] H. Hermawan, D. Dube, and D. Mantovani, *Developments in metallic biodegradable stents.* Acta Biomaterialia, 2010. **6**(5): p. 1693-1697.

[54] N.T. Kirkland, J. Lespagnol, N. Birbilis, and M.P. Staiger, *A survey of bio-corrosion rates of magnesium alloys.* Corrosion Science, 2010. **52**(2): p. 287-291.

[55] W.D. Mueller, M.L. Nascimento, and M.F.L. de Mele, *Critical discussion of the results from different corrosion studies of Mg and Mg alloys for biomaterial applications.* Acta Biomaterialia, 2010. **6**(5): p. 1749-1755.

[56] W.C. Kim, J.G. Kim, J.Y. Lee, and H.K. Seok, *Influence of Ca on the corrosion properties of magnesium for biomaterials.* Materials Letters, 2008. **62**(25): p. 4146-4148.

[57] Y.Z. Wan, G.Y. Xiong, H.L. Luo, F. He, Y. Huang, and X.S. Zhou, *Preparation and characterization of a new biomedical magnesium-calcium alloy.* Materials & Design, 2008. **29**(10): p. 2034-2037.

[58] E.L. Zhang and L. Yang, *Microstructure, mechanical properties and bio-corrosion properties of Mg-Zn-Mn-Ca alloy for biomedical application.* Materials Science and Engineering A - Structural Materials Properties Microstructure and Processing, 2008. **497**(1-2): p. 111-118.

[59] N. Hort, Y. Huang, D. Fechner, M. Stormer, C. Blawert, F. Witte, C. Vogt, H. Drucker, R. Willumeit, K.U. Kainer, and F. Feyerabend, *Magnesium alloys as implant materials - Principles of property design for Mg-RE alloys.* Acta Biomaterialia, 2010. **6**(5): p. 1714-1725.

[60] Q.M. Peng, Y.D. Huang, L. Zhou, N. Hort, and K.U. Kainer, *Preparation and properties of high purity Mg-Y biomaterials.* Biomaterials, 2010. **31**(3): p. 398-403.

[61] G.L. Song and A. Atrens, *Understanding magnesium corrosion - A framework for improved alloy performance.* Advanced Engineering Materials, 2003. **5**(12): p. 837-858.

[62] W.S. Loose, *Corrosion and Protection of Magnesium*, ed. L.M. Pidgeon, J.C. Mathes, and N.E. Woldmen1946: ASM International, Materials Park. p.173-260.

[63] E.F. Emley, *Principles of magnesium technology*1966, New York: Pregamon Press.

[64] Y.C. Xin, C.L. Liu, X.M. Zhang, G.Y. Tang, X.B. Tian, and P.K. Chu, *Corrosion behavior of biomedical AZ91 magnesium alloy in simulated body fluids.* Journal of Materials Research, 2007. **22**(7): p. 2004-2011.

[65] C.H. Ku, D.P. Piolettli, M. Browne, and P.J. Gregson, *Effect of different Ti-6A1-4V surface treatments on osteoblasts behaviour.* Biomaterials, 2002. **23**(6): p. 1447-1454.

[66] M. Shingde, J. Hughes, R. Boadle, E.J. Wills, and R. Pamphlett, *Macrophagic myofasciitis associated with vaccine-derived aluminium.* Medical Journal of Australia, 2005. **183**(3): p. 145-146.

[67] S.S. Abd El-Rahman, *Neuropathology of aluminum toxicity in rats (glutamate and GABA impairment).* Pharmacological Research, 2003. **47**(3): p. 189-194.

[68] J.J. Jacobs, A.K. Skipor, J. Black, R.M. Urban, and J.O. Galante, *Release and excretion of metal in patients who have a total hip-replacement component made of titanium-base alloy.* Journal of Bone and Joint Surgery - American Volume, 1991. **73A**(10): p. 1475-1486.

[69] J.Z. Ilich and J.E. Kerstetter, *Nutrition in bone health revisited: A story beyond calcium.* Journal of the American College of Nutrition, 2000. **19**(6): p. 715-737.

[70] M.M. Avedesian and H. Baker, *ASM Specialty Handbook: Magnesium and magnesium alloys,* 1999: ASM international. p.17.

[71] J.E. Hillis, *The effects of heavy-metal contamination on magnesium corrosion performance.* Light Metal Age, 1983. **41**(5-6): p. 25-29.

[72] I.J. Polmear, *Light Alloys: From traditional alloys to nanocrystals.* 2006, Oxford: Butterworth-Heinemann, Elsevier. 237.

[73] C.H. Caceres and A. Blake, *The strength of concentrated Mg-Zn solid solutions.* Physica Status Solidi A - Applied Research, 2002. **194**(1): p. 147-158.

[74] S.A. Khan, Y. Miyashita, Y. Mutoh, and Z. Bin Sajuri, *Influence of Mn content on mechanical properties and fatigue behavior of extruded Mg alloys.* Materials Science and Engineering A - Structural Materials Properties Microstructure and Processing, 2006. **420**(1-2): p. 315-321.

[75] J.A. Helsen and H.J. Breme, *Metals as biomaterials.* 1998: Wiley. p.23.

[76] F. Baruthio, O. Guillard, J. Arnaud, F. Pierre, and R. Zawislak, *Determination of Manganese in Biological-Materials by Electrothermal Atomic-Absorption Spectrometry - A Review.* Clinical Chemistry, 1988. **34**(2): p. 227-234.

[77] M. Aschner, T.R. Guilarte, J.S. Schneider, and W. Zheng, *Manganese: Recent advances in understanding its transport and neurotoxicity.* Toxicology and Applied Pharmacology, 2007. **221**(2): p. 131-147.

[78] N.A. Bock, F.F. Paiva, G.C. Nascimento, J.D. Newman, and A.C. Silva, *Cerebrospinal fluid to brain transport of manganese in a non-human primate revealed by MRI.* Brain Research, 2008. **1198**: p. 160-170.

[79] T.J. Haley, H.C. Upham, K. Raymond, and N. Komesu, *Toxicological and pharmacological effects of gadolinium and samarium chlorides.* British

Journal of Pharmacology and Chemotherapy, 1961. **17**(3): p. 526-532.

[80] D.W. Bruce, B.E. Hietbrink, and K.P. DuBios, *The acute mammalian toxicity of rare earth nitrates and oxides.* 1963. **5**(6): p. 750-759.

[81] W.D. Yang, P. Zhang, J.S. Liu, and Y.F. Xue, *Effect of long-term intake of Y3+ in drinking water on gene expression in brains of rats.* Journal of Rare Earths, 2006. **24**(3): p. 369-373.

[82] C.L. Liu, Y.C. Xin, G.Y. Tang, and P.K. Chu, *Influence of heat treatment on degradation behavior of bio-degradable die-cast AZ63 magnesium alloy in simulated body fluid.* Materials Science and Engineering A - Structural Materials Properties Microstructure and Processing, 2007. **456**(1-2): p. 350-357.

[83] L. Yang, Y.D. Huang, F. Feyerabend, R. Willumeit, K.U. Kainer, and N. Hort, *Influence of ageing treatment on microstructure, mechanical and bio-corrosion properties of Mg-Dy alloys.* Journal of the Mechanical Behavior of Biomedical Materials, 2012. **13**: p. 36-44.

[84] S.Q. Liang, D.K. Guan, and X.P. Tan, *The relation between heat treatment and corrosion behavior of Mg-Gd-Y-Zr alloy.* Materials & Design, 2011. **32**(3): p. 1194-1199.

[85] L.M. Peng, J.W. Chang, X.W. Guo, A. Atrens, W.J. Ding, and Y.H. Peng, *Influence of heat treatment and microstructure on the corrosion of magnesium alloy Mg-10Gd-3Y-0.4Zr.* Journal of Applied Electrochemistry, 2009. **39**(6): p. 913-920.

[86] L.C. Junqueira and J. Carneiro, *Basic Histology: Text and Atlas (10th Ed)*, ed. J. Foltin, H. Lebowitz, and P. Boyle2003, New York: McGraw-Hill Companies. p.144.

[87] H.W. Denissen, K. Degroot, P.C. Makkes, A. Vandenhooff, and P.J. Klopper, *Tissue - response to dense apatite implants in rats.* Journal of Biomedical Materials Research, 1980. **14**(6): p. 713-721.

[88] R. Narayanan and S.K. Seshadri, *Synthesis and corrosion of functionally gradient TiO2 and hydroxyapatite coatings on Ti-6Al-4V.* Materials Chemistry and Physics, 2007. **106**(2-3): p. 406-411.

[89] N. Durnelie, H. Benhayoune, D. Richard, D. Laurent-Maquin, and G. Balossier, *In vitro precipitation of electrodeposited calcium-deficient hydroxyapatite coatings on Ti6Al4V substrate.* Materials Characterization, 2008. **59**(2): p. 129-133.

[90] M.C. Kuo and S.K. Yen, *The process of electrochemical deposited hydroxyapatite coatings on biomedical titanium at room temperature.* Materials Science & Engineering C - Biomimetic and Supramolecular Systems, 2002. **20**(1-2): p. 153-160.

[91] C.T. Wu, Y. Ramaswamy, D. Gale, W.R. Yang, K.Q. Xiao, L.C. Zhang, Y.B. Yin, and H. Zreiqat, *Novel sphene coatings on Ti-6Al-4V for orthopedic implants using sol-gel method.* Acta Biomaterialia, 2008. **4**(3): p. 569-576.

[92] H.W. Kim, H.E. Kim, and J.C. Knowles, *Fluor-hydroxyapatite sol-gel coating on titanium substrate for hard tissue implants.* Biomaterials, 2004. **25**(17):

p. 3351-3358.

[93] M. Javidi, S. Javadpour, M.E. Bahrololoom, and J. Ma, *Electrophoretic deposition of natural hydroxyapatite on medical grade 316L stainless steel.* Materials Science & Engineering C - Biomimetic and Supramolecular Systems, 2008. **28**(8): p. 1509-1515.

[94] M. Wei, A.J. Ruys, B.K. Milthorpe, C.C. Sorrell, and J.H. Evans, *Electrophoretic deposition of hydroxyapatite coatings on metal substrates: A nanoparticulate dual-coating approach.* Journal of Sol-Gel Science and Technology, 2001. **21**(1-2): p. 39-48.

[95] Y.Z. Yang, K.H. Kim, and J.L. Ong, *A review on calcium phosphate coatings produced using a sputtering process - an alternative to plasma spraying.* Biomaterials, 2005. **26**(3): p. 327-337.

[96] C. Sella, J.C. Martin, J. Lecoeur, A. Lechanu, M.F. Harmand, A. Naji, and J.P. Davidas, *Biocompatibility and corrosion-resistance in biological media of hard ceramic coatings sputter deposited on metal implants.* Materials Science and Engineering A - Structural Materials Properties Microstructure and Processing, 1991. **139**: p. 49-57.

[97] A.L.K. Tan, A.M. Soutar, I.F. Annergren, and Y.N. Liu, *Multilayer sol-gel coatings for corrosion protection of magnesium.* Surface & Coatings Technology, 2005. **198**(1-3): p. 478-482.

[98] P. Ducheyne, W. Vanraemdonck, J.C. Heughebaert, and M. Heughebaert, *Structural analysis of hydroxyapatite coatings on titanium.* Biomaterials, 1986. **7**(2): p. 97-103.

[99] M. Saremi and B.M. Golshan, *Microstructural study of nano hydroxyapatite coating obtained by pulse electrodeposition process on Ti-6Al-(4)V.* Transactions of the Institute of Metal Finishing, 2007. **85**(2): p. 99-102.

[100] N. Eliaz, T.M. Sridhar, U.K. Mudali, and B. Raj, *Electrochemical and electrophoretic deposition of hydroxyapatite for orthopaedic applications.* Surface Engineering, 2005. **21**(3): p. 238-242.

[101] M. Manso, C. Jimenez, C. Morant, P. Herrero, and J.M. Martinez-Duart, *Electrodeposition of hydroxyapatite coatings in basic conditions.* Biomaterials, 2000. **21**(17): p. 1755-1761.

[102] M.B. Kannan, Y.H. He, and A. Sandham, *Calcium phosphate deposition on magnesium alloy for bioimplant applications.* PRICM 7, Pts 1-3, 2010. **654-656**: p. 2196-2199.

[103] M.B. Kannan and L. Orr, *In vitro mechanical integrity of hydroxyapatite coated magnesium alloy.* Biomedical Materials, 2011. **6**(4).

[104] S.X. Zhang, X.N. Zhang, C.L. Zhao, J.A. Li, Y. Song, C.Y. Xie, H.R. Tao, Y. Zhang, Y.H. He, Y. Jiang, and Y.J. Bian, *Research on an Mg-Zn alloy as a degradable biomaterial.* Acta Biomaterialia, 2010. **6**(2): p. 626-640.

[105] E.L. Zhang, D.S. Yin, L.P. Xu, L. Yang, and K. Yang, *Microstructure, mechanical and corrosion properties and biocompatibility of Mg-Zn-Mn alloys for biomedical application.* Materials Science & Engineering C - Biomimetic and Supramolecular Systems, 2009. **29**(3): p. 987-993.

[106] H.S. Brar, J. Wong, and M.V. Manuel, *Investigation of the mechanical and degradation properties of Mg-Sr and Mg-Zn-Sr alloys for use as potential biodegradable implant materials.* Journal of the Mechanical Behavior of Biomedical Materials, 2012. **7**: p. 87-95.

[107] X.N. Gu, X.H. Xie, N. Li, Y.F. Zheng, and L. Qin, *In vitro and in vivo studies on a Mg-Sr binary alloy system developed as a new kind of biodegradable metal.* Acta Biomaterialia, 2012. **8**(6): p. 2360-2374.

[108] H. Du, Z.J. Wei, X.W. Liu, and E.L. Zhang, *Effects of Zn on the microstructure, mechanical property and bio-corrosion property of Mg-3Ca alloys for biomedical application.* Materials Chemistry and Physics, 2011. **125**(3): p. 568-575.

[109] X.N. Gu and Y.F. Zheng, *A review on magnesium alloys as biodegradable materials.* Frontiers of Materials Science in China, 2010. **4**(2): p. 111-115.

[110] D.S. Yin, E.L. Zhang, and S.Y. Zeng, *Effect of Zn on mechanical property and corrosion property of extruded Mg-Zn-Mn alloy.* Transactions of Nonferrous Metals Society of China, 2008. **18**(4): p. 763-768.

[111] Y. Sun, B.P. Zhang, Y. Wang, L. Geng, and X.H. Jiao, *Preparation and characterization of a new biomedical Mg-Zn-Ca alloy.* Materials & Design, 2012. **34**: p. 58-64.

[112] Y. Chino, M. Kobata, H. Iwasaki, and M. Mabuchi, *Tensile properties from room temperature to 673 K of Mg-0.9 mass% Ca alloy containing lamella Mg2Ca.* Materials Transactions, 2002. **43**(10): p. 2643-2646.

[113] F.O. Riemelmoser, M. Kuhlein, H. Kilian, M. Kettner, A.C. Hanzi, and P.J. Uggowitzer, *Micro-alloyed wrought magnesium for room-temperature forming.* Advanced Engineering Materials, 2007. **9**(9): p. 799-802.

[114] F.H. Dalla Torre, A.C. Hanzi, and P.J. Uggowitzer, *Microstructure and mechanical properties of microalloyed and equal channel angular extruded Mg alloys.* Scripta Materialia, 2008. **59**(2): p. 207-210.

[115] L.P. Xu, E.L. Zhang, D.S. Yin, S.Y. Zeng, and K. Yang, *In vitro corrosion behaviour of Mg alloys in a phosphate buffered solution for bone implant application.* Journal of Materials Science-Materials in Medicine, 2008. **19**(3): p. 1017-1025.

[116] B.P. Zhang, Y.L. Hou, X.D. Wang, Y. Wang, and L. Geng, *Mechanical properties, degradation performance and cytotoxicity of Mg-Zn-Ca biomedical alloys with different compositions.* Materials Science & Engineering C - Materials for Biological Applications, 2011. **31**(8): p. 1667-1673.

[117] Z.G. Xu, C. Smith, S.O. Chen, and J. Sankar, *Development and microstructural characterizations of Mg-Zn-Ca alloys for biomedical applications.* Materials Science and Engineering B - Advanced Functional Solid-State Materials, 2011. **176**(20): p. 1660-1665.

[118] A.C. Hanzi, A.S. Sologubenko, and P.J. Uggowitzer, *Design strategy for new biodegradable Mg-Y-Zn alloys for medical applications.* International Journal of Materials Research, 2009. **100**(8): p. 1127-1136.

[119] M.D. Carlo Di Mario, et al., *Drug‐eluting bioabsorbable magnesium stent.* Journal of Interventional Cardiology, 2004. **17**(6): p. 391-395.
[120] J.B. Clark and F.N. Rhines, *Central region of the Mg-Zn phase diagram.* Transactions of the American Institute of Mining and Metallurgical Engineers, 1957. **209**: p. 425-430.
[121] J.B. Clark, L. Zabdyr, and Z. Moser, *Phase diagrams of binary magnesium alloys,* 1988: ASM International, Materials Park. p. 353.
[122] I. Higashi, N. Shiotani, M. Uda, T. Mizoguchi, and H. Katoh, *The crystal-structure of Mg51Zn20.* Journal of Solid State Chemistry, 1981. **36**(2): p. 225-233.
[123] Y. Khan, *Dynamic temperature crystallization behavior of amorphous and liquid Mg70Zn30 alloy.* Journal of Materials Science, 1989. **24**(3): p. 963-973.
[124] X. Gao and J.F. Nie, *Structure and thermal stability of primary intermetallic particles in an Mg-Zn casting alloy.* Scripta Materialia, 2007. **57**(7): p. 655-658.
[125] J. Gallot, and R. Graf. , *X-Ray Investigation of the Equilibrium Phase in a 60% Zinc Containing Magnesium-Zinc Alloy.* Comptes rendus, 1966. **262**: p. 1219-1222.
[126] Y. Komura and K. Tokunaga, *Structural studies of stacking variants in Mg-base Friauf-Laves phases.* Acta Crystallographica Section B - Structural Science, 1980. **36**(Jul): p. 1548-1554.
[127] S. Samson, *The crystal structure of Mg2Zn11: isomorphism between Mg2Zn11 and Mg2Cu6Al5.* Acta Chemica Scandinavica, 1949. **3**: p. 835-843.
[128] L. Sturkey and J.B. Clark, *Mechanism of age-hardening in magnesium zinc alloys.* Journal of the Institute of Metals, 1959. **88**(4): p. 177-181.
[129] J.B. Clark, *Transmission electron microscopy study of age hardening in a Mg-5 wt% Zn alloy.* Acta Metallurgica, 1965. **13**(12): p. 1281-1289.
[130] M. Bernole, J. Gallot, and R. Graf, *Electron micrography of Mg-6% Zn alloy using electrolytic thinning.* Journal of Microscopy, 1965. **4**: p. 787-792.
[131] G. Mima and Y. Tanaka, *The main factors affecting the aging of magnesium-zinc alloys.* Transactions of Journal of Japan Institute of Metals and Materials (JIM), 1971. **12**: p. 76-81.
[132] J. Buha, *Reduced temperature (22-100 degrees C) ageing of an Mg-Zn alloy.* Materials Science and Engineering A - Structural Materials Properties Microstructure and Processing, 2008. **492**(1-2): p. 11-19.
[133] J.F. Nie, *Precipitation and hardening in magnesium alloys.* Metallurgical and Materials Transactions A - Physical Metallurgy and Materials Science, 2012. **43A**(11): p. 3891-3939.
[134] X. Gao and J.F. Nie, *Characterization of strengthening precipitate phases in a Mg-Zn alloy.* Scripta Materialia, 2007. **56**(8): p. 645-648.
[135] C.S. Roberts, *Magnesium and its alloys*, ed. J.H. Hollomon1960, USA. p. 48.
[136] J.B. Clark, *The solid constitution in the magnesium-rich region of the Mg-Ca-*

*Zn phase diagram.* Transactions of the Metallurgical Society of AIME, 1961. **221**(3): p. 644-645.

[137] G.E. Pellissier, *Stereology and quantitative metallography,* 1972, Atlantic City: American Society for Testing and Materials.

[138] E.E. Underwood, *Stereology, or the quantitative evaluation of microstructures.* Journal of Microscopy, 1969. **89**: p. 161-180.

[139] E.E. Underwood, *Quantitative stereology,* 1970: Addison-Wesley Publishing Co.

[140] W.D. Callister and J. Callister, *Materials science and engineering : an introduction (3rd Ed)*1994: John Wiley & Sons. p.555.

[141] M. Pourbaix, *Atlas of electrochemical equilibria in aqueous solutions.* 1974: National Association of Corrosion Engineers.

[142] R. Ambat, N.N. Aung, and W. Zhou, *Studies on the influence of chloride ion and pH on the corrosion and electrochemical behaviour of AZ91D magnesium alloy.* Journal of Applied Electrochemistry, 2000. **30**(7): p. 865-874.

[143] R. Ambat, N.N. Aung, and W. Zhou, *Evaluation of microstructural effects on corrosion behaviour of AZ91D magnesium alloy.* Corrosion Science, 2000. **42**(8): p. 1433-1455.

[144] http://corrosion.ksc.nasa.gov/pittcor.htm. *NASA Corrosion Technology Laboratory*.

[145] G.L. Makar and J. Kruger, *Corrosion of Magnesium.* International Materials Reviews, 1993. **38**(3): p. 138-153.

[146] A. Fones, *The corrosion of magnesium*, in *School of metallurgy and materials*2005, University of Birmingham: Birmingham. p. 13.

[147] B.Y. Hur, K.W. Kim, H.J. Ah, and K.H. Kim, in *The Third International Magnesium Conference*, G.W. Lorimer, Editor 1997: London. p. 557-564.

[148] M.G. Fontana, *Corrosion engineering.* 1967, New York: McGraw-Hill Book Company.

[149] K.R. Tretheway, *Corrosion: For science and engineering.* 1995, England: Addison-Wesley Longman.

[150] R.C. Zeng, W. Dietzel, F. Witte, N. Hort, and C. Blawert, *Progress and challenge for magnesium alloys as biomaterials.* Advanced Engineering Materials, 2008. **10**(8): p. B3-B14.

[151] A. Froats, T.K. Aune, D. Hawke, W. Unsworth, and J. Hillis, *Metals handbook (9th Ed)*. Vol. 13. 1987: ASM International. p.740-754.

[152] O. Lunder, J.H. Nordien, and K. Nisancioglu, *Corrosion resistance of cast Mg-Al alloys.* Corrosion Reviews, 1997. **15**(3-4): p. 439-470.

[153] L. Wei, H. Westengen, T.K. Aune, and D. Albright, *Magnesium technology 2000.* Warendale, 2000: p. 153-160.

[154] J.D. Hanawalt, C.E. Nelson, and J.A. Peloubet, *Corrosion studies of magnesium and its alloys.* Transactions of the American Institute of Mining and Metallurgical Engineers, 1942. **147**: p. 273-298.

[155] R.W. Revie, *Uhlig's corrosion handbook (2nd Ed.).* 2000, New York: John

Wiley& Sons. .

[156] O. Lunder, J.E. Lein, T.K. Aune, and K. Nisancioglu, *The role of Mg17Al12 phase in the corrosion of Mg alloy AZ91.* Corrosion, 1989. **45**(9): p. 741-748.

[157] T. Beldjoudi, C. Fiaud, and L. Robbiola, *Influence of homogenization and artificial aging heat-treatments on corrosion behavior of Mg-Al alloys.* Corrosion, 1993. **49**(9): p. 738-745.

[158] K. Nisancioglu, O. Lunder, and T.K. Aune, *Corrosion mechanism of AZ91 magnesium alloy.* 47th Annual World Magnesium Conference : Past to Future, 1990: p. 43-50.

[159] O. Lunder, Videm, M., Nisancioglu, K., *Corrosion resistant magnesium alloys.* Journal of Materials & Manufacturing, 1995. **104**: p. 352-357.

[160] G.L. Song, A. Atrens, and M. Dargusch, *Influence of microstructure on the corrosion of diecast AZ91D.* Corrosion Science, 1999. **41**(2): p. 249-273.

[161] G.L. Song, StJohn, D., *The effect of zirconium grain refinement on the corrosion behaviour of magnesium-rare earth alloy MEZ.* Journal of Light Metals, 2002. **2**(1): p. 1-16.

[162] A. Srinivasan, S. Ningshen, U.K. Mudali, U.T.S. Pillai, and B.C. Pai, *Influence of Si and Sb additions on the corrosion behavior of AZ91 magnesium alloy.* Intermetallics, 2007. **15**(12): p. 1511-1517.

[163] N.N. Aung and W. Zhou, *Effect of grain size and twins on corrosion behaviour of AZ31B magnesium alloy.* Corrosion Science, 2010. **52**(2): p. 589-594.

[164] G. Ben Hamu, D. Eliezer, and L. Wagner, *The relation between severe plastic deformation microstructure and corrosion behavior of AZ31 magnesium alloy.* Journal of Alloys and Compounds, 2009. **468**(1-2): p. 222-229.

[165] N. Birbilis, K.D. Ralston, S. Virtanen, H.L. Fraser, and C.H.J. Davies, *Grain character influences on corrosion of ECAPed pure magnesium.* Corrosion Engineering Science and Technology, 2010. **45**(3): p. 224-230.

[166] C.O. Hoog, N. Birbilis, and Y. Estrin, *Corrosion of pure Mg as a function of grain size and processing route.* Advanced Engineering Materials, 2008. **10**(6): p. 579-582.

[167] Y.H. Jang, S.S. Kim, C.D. Yim, C.G. Lee, and S.J. Kim, *Corrosion behaviour of friction stir welded AZ31B Mg in 3.5% NaCl solution.* Corrosion Engineering Science and Technology, 2007. **42**(2): p. 119-122.

[168] E. Sikora, X.J. Wei, and B.A. Shaw, *Corrosion behavior of nanocrystalline bulk Al-Mg-based alloys.* Corrosion, 2004. **60**(4): p. 387-398.

[169] K.D. Ralston, N. Birbilis, and C.H.J. Davies, *Revealing the relationship between grain size and corrosion rate of metals.* Scripta Materialia, 2010. **63**(12): p. 1201-1204.

[170] M. Andrei, A. Eliezer, P.L. Bonora, and E.M. Gutman, *DC and AC polarisation study on magnesium alloys - Influence of the mechanical deformation.* Materials and Corrosion - Werkstoffe Und Korrosion, 2002. **53**(7): p. 455-461.

[171] R.L. Xin, M.Y. Wang, J.C. Gao, P. Liu, and Q. Liu, *Effect of microstructure and texture on corrosion resistance of magnesium alloy.* Materials Research, Pts 1 and 2, 2009. **610-613**: p. 1160-1163.

[172] P. Schmutz, V. Guillaumin, R.S. Lillard, J.A. Lillard, and G.S. Frankel, *Influence of dichromate ions on corrosion processes on pure magnesium.* Journal of the Electrochemical Society, 2003. **150**(4): p. B99-B110.

[173] R.A. Kaya, H. Cavusoglu, C. Tanik, A.A. Kaya, O. Duygulu, Z. Mutlu, E. Zengin, and Y. Aydin, *The effects of magnesium particles in posterolateral spinal fusion: an experimental in vivo study in a sheep model.* Journal of Neurosurgery - Spine, 2007. **6**(2): p. 141-149.

[174] S. Jalota, S.B. Bhaduri, and A.C. Tas, *Using a synthetic body fluid (SBF) solution of 27 mM HCO3- to make bone substitutes more osteointegrative.* Materials Science & Engineering C - Biomimetic and Supramolecular Systems, 2008. **28**(1): p. 129-140.

[175] X.B. Zhang, G.Y. Yuan, J.L. Niu, P.H. Fu, and W.J. Ding, *Microstructure, mechanical properties, biocorrosion behavior, and cytotoxicity of as-extruded Mg-Nd-Zn-Zr alloy with different extrusion ratios.* Journal of the Mechanical Behavior of Biomedical Materials, 2012. **9**: p. 153-162.

[176] H. Wang, Y. Estrin, H. Fu, G. Song, and Z. Zuberova, *The effect of pre-processing and grain structure on the bio-corrosion and fatigue resistance of magnesium alloy AZ31.* Advanced Engineering Materials, 2007. **9**(11): p. 967-972.

[177] F. Witte, F. Feyerabend, P. Maier, J. Fischer, M. Stormer, C. Blawert, W. Dietzel, and N. Hort, *Biodegradable magnesium-hydroxyapatite metal matrix composites.* Biomaterials, 2007. **28**(13): p. 2163-2174.

[178] Y. Wang, M. Wei, and J.C. Gao, *Improve corrosion resistance of magnesium in simulated body fluid by dicalcium phosphate dihydrate coating.* Materials Science & Engineering C - Biomimetic and Supramolecular Systems, 2009. **29**(4): p. 1311-1316.

[179] G.L. Song, A. Atrens, and D.H. St. John, *Magnesium technology*, ed. J. Hryn2001, New Orleans, LA: TMS. p. 255.

[180] N.I.Z. Abidin, D. Martin, and A. Atrens, *Corrosion of high purity Mg, AZ91, ZE41 and Mg2Zn0.2Mn in Hank's solution at room temperature.* Corrosion Science, 2011. **53**(3): p. 862-872.

[181] X.N. Gu, N. Li, Y.F. Zheng, and L.Q. Ruan, *In vitro degradation performance and biological response of a Mg-Zn-Zr alloy.* Materials Science and Engineering B - Advanced Functional Solid-State Materials, 2011. **176**(20): p. 1778-1784.

[182] Y.B. Ren, H. Wang, J.J. Huang, B.C. Zhang, and K. Yang, *Study of biodegradation of pure magnesium.* Key Engineering Materials, 2007. **342-343**: p. 601-604.

[183] W.F. Ng, K.Y. Chiu, and F.T. Cheng, *Effect of pH on the in vitro corrosion rate of magnesium degradable implant material.* Materials Science and Engineering C - Materials for Biological Applications, 2010. **30**(6): p. 898-

903.

[184] M. Alvarez-Lopez, M.D. Pereda, J.A. del Valle, M. Fernandez-Lorenzo, M.C. Garcia-Alonso, O.A. Ruano, and M.L. Escudero, *Corrosion behaviour of AZ31 magnesium alloy with different grain sizes in simulated biological fluids.* Acta Biomaterialia, 2010. **6**(5): p. 1763-1771.

[185] M.B. Kannan, *Influence of microstructure on the in-vitro degradation behaviour of magnesium alloys.* Materials Letters, 2010. **64**(6): p. 739-742.

[186] J.H. Gao, S.K. Guan, Z.W. Ren, Y.F. Sun, S.J. Zhu, and B. Wang, *Homogeneous corrosion of high pressure torsion treated Mg-Zn-Ca alloy in simulated body fluid.* Materials Letters, 2011. **65**(4): p. 691-693.

[187] W.W. He, E.L. Zhang, and K. Yang, *Effect of Y on the bio-corrosion behavior of extruded Mg-Zn-Mn alloy in Hank's solution.* Materials Science & Engineering C - Materials for Biological Applications, 2010. **30**(1): p. 167-174.

[188] N.T. Kirkland, N. Birbilis, and M.P. Staiger, *Assessing the corrosion of biodegradable magnesium implants: A critical review of current methodologies and their limitations.* Acta Biomaterialia, 2012. **8**(3): p. 925-936.

[189] G.L. Song, A. Atrens, X.L. Wu, and B. Zhang, *Corrosion behaviour of AZ21, AZ501 and AZ91 in sodium chloride.* Corrosion Science, 1998. **40**(10): p. 1769-1791.

[190] Y.C. Li, C. Wen, D. Mushahary, R. Sravanthi, N. Harishankar, G. Pande, and P. Hodgson, *Mg-Zr-Sr alloys as biodegradable implant materials.* Acta Biomaterialia, 2012. **8**(8): p. 3177-3188.

[191] N.I.Z. Abidin, A.D. Atrens, D. Martin, and A. Atrens, *Corrosion of high purity Mg, Mg2Zn0.2Mn, ZE41 and AZ91 in Hank's solution at 37 degrees C.* Corrosion Science, 2011. **53**(11): p. 3542-3556.

[192] G.O. Hofmann, *Biodegradable implants in orthopaedic surgery - A review on the state-of-the-art.* Clinical Materials, 1992. **10**(1-2): p. 75-80.

[193] R. Erbel, C. Di Mario, J. Bartunek, J. Bonnier, B. de Bruyne, F.R. Eberli, P. Erne, M. Haude, B. Heublein, M. Horrigan, C. Ilsley, D. Bose, J. Koolen, T.F. Luscher, N. Weissman, and R. Waksman, *Temporary scaffolding of coronary arteries with bioabsorbable magnesium stents: A prospective, non-randomised multicentre trial.* Lancet, 2007. **369**(9576): p. 1869-1875.

[194] E. Willbold, A.A. Kaya, R.A. Kaya, F. Beckmann, and F. Witte, *Corrosion of magnesium alloy AZ31 screws is dependent on the implantation site.* Materials Science and Engineering B - Advanced Functional Solid-State Materials, 2011. **176**(20): p. 1835-1840.

[195] X.Y. Chang, *Degradation mechanism and surface modification of biomedical magnesium alloy*, in *Department of physics and materials science.* 2009, City University of Hong Kong: Hong Kong. p. 9.

[196] H. Waizy, J.M. Seitz, J. Reifenrath, A. Weizbauer, F.W. Bach, A. Meyer-Lindenberg, B. Denkena, and H. Windhagen, *Biodegradable magnesium implants for orthopedic applications.* Journal of Materials Science, 2013.

**48**(1): p. 39-50.
[197] D.W. Holdsworth and M.M. Thornton, *Micro-CT in small animal and specimen imaging.* Trends in Biotechnology, 2002. **20**(8): p. S34-S39.
[198] J. Jain, P. Cizek, W.J. Poole, and M.R. Barnett, *Precipitate characteristics and their effect on the prismatic-slip-dominated deformation behaviour of an Mg-6 Zn alloy.* Acta Materialia, 2013. **61**(11): p. 4091-4102.
[199] E. Nembach, *Particle strengthening of metals and alloys.* 1997, New York: John Wiley.
[200] P.M. Kelly, A. Jostsons, R.G. Blake, and J.G. Napier, *The determination of foil thickness by scanning transmission electron microscopy.* Physica status solidi (A), 1975. **31**(2): p. 771-780.
[201] D.B. Williams and C.B. Cater, *Transmission electron microscopy: A textbook for materials science*2009, New York, USA: Springer. P. 352.
[202] T. Kokubo and H. Takadama, *How useful is SBF in predicting in vivo bone bioactivity?* Biomaterials, 2006. **27**(15): p. 2907-2915.
[203] C.S. Roberts, *Magnesium and its alloys*, ed. J.H. Hollomon1960, USA. p.66.
[204] S. Wasiur-Rahman and M. Medraj, *Critical assessment and thermodynamic modeling of the binary Mg-Zn, Ca-Zn and ternary Mg-Ca-Zn systems.* Intermetallics, 2009. **17**(10): p. 847-864.
[205] P.M. Jardim, G. Solorzano, and J.B. Vander Sande, *Precipitate crystal structure determination in melt spun Mg-1.5wt%Ca-6wt%Zn alloy.* Microscopy and Microanalysis, 2002. **8**(6): p. 487-496.
[206] C.L. Mendis, K. Oh-ishi, and K. Hono, *Enhanced age hardening in a Mg-2.4 at.% Zn alloy by trace additions of Ag and Ca.* Scripta Materialia, 2007. **57**(6): p. 485-488.
[207] L.Y. Wei, G.L. Dunlop, and H. Westengen, *Precipitation hardening of Mg-Zn and Mg-Zn-Re alloys.* Metallurgical and Materials Transactions A - Physical Metallurgy and Materials Science, 1995. **26**(7): p. 1705-1716.
[208] J.S. Chun and J.G. Byrne, *Precipitate strengthening mechanisms in magnesium zinc alloy single crystals.* Journal of Materials Science, 1969. **4**(10): p. 861-872.
[209] L.L. Rokhlin and A.A. Oreshkina, *Research into the structure of a metastable phase formed during the breakdown of a supersaturated solution in magnesium-zinc alloy.* Fiz. Met. Metalloved., 1988. **66**: p. 559-562.
[210] M.A. Easton and D.H. StJohn, *A model of grain refinement incorporating alloy constitution and potency of heterogeneous nucleant particles.* Acta Materialia, 2001. **49**(10): p. 1867-1878.
[211] M. Easton and D. StJohn, *Grain refinement of aluminum alloys: Part I. The nucleant and salute paradigms - A review of the literature.* Metallurgical and Materials Transactions A - Physical Metallurgy and Materials Science, 1999. **30**(6): p. 1613-1623.
[212] M. Easton and D. StJohn, *Grain refinement of aluminum alloys: Part II. Confirmation of, and a mechanism for, the solute paradigm.* Metallurgical and Materials Transactions A - Physical Metallurgy and Materials Science,

1999. **30**(6): p. 1625-1633.

[213] D.H. StJohn, M. Qian, M.A. Easton, P. Cao, and Z. Hildebrand, *Grain refinement of magnesium alloys.* Metallurgical and Materials Transactions A - Physical Metallurgy and Materials Science, 2005. **36A**(7): p. 1669-1679.

[214] Y.C. Lee, A.K. Dahle, and D.H. StJohn, *The role of solute in grain refinement of magnesium.* Metallurgical and Materials Transactions A - Physical Metallurgy and Materials Science, 2000. **31**(11): p. 2895-2906.

[215] G. Mima and Y. Tanaka, *The ageing characteristics of Magnesium-4wt% Zinc alloy.* Transactions of Journal of Japan Institute of Metals and Materials (JIM), 1971. **12**: p. 71-75.

[216] Y. Murakami, O. Kawano, and H. Tamura, *On precipitation phenomena in magnesium-zinc alloys.* Memoirs of the Faculty of Engineering, Kyoto University, 1962. **24**: p. 93.

[217] G. Mima and Y. Tanaka, *Mechanism of precipitation hardening of magnesium-zinc alloys.* Transactions of the Japan Institute of Metals, 1971. **12**(5): p. 323-328.

[218] H. Kalb, A. Rzany, and B. Hensel, *Impact of microgalvanic corrosion on the degradation morphology of WE43 and pure magnesium under exposure to simulated body fluid.* Corrosion Science, 2012. **57**: p. 122-130.

[219] Y.W. Song, D.Y. Shan, R.S. Chen, F. Zhang, and E.H. Han, *Biodegradable behaviors of AZ31 magnesium alloy in simulated body fluid.* Materials Science & Engineering C - Biomimetic and Supramolecular Systems, 2009. **29**(3): p. 1039-1045.

[220] D.R. Lide, *CRC Handbook of chemistry and physics,* 2004: CRC Press, Boca Raton.

[221] J.W. Chang, X.W. Guo, S.M. He, P.H. Fu, L.M. Peng, and W.J. Ding, *Investigation of the corrosion for Mg-xGd-3Y-0.4Zr (x=6,8,10,12 wt%) alloys in a peak-aged condition.* Corrosion Science, 2008. **50**(1): p. 166-177.

[222] M. Kiryuu, H. Okumura, S. Kamado, Y. Kojima, R. Ninomiya, and I. Nakatsugawa, *Corrosion resistance of heat resistant magnesium alloys containing heavy rare earth elements.* Journal of Japan Institute of Light Metals, 1996. **46**: p. 39-44.

[223] D. Orlov, K.D. Ralston, N. Birbilis, and Y. Estrin, *Enhanced corrosion resistance of Mg alloy ZK60 after processing by integrated extrusion and equal channel angular pressing.* Acta Materialia, 2011. **59**(15): p. 6176-6186.

[224] K.D. Ralston, D. Fabijanic, and N. Birbilis, *Effect of grain size on corrosion of high purity aluminium.* Electrochimica Acta, 2011. **56**(4): p. 1729-1736.

[225] G.R. Argade, S.K. Panigrahi, and R.S. Mishra, *Effects of grain size on the corrosion resistance of wrought magnesium alloys containing neodymium.* Corrosion Science, 2012. **58**: p. 145-151.

[226] D.A. Jones, *Principles and prevention of corrosion,* 1996, New York: Prentice- Hall.

[227] K.D. Ralston and N. Birbilis, *Effect of grain size on corrosion: a review.* Corrosion Science, 2010. **66**(7): p. 075005-075005-13.

[228] B. Viswanath and N. Ravishankar, *Controlled synthesis of plate-shaped hydroxyapatite and implications for the morphology of the apatite phase in bone.* Biomaterials, 2008. **29**(36): p. 4855-4863.

[229] R. Narayanan, T.Y. Kwon, and K.H. Kim, *Direct nanocrystalline hydroxyapatite formation on titanium from ultrasonated electrochemical bath at physiological pH.* Materials Science & Engineering C - Biomimetic and Supramolecular Systems, 2008. **28**(8): p. 1265-1270.

[230] D.J. Blackwood and K.H.W. Seah, *Electrochemical cathodic deposition of hydroxyapatite: Improvements in adhesion and crystallinity.* Materials Science & Engineering C - Biomimetic and Supramolecular Systems, 2009. **29**(4): p. 1233-1238.

[231] P. Habibovic, J.P. Li, C.M. van der Valk, G. Meijer, P. Layrolle, C.A. van Blitterswijk, and K. de Groot, *Biological performance of uncoated and octacalcium phosphate-coated Ti6A14V.* Biomaterials, 2005. **26**(1): p. 23-36.

[232] S. Kamakura, Y. Sasano, H. Homma, O. Suzuki, M. Kagayama, and K. Motegi, *Implantation of octacalcium phosphate (OCP) in rat skull defects enhances bone repair.* Journal of Dental Research, 1999. **78**(11): p. 1682-1687.

[233] Y. Song, S.X. Zhang, J.A. Li, C.L. Zhao, and X.N. Zhang, *Electrodeposition of Ca-P coatings on biodegradable Mg alloy: In vitro biomineralization behavior.* Acta Biomaterialia, 2010. **6**(5): p. 1736-1742.